Nonlinear Dynamics of a Slender Flexible Cylinder Subjected to Axial Flow

by

Yahya Modarres-Sadeghi

Department of Mechanical Engineering
McGill University
Montréal, Québec, Canada

June 2006

A Thesis submitted to McGill University
in partial fulfillment of the requirements of the degree of
Doctor of Philosophy.

Library and
Archives Canada

Published Heritage
Branch

395 Wellington Street
Ottawa ON K1A 0N4
Canada

Bibliothèque et
Archives Canada

Direction du
Patrimoine de l'édition

395, rue Wellington
Ottawa ON K1A 0N4
Canada

Your file Votre référence
ISBN: 978-0-494-27820-8
Our file Notre référence
ISBN: 978-0-494-27820-8

NOTICE:
The author has granted a non-exclusive license allowing Library and Archives Canada to reproduce, publish, archive, preserve, conserve, communicate to the public by telecommunication or on the Internet, loan, distribute and sell theses worldwide, for commercial or non-commercial purposes, in microform, paper, electronic and/or any other formats.

The author retains copyright ownership and moral rights in this thesis. Neither the thesis nor substantial extracts from it may be printed or otherwise reproduced without the author's permission.

AVIS:
L'auteur a accordé une licence non exclusive permettant à la Bibliothèque et Archives Canada de reproduire, publier, archiver, sauvegarder, conserver, transmettre au public par télécommunication ou par l'Internet, prêter, distribuer et vendre des thèses partout dans le monde, à des fins commerciales ou autres, sur support microforme, papier, électronique et/ou autres formats.

L'auteur conserve la propriété du droit d'auteur et des droits moraux qui protège cette thèse. Ni la thèse ni des extraits substantiels de celle-ci ne doivent être imprimés ou autrement reproduits sans son autorisation.

In compliance with the Canadian Privacy Act some supporting forms may have been removed from this thesis.

While these forms may be included in the document page count, their removal does not represent any loss of content from the thesis.

Conformément à la loi canadienne sur la protection de la vie privée, quelques formulaires secondaires ont été enlevés de cette thèse.

Bien que ces formulaires aient inclus dans la pagination, il n'y aura aucun contenu manquant.

Canada

Abstract

This thesis deals with the nonlinear dynamics of a vertical slender flexible cylinder supported at both ends and subjected to axial flow. The goal is to study the dynamical behaviour of this system from a nonlinear point of view, both theoretically and experimentally.

A weakly nonlinear model is derived assuming that the cylinder centreline is extensible. Nonlinear Euler-Bernoulli beam theory is used for the structure and, the fluid forces acting on the cylinder are assumed to be inviscid, frictional and hydrostatic ones. The derivation of the equations of motion is carried out in a Lagrangian framework, and the resultant equations are correct to third order of magnitude. These nonlinear partial differential equations are then recast in nondimensional form and discretized by using Galerkin's technique, giving a set of nonlinear second-order ordinary differential equations.

Houbolt's finite difference method and AUTO are used as two numerical methods to solve the resulting set of ordinary differential equations. The centre manifold reduction method is also used as an analytical method to study the behaviour of the system in the vicinity of the pitchfork bifurcation point.

The results for a cylinder with various boundary conditions are presented in the form of bifurcation diagrams with flow velocity as the independent variable, supported by time histories, phase-plane plots, PSD plots and Poincaré maps. The influence of different parameters on the behaviour of the system is also investigated.

Three series of experiments were conducted on vertical clamped-clamped cylinders. In the first series of experiments, the downstream end of the clamped-clamped cylinder was free to slide axially, while in the second series of experiments, the downstream end was fixed. The influence of externally applied axial compression has also been studied in the second series of experiments. In the third series of experiments, a more flexible cylinder was used, and the effect of externally applied axial compression on the dynamic instability of the cylinder was also studied.

Sommaire

Cette thèse traite de la dynamique non-linéaire d'un cylindre vertical flexible mince qui est soutenu aux deux extrémités et qui est soumis à un écoulement axial. Le but est d'étudier le comportement dynamique de ce système d'un point de vue non-linéaire, théoriquement et expérimentalement.

Un modèle faiblement non-linéaire est dérivé supposant que la ligne centrale du cylindre est extensible. La théorie non-linéaire de poutre d'Euler-Bernoulli est employée pour la structure et on suppose que les forces dues au fluide agissant sur le cylindre sont (i) non visqueuses, (ii) visqueuses et (iii) hydrostatiques. La dérivation des équations du mouvement est effectuée dans un cadre Lagrangien, et les équations résultantes sont correctes au troisième ordre de grandeur. Ces équations différentielles partielles non-linéaires sont alors remaniées sous une forme nondimensionalisée et discrétisées en employant la technique de Galerkin, donnant un ensemble d'équations ordinaires de second ordre non-linéaires.

La méthode des differences finis de Houbolt et l'AUTO sont employés comme deux méthodes numériques pour résoudre l'ensemble des équations ordinaires. La méthode des variétés centrales est également employée comme méthode analytique pour étudier le comportement du système à proximité du point de bifurcation de fourche (pitchfork).

Les résultats pour un cylindre avec de divers états de frontière sont présentés sous forme de diagrammes de bifurcation avec la vitesse d'écoulement comme la variable indépendante, et sont complétés par des lois horaires, portraits de phase, les tracés DSP et cartes de Poincaré. L'influence de différents paramètres sur le comportement du système est également étudiée.

Trois séries d'expériences sont entreprises sur les cylindres verticaux aux bouts encastrés. Dans la première série d'expériences, l'extrémité basse du cylindre encastré-encastré est libre à glisser axialement, tandis que dans la deuxième série d'expériences, l'extrémité basse est fixe. L'influence de la compression axiale extérieurement appliquée est également étudiée dans la deuxième série d'expériences. Dans la troisième série d'expériences, un cylindre plus flexible est utilisé et l'effet de la compression axiale extérieurement appliquée sur l'instabilité dynamique du cylindre est également étudié.

Acknowledgements

I would like to express my deepest gratitude to Professor Païdoussis for his endless support, invaluable guidance and constant encouragement throughout the years. His depth of knowledge, innovative ideas and enthusiasm are quite unique and his pedagogical approach exceptional. In fact Professor Païdoussis' character has inspired me to choose an academic carrier in the first place. He also gave me the opportunity to participate in several international conferences, where I was able to meet experts in the field from whom I learned much.

I am indebted to Professor Misra for his consistent support, his encouragement and his advices. His insightful questions and perceptive suggestions were very useful to me.

Very special thanks go to Dr. Christian Semler for his co-supervision of this work, his help with methods of solution and analysis, his suggestions during our discussions and on this thesis. While this thesis has much profited from his insight and knowledge, his friendship has become equally invaluable to me.

Special thanks are due to Dr. Eugeni Grinevich for his technical help with the experiments, to Dr. Waldir Pinto for his help with Labview software, to Professor Eusebius Doedel for his software AUTO and for his time and suggestions, to Professor Emmanuel de Langre for our discussions on long cylinders in axial flow, as well as his suggestions on extensible cantilever cylinder.

I am grateful to Mrs. Mary Fiorilly-St-Germain for her help with the administrative tasks.

The constructive discussions with fellow colleagues in the fluid-structure interaction research group: Konstantinos Karagiozis, Liaosha Tang, James Wang, Matthew Wadham-Gagnon and Frederick Gosselin are greatly appreciated, and so is their friendship.

Very special thanks go to my parents for their support and encouragement.

And, thank you Pari, for your presence, your patience, your support and your love.

Statement of Contribution to Original Knowledge

The nonlinear dynamics of a slender flexible cylinder supported at both ends and subjected to axial flow is the subject of this thesis study. To the author's best knowledge, this is the first time that a study of such a system has been undertaken from a nonlinear point of view, both theoretically and experimentally. Below is a summary of the main contributions of this thesis to original knowledge.

1. A detailed derivation of a nonlinear model for a slender flexible cylinder supported at both ends and subjected to axial flow is undertaken with the assumption of an extensible centreline. This is the first nonlinear model for such a system.

2. Various dynamical tools, such as bifurcation diagrams, phase plane plots, power spectral densities and Poincaré maps are used to conduct an in-depth nonlinear analysis of the system with various boundary conditions (pinned or clamped at both ends, or with mixed supports); the influence of various parameters on the system behaviour is studied. The existence of post-divergence dynamic instabilities and a quasiperiodic route to chaos are observed theoretically. The centre manifold reduction theory has also been used as a tool of modern nonlinear dynamics theory to study analytically the behaviour of the system in the neighbourhood of the pitchfork bifurcation. This nonlinear analysis is believed to be the first.

3. A series of experiments are conducted on vertical cylinders clamped at both ends and subjected to axial flow. The post-divergence dynamic instability was observed experimentally, confirming the behaviour obtained from the theoretical analysis. The influence of externally applied compression on the dynamical behaviour of the system was investigated experimentally as well. These are considered to be the first series of experiments on such system from a nonlinear point of view.

Contents

1.1 Motivation and a review of the literature

List of Symbols

A	cross-sectional area of the cylinder
C_b	base drag coefficient
c_b	normalized base drag coefficient
C_D	form drag coefficient
C_{DP}	form drag coefficient
c_d	normalized form drag coefficient
C_f	friction drag coefficient
C_N	frictional coefficient in the normal direction
c_n	normalized frictional coefficient in the normal direction
C_T	frictional coefficient in the tangential direction
c_t	normalized frictional coefficient in the transverse direction
D_{ch}	channel diameter
D_h	hydraulic diameter
E^*	a viscoelastic constant
EI	flexural rigidity of the cylinder
F_A	inviscid hydrodynamic force per unit length
F_L	viscous force per unit length in the longitudinal direction
F_N	viscous force per unit length in the normal direction
F_{px}	hydrostatic pressure force in the x-direction
F_{py}	hydrostatic pressure force in the y-direction
h	a hydraulic confinement coefficient
I	area-moment of inertia
i	angle between the relative fluid-body velocity and the centreline of the body
$\vec{I}$	momentum of the fluid
$\mathbf{J}$	Jacobian
L	cylinder length
$\mathcal{L}$	Lagrangian of the system

M	added mass of the fluid per unit length
$\mathcal{M}$	bending moment
m	mass per unit length of the cylinder
N_t	total Number of modes
N_u	number of modes in the axial direction
N_v	number of modes in the transverse direction
$\mathbf{P}$	modal matrix
p_j	generalized coordinates in the axial direction
Q	lateral shear force
q_j	generalized coordinates in the transverse direction
s	curvilinear coordinate along the cylinder
T	axial tension
t	time
$\mathcal{T}$	kinetic energy
$\bar{T}$	externally imposed uniform tension
u	displacement in x-direction
U	flow velocity
U_f	axial flow velocity relative to an axially deforming cylinder
$\mathcal{U}$	nondimensional flow velocity
v	displacement in y-direction
V	potential energy
V_G	gravitational energy
V_S	strain energy
w	displacement in z-direction
x,y,z	Eulerian coordinates
X,Y,Z	Lagrangian coordinates
γ	nondimensional gravity coefficient
$\bar{\Gamma}$	nondimensional externally imposed uniform tension
Δ	pre-shortening

δ, $\bar{\delta}$	a parameter signifying that the downstream end is free to slide axially or not
δ	variational operator (in Chapter 2)
δ_j	modal damping
δ_{ij}	Kronecker delta
ΔW	work done by the fluid on the cylinder during a cycle of oscillation
ε	slenderness ratio
ϵ	order of magnitude
ε^*	axial strain
ζ	nondimensional displacement in the longitudinal direction
η	nondimensional displacement in the transverse direction
θ_1	angle between the centreline of the cylinder and the X-axis
θ_2	angle between the relative fluid-body velocity and the X-axis
κ	curvature
ν	Poisson's ratio
ν^*	kinematic viscosity
Π_0	nondimensional measures of axial flexibility
$\bar{\Pi}$	nondimensional pressurization
τ	nondimensional time
Φ	gravitational potential per unit mass
ϕ_j	eigenfucntions in transverse direction
χ	a nondimensional added mass coefficient
ψ_j	eigenfucntions in longitudinal direction
ω	nondimensional complex frequency
Ω	radian frequency

1. Introduction

1.1 Motivation and a review of the literature

The behaviour of slender structures subjected to flow is a rather complex phenomenon mainly due to the complexity in the flow. In general, the angle of incidence of the flow with respect to the structure can be arbitrary, but to model these systems, an idealization is often made that the flow is nominally either purely normal to the cylinder axis (cross-flow), or purely axial with respect to the axis (axial flow). Cases of structures in cross-flow have been studied extensively, and Blevins (1994) in his book has collected a series of theoretical and experimental work on these systems, together with their applications. Structures in axial flow have been studied extensively, as well. Païdoussis (1998, 2004) has discussed the work on structures subjected to axial flow including the pipes conveying flow, cylinders, shells and plates in axial flow in a two-volume book.

This thesis deals with the case of structures subjected to axial flow; in particular, the system of a slender flexible cylinder subjected to external axial flow is studied. This system can be found in many engineering constructions, including nuclear reactor fuel-element bundles, monitoring tubes and control rods, boiling water reactors, gas-cooled reactor fuel clusters, steam generators, heat exchanger tubes, Dracone barges and towed acoustic arrays used in oil exploration, etc. (see Figure 1-1), in all of which, the mean flow is mainly axial [see Païdoussis (2004) for more applications]. The dynamics of cylinders in axial flow is also dynamically similar to that of axially moving one-dimensional structures in quiescent fluid, such as paper web in paper-making, and travelling chains, bands and tapes (Mote, 1968; Pramila, 1987). Païdoussis (1980) reported a number of case histories involving problems caused by flow-induced vibration, including those due to the external axial flow. However, the study of this thesis is not only motivated by these industrial applications but is also "curiosity driven" (Païdoussis, 1993). There have been many studies on slender cylinders in axial flow so far, using linear models, as will be discussed in what follows. Using a linear model, one can predict reliably the first point of instability, but what is predicted thereafter needs to be proven by using nonlinear theories. This has been done for a cantilever cylinder, supported by a series of experiments. The aim here is to derive a nonlinear model and conduct a series of experiments to observe the behaviour of a cylinder supported at both ends, in axial flow, especially after the first point of instability.

In this Introduction, a review of the previous studies on the system of a slender cylinder subjected to axial flow will be presented, starting from the studies done using the linear models. Then a review of the linear work on very similar systems is presented, followed by a review of the nonlinear as well as experimental studies conducted so far on a cylinder in axial flow. The problem of a pipe conveying fluid, which is very similar to the present problem and is known as a "paradigm in the study of fluid-structure interaction" (Païdoussis, 1991) will be reviewed next, to give the reader a flavour of the typical behaviour of such systems. The reader is also referred to Païdoussis (1998, 2004) for a comprehensive study on structures in axial flow.

According to Païdoussis (2004), most of the early interest in the low-amplitude vibration of cylindrical structures in axial flow was directly related to the power generating industry and was conducted for one of the following reasons: (i) measurement of the amplitude of vibration of particular cylindrical structure configurations, modelling nuclear reactor components and flow conditions; (ii) understanding the causes of vibration; (iii) development of means for predicting the vibration amplitude. Païdoussis (2004) mentions some of the very early publications on this field: in the United States (Burgreen et al. 1958; Shields 1960; Quinn 1962, 1965; Pavilica and Marshall 1966), in France (SOGREAH 1962), in Sweden (Roström and Andersson 1964a,b; Roström 1964), and in Canada (Païdoussis 1965, 1966a).

1.2 A slender flexible cylinder in external axial flow: linear studies

1.2.1 Linear model

The most complete linear model for a slender cylinder subjected to axial flow was presented by Païdoussis (1973), after some earlier work by Hawthorne (1961) and Païdoussis (1966b). One of the first specific studies on the dynamics of a slender flexible cylinder subjected to axial flow was by Hawthorne (1961) and was concerned with the stability of the Dracone barge, which is a long flexible towed tubular container with tapering ends, designed to carry oil and other liquids lighter than sea-water. Hawthorne's work was extended and generalized for cylinders with any boundary conditions and supported by experiments by Païdoussis (1966b,c). This model itself was later extended and corrected leading to the most complete linear model of Païdoussis (1973). This work is of great importance for this thesis, because the main ideas behind the derivation of the nonlinear equations of motion come from there. Here we follow Païdoussis' derivation, for the linear model.

The cylinder was assumed to be a flexible cylindrical body of circular cross-section, immersed in an incompressible fluid of density ρ with uniform flow velocity U parallel to x-axis, which coincides with the position of rest of the cylinder axis (Figure 1-2). Small lateral motions of the cylinder were considered during which (i) no separation occurs in cross-flow and (ii) the fluid forces on each element of the cylinder may be assumed to be the same as those acting on a corresponding element of a long straight cylinder of the same cross-sectional area and inclination.

When the cylinder is given a small lateral displacement, $y(x,t)$, from the straight position, the resultant relative transverse velocity between the cylinder and the flow is (Lighthill, 1960)

$$v(x,t)=\frac{\mathrm{D}y}{\mathrm{D}t}=\frac{\partial y}{\partial t}+U\frac{\partial y}{\partial x}. \tag{1-1}$$

This lateral flow is identical to the 2-D potential flow that would result from the motion of the cylinder with velocity $v(x,t)$ through fluid at rest. If M is the added mass of the fluid per unit length, the momentum of this flow is considered to be Mv per unit length of cylinder. The rate of change of this momentum per unit length gives rise to an equal and opposite lateral force on the cylinder, which is the inviscid force per unit length (Lighthill, 1960), namely

$$F_A=\frac{\mathrm{D}(Mv)}{\mathrm{D}t}=\left(\frac{\partial}{\partial t}+U\frac{\partial}{\partial x}\right)\left[M\left(\frac{\partial y}{\partial t}+U\frac{\partial y}{\partial x}\right)\right]. \tag{1-2}$$

There are also viscous forces per unit length (F_N and F_L in the normal and longitudinal directions, respectively) and hydrostatic pressure forces (F_{px} and F_{py} in the x- and y-direction, respectively) acting on the cylinder. An element of the cylinder undergoing small oscillations with the forces acting on it is shown in Figure 1-3, in which Q is the lateral shear force, $\mathcal{M}$ the bending moment, T the axial tension.

Taylor (1952) discussed the viscous forces acting on a cylinder and explained their dependence on the exact nature of surface roughness and proposed the following relation:

$$F_N = \tfrac{1}{2}\rho D U^2 \left(C_f \sin i + C_{DP} \sin^2 i\right), \tag{1-3}$$

$$F_L = \tfrac{1}{2}\rho D U^2 C_f \cos i, \tag{1-4}$$

where C_f and C_{DP} are the coefficients associated with friction and form drag, respectively, for a cylinder in cross-flow, and

$$i = \tan^{-1}\left(\frac{\partial y}{\partial x}\right) + \tan^{-1}\left(\frac{\partial y/\partial t}{U}\right). \tag{1-5}$$

For small motions, however, the linearized and more general form of relations (1-3) and (1-4) is

$$F_N = \tfrac{1}{2}\rho D U^2 C_N \left(\frac{\partial y}{\partial t} + U\frac{\partial y}{\partial x}\right) + \tfrac{1}{2}\rho D C_D \frac{\partial y}{\partial t}, \tag{1-6}$$

$$F_L = \tfrac{1}{2}\rho D U^2 C_T, \tag{1-7}$$

where C_N and C_T are the frictional coefficients in the normal and tangential directions, respectively, and C_D is the form drag coefficient.

The hydrostatic pressure forces have been derived by assuming that the element of Figure 1-3 is momentary frozen and immersed in fluid on all sides. Then there will be additional forces pA and $pA + \left[\partial(pA)/\partial x\right]\delta x$, on the other faces of the element. The resultant of these forces and of forces $F_{px}\delta x$ and $F_{py}\delta x$ is the buoyancy force. Assuming that the pressure is a linear function of x, the relations for hydrostatic frictional forces are

$$-F_{px} = -\frac{\partial p}{\partial x}A + \frac{\partial(pA)}{\partial x}, \tag{1-8}$$

$$F_{py} = \frac{\partial}{\partial x}\left(pA\frac{\partial y}{\partial x}\right). \tag{1-9}$$

Considering the relation

$$(T+pA)_L = \tfrac{1}{2}\rho D^2 U^2 C_b, \tag{1-10}$$

for the tension and pressure terms at the downstream end of the cylinder in the case of a free end, the resulting linear equation of motion for small lateral motions, derived using force and moment balances is (Païdoussis, 1973)

$$\begin{aligned}
&\left(E^{*}\frac{\partial}{\partial t}+E\right)I\frac{\partial^4 y}{\partial x^4}+\chi\rho A\left(\frac{\partial}{\partial t}+U\frac{\partial}{\partial x}\right)^2-\biggl\{\delta\left[\overline{T}+(1-2v)\left(\overline{pA}\right)\right]+\tfrac{1}{2}\rho D^2U^2(1-\delta)C_b\\
&+\left[\tfrac{1}{2}\rho DU^2C_T\left(1+\frac{D}{D_h}\right)+(m-\rho A)g\right]\left[\left(1-\tfrac{1}{2}\delta\right)L-x\right]\biggr\}\frac{\partial^2 y}{\partial x^2}+\tfrac{1}{2}\rho DU^2C_N\left(\frac{\partial y}{\partial t}+U\frac{\partial y}{\partial x}\right)\\
&+\tfrac{1}{2}\rho DC_D\frac{\partial y}{\partial t}+\left[(m-\rho A)g+\tfrac{1}{2}\rho DU^2C_N\left(\frac{D}{D_h}\right)\right]\frac{\partial y}{\partial x}+m\frac{\partial^2 y}{\partial t^2}=0,
\end{aligned} \tag{1-11}$$

where U is the flow velocity; A and L are the cross-sectional area and the length of the cylinder, respectively; D_h is the hydraulic diameter; C_b is the base drag coefficient; C_N and C_T are the frictional coefficients in the normal and tangential directions, respectively; C_D is the form drag coefficient; m is the mass per unit length of the cylinder; χ is an added mass coefficient; v is Poisson's ratio; EI is the flexural rigidity of the cylinder; E^* is the corresponding viscoelastic constant, assuming dissipation in the cylinder to be of the Kelvin-Voigt type; $\delta=0$ signifies that the downstream end is free to slide axially, and $\delta=1$ if the supports do not allow net axial extension. Solution of this equation, in dimensionless form, subject to appropriate boundary conditions was obtained via the Galerkin procedure (and by other methods). In Section 1.2.2 we shall discuss some of the results obtained.

1.2.2 Linear results

The dimensionless complex frequency ω for cylinders with simply supported ends or cantilevered ones was plotted as an Argand diagram with the dimensionless flow velocity $\mathcal{U}$ as the independent parameter (Païdoussis, 1973). In the case of a simply supported cylinder, it was shown (Figure 1-4) that for small flow velocities, the free motion of the cylinder is damped, Im(ω)>0. However, for sufficiently high flow velocities, all the first three modes become purely imaginary in turn. The first crossing of the Im(ω) to the negative half plane corresponds to the onset of instability. In this case, since this occurs while Re(ω)=0, this corresponds to the onset of divergence. The first divergence occurs in the first mode, followed by divergence in the second mode. At slightly higher flow velocity, the negative branches of the first- and second-mode loci coalesce and leave the axis at a point where Im(ω)<0, indicating the onset of coupled-mode flutter. Finally, there is a divergence in the third mode. Also, close spacing in a cluster of cylinders was shown to destabilize the system dramatically.

For a cantilevered cylinder with fairly well-streamlined free end, it was shown that the cylinder loses stability by divergence in its first mode and then is restabilized; subsequently, it loses stability by single-mode or coupled-mode flutter, depending on the system parameters. At higher flow velocities, the cylinder loses stability in the third mode.

Similar work has been done by others, e.g. Grigoryev et al. (1979) and Prokhorovich et al. (1982). Vendhan et al. (1997) studied the stability characteristics of slender flexible cylinders in axial flow by the finite element method. They have used the linear equation of motion derived by Païdoussis (1973) and have reduced it to a variational form so that the finite element approximation can directly follow from it. Their finite element method can solve cases with both ends supported but cannot treat the problem of towed or cantilevered cylinders because in these cases the shape of the end (tapered or blunt) plays a significant role in the stability of the system. Lopes et al. (1999), Augu (1999) and Semler et al. (2002) have also done a great deal of linear work.

1.2.3 Mechanism of instabilities

Païdoussis (1966b, 2004) studied the mechanism of static instability of the cylinder by considering static equilibrium of a cylinder, assuming it to have momentarily taken an arbitrary bowed shape. By analogy to internal flow, it was shown that for a simply supported cylinder, the divergence is due to the term $MU^2\left(\mathrm{d}^2y/\mathrm{d}x^2\right)$ in (1-11) representing a centrifugal force, where $M=\chi\,\rho A$, which tends to exaggerate the assumed initial bow; (for a solitary cylinder in unconfined flow, χ=1 and therefore M=ρA). Eventually, for sufficiently large flow velocity, this force overcomes the flexural restoring force, resulting in divergence. This simple picture is modified by the presence of the viscous force terms. Externally applied tension and pressurization, clearly stabilize the system, as expected. The stabilizing effect of external pressurization becomes obvious considering that the bowed cylinder has a greater surface area on the outer side than on the inner side (Païdoussis, 2004). For a cantilever cylinder, based on work-energy considerations, it was found that divergence is principally dependent on the presence of the tapering end, specifically on having a free-end shape such that $dA/dx \neq 0$; A being the cross-sectional area. The added drag at the free end of the cylinder destabilizes the system for divergence (Païdoussis et al., 2002).

The situation for flutter is more complex and more interesting. The condition for flutter to occur is that the work (ΔW) done by the fluid on the cylinder during a cycle of oscillation be positive, i.e., $\Delta W>0$. This condition for a simply supported cylinder eventually requires that (Païdoussis, 2004)

$$-(c_N - c_T)U^2 \int_0^L \overline{\dot{y}y'}\mathrm{d}x - (c_N U + c^*) \int_0^L \overline{\dot{y}^2}\mathrm{d}x > 0, \tag{1-12}$$

the overbar denoting long time averaging. The second term including the negative sign is always positive. Hence, for inequality (1-12) to be satisfied, presuming that $c_N > c_T$, we must have $\int_0^L \overline{\dot{y}y'}\mathrm{d}x < 0$, which implies that different parts of the cylinder must vibrate in quadrature. This is an effect that can only be produced by the action of the flow (Païdoussis, 1966, 2004). For a cantilever cylinder, the system is stabilized as the free-end shape becomes blunter, yet at the same time it becomes more capable of extracting energy from the fluid (it becomes more strongly nonconservative). It is shown that, in principle, flutter could occur for a blunt downstream end, if only the naturally occurring form (base) drag at the free end could be suppressed. For flutter, increased drag at the free end stabilizes the system (Païdoussis et al., 2002).

1.2.4 Linear studies on similar problems

In practical applications, there exist many cases where the system is in principle very similar to the system of a slender flexible cylinder in axial flow. Some studies on these systems including long cylinders, clustered cylinders, cylinders in annular flow, etc. are reviewed in this sub-section.

1.2.4.1 Towed and very long cylinders. The original work by Païdoussis (1966b) was later extended to the case for towed cylinders (Païdoussis, 1968, 1970a) (see Figure 1-5(a)). Païdoussis (1968) and Sudarsan et al. (1997) conducted some experimental studies on towed flexible cylinders. In general, for a towed flexible cylinder, the typical dynamical behaviour with increasing dimensionless towing speed, if the tail is not blunt and the towrope not too short, may be summarized as follows: (i) at low towing speed, a criss-crossing, essentially rigid-body oscillation develops, with the cylinder inclination opposite to that of the towrope, or alternatively stationary yawing; (ii) at slightly higher speed, a narrow region of stability occurs in some cases, or alternatively a region of yawing/buckling; (iii) at higher speed, second-mode and then third-mode flexural oscillation develops. If the tail is blunt or the towrope is sufficiently short, the system remains stable for all towing speeds. It should be remarked that the dynamics of towed cylinders is of interest not only for the Dracone problem, but also for the towed arrays used in oil exploration. Apart from Hawthorne's (1961) and Païdoussis' (1968, 1970a) original work, studies on towed systems were made by Pao (1970), Païdoussis and Yu (1976), Latorre and Zachariadis (1983), Theodoracatos and Calkins (1986), Dowling (1988a,b), Bhattacharyya et al. (2000) and many others; see, e.g., Païdoussis (2004).

Triantafyllou and Chryssostomidis (1984) studied analytically the problem of a towed slender cylindrical beam and found that, as the cylinder length increases, the divergence persists, except for the blunt cylinders. The dynamics of long, very slender cylinders – modelled as strings, rather than beams by neglecting bending stiffness – has been studied by Triantafyllou and Chryssostomidis (1985). They presented the necessary criteria for a string, hinged at the upstream end and free at the downstream one, to be stable in terms of the flow velocity, added mass, string length and diameter as well as the frictional coefficient. Their results suggest that long cylinders should not flutter at all. The same conclusion was reached by Dowling (1988a). De Langre et al. (2006) showed that contrary to the previous predictions using simplified theories, flutter exists for very long cylinders as a secondary bifurcation, provided that the free downstream end is well-streamlined. They also conducted a nonlinear analysis, showing that the Hopf bifurcation (the onset of oscillatory motions) occurs at high flow velocities, when the cylinder is already buckled.[1]

1.2.4.2 Clustered cylinders. The dynamics of clustered cylinders in axial flow (Figure 1-5(b)) has been extensively studied, both because of its inherent interest and for applications, to tube-in-shell type heat exchangers for example. Chen (1975) was the first to study this system by obtaining the equation of motion for cylinders in unbounded flow. His study was followed by a study of clusters in bounded axial flow (Païdoussis and Suss 1977), which was later extended and complemented by experiments (Païdoussis 1979). Both theory and experiment show that with increasing flow the system loses stability by buckling in one of its coupled modes, commonly in a pattern where cylinders move toward one another symmetrically, maximum displacement occurring just downstream of their midpoints. With increasing flow, theory predicts that other buckling instabilities are superimposed on the first; in the experiments the system remains buckled, changing modal patterns constantly; some of them correspond to those predicted by theory. At sufficiently high flow velocity, oscillatory motion is observed, corresponding to theoretical flutter. Païdoussis (2004, Chapter 9) gives a comprehensive study of the behaviour of clustered cylinders in axial flow together with a list of more publications; some of them being Dalton (1980), Païdoussis and Besançon (1981), Païdoussis et al. (1982, 1983a,b), and Lin and Raptis (1986).

1.2.4.3 Cylinders in annular flow. Additional extensions to the Païdoussis original theory (Païdoussis, 1966b) have been made to deal with the dynamics of slender cylinders in highly confined annular flow [e.g. by Païdoussis et al. (1990), see Figure 1-5(c)]. In general, for a typical system with fixed ends, as the annular gap becomes narrower, the system loses stability by divergence at smaller flow velocities, provided the gap size is such that the inviscid fluid forces are dominant. For very narrow annuli, however, where viscous forces predominate, this trend is reversed, and further narrowing of the annular

---

[1] This nonlinear work followed some other nonlinear work, which will be discussed later, including the work of this thesis!

gap has a stabilizing effect on the system; furthermore, in some cases the system loses stability by flutter rather than divergence. There is much more work on cylinders in confined flow, e.g. by Païdoussis and Ostroja-Starzewski (1981), Hobson (1982), Mateescu and Païdoussis (1985, 1987), and Mateescu et al. (1988, 1994a,b).

1.2.4.4 Conical beams. Hannoyer and Païdoussis (1979a,b) have studied the effect of nonuniformity of cantilevered axisymmetric beams on their stability in internal and external flows (Figure 1-5(d)). Conical beams subjected to internal flow are less stable than cylindrical ones. In the external flow case, the opposite is true; fully conical cantilevered beams do not become unstable, while for truncated conical cantilevers, instabilities are possible at higher flow velocities than for the cylindrical ones, if the free end is streamlined sufficiently.

1.2.4.5 Articulated cylinders. Articulated cylindrical systems in external axial flow (Figure 1-5(e)) have been studied in conjunction with the dynamics of fuel strings (Païdoussis 1976) and underwater systems towed by submarine (Hamy 1971; Païdoussis 1986) by using linear models. It was shown that, if a sufficient number of degrees of freedom is considered, with increasing flow velocity the system is subject to first-mode divergence; then it is restabilized, and at higher flow velocity the system becomes unstable by flutter. A nonlinear study of this system has also been conducted, which will be discussed in Section 1.3.1.

1.3 A slender flexible cylinder in external axial flow: nonlinear studies

Unlike the case of internal flow, in which there have been many nonlinear studies on the system with cantilevered or both-end-supported boundary conditions (see Section 1.5), nonlinear studies on the system of slender cylinders subjected to axial flow have been very limited. The first nonlinear study on slender cylinders subjected to axial flow was on cantilevered articulated cylinders in annular flow, followed by work on a continuous cantilevered cylinder, which was also supported by experiments as will be discussed in what follows.

1.3.1 Articulated cylinders

Using a nonlinear model, the dynamics of an articulated cylinder in annular flow has been studied by Païdoussis and Botez (1993, 1995) and Botez and Païdoussis (1996). They studied the dynamics of a cantilevered articulated system of rigid cylinders interconnected by rotational springs, within a pipe containing fluid flow. The motions were considered to be planar, and the equations of motion, apart from impacting terms, were linearized. Impacting of the articulated cylinder system on the outer pipe was modelled by either a cubic spring (for analytical convenience) or, more realistically, by a trilinear spring model. The critical flow velocities for which the system loses stability by divergence (pitchfork bifurcation) or flutter (Hopf bifurcation) were determined by an eigenvalue analysis. Beyond these first bifurcations, it is shown that, for different values of the system parameters, chaos is obtained through three different routes as the flow is increased: a period-doubling cascade, the quasiperiodic route, and type III intermittency. The dynamical behaviour of the system and different routes to chaos were illustrated by bifurcation diagrams, phase-plane portraits, power spectra, Poincaré sections, and Lyapunov exponent calculations.

1.3.2 Cantilever cylinders in external axial flow

Lopes et al. (2002), derived a nonlinear equation of motion to describe the dynamics of a slender cantilevered cylinder in axial flow, generally terminated by an ogival free end using the inextensibility assumption, which is reasonable for cantilevered cylinders. Inviscid forces were modelled by an extension of Lighthill's slender-body work to third-order accuracy. The viscous, hydrostatic and gravity-related terms were derived separately, to the same accuracy. The equation of motion was obtained via Hamilton's principle. The boundary conditions related to the ogival free end were also derived separately.

Using this model, the nonlinear dynamics of the system was studied (Semler et al., 2002). It was found that the cylinder first loses stability by divergence in its first mode, the amplitude of which increases with flow. This is gradually transformed to divergence of predominantly second-mode shape, before the system is restabilized. At slightly higher flow velocities, the system loses stability by second-mode flutter, which at still higher flows is succeeded by third-mode flutter. No chaotic oscillation was observed in this study. One important result, obtained by examining the system from the nonlinear point of view, is that post-divergence flutter does materialize as predicted by linear theory, whether there is post-divergence restabilization or not. One of the motivations for the present work is to possibly observe the same phenomenon (occurrence of post-divergence flutter) for the case of cylinders with both ends supported.

1.4 A slender flexible cylinder in external axial flow: experimental studies

There have been two series of experimental studies on slender flexible cylinders in axial flow. The first series of experiments were conducted by Païdoussis (1966c) on horizontal cylinders and were used to validate a linear model. The second series of experiments were conducted by Païdoussis et al. (2002) on a vertical cantilevered cylinder and were used to validate the nonlinear model of Lopes et al. (2002).

1.4.1 First series of experiments

Païdoussis (1966c) conducted a series of experiments to study the dynamical behaviour of the flexible cylinders in axial flow and to measure the limits of stability, and compared them with the theoretical results found using the linear model. The apparatus used was a water-tunnel with a horizontal test-section in which various test cylinders could be mounted horizontally. The supported ends of the flexible cylinders were anchored on slender struts; for experiments with clamped-free cylinders, tapered plastic end-pieces of the same specific gravity as the cylinder were glued to the free end. For simply supported cylinders, very short tapered ends were glued to the flexible cylinder and were connected to the fixed supports on either side of the cylinder by thin, narrow, polyethylene strips. In experiments with clamped-free cylinders a thin metal strip was embedded in the cylinder along its length, in the vertical plane of symmetry, effectively limiting all motion to the horizontal plane and also providing additional support in the vertical plane in cases where the weight of the cylinder was considerably greater, or smaller, than that of the displaced water. Cylinders with both ends supported were not fitted with a metal strip, so that the development of instability would not be impeded by excessive resistance to axial tension.

In all the tests, at small flow velocities, small random vibrations were damped. For a clamped-free cylinder, at sufficiently high flow velocity, the system became unstable, for smoothly tapered free ends. The system first buckled and then, as the flow velocity was increased, developed second-mode oscillation, followed by third-mode oscillation. Similar observations were made with a cylinder pinned at the upstream end and free at the other end.

For a very long simply supported cylinder, it was observed that it sagged slightly at its midpoint under its own weight. Increasing the flow velocity in such cases exaggerated this sag and slowly shifted it to the horizontal plane, but no distinct threshold of buckling and no oscillatory motions were observed. For shorter cylinders, however, at a sufficiently high flow velocity, a small bow developed just downstream of the midpoint of the cylinder, increasing in amplitude with flow; thus the system lost stability by divergence (buckling). This was followed by a spontaneous second-mode oscillation.

1.4.2 Second series of experiments

The second series of experiments were conducted by Païdoussis et al. (2002) using a water-tunnel with a vertical test-section, in the middle of which the flexible cylinder was mounted vertically, with no central metal strip embedded in it, as it was no longer essential compared with the 1966 experiments on a horizontal cylinder. Initially, as the flow was increased, flow-induced damping was generated, but small vibration could be observed in which the cylinder responded to the turbulence-induced fluctuating pressure field. At higher flow velocities, the system developed divergence in its first mode, then regained its equilibrium configuration, before developing flutter spontaneously in its second mode. As the flow velocity continued to increase, second mode flutter was succeeded by third-mode flutter, and in some cases fourth-mode flutter. This was the dynamical behaviour for a cylinder with a reasonably well-streamlined ogival end-shape at the free end. If, however, the end was completely blunt, then neither static (divergence) nor dynamic (flutter) instabilities materialized.

1.5 Pipes conveying fluid (internal axial flow)

The dynamics of cylinders in external axial flow is closely related to that of pipes conveying fluid (internal axial flow), which has been studied extensively using both linear and nonlinear models (Païdoussis, 1998, 2004). Here a short review is given for the cases of cantilevered pipes and pipes with both ends supported conveying fluid.

1.5.1 Cantilevered pipes conveying fluid

Benjamin (1961a,b) was the first to study the dynamics of a cantilevered pipe conveying fluid (with no mass or spring attached to the pipe). Later, it was shown [Païdoussis (1963, 1970b); Gregory and Païdoussis (1966a,b); refer also to Païdoussis (1998)] that cantilevered pipes conveying fluid lose stability via flutter for sufficiently high flow velocities. The nonlinear equations of motion for this system were derived as early as the 1930s by Bourrières (1939) and then by Ashley and Haviland (1950), Rousselet and Herrmann (1977, 1981) and by Lundgren et al. (1979). Applying the centre manifold reduction and normal form techniques on a nonlinear model, Bajaj and Sethna (1984, 1991) found that a plain cantilevered pipe conveying fluid loses stability by a Hopf bifurcation and develops either planar or three-dimensional flutter in multiple interspersed ranges of mass parameter, β.

It was also found that additional masses or springs attached to the pipe could either stabilize or destabilize the system *vis-à-vis* the plain pipe, depending on the system parameters and location of the additional mass or spring [see Hill and Swanson (1970), Chen (1971), Jendrzejczyk and Chen (1985), Sugiyama et al. (1988) and Païdoussis (1998)]. Nonlinear studies by Copeland and Moon (1992), Païdoussis and Semler (1993a,b, 1998), Semler and Païdoussis (1995), and Steindl and Troger (1996) showed that in the case of a pipe with an intermediate spring support or an end-mass, at sufficiently high flow velocities, the system undergoes a very rich dynamical behaviour, involving quasiperiodic and chaotic oscillations [see also Païdoussis (1998) for a comprehensive discussion]. Recently, by using a three-dimensional version of the nonlinear equations of motion for a cantilevered cylinder (Wadham-Gagnon et al., 2006), three-dimensional oscillations of a pipe conveying fluid with a spring attached to it (Païdoussis et al., 2006) and in the presence of an end mass (Modarres-Sadeghi et al.,

2006) have been studied. It was shown that in the case of a pipe with intra-span spring supports, depending on the spring configurations, points of attachment and stiffness, in some cases the system loses stability by planar flutter, and thereafter performs 2-D or 3-D periodic, quasiperiodic and chaotic oscillations; in other cases, the system loses stability by divergence, followed by oscillations in the plane of divergence or perpendicular to it, again periodic, quasiperiodic or chaotic. In the case of a pipe with an end-mass, it was shown that the pipe loses stability by a Hopf bifurcation, leading to planar periodic oscillations. At higher flow velocities, planar quasiperiodic and chaotic oscillations were observed, followed by three-dimensional quasiperiodic and chaotic motions.

1.5.2 Pipes conveying fluid supported at both ends

Feodos'ev (1951), Housner (1952) and Niordson (1953) were the first to study the dynamics of such systems. In this case, it has been known for a long time that, for sufficiently high flow, the pipe loses stability by divergence. This has been confirmed by experiments, by Dodds and Runyan (1965) and others. Then, in the 1970s, Païdoussis and Issid (1974) found that linear theory predicts the existence of post-divergence coupled-mode flutter, at higher flow velocities. On the other hand, the work done by the fluid on the pipe in a presumed cycle of oscillation is zero. This, then, constitutes a paradox: for how is it possible for the pipe to flutter if the system is conservative and no energy is supplied to sustain the oscillation (Païdoussis, 2005, 1998)? To find an answer to this paradox, the system was analysed by a nonlinear model to ascertain the reliability of the post-divergence results, as linear theory is valid only up to the first point of instability. Nonlinear aspects of the behaviour of pipes with supported ends were first studied by Thurman and Mote (1969). They consider an axially extensible pipe and therefore the nonlinearities in their equations are associated with the axial elongation and the extension-induced tension in the pipe. Holmes (1978) studied this problem by adding simply one nonlinear term due to this extension-induced tension to the linear equation; he used this equation to show that pipes supported at both ends cannot flutter. Semler et al. (1994) have derived a set of nonlinear equations of motion correct to third order of magnitude for an extensible fluid-conveying pipe supported at both ends. In this model, which was corrected by Païdoussis (2004, Appendix T), the effect of gravity has been taken into account and it is assumed that in general the flow can be steady or unsteady and that the moment-curvature relationship is nonlinear; so far, this is the most complete nonlinear equation of motion for this system.

Recently, Nikolić and Rajković (2006) used Lyapunov-Schmidt reduction and singularity theory to study the behaviour of this system in the vicinity of the bifurcation points by using the three above-mentioned models. For certain ranges of parameters, they found that a subcritical pitchfork bifurcation is possible in the two models other than Holmes' simplified model. Modarres-Sadeghi et al. (2006) used the complete extensible nonlinear model of Païdoussis (2004) to show that the pipe remains in its undeformed static equilibrium at low flow velocities and then undergoes a static pitchfork bifurcation at a critical flow velocity, which depends on the physical parameters of the system. The amplitude of the buckled pipe increases with flow, but no secondary bifurcation is observed, in agreement with the results of Holmes. They also studied the influence of different parameters on the stability and the amplitude of the buckled solution.

The dynamics of the pipe problem (internal flow) has been shown to be independent of frictional forces, since they are exactly counterbalanced by the pressure-loss forces along the pipe. As a result, both pressure-loss and frictional forces vanish from the equation of motion. This is not true for external flow over a cylinder, in which the mean pressure is largely unaffected by frictional effects on the cylinder surface. Some of these frictional terms give rise to terms in the equation of motion of a different derivative form *vis-à-vis* the inviscid-force terms and hence *vis-à-vis* the internal flow case (Païdoussis, 2005). The linear theory for both internal and external flow predicts a post-divergence dynamic instability (coupled-mode or single-mode flutter), but this was not obtained for the internal flow using a nonlinear model. The question here is what is the post-divergence behaviour of a cylinder in external flow according to the nonlinear model? Will the cylinder flutter or is it similar to the case of internal flow, for which when the pipe is supported at both ends, no secondary bifurcations occur? This is one of the "curiosity-driven" motivations behind the present work.

1.6 Outline of this thesis

This thesis deals with the nonlinear dynamics of a vertical slender flexible cylinder supported at both ends and subjected to axial flow. Based on what has been presented in the review of the literature, the aim is

- to derive the nonlinear equations of motion for the system of a slender flexible cylinder supported at both ends and subjected to axial flow;
- to study theoretically the post-divergence behaviour of such systems from a nonlinear point of view for various boundary conditions;
- if there is any post-divergence instability, to study the post-instability behaviour of the system and to investigate the possibilities of the existence of chaotic oscillations in the system, and to study the route(s) to chaos;
- to conduct a series of experiments (i) to observe the post-divergence behaviour of the system and (ii) to validate the theoretical results by measuring the amplitude of buckling and, in the case of oscillatory motions, the frequency and the amplitude of oscillations.

This thesis consists of seven chapters. In Chapter 1, here, a brief review of the previous related studies is given. The goals of the thesis have been stated, and now the outline of the thesis is being presented.

In Chapter 2, the weakly nonlinear equations of motion are derived for a slender flexible cylinder with an extensible centreline subjected to axial flow. The fluid forces are formulated in terms of several components; inviscid, frictional, hydrostatic and pressure-loss forces are taken into account. The derivation of the equations of motion is carried out in a Lagrangian framework, and the resultant equations are correct to third order of magnitude, where the transverse and the axial displacements of the cylinder are of the first- and the second-order of magnitude, respectively. Because the cylinder centreline is considered to be extensible, two coupled nonlinear partial differential equations describe its motions, involving both longitudinal and transverse displacements. These nonlinear partial differential equations are then recast in a nondimensional form and discretized by using Galerkin's technique, giving a set of nonlinear second-order ordinary differential equations, which can be recast in a first-order form.

In Chapter 3, methods of solution used to analyse the nonlinear equations of motion are introduced. Houbolt's finite difference method (FDM) and AUTO are used as two numerical methods to solve the set of ordinary differential equations after the system has been discretized. FDM is applied on the second-order ordinary differential equations directly, while to use AUTO one has to employ the first-order form of the ordinary differential equations. The centre manifold reduction method is also discussed as an analytical method to study the behaviour of the system in the vicinity of the pitchfork bifurcation point.

In Chapter 4, the results for a simply supported cylinder are presented in the form of bifurcation diagrams with flow velocity as the independent variable, supported by time histories, phase-plane plots, PSD plots and Poincaré maps. The influence of different parameters on the stability and the amplitude of the solution is studied. The effect of number of modes used in discretizing the partial differential equations by Galerkin's technique on the results is also presented. The behaviour of the system for the case of linear fluid forces and nonlinear structural equation is studied. The centre manifold reduction is used to study the behaviour of the system in the vicinity of the pitchfork bifurcation.

In Chapter 5, the results for a vertical cylinder clamped at both ends (clamped-clamped) or clamped at the upper end and hinged at the lower one (clamped-hinged) or hinged at the upper end and clamped at the lower one (hinged-clamped) are presented in the form of bifurcation diagrams and supported by time histories, phase-plane and PSD plots and Poincaré maps; and the effect of boundary conditions on the cylinder behaviour is then summarized. For all these cases, the centre manifold reduction is also used to study the system behaviour in the neighbourhood of the pitchfork bifurcation.

In Chapter 6, the results of three series of experiments conducted on vertical clamped-clamped cylinders are presented, together with the comparison with the theoretical calculations for each case. In the first series of experiments, the downstream end of the clamped-clamped cylinder is free to slide axially, while in the second series of experiments, the downstream end is fixed. The influence of externally applied axial compression is also studied in the second series of experiments. In the third series of experiments, a more flexible cylinder is used and the effect of externally applied axial compression on dynamic instability of the cylinder is also studied.

Chapter 7 wraps up the thesis with a summary of general conclusions and suggestions for future work.

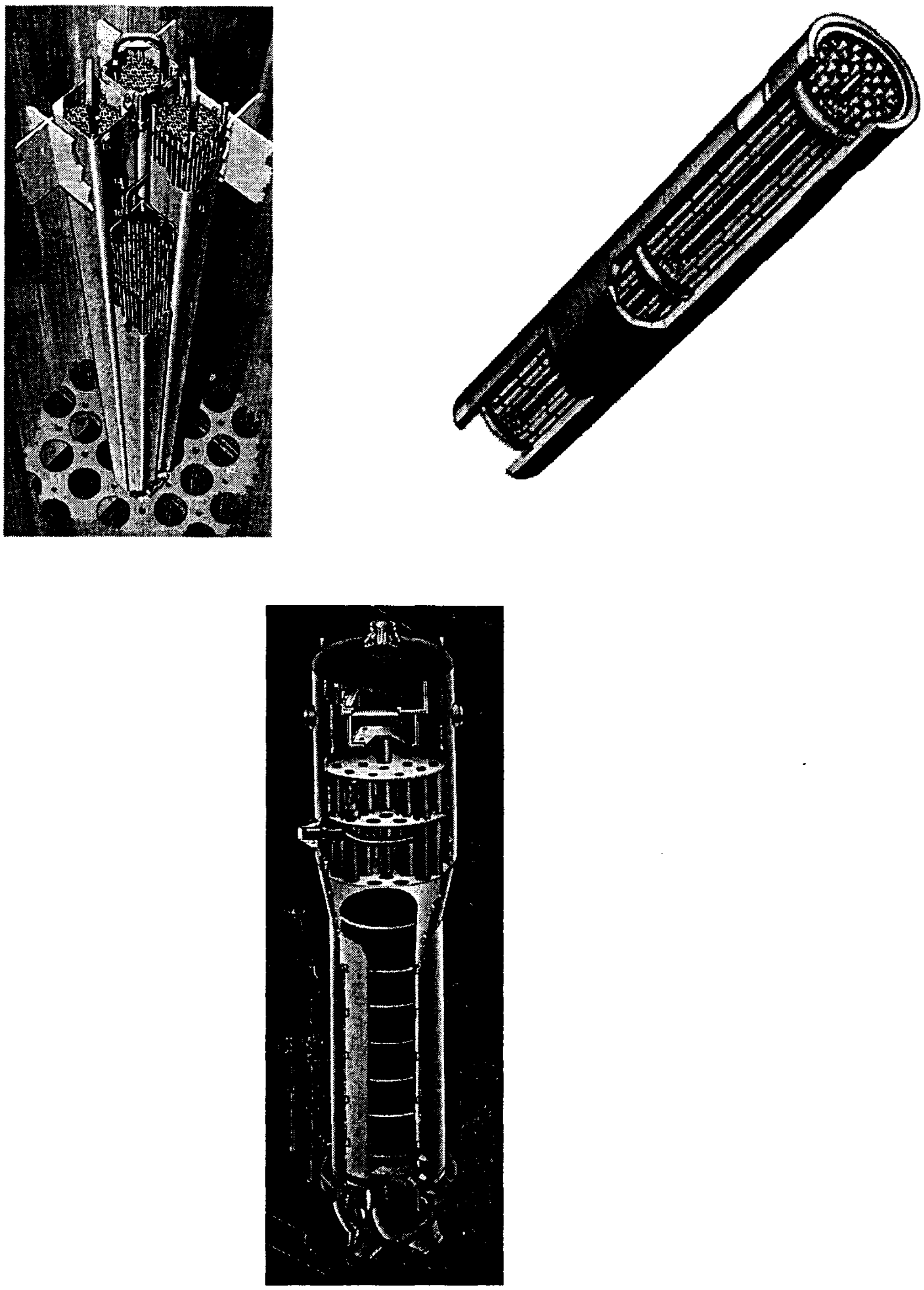

Figure 1-1 Some practical applications of slender cylinders subjected to axial flow: (a) part of the core of the boiling water reactor; (b) gas-cooled reactor fuel cluster; (c) steam generator.

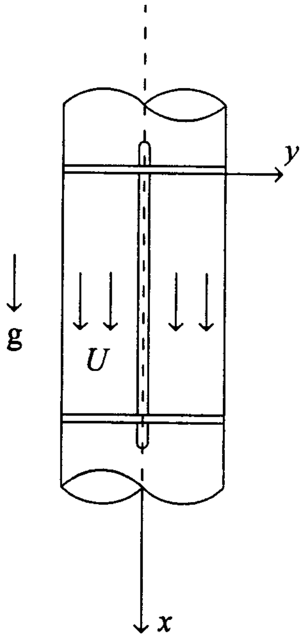

Figure 1-2 A vertical slender flexible cylinder subjected to axial flow.

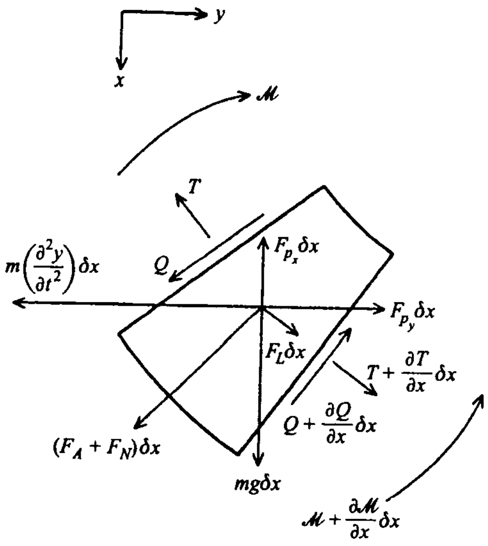

Figure 1-3 An element δx of the cylinder showing forces and moments acting on it (Païdoussis 1973, 2004).

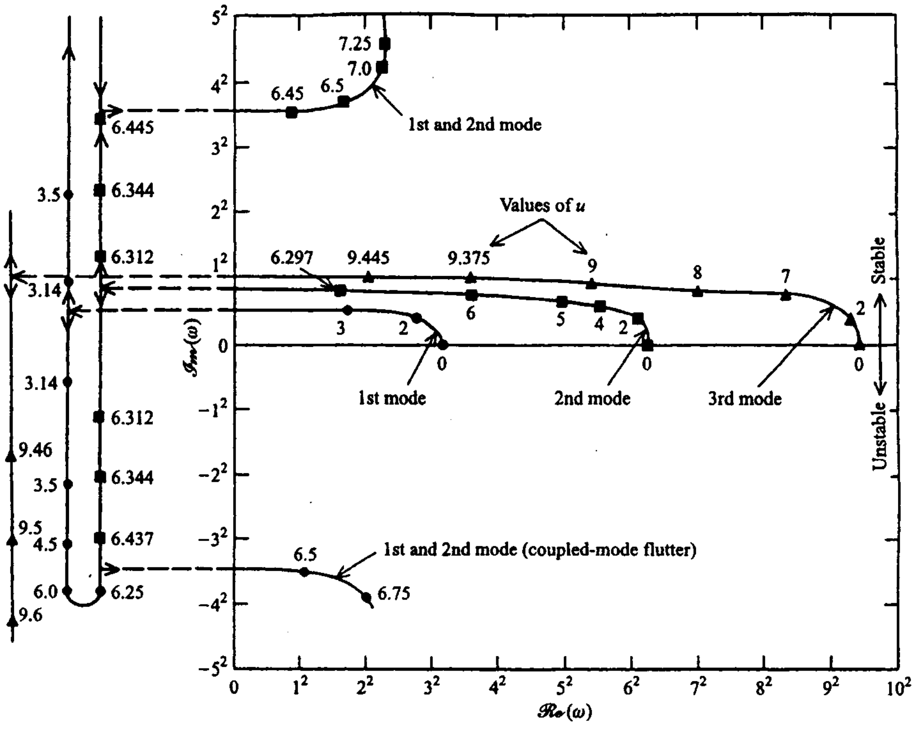

Figure 1-4 Argand diagram for the complex frequency, ω, of the lowest three modes of a simply supported cylinder in unconfined axial flow, as function of flow velocity, u (Païdoussis 1973, 2004).

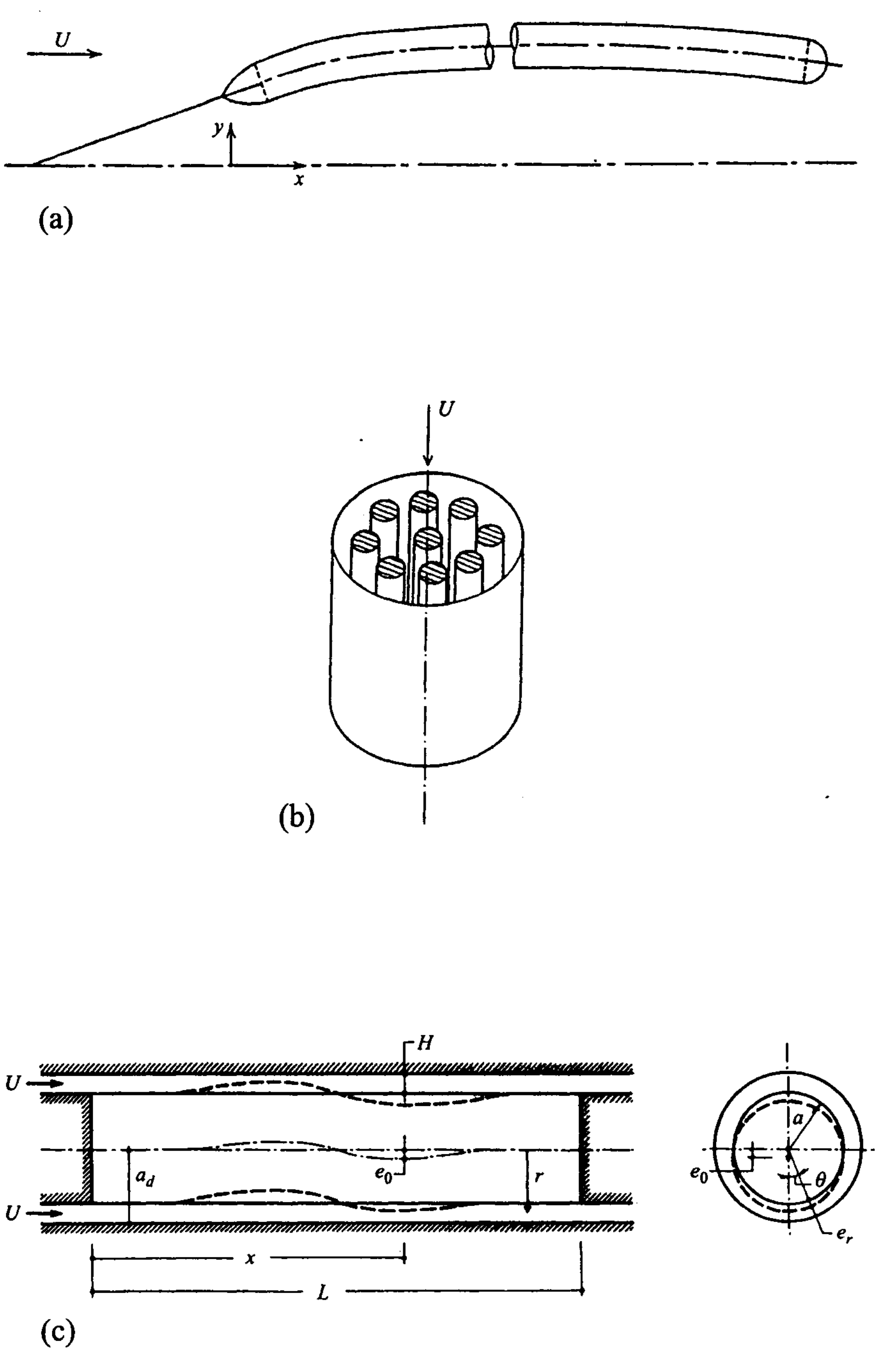

Figure 1-5; see next page.

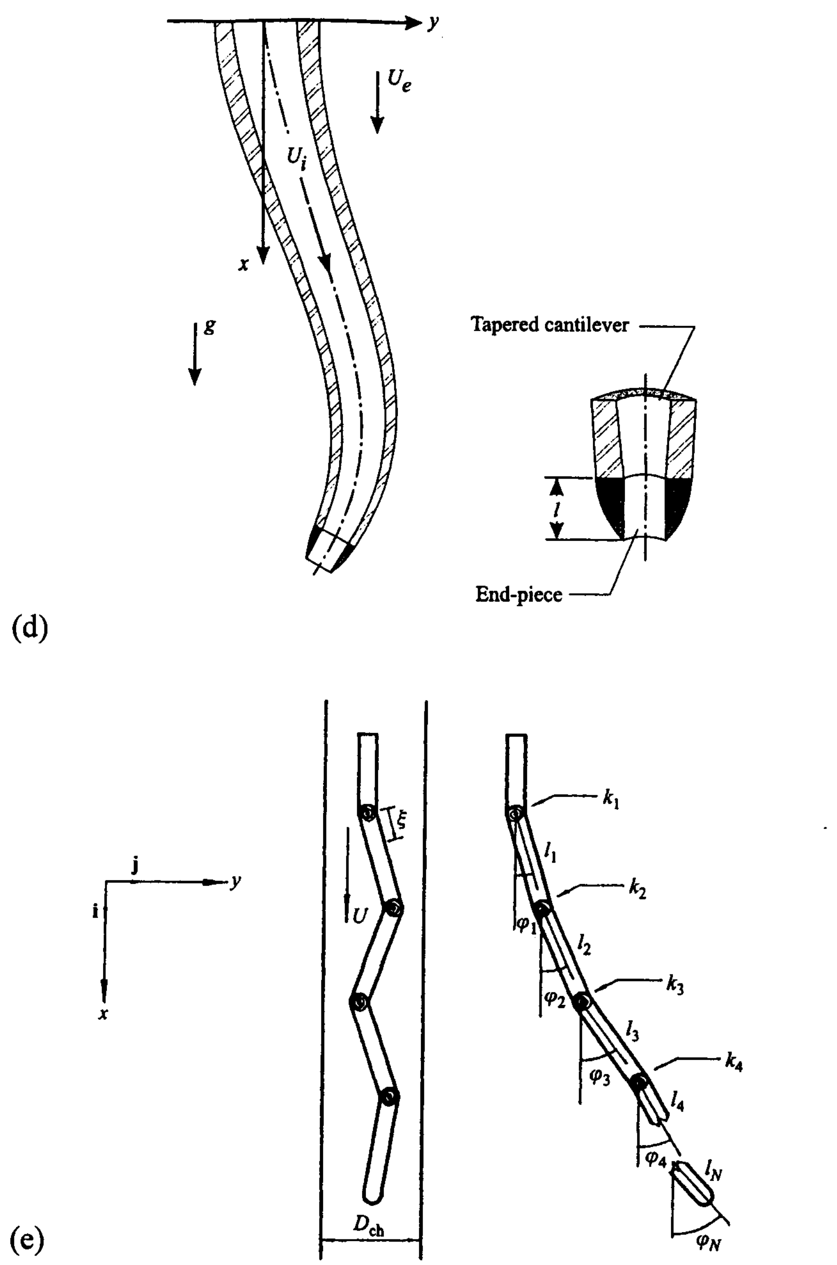

Figure 1-5 Problems similar to the subject of this thesis: (a) idealized system of a towed cylinder (Païdoussis, 1968, 2004); (b) a cluster of cylinders (Païdoussis, 2004); (c) a flexible cylinder in annular flow (Païdoussis, 1990, 2004); (d) a flexible cantilever, tapered both externally and internally (Hannoyer and Païdoussis, 1979; Païdoussis, 2004) and (e) articulated cylindrical system in a flow-channel (Païdoussis and Botez, 1993; Païdoussis, 2004).

2. A Nonlinear Model for an Extensible Slender Flexible Cylinder Subjected to Axial Flow

2.1 Introduction

In this chapter, the weakly nonlinear equations of motion are derived for a slender flexible cylinder subjected to axial flow. The cylinder centreline is considered to be extensible, and hence two coupled nonlinear equations describe its motion, involving both longitudinal and transverse displacements. The fluid forces are formulated in terms of several components, for convenience. For high Reynolds number flows, the dominant, inviscid component is modelled by an extension of Lighthill's slender-body work; frictional, hydrostatic and pressure-loss forces are then added to the inviscid component. The derivation of the equations of motion is carried out in a Lagrangian framework, and the resultant equations are correct to third order of magnitude, $O(\epsilon^3)$, where the transverse displacement of the cylinder is of $O(\epsilon)$. The resulting nonlinear partial differential equations are discretized using the Galerkin technique; leading to a set of second-order ordinary differential equations, which can be recast in first-order form.

2.2 Definitions and preliminaries

2.2.1 Basic assumptions and concepts

The system under consideration consists of a cylinder of length L, cross-sectional area A, mass per unit length m, and flexural rigidity EI, centrally located in a rigid channel within which a fluid flows with velocity U parallel to the channel centreline. The undeformed cylinder axis coincides with the X-axis (in the direction of gravity) and the cylinder is assumed to oscillate in the (X, Y) plane (see Figure 2-1).

The basic assumptions made for the cylinder and the fluid are as follows: (i) the fluid is incompressible; (ii) the mean flow velocity is constant; (iii) the cylinder is slender, so that the Euler-Bernoulli beam theory is applicable; (iv) although the deflections of the cylinder may be large, the strains are small; (v) the cylinder centreline is extensible.

The derivation to be presented here, so far as the fluid dynamics of the system is concerned, is similar in spirit and procedure to that of Païdoussis (1966b, 1973). Thus, for convenience, the inviscid, viscous and hydrostatic forces are determined separately, rather than being determined together, say by direct application of the Navier-Stokes equations.

2.2.2 *Notation and coordinate systems*

One usually has the choice between two sets of coordinate systems: one for the undeformed body (Lagrangian coordinates) and the other for the deformed body (Eulerian coordinates). The deformation of a point is described by the relation of the coordinates of the same material point in the undeformed and deformed states. Let (X,Y,Z) represent the position of a material point P in its original state, and (x,y,z) the position of the same point in the deformed state. Then, the displacement of that material point is defined as $u = x - X, v = y - Y$ and $w = z - Z$. For a slender cylinder with its initially undeformed state along the X-axis and undergoing motions in the (X,Y) plane, we have $Y = 0$, hence $y = v$; and $w = z = Z = 0$.

Defining ε^* as the axial strain along the centreline of the cylinder, one may relate δX and δs, where s is the curvilinear coordinate along the cylinder, through the condition

$$\varepsilon^* = \frac{\delta s - \delta X}{\delta X}, \tag{2-1}$$

where

$$\delta s = \sqrt{\delta x^2 + \delta y^2}, \tag{2-2}$$

leading to

$$s' = \sqrt{(1+u')^2 + v'^2}, \tag{2-3}$$

and therefore using (2-1),

$$\varepsilon^*(X) = \sqrt{(1+u')^2 + v'^2} - 1, \tag{2-4}$$

where $(\ )' = \partial(\ )/\partial X$.

Let θ_1 be the angle between the centreline of the cylinder and the *X*-axis (see Figure 2-2). For a cylinder undergoing planar motion, extensible or inextensible, the curvature is given by

$$\kappa = \frac{\partial \theta_1}{\partial s}. \tag{2-5}$$

For an extensible cylinder, θ_1 is defined via

$$\cos\theta_1 = \frac{\delta x}{\delta s} = \frac{\partial x/\partial X}{\partial s/\partial X} = \frac{\partial x/\partial X}{1+\varepsilon^*}, \tag{2-6}$$

$$\sin\theta_1 = \frac{\delta y}{\delta s} = \frac{\partial y/\partial X}{\partial s/\partial X} = \frac{\partial y/\partial X}{1+\varepsilon^*}. \tag{2-7}$$

In terms of the *X*-coordinate, Equation (2-5) becomes

$$\kappa = \frac{\partial \theta_1}{\partial X}\frac{\partial X}{\partial s} = \frac{1}{1+\varepsilon^*}\frac{\partial \theta_1}{\partial X}. \tag{2-8}$$

Then, using (2-6) and (2-7), one can find

$$\frac{\partial^2 x}{\partial X^2} = \frac{\partial \varepsilon^*}{\partial X}\cos\theta_1 - \left(1+\varepsilon^*\right)\sin\theta_1 \frac{\partial \theta_1}{\partial X} \tag{2-9}$$

and

$$\frac{\partial^2 y}{\partial X^2} = \frac{\partial \varepsilon^*}{\partial X}\sin\theta_1 + \left(1+\varepsilon^*\right)\cos\theta_1 \frac{\partial \theta_1}{\partial X}. \tag{2-10}$$

Solving the set of equations (2-9) and (2-10) for $\frac{\partial \theta_1}{\partial X}$, leads to

$$\frac{\partial \theta_1}{\partial X} = \frac{1}{1+\varepsilon^*}\left(-\sin\theta_1 \frac{\partial^2 x}{\partial X^2} + \cos\theta_1 \frac{\partial^2 y}{\partial X^2}\right). \tag{2-11}$$

Using (2-6) and (2-7) again, one can find

$$\theta_1' \equiv \frac{\partial \theta_1}{\partial X} = \frac{y''x' - y'x''}{\left(1+\varepsilon^*\right)^2}, \tag{2-12}$$

thus yielding the curvature for cylinders with an extensible centreline, namely

$$\kappa = \frac{y''x' - y'x''}{\left(1+\varepsilon^*\right)^3}. \tag{2-13}$$

2.2.3 *On the derivation of the nonlinear equations of motion*

Large motions imply that terms of higher order than the linear ones have to be kept in the equation; here, only quadratic and cubic nonlinear terms are retained. For planar motions, the lateral displacement may be supposed to be small, relative to the length of the cylinder, i.e. $y = v \sim O(\epsilon)$, where $O(\epsilon)$ denotes the first order. One can see that the longitudinal displacement u is one order higher than v, i.e. $u \sim O(\epsilon^2)$.

Because we have assumed that the cylinder is extensible, no relation between the virtual displacements δX and δY exists. Therefore, two equations of motion are necessary: one mainly in the X- and the other mainly in the Y-direction.

To derive the equations of motion we shall use Hamilton's principle, usually written as

$$\delta \int_{t_1}^{t_2} \mathcal{L} dt + \int_{t_1}^{t_2} \delta W dt = 0, \tag{2-14}$$

where $\mathcal{L} = \mathcal{T} - V$ is the Lagrangian of the system, in which $\mathcal{T}$ and V are, respectively, the kinetic and potential energy associated with the cylinder, and δW is the virtual work due to the forces acting on the cylinder; δ is the variational operator. This variational technique requires that the quantities involved be correct to one order higher than that sought: in this case to $O(\epsilon^4)$ at least, so that, after applying the variational technique, the third-order terms will still remain in the resulting equations of motion.

2.3 Kinetic and potential energies of the cylinder

The kinetic energy of the cylinder is defined by

$$\mathcal{T}=\tfrac{1}{2}m\int_0^L V_c^2\,dX=\tfrac{1}{2}m\int_0^L\left(\dot{u}^2+\dot{v}^2\right)dX, \tag{2-15}$$

and hence the variation of the kinetic energy is given by

$$\delta\int_{t_1}^{t_2}\mathcal{T}\,dt=m\iint\left(\dot{u}\delta\dot{u}+\dot{v}\delta\dot{v}\right)dX=m\int_0^L\left[\dot{u}\delta u\Big|_0^t-\int_0^t\ddot{u}\delta u\,dt+\dot{v}\delta v\Big|_0^t-\int_0^t\ddot{v}\delta v\,dt\right]dX$$

$$=-m\iint\left(\ddot{u}\delta u+\ddot{v}\delta v\right)dX\,dt, \tag{2-16}$$

where $\dot{(\ )}=\partial(\ )/\partial t$.

The potential energy of the cylinder comprises gravitational and strain energy components. In general, the gravitational energy depends on the distribution of mass, and is written as $V_G=\int\rho\,\phi(\xi)\,dV$, where ϕ is the gravitational potential per unit mass. In a uniform gravitational field as for the system at hand, it becomes

$$V_G=-mg\int_0^L\left(X+u\right)dX; \tag{2-17}$$

hence,

$$\delta\int_{t_1}^{t_2}V_G\,dt=-mg\iint\delta u\,dX\,dt. \tag{2-18}$$

An exact form of the strain energy, in the case of large deflections and correct to $\mathrm{O}\left(\epsilon^4\right)$, was obtained by Stoker (1968) with only one major assumption: the strain is small, even though the deflection may be large. Stoker's analysis finally leads to

$$V_S=\tfrac{1}{2}E\int_0^L\left[A\varepsilon^2+I\left(1+\varepsilon^*\right)^2\kappa^2\right]dX, \tag{2-19}$$

where X represents the Lagrangian coordinate, A the cross-sectional area, I the area-moment of inertia, and ε^* the axial strain.

The axial strain may itself be decomposed into two components: (i) a steady-state strain due to a tension T externally applied or associated with gravity and friction, and (ii) a time-varying strain due to cylinder oscillation. By reference to Equation (2-19) and using Equation (2-8), this strain energy may be expressed as

$$V_S=\tfrac{1}{2}EA\int_0^L\left(\frac{T}{EA}+\varepsilon^*\right)^2dX+\tfrac{1}{2}EI\int_0^L\left(\frac{\partial\theta_1}{\partial X}\right)^2dX. \tag{2-20}$$

Following Païdoussis (1973), the gradient of the tension T can be expressed as

$$\frac{\partial T}{\partial x} = -\left(\tfrac{1}{2}\rho D U^2 C_T + mg\right); \tag{2-21}$$

where C_T is the frictional coefficient in the tangential direction. Then, using $\partial T/\partial X = (\partial T/\partial x)(\partial x/\partial X) = (\partial T/\partial x)(1+u')$ and integrating the resulting equation from X to L, one can find

$$T(X) = \left(\tfrac{1}{2}\rho D U^2 C_T + mg\right)\left[L - X + u(L)(1-\bar{\delta}) - u\right] + T(L), \tag{2-22}$$

where $T(L)$ is the tension at the downstream end, which can be written as

$$T(L) = \bar{T}\bar{\delta} + \tfrac{1}{2}\rho D^2 U^2 C_b (1-\bar{\delta}) - \left[\tfrac{1}{2}\rho D U^2 C_T \left(1 + \frac{D}{D_h}\right) + mg\right]\frac{L}{2}\bar{\delta}; \tag{2-23}$$

$\bar{T}$ is an externally imposed uniform tension and C_b is a base pressure coefficient, in case the downstream end of the cylinder is exposed to the flow and is free to slide axially. The terms inside the brackets are due to the compressive load at $x=L$ when the length of the cylinder is fixed. The existence of the last term in (2-23) depends on whether the length is fixed while the cylinder is horizontal or not (Païdoussis, 1973); $\bar{\delta}$ in Equation (2-22) and (2-23) is an index: $\bar{\delta} = 0$ signifies that the downstream end is free to slide axially, and $\bar{\delta} = 1$ if the supports do not allow net axial extension.

Therefore, the final form of the tension becomes

$$\begin{aligned} T(X) = {} & \left(\tfrac{1}{2}\rho D U^2 C_T + mg\right)\left[L\left(1 - \tfrac{1}{2}\bar{\delta}\right) - X + u(L)(1-\bar{\delta}) - u\right] \\ & - \tfrac{1}{2}\rho D U^2 C_T \frac{D}{D_h}\frac{L}{2}\bar{\delta} + \tfrac{1}{2}\rho D^2 U^2 C_b (1-\bar{\delta}) + \bar{T}\bar{\delta}, \end{aligned} \tag{2-24}$$

where it is obvious that when $\bar{\delta} = 1$, $u(L) = 0$.

Recalling that $u \sim O(\epsilon^2)$ and $v \sim O(\epsilon)$, and using Equations (2-4) and (2-12), one may obtain

$$\left(\frac{\partial \theta_1}{\partial X}\right)^2 = v''^2 - 2v''^2 u' - 2v''^2 v'^2 - 2v'v''u'' + O(\epsilon^5). \tag{2-25}$$

Therefore, using Equations (2-20), (2-24) and (2-25),

$$\begin{aligned}
\delta \int_{t_1}^{t_2} V_S \, dt = \int_{t_1}^{t_2} \int_0^L \Big\{ & -EA\left(u'' + v'v''\right) - EI\left(v''v''' + v'v''''\right) \\
& + \left[\tfrac{1}{2}\rho D^2 U^2 C_b \left(1-\bar{\delta}\right) + \left(\bar{T} - \tfrac{1}{2}\rho D U^2 C_T \frac{D}{D_h}\frac{L}{2} \right)\bar{\delta} \right] v'v'' \\
& + \left(mg + \tfrac{1}{2}\rho D U^2 C_T \right)\left[1 + u' - \tfrac{1}{2}v'^2 + \left(L - X - \frac{L\bar{\delta}}{2} \right) v'v'' \right] \Big\} \delta u \, dX \, dt \\
+ \int_{t_1}^{t_2} \int_0^L \Big\{ & -EA\left(v'u'' + v''u' + \tfrac{3}{2}v'^2 v'' \right) + EIv'''' \\
& - EI\left(3u'''v'' + 4u''v''' + 2u'v'''' + v'u'''' + 2v''^3 + 2v'^2 v'''' + 8v'v''v''' \right) \\
& + \left(mg + \tfrac{1}{2}\rho D U^2 C_T \right) \\
& \times \left[v' - \tfrac{1}{2}v'^3 + \left(L - X - \frac{L\bar{\delta}}{2} \right)\left(-v'' + v'u'' + v''u' + \tfrac{3}{2}v'^2 v'' \right) + \left(u - u(L) \right) v'' \right] \\
& + \left[\tfrac{1}{2}\rho D^2 U^2 C_b \left(1-\bar{\delta}\right) + \left(\bar{T} - \tfrac{1}{2}\rho D U^2 C_T \frac{D}{D_h}\frac{L}{2} \right)\bar{\delta} \right] \\
& \times \left(-v'' + v'u'' + v''u' + \tfrac{3}{2}v'^2 v'' \right) \Big\} \delta v \, dX \, dt, \qquad (2\text{-}26)
\end{aligned}$$

where, the terms giving the boundary conditions have been omitted in this equation due to the fact that the variation of v and u at the two boundaries are zero for a both-ends-supported cylinder, i.e. $\delta u = \delta v = 0$ at $X = 0$ and $X = L$. Also, for a sliding end, $\delta v = u' = 0$ at $X = L$.

2.4 Virtual work of the fluid forces acting on the cylinder

The fluid-related forces acting on the cylinder are: F_A, the inviscid hydrodynamic force, which acts in the transverse direction; F_N and F_L, the normal and longitudinal frictional forces; and F_{px} and F_{py}, the hydrostatic pressure forces in the x- and y-direction, respectively, as shown in Figure 2-2.

2.4.1 Some preliminary relationships

In subsequent calculations, we define by U the axial flow velocity of the undisturbed flow; we also utilize U_f, which represents an axial flow velocity relative to an axially deforming cylinder (see Figure 2-3). We can relate one to the other by the following relation (Lopes et al., 2002):

$$U_f = U\left(1-\frac{\partial u}{\partial X}\right)+O\left(\epsilon^4\right). \tag{2-27}$$

Let us consider Figure 2-3, showing an element δx subjected to deformation induced by the fluid. This representation enables one to define the angles required in the determination of the forces: i.e., θ_1, the angle between the longitudinal axis of the element and the X-axis,

$$\theta_1 = \tan^{-1}\left[\frac{\partial y/\partial X}{\partial x/\partial X}\right], \tag{2-28}$$

and θ_2, the angle between the relative fluid-body velocity (see Equation (2-34) further on) and the X-axis,

$$\theta_2 = \tan^{-1}\left[\frac{\partial y/\partial t}{U_f-\left(\partial x/\partial t\right)}\right]. \tag{2-29}$$

In the definition of θ_2, we notice that the axial velocity of the cylinder is indeed taken into account. It should be mentioned that, because U_f is of order zero and $\partial x/\partial t$ is of second order, the expression $U_f-\partial x/\partial t$ in equation of θ_2 is always positive.

The angles θ_1 and θ_2 may be expressed as

$$\theta_1 = v' - u'v' - \tfrac{1}{3}v'^3 + O\left(\epsilon^5\right), \tag{2-30}$$

$$\theta_2 = \frac{\dot{v}}{U_f} + \frac{\dot{x}\dot{v}}{U_f^2} - \tfrac{1}{3}\frac{\dot{v}^3}{U_f^3} + O\left(\epsilon^5\right), \tag{2-31}$$

where primes and dots denote derivatives with respect to X and t, respectively. Hence, using series expansions, we can write

$$\cos\theta_1 = 1 - \tfrac{1}{2} v'^2 + O\left(\epsilon^4\right),$$

$$\sin\theta_1 = v' - u'v' - \tfrac{1}{2} v'^3 + O\left(\epsilon^5\right). \tag{2-32}$$

Based on Figure 2-3, we define the angle of incidence $i = \theta_1 + \theta_2$, which will be used later; it corresponds to the angle between the relative fluid-body velocity and the centreline of the body, so that

$$\cos i = 1 - \tfrac{1}{2}\left(v'^2 + 2\frac{v'\dot{v}}{U_f} + \frac{\dot{v}^2}{U_f^2} \right) + O\left(\epsilon^4\right),$$

$$\sin i = v' + \frac{\dot{v}}{U_f} - u'v' + \frac{\dot{u}\dot{v}}{U_f^2} - \tfrac{1}{2}\left(v'^3 + \frac{\dot{v}^3}{U_f^3} + \frac{v'^2\dot{v}}{U_f} + \frac{v'\dot{v}^2}{U_f^2} \right) + O\left(\epsilon^5\right). \tag{2-33}$$

2.4.2 *The inviscid hydrodynamic forces*

To determine the inviscid hydrodynamic forces to $O\left(\epsilon^3\right)$, we adapt Lighthill's work (1960), which is essentially an application of slender body theory [see Lopes et al. (2002) for details].

In Figure 2-3, we introduce the new system of unit vectors $\left(\mathbf{i}_1, \mathbf{j}_1\right)$, which corresponds to $\left(\mathbf{i}, \mathbf{j}\right)$ rotated by an angle θ_1 in the counterclockwise direction. We isolate an element of the cylinder as in Figure 2-3, and define the relative fluid-body velocity as

$$V = \dot{y} + \dot{x} - U_f\,. \tag{2-34}$$

Then, projecting this relative fluid-body velocity on $\mathbf{j}_1$, the direction normal to the element, considering the trigonometric expressions (2-32), and replacing U_f by U by means of expression (2-27), the relative fluid-body velocity becomes

$$V\left(X,t\right) = \dot{v} + U\, v' - \tfrac{1}{2}\dot{v}v'^2 - 2U\, u'v' - \tfrac{1}{2}U\, v'^3 - \dot{x}v' + O\left(\epsilon^5\right). \tag{2-35}$$

The next step involves the extension of Lighthill's potential flow theory to a third-order nonlinear formulation, subject to a number of assumptions. Eventually, a nonlinear expression of the lift is derived, correct to third-order of magnitude (Lopes et al., 2002).

The inviscid hydrodynamic force, as used here, has the same magnitude as the lift, but acts in the opposite direction. For a cylinder of constant cross-section, i.e., $(\partial A/\partial X)=0$ and added mass $M(X)=M=\chi\rho A$, the inviscid hydrodynamic force, may be obtained as

$$F_A(X,t)=\left\{\frac{\partial}{\partial t}+\left[U(1-u')-(\dot{u}+Uu')\right]\frac{\partial}{\partial X}\right\}$$

$$\times\left[V_l-(\dot{u}v'+2Uu'v')-\tfrac{1}{2}V_l v'^2\right]M-\tfrac{1}{2}MV_l v'V_l'+O(\epsilon^5), \tag{2-36}$$

where $V_l=\dot{v}+Uv'$, and therefore

$$F_A(X,t)=M\Big[\ddot{v}-\ddot{u}v'-2\dot{u}\dot{v}'-\tfrac{1}{2}\ddot{v}v'^2-\tfrac{3}{2}\dot{v}\dot{v}'v'$$

$$+U\left(2\dot{v}'-3\dot{u}'v'-4u'\dot{v}'-\tfrac{5}{2}\dot{v}'v'^2-2\dot{u}v''-\tfrac{3}{2}\dot{v}v'v''\right)$$

$$+U^2\left(v''-2u''v'-4u'v''-2v'^2v''\right)\Big]+O(\epsilon^5). \tag{2-37}$$

2.4.3 *The frictional forces*

The frictional forces are formulated essentially as proposed by G. I. Taylor (1952), i.e.,

$$F_N=\tfrac{1}{2}\rho DU^2\left(C_N\sin i+C_{Dp}\sin^2 i\right), \tag{2-38}$$

$$F_L=\tfrac{1}{2}\rho DU^2C_T\cos i, \tag{2-39}$$

respectively, in the normal and longitudinal directions; D is the cylinder diameter, C_{Dp} the form drag coefficient due to the normal component, and C_N and C_T, in general not equal, are the coefficients associated with friction in the normal and tangential directions, respectively.

Substituting (2-33) into expressions (2-38) and (2-39) and relating U_f to U through Equation (2-27), one obtains

$$F_N = \tfrac{1}{2}\rho D U^2 \left[C_N \left(v' + \frac{\dot{v}}{U} + \frac{\dot{v}u'}{U} - u'v' + \frac{\dot{u}\dot{v}}{U^2} - \tfrac{1}{2}\left(v'^3 + \frac{\dot{v}^3}{U^3} + \frac{v'^2\dot{v}}{U} + \frac{v'\dot{v}^2}{U^2} \right) \right) \right.$$

$$\left. + C_{Dp}\left(v'|v'| + \frac{v'|\dot{v}| + |v'|\dot{v}}{U} + \frac{\dot{v}|\dot{v}|}{U^2} \right) \right] + O\left(\epsilon^4\right), \tag{2-40}$$

$$F_L = \tfrac{1}{2}\rho D U^2 C_T \left(1 - \tfrac{1}{2}\left(v'^2 + 2\frac{v'\dot{v}}{U} + \frac{\dot{v}^2}{U^2} \right) \right) + O\left(\epsilon^4\right). \tag{2-41}$$

The quadratic terms in the expression for F_N are modified by using the method proposed by Triantafyllou & Chryssostomidis (1989), in order to obtain forces, which are odd with respect to v' and $\dot{v}$, thus forces always opposing motion. In Equations (2-40) and (2-41), C_N, C_T and C_{Dp} are supposed to be longitudinally averaged, independent of axial location, for simplicity.

2.4.4 The hydrostatic pressure forces

F_{px} and F_{py}, which are the resultants of the steady-state pressure p acting on the outer surface of the element, will be determined following Païdoussis' procedure (1973). Consider the element of Figure 2-4 momentarily frozen and immersed in fluid on all sides. Then, there will be additional forces, pA and $pA + \left[\partial(pA)/\partial X\right]\delta X$, on the two flat, normally dry faces of the element, in addition to the pressure resultant on the wet surfaces, $F_{px}\delta X$ and $F_{py}\delta X$; the net resultant of all forces is known and is equal to the buoyancy force. The pressure is assumed to be of the form $p(x) = a + bx$, which covers both purely hydrostatic and pressure-drop-modified pressure distributions. Consequently, one may write

$$\frac{D\vec{I}}{Dt} = \sum \vec{F} = \vec{F}_e + \vec{F}_P, \tag{2-42}$$

where $\vec{I}$ is the momentum of the fluid, $\vec{F}_e$ is the resultant of external forces, which is equal to zero in this case, and $\vec{F}_P$ is the resultant of pressure forces, $\vec{F}_P = -\oiint_A p\hat{n}\, dA$.

Therefore, considering the forces in Figure 2-4, one can write

$$\left[-F_{px}-\frac{\partial}{\partial X}\left(pA\cos\theta_1\right)\right]\,\delta X\,\mathbf{i}+\left[F_{py}-\frac{\partial}{\partial X}\left(pA\sin\theta_1\right)\right]\,\delta X\,\mathbf{j}=-\oiint_A p\hat{n}\,dA \tag{2-43}$$

where $\hat{n}$ is the outwardly pointing normal.

According to the Gauss' theorem,

$$\oiint_A p\hat{n}\,dA=\oiiint_V \nabla p\,dV \tag{2-44}$$

and therefore (2-43) becomes

$$\left[-F_{px}-\frac{\partial}{\partial X}\left(pA\cos\theta_1\right)\right]\,\delta X\,\mathbf{i}+\left[F_{py}-\frac{\partial}{\partial X}\left(pA\sin\theta_1\right)\right]\,\delta X\,\mathbf{j}=-\oiiint_V \nabla p\,dV. \tag{2-45}$$

Having assumed that p is a function of x only, the pressure gradient is in the x-direction only,

$$\nabla p=\frac{\partial p}{\partial x}\mathbf{i}+\frac{\partial p}{\partial y}\mathbf{j}+\frac{\partial p}{\partial z}\mathbf{k}=\frac{\partial p}{\partial x}\mathbf{i} \tag{2-46}$$

and the elemental volume is

$$\delta V=A\,\delta X; \tag{2-47}$$

therefore,

$$\left[-F_{px}-\frac{\partial}{\partial X}\left(pA\cos\theta_1\right)\right]\,\delta X\,\mathbf{i}+\left[F_{py}-\frac{\partial}{\partial X}\left(pA\cos\theta_1\right)\right]\,\delta X\,\mathbf{j}=\left(-\frac{\partial p}{\partial x}\mathbf{i}\right)A\delta X. \tag{2-48}$$

Equating the terms in the **i**- and **j**-direction, one obtains

$$-F_{px}-\frac{\partial}{\partial X}\left(pA\cos\theta_1\right)=-\frac{\partial p}{\partial x}A,$$

$$F_{py}-\frac{\partial}{\partial X}\left(pA\sin\theta_1\right)=0, \tag{2-49}$$

and for a constant cross-section, ($\frac{\partial A}{\partial X}=0$),

$$-F_{px} = \frac{\partial p}{\partial X} A\cos\theta_1 + pA\frac{\partial}{\partial X}(\cos\theta_1) - \frac{\partial p}{\partial x}A,$$

$$F_{py} = \frac{\partial p}{\partial X} A\sin\theta_1 + pA\frac{\partial}{\partial X}(\sin\theta_1). \tag{2-50}$$

Substituting $\frac{\partial p}{\partial X}$ in this set of equations by $\partial p/\partial X = (\partial p/\partial x)(\partial x/\partial X) = (\partial p/\partial x)(1+u')$, one may find

$$-F_{px} = \frac{\partial p}{\partial x}(1+u') A\cos\theta_1 + pA\frac{\partial}{\partial X}(\cos\theta_1) - \frac{\partial p}{\partial x}A,$$

$$F_{py} = \frac{\partial p}{\partial x}(1+u') A\sin\theta_1 + pA\frac{\partial}{\partial X}(\sin\theta_1). \tag{2-51}$$

Finally, substituting (2-6) and (2-7) into (2-51) and keeping terms up to the third order of magnitude, one finds

$$-F_{px} = \frac{\partial p}{\partial x}A\left(-\tfrac{1}{2}v'^2 + u'\right) - v'v''pA + O\left(\epsilon^4\right), \tag{2-52}$$

$$F_{py} = \frac{\partial p}{\partial x}A\left(v' - \tfrac{1}{2}v'^3\right) + pA\left(v'' - u''v' - u'v'' - \tfrac{3}{2}v'^2v''\right) + O\left(\epsilon^5\right). \tag{2-53}$$

Furthermore, by considering that the lateral movement of the cylinder has a negligible effect on the axial pressure distribution in the fluid at large (its velocity then being U), one may write (Païdoussis, 1973)

$$A\frac{\partial p}{\partial x} = -\tfrac{1}{2}\rho D U^2 C_T \frac{D}{D_h} + \rho g A, \tag{2-54}$$

where D is the diameter of the cylinder, D_h is the hydraulic diameter, and C_T is the uniform frictional coefficient, as in Equation (2-41).

Knowing that $A(\partial p/\partial X) = A(\partial p/\partial x)(1+u')$ and using Equation (2-54), one can integrate the resulting equation from X=X to X=L, assuming the cross-sectional area to be constant, and thus obtain

$$Ap(X) = Ap(L) + \left(\tfrac{1}{2}\rho D U^2 C_T \frac{D}{D_h} - \rho g A\right)\left[L - X + u(L)(1-\bar{\delta}) - u\right] + O\left(\epsilon^4\right), \tag{2-55}$$

where $p(L)$ is the pressure at the downstream end of the cylinder, which may be represented by

$$Ap(L)=\left[\left(1-2\nu\right)\overline{P}A+\rho gA\frac{L}{2}\right]\overline{\delta}, \tag{2-56}$$

where the $-2\nu\overline{P}A$ term is the compressive load due to pressurization-induced radial contraction; ν is the Poisson ratio; as before, $\overline{\delta}=1$ if there is no sliding at the ends, and $\overline{\delta}=0$ if the downstream end can slide axially; $\overline{P}$ stands for the value of p (the static pressure) at $X=\frac{1}{2}L$.

Combining expression (2-54) with (2-52) and (2-53), we get

$$-F_{px}=\left(-\tfrac{1}{2}v'^2+u'\right)\left(-\tfrac{1}{2}\rho DU^2C_T\frac{D}{D_h}+\rho gA\right)-v'v''Ap+O\left(\epsilon^4\right), \tag{2-57}$$

$$F_{py}=\left(v'-\tfrac{1}{2}v'^3\right)\left(-\tfrac{1}{2}\rho DU^2C_T\frac{D}{D_h}+\rho gA\right)+\left(v''-u''v'-u'v''-\tfrac{3}{2}v'^2v''\right)Ap+O\left(\epsilon^5\right). \tag{2-58}$$

2.4.5 The total virtual work of the fluid forces

The virtual work of the fluid forces on the whole body may be written as

$$\int_{t_1}^{t_2}\delta W\,dt=\int_{t_1}^{t_2}\int_0^L\Big\{\left[-F_{Px}+F_L\cos\theta_1+\left(F_A+F_N\right)\sin\theta_1\right]\delta x$$

$$+\left[F_{Py}+F_L\sin\theta_1-\left(F_A+F_N\right)\cos\theta_1\right]\delta y\Big\}\,dX\,dt. \tag{2-59}$$

One should be very careful when developing expression (2-59), in the use of the expressions for the forces and trigonometric expressions, Equations (2-32), (2-37), (2-40), (2-41), (2-57) and (2-58), to ensure that third-order accuracy is maintained.

For an extensible cylinder, considering two independent variables, one eventually obtains

$$
\begin{aligned}
\int_{t_1}^{t_2} \delta \mathrm{W}\, dt = &-\int_{t_1}^{t_2} \int_0^L \Bigg\{ -\tfrac{1}{2}\rho D U^2 C_T \left(1-\tfrac{1}{2}\frac{\dot{v}^2}{U^2}-\frac{\dot{v}v'}{U}-v'^2\right) - M\left(\ddot{v}v' + 2U\dot{v}'v' + U^2 v'v''\right) \\
&-\tfrac{1}{2}\rho D U^2 C_N \left(\frac{\dot{v}v'}{U}+v'^2\right) - \left(\tfrac{1}{2}\rho D U^2 C_T \frac{D}{D_h} - \rho g A\right)\left(-u' + \tfrac{1}{2}v'^2 - (L-X)v'v''\right) \\
&-\tfrac{1}{2}\rho D U^2 C_{Dp} v' \left(v'|v'| + \frac{v'|\dot{v}| + \dot{v}|v'|}{U} + \frac{\dot{v}|\dot{v}|}{U^2}\right) + \left[\tfrac{1}{2}\rho g L \bar{\delta} + (1-2\nu)\bar{p}\right] A v'v'' \Bigg\} \delta u\, dX\, dt \\
&-\int_{t_1}^{t_2} \int_0^L \Bigg\{ M\ddot{v}\left(1-v'^2\right) + 2MU\dot{v}'\left(1-\tfrac{7}{4}v'^2\right) + MU^2 v''\left(1-\tfrac{5}{2}v'^2\right) - Mv'\left(\ddot{u} + 3U\dot{u}' + 2U^2 u''\right) \\
&-M\left(4Uu' + 2\dot{u} + \tfrac{3}{2}\dot{v}v'\right)\left(\dot{v}' + Uv''\right) - \tfrac{1}{2}\rho D U^2 \left(C_T - C_N\right)\left(v' - \tfrac{1}{2}\frac{v'\dot{v}^2}{U^2} - u'v' - \frac{\dot{v}v'^2}{U} - v'^3\right) \\
&+\left(\tfrac{1}{2}\rho D U^2 C_T \frac{D}{D_h} - \rho g A\right) \\
&\times\left(v' - \tfrac{1}{2}v'^3 + \left[u - u(L)\left(1-\bar{\delta}\right)\right]v'' - (L-X)\left(v'' - u''v' - u'v'' - \tfrac{3}{2}v'^2 v''\right)\right) \\
&-\left[\tfrac{1}{2}\rho g L \bar{\delta} + (1-2\nu)\bar{P}\right] A\left(v'' - u''v' - u'v'' - \tfrac{3}{2}v'^2 v''\right) \\
&+\tfrac{1}{2}\rho D U^2 C_N \left(\frac{\dot{v}}{U} + \frac{u'\dot{v}}{U} + \frac{\dot{u}\dot{v}}{U^2} - \tfrac{1}{2}\frac{\dot{v}^3}{U^3}\right) \\
&+\tfrac{1}{2}\rho D U^2 C_{Dp} \left(v'|v'| + \frac{v'|\dot{v}| + \dot{v}|v'|}{U} + \frac{\dot{v}|\dot{v}|}{U^2}\right)\Bigg\} \delta v\, dX\, dt + O\left(\epsilon^5\right). \qquad (2\text{-}60)
\end{aligned}
$$

2.5 Equations of motion

Substituting Equations (2-16), (2-18), (2-26) and (2-60) into Hamilton's principle, Equation (2-14), one finds a large equation involving a double integral from t_1 to t_2 and from 0 to L, but since the terms multiplied by δu are independent of the terms multiplied by δv and the domains of integration remain arbitrary, the integrand itself must be equal to zero. The resulting equations are two coupled partial differential equations, one mainly associated with the X- and the other mainly with the Y-direction, describing the behaviour of an extensible cylinder subjected to axial flow:

$$
\begin{aligned}
& m\ddot{u} - M\left(\ddot{v}v' + 2U\dot{v}'v' + U^2 v''v'\right) - EA\left(u'' + v'v''\right) - EI\left(v''v''' + v'v''''\right) \\
& -\tfrac{1}{2}\rho D U^2 \left(C_N - C_T\right)\left(\frac{\dot{v}v'}{U} + v'^2\right) + \tfrac{1}{4}\rho D C_T \dot{v}^2 \\
& +\tfrac{1}{2}\rho D U^2 C_T \left(1 + \frac{D}{D_h}\right)\left\{u' - \frac{v'^2}{2} + \left[\left(1 - \tfrac{1}{2}\delta\right)L - X\right]v'v''\right\} \\
& -\tfrac{1}{2}\rho D U^2 C_{Dp} v' \left(v'\left|v'\right| + \frac{v'\left|\dot{v}\right| + \dot{v}\left|v'\right|}{U} + \frac{\dot{v}\left|\dot{v}\right|}{U^2}\right) + \left[\tfrac{1}{2}\rho D^2 U^2 C_b \left(1 - \delta\right) + \overline{T}\delta + \left(1 - 2\nu\right)A\overline{P}\delta\right]v'v'' \\
& +\left(mg - \rho g A\right)\left\{u' - \frac{v'^2}{2} + \left[\left(1 - \tfrac{1}{2}\delta\right)L - X\right]v'v''\right\} + O\left(\epsilon^5\right) = 0,
\end{aligned}
\tag{2-61}
$$

$$
\begin{aligned}
& \left(m + M\right)\ddot{v} + 2MU\dot{v}'\left(1 - \tfrac{7}{4}v'^2\right) + MU^2 v''\left(1 - \tfrac{5}{2}v'^2\right) - Mv'\left(\ddot{u} + 3U\dot{u}' + 2U^2 u''\right) - M\ddot{v}v'^2 \\
& -M\left(4Uu' + 2\dot{u} + \tfrac{3}{2}\dot{v}v'\right)\left(\dot{v}' + Uv''\right) \\
& +\left[\tfrac{1}{2}\rho D^2 U^2 C_b \left(1 - \delta\right) + \overline{T}\delta + \left(1 - 2\nu\right)A\overline{P}\delta\right]\left(-v'' + v'u'' + v''u' + \tfrac{3}{2}v'^2 v''\right) \\
& +\tfrac{1}{2}\rho D U^2 C_{Dp}\left(v'\left|v'\right| + \frac{v'\left|\dot{v}\right| + \dot{v}\left|v'\right|}{U} + \frac{\dot{v}\left|\dot{v}\right|}{U^2}\right) - EA\left(u''v' + u'v'' + \tfrac{3}{2}v'^2 v''\right) \\
& +EIv'''' - EI\left(8v'v''v''' + v'u^{(4)} + 2v'^2 v^{(4)} + 2v''^3 + 2u'v^{(4)} + 4u''v''' + 3u'''v''\right) \\
& +\tfrac{1}{2}\rho D U^2 C_T \left(1 + \frac{D}{D_h}\right) \\
& \times\left[-\tfrac{1}{2}v'^3 + \left[u - u\left(L\right)\left(1 - \delta\right)\right]v'' + \left(\left(1 - \tfrac{1}{2}\delta\right)L - X\right)\left(-v'' + v'u'' + v''u' + \tfrac{3}{2}v'^2 v''\right)\right] \\
& -\tfrac{1}{2}\rho D U^2 \left(C_N - C_T\right)\left(v'^3 + v'u' + \frac{\dot{v}v'^2}{U} + \frac{1}{2}\frac{\dot{v}^2 v'}{U^2}\right) + \tfrac{1}{2}\rho D U^2 \left(C_N + C_T \frac{D}{D_h}\right)v' \\
& +\tfrac{1}{2}\rho D U^2 C_N \left(\frac{\dot{v}}{U} + \frac{u'\dot{v}}{U} + \frac{\dot{u}\dot{v}}{U^2} - \frac{1}{2}\frac{\dot{v}^3}{U^3}\right) \\
& +\left(mg - \rho g A\right)\Big\{v' - \tfrac{1}{2}v'^3 + \left[u - u\left(L\right)\left(1 - \delta\right)\right]v'' \\
& +\left[\left(1 - \tfrac{1}{2}\delta\right)L - X\right]\left(-v'' + v'u'' + v''u' + \tfrac{3}{2}v'^2 v''\right)\Big\} + O(\epsilon^5) = 0.
\end{aligned}
\tag{2-62}
$$

In Equations (2-61), (2-62) and what follows, $\overline{\delta}$ (defined in conjunction with Equations (2-22) and (2-55)) has been replaced by δ for notational simplicity. In order to find the nondimensional form of the equations of motion, which makes the analysis of the system more general and not restricted to one specific system, we first introduce the following nondimensional quantities:

$$\xi=\frac{X}{L},\quad \zeta=\frac{u}{L},\quad \eta=\frac{v}{L},\quad \tau=\left(\frac{EI}{m+\rho A}\right)^{1/2}\frac{t}{L^2},$$

$$\begin{gathered}\mathcal{U}=\left(\frac{\rho A}{EI}\right)^{1/2}UL,\quad \beta=\frac{\rho A}{m+\rho A},\quad \gamma=\frac{(m-\rho A)gL^3}{EI},\\ c_n=\frac{4}{\pi}C_N,\quad c_t=\frac{4}{\pi}C_T,\quad c_d=\frac{4}{\pi}C_{Dp},\quad c_b=\frac{4}{\pi}C_b,\quad \varepsilon=\frac{L}{D},\quad h=\frac{D}{D_h},\\ \overline{\Pi}=\frac{\overline{P}AL^2}{EI},\quad \overline{\Gamma}=\frac{\overline{T}L^2}{EI},\quad \Pi_0=\frac{EAL^2}{EI},\quad \chi=\frac{M}{\rho A}.\end{gathered}\tag{2-63}$$

Next, we replace X, u, v, C_N, C_T and C_{Dp} by their corresponding nondimensional values, ξ, ζ, η, c_n, c_t and c_d, respectively, as defined in (2-63), to yield the following form for the dimensionless equations:

$$\begin{aligned}&(1-\beta)\ddot{\zeta}-\chi\left(\beta\,\ddot{\eta}\eta'+2\mathcal{U}\sqrt{\beta}\dot{\eta}'\eta'+\mathcal{U}^2\eta''\eta'\right)-\Pi_0\,\left(\zeta''+\eta'\eta''\right)-\left(\eta''\eta'''+\eta'\eta^{(4)}\right)\\ &-\tfrac{1}{2}\varepsilon\,\mathcal{U}^2\left(c_n-c_t\right)\left(\frac{\sqrt{\beta}}{\mathcal{U}}\dot{\eta}\eta'+\eta'^2\right)+\tfrac{1}{4}\varepsilon\,c_t\beta\dot{\eta}^2+\tfrac{1}{2}\varepsilon\,\mathcal{U}^2c_t\left(1+h\right)\left[\zeta'-\frac{\eta'^2}{2}+\left(1-\tfrac{1}{2}\delta-\xi\right)\eta'\eta''\right]\\ &-\tfrac{1}{2}\varepsilon\,\mathcal{U}^2c_d\eta'\left(\eta'|\eta'|+\frac{\sqrt{\beta}\left(\eta'|\dot{\eta}|+\dot{\eta}|\eta'|\right)}{\mathcal{U}}+\frac{\beta\dot{\eta}|\dot{\eta}|}{\mathcal{U}^2}\right)+\left[\tfrac{1}{2}\mathcal{U}^2c_b\left(1-\delta\right)+\overline{\Gamma}\delta+\left(1-2\nu\right)\overline{\Pi}\delta\right]\eta'\eta''\\ &+\gamma\left[\zeta'-\frac{\eta'^2}{2}+\left(1-\tfrac{1}{2}\delta-\xi\right)\,\eta'\eta''\right]+O\left(\epsilon^5\right)=0,\end{aligned}\tag{2-64}$$

$$
\begin{aligned}
&\left(1+(\chi-1)\beta\right)\ddot{\eta}+2\chi\mathcal{U}\sqrt{\beta}\;\dot{\eta}'\left(1-\tfrac{7}{4}\eta'^{2}\right)+\chi\mathcal{U}^{2}\eta''\left(1-\tfrac{5}{2}\eta'^{2}\right)-\chi\eta'\left(\beta\ddot{\zeta}+3\sqrt{\beta}\,\mathcal{U}\dot{\zeta}'+2\mathcal{U}^{2}\zeta''\right)-\chi\beta\ddot{\eta}\eta'^{2}\\
&-\chi\left(4\mathcal{U}\zeta'+2\sqrt{\beta}\dot{\zeta}+\tfrac{3}{2}\sqrt{\beta}\dot{\eta}\eta'\right)\left(\sqrt{\beta}\dot{\eta}'+\mathcal{U}\eta''\right)\\
&+\left[\tfrac{1}{2}\mathcal{U}^{2}c_{b}\left(1-\delta\right)+\bar{\Gamma}\delta+\left(1-2\nu\right)\bar{\Pi}\delta\right]\left(-\eta''+\eta'\zeta''+\eta''\zeta'+\tfrac{3}{2}\eta'^{2}\eta''\right)\\
&+\tfrac{1}{2}\varepsilon\mathcal{U}^{2}c_{d}\left(\eta'\left|\eta'\right|+\frac{\sqrt{\beta}\left(\eta'\left|\dot{\eta}\right|+\dot{\eta}\left|\eta'\right|\right)}{\mathcal{U}}+\frac{\beta\dot{\eta}\left|\dot{\eta}\right|}{\mathcal{U}^{2}}\right)-\Pi_{0}\left(\zeta''\eta'+\zeta'\eta''+\tfrac{3}{2}\eta'^{2}\eta''\right)\\
&+\nu^{(4)}-\left(8\eta'\eta''\eta'''+\eta'\zeta^{(4)}+2\eta'^{2}\eta^{(4)}+2\eta''^{3}+2\zeta'\eta^{(4)}+4\zeta''\eta'''+3\zeta'''\eta''\right)\\
&+\tfrac{1}{2}\varepsilon\mathcal{U}^{2}c_{t}\left(1+h\right)\\
&\times\left(-\tfrac{1}{2}\eta'^{3}+\left[\zeta-\zeta(1)\left(1-\delta\right)\right]\eta''+\left(1-\tfrac{1}{2}\delta-\xi\right)\left(-\eta''+\eta'\zeta''+\eta''\zeta'+\tfrac{3}{2}\eta'^{2}\eta''\right)\right)\\
&-\tfrac{1}{2}\varepsilon\mathcal{U}^{2}\left(c_{n}-c_{t}\right)\left(\eta'^{3}+\eta'\zeta'+\beta\frac{\dot{\eta}\eta'^{2}}{\mathcal{U}}+\tfrac{1}{2}\beta\frac{\dot{\eta}^{2}\eta'}{\mathcal{U}^{2}}\right)+\tfrac{1}{2}\varepsilon\mathcal{U}^{2}\left(c_{n}+c_{t}h\right)\eta'\\
&+\tfrac{1}{2}\varepsilon\mathcal{U}^{2}c_{n}\left(\frac{\sqrt{\beta}}{\mathcal{U}}\dot{\eta}+\frac{\sqrt{\beta}}{\mathcal{U}}\zeta'\dot{\eta}+\frac{\beta}{\mathcal{U}^{2}}\dot{\zeta}\,\eta-\tfrac{1}{2}\frac{\beta^{3/2}}{\mathcal{U}^{3}}\dot{\eta}^{3}\right)\\
&+\gamma\Big\{\eta'-\tfrac{1}{2}\eta'^{3}+\left[\zeta-\zeta(1)\left(1-\delta\right)\right]\eta''\\
&+\left(1-\tfrac{1}{2}\delta-\xi\right)\left(-\eta''+\eta'\zeta''+\eta''\zeta'+\tfrac{3}{2}\eta'^{2}\eta''\right)\Big\}+O\left(\epsilon^{5}\right)=0. \qquad (2\text{-}65)
\end{aligned}
$$

In these equations, ζ and η are, respectively, the nondimensional displacements in the longitudinal and transverse direction; $\mathcal{U}$ is the dimensionless flow velocity, used extensively as the independent parameter in studying the dynamics of the system; $\beta = \rho A/(m+\rho A)$ is a mass ratio; $\Pi_0 = EAL^2/EI$, $\bar{\Pi} = \bar{P}AL^2/EI$ and $\bar{\Gamma} = \bar{T}L^2/EI$ are dimensionless measures of axial flexibility, pressurization and externally imposed uniform tension, respectively; c_n and c_t are the coefficients of frictional forces in the normal and tangential (longitudinal) directions, respectively; c_d is the coefficient of transverse form drag; $\delta = 0$ or 1 if the downstream end is free to slide axially (or wholly free), or is axially fixed; ν is the Poisson ratio; $\gamma = (m-\rho A)gL^3/EI$ is a gravity coefficient; c_b is the base-drag coefficient acting in the longitudinal direction at the free end of the cylinder when $\delta = 0$; $\varepsilon = L/D$ is the slenderness ratio; $h = D/D_h$ is a hydraulic confinement coefficient, D_h being the hydraulic diameter; and $\chi = M/\rho A$ is an added mass coefficient which increases with increasing confinement.

These equations of motion are valid for all boundary conditions of a slender flexible cylinder subjected to axial flow, either supported at both ends or free at the downstream end.* The equation of motion derived in Lopes et al. (2002) is valid only for cantilevered cylinders. In that derivation the inextensibility assumption has been invoked which relates the displacement in the transverse direction to that in the axial direction, leading to a single equation of motion. In the present equations of motion, however, no such assumption has been made, and hence we have obtained two coupled equations of motion, one mainly for the axial and the other mainly for the transverse direction. In these equations, there are some terms, which would vanish if the inextensibility assumption had been used.† There are also some terms in Equations (2-64) and (2-65) containing external pressure and externally imposed tension on the cylinder, which are not present in the equations of motion for the cantilevered cylinder, because such terms do not exist when there is a free end $(\delta = 0)$. There is also a new essential parameter defined in this set of equations, relating the axial and transverse rigidities of the cylinder (Π_0), which also does not arise if the centreline is inextensible.

2.6 Descretization of the partial differential equation

As a first step towards solving the partial differential equations of motion, (2-64) and (2-65), they are transformed into a set of second-order ordinary differential equations using Galerkin's technique with the bar and beam eigenfunctions $\psi_j(\xi)$ and $\phi_j(\xi)$ used as a suitable set of base functions and with $p_j(\tau)$ and $q_j(\tau)$ being the corresponding generalized coordinates; thus,

---

* If the end is free, however, special boundary conditions may have to be introduced, to represent the possibly tapering tip of the cylinder (Lopes et al., 2002; Païdoussis, 2004).

† Taking the inextensibility assumption into account, one finds $\varepsilon = 0$ in Equation (2-4) leading to $\zeta' = -\frac{1}{2}\eta'^2$.

$$\zeta(\xi,\tau)=\sum_{j=1}^{N_u}\psi_j(\xi)p_j(\tau), \tag{2-66}$$

$$\eta(\xi,\tau)=\sum_{j=1}^{N_v}\phi_j(\xi)q_j(\tau), \tag{2-67}$$

where N_u and N_v represent the number of modes in the longitudinal and the lateral direction, respectively. Substituting expressions (2-66) and (2-67) into (2-64) and (2-65), multiplying (2-64) by $\psi_i(\xi)$ and (2-65) by $\phi_i(\xi)$ and integrating from 0 to 1, using the fact that $\int_0^1\psi_i(\xi)\psi_j(\xi)d\xi=\int_0^1\phi_i(\xi)\phi_j(\xi)d\xi=\delta_{ij}$ (δ_{ij} being the Kronecker delta), leads to the following equations in indicial form:

$$\begin{aligned}&M_{ij}^{u}\ddot{p}_j+C_{ij}^{u}\dot{p}_j+K_{ij}^{u}p_j+A_{ijk}^{1}q_jq_k+A_{ijk}^{2}q_j\dot{q}_k+A_{ijk}^{3}\dot{q}_j\dot{q}_k+A_{ijk}^{4}q_j\ddot{q}_k\\&+B_{ijkl}^{1}q_jq_k\left|q_l\right|+B_{ijkl}^{2}q_j\dot{q}_k\left|q_l\right|+B_{ijkl}^{3}q_jq_k\left|\dot{q}_l\right|+B_{ijkl}^{4}q_j\dot{q}_k\left|\dot{q}_l\right|=0\end{aligned} \tag{2-68}$$

and

$$\begin{aligned}&M_{ij}^{v}\ddot{q}_j+C_{ij}^{v}\dot{q}_j+K_{ij}^{v}q_j+D_{ijk}^{1}p_jq_k+D_{ijk}^{2}\dot{p}_jq_k+D_{ijk}^{3}p_j\dot{q}_k+D_{ijk}^{4}\dot{p}_j\dot{q}_k+D_{ijk}^{5}\ddot{p}_jq_k\\&+E_{ijk}^{1}q_j\left|q_k\right|+E_{ijk}^{2}\dot{q}_j\left|q_k\right|+E_{ijk}^{3}q_j\left|\dot{q}_k\right|+E_{ijk}^{4}\dot{q}_j\left|\dot{q}_k\right|\\&+F_{ijkl}^{1}q_jq_kq_l+F_{ijkl}^{2}q_jq_k\dot{q}_l+F_{ijkl}^{3}q_j\dot{q}_k\dot{q}_l+F_{ijkl}^{4}\dot{q}_j\dot{q}_k\dot{q}_l+F_{ijkl}^{5}q_jq_k\ddot{q}_l=0,\end{aligned} \tag{2-69}$$

where the coefficients are given in Appendix A.

Concerning the linear terms, M_{ij}^u, C_{ij}^u and K_{ij}^u correspond respectively to the mass, damping and stiffness matrices in the *u*-direction and M_{ij}^v, C_{ij}^v and K_{ij}^v to the corresponding matrices in the *v*-direction. All the other terms are related to coefficients of the nonlinear terms in the *u* and *v* directions.

In the foregoing, internal dissipation in the material of the cylinder was neglected; for generality, it is now introduced into the equations of motion, via the simplest possible model. The internal dissipation of the cylinder is assumed to be viscous and linear. In order to find the related terms, we look at the linear equations of motion in the axial and the transverse directions, assuming that there are no flow- and gravity-related forces. The linear equations of motion become $M_{ij}^u\ddot{p}_j+K_{ij}^u p_j=0$ and $M_{ij}^v\ddot{q}_j+K_{ij}^v q_j=0$, in the axial and the transverse directions, respectively, in which $M_{ij}^u=\int_0^1\psi_i\psi_j d\xi=\delta_{ij}$,

$K_{ij}^{u} = -\Pi_0 \int_0^1 \psi_i \psi_j'' d\xi$, $M_{ij}^{v} = \int_0^1 \phi_i \phi_j d\xi = \delta_{ij}$, $K_{ij}^{v} = \int_0^1 \phi_i \phi_j^{(4)} d\xi$. In the axial direction, the linear viscous damping can be written as $C_{ij,viscous}^{u} = 2\varsigma \left(K_{ij}^{u} M_{ij}^{u}\right)^{\frac{1}{2}} = 2\varsigma \left(-\Pi_0 \int_0^1 \psi_i \psi_j'' d\xi\right)^{\frac{1}{2}}$ $= 2\varsigma \sqrt{\Pi_0} \lambda_i^{u}$; λ_i^{u} being the ith eigenvalue of a bar in axial vibration, with the same boundary conditions as the cylinder, and ς being the damping ratio. In the same manner, one can find the viscous damping in the transverse direction as $C_{ij,viscous}^{v} = 2\varsigma \left(\lambda_i^{v}\right)^2$; λ_i^{v} being the ith eigenvalue of a beam in transverse vibration. C_{ij}^{u} and the third term in C_{ij}^{v} in Appendix A are terms associated with this dissipation.

2.7 The equations of motion recast in first-order form

In order to make it possible to analyse the system using AUTO as will be described in the following chapter, one needs to recast the second-order ordinary differential equations, (2-68) and (2-69), in the first-order form. After some switching in the indices and re-grouping of terms, Equations (2-68) and (2-69) can be written as

$$\begin{aligned} &M_{ij}^{u} \ddot{p}_j + A_{ikj}^{4} q_k \ddot{q}_j \\ &+C_{ij}^{u} \dot{p}_j + \left(A_{ikj}^{2} q_k + A_{ikj}^{3} \dot{q}_k + B_{iljk}^{2} q_l \left|q_k\right| + B_{ikjl}^{4} q_k \left|\dot{q}_l\right|\right) \dot{q}_j \\ &+K_{ij}^{u} p_j + \left(A_{ijk}^{1} q_k + B_{ijkl}^{1} q_k \left|q_l\right| + B_{ijkl}^{3} q_k \left|\dot{q}_l\right|\right) q_j = 0, \end{aligned} \tag{2-70}$$

$$\begin{aligned} &D_{ijk}^{5} \ddot{p}_j q_k + \left(M_{ij}^{v} + F_{ilkj}^{5} q_l q_k\right) \ddot{q}_j \\ &+\left(D_{ijk}^{2} q_k + D_{ijk}^{4} \dot{q}_k\right) \dot{p}_j + \left(C_{ij}^{v} + D_{ikj}^{3} p_k + E_{ijk}^{2} \left|q_k\right| + E_{ijk}^{4} \left|\dot{q}_k\right| + F_{ilkj}^{2} q_l q_k + F_{ilkj}^{3} q_l \dot{q}_k + F_{ijkl}^{4} \dot{q}_k \dot{q}_l\right) \dot{q}_j \\ &+D_{ijk}^{1} p_j q_k + \left(K_{ij}^{v} + E_{ijk}^{1} \left|q_k\right| + E_{ijk}^{3} \left|\dot{q}_k\right| + F_{ijkl}^{1} q_k q_l\right) q_j = 0. \end{aligned} \tag{2-71}$$

These two equations, can then be put together as one single set of equations in the following matrix form:

$$\begin{bmatrix} \left[M_{ij}^{u}\right]_{N_u \times N_u} & \left[A_{ikj}^{4} q_k\right]_{N_u \times N_v} \\ \left[D_{ijk}^{5} q_k\right]_{N_v \times N_u} & \left[M_{ij}^{v} + F_{ilkj}^{5} q_l q_k\right]_{N_v \times N_v} \end{bmatrix}_{N_t \times N_t} \begin{Bmatrix} \left\{\ddot{p}_j\right\} \\ \left\{\ddot{q}_j\right\} \end{Bmatrix}$$

$$+\begin{bmatrix} \left[C_{ij}^{u}\right]_{N_u\times N_u} & \left[A_{ikj}^{2}q_k+A_{ikj}^{3}\dot{q}_k+B_{iljk}^{2}q_l\left|q_k\right|+B_{ikjl}^{4}q_k\left|\dot{q}_l\right|\right]_{N_u\times N_v} \\ \left[D_{ijk}^{2}q_k+D_{ijk}^{4}\dot{q}_k\right]_{N_v\times N_u} & \left[C_{ij}^{v}+D_{ikj}^{3}p_k+E_{ijk}^{2}\left|q_k\right|+E_{ijk}^{4}\left|\dot{q}_k\right|+F_{ilkj}^{2}q_lq_k+F_{ilkj}^{3}q_l\dot{q}_k+F_{ijkl}^{4}\dot{q}_k\dot{q}_l\right]_{N_v\times N_v} \end{bmatrix}\begin{Bmatrix}\{\dot{p}_j\}\\ \{\dot{q}_j\}\end{Bmatrix}$$

$$+\begin{bmatrix} \left[K_{ij}^{u}\right]_{N_u\times N_u} & \left[A_{ijk}^{1}q_k+B_{ijkl}^{1}q_k\left|q_l\right|+B_{ijkl}^{3}q_k\left|\dot{q}_l\right|\right]_{N_u\times N_v} \\ \left[D_{ijk}^{1}q_k\right]_{N_v\times N_u} & \left[K_{ij}^{v}+E_{ijk}^{1}\left|q_k\right|+E_{ijk}^{3}\left|\dot{q}_k\right|+F_{ijkl}^{1}q_kq_l\right]_{N_v\times N_v} \end{bmatrix}_{N_t\times N_t}\begin{Bmatrix}\{p_j\}\\ \{q_j\}\end{Bmatrix}=0, \qquad (2\text{-}72)$$

which can then be written as

$$\left\{\ddot{X}_j\right\}_{N_t\times 1}=-\left[M_{ij}\right]_{2N_t\times 2N_t}^{-1}\left[C_{ij}\right]_{2N_t\times 2N_t}\left\{\dot{X}_j\right\}_{N_t\times 1}-\left[M_{ij}\right]_{2N_t\times 2N_t}^{-1}\left[K_{ij}\right]_{2N_t\times 2N_t}\left\{X_j\right\}_{N_t\times 1}, \qquad (2\text{-}73)$$

where $N_t = N_u + N_v$.

Assuming $\{\dot{X}\}=\{Y\}$, the standard first-order form of the ordinary differential equations can be written as

$$\begin{Bmatrix}\dot{X}\\ \dot{Y}\end{Bmatrix}_{2N_t\times 1}=\begin{bmatrix}[0]_{N_t\times N_t} & I_{N_t\times N_t}\\ -\left[M_{ij}\right]^{-1}\left[K_{ij}\right] & -\left[M_{ij}\right]^{-1}\left[C_{ij}\right]\end{bmatrix}_{2N_t\times 2N_t}\begin{Bmatrix}X\\ Y\end{Bmatrix}_{2N_t\times 1}. \qquad (2\text{-}74)$$

2.8 Summary

In this chapter, weakly nonlinear equations of motion, correct to third order of magnitude, were derived using Hamilton's principle for the dynamics of an extensible slender cylinder subjected to axial flow. Here, lateral deflections were assumed to be of first-order magnitude, while axial ones of second-order. For convenience, inviscid, hydrostatic and viscous forces were determined separately, not together, say by direct application of the Navier-Stokes equations. The inviscid component was modelled by an extension to Lighthill's slender-body work. Frictional forces were formulated as proposed by G. I. Taylor and hydrodynamic pressure forces were the nonlinear extension of Païdoussis' formulation. The resulting equations were two coupled nonlinear partial differential equations, one mainly associated with the axial and the other mainly with the transverse direction. These nonlinear partial differential equations were nondimensionalized and then discretized by the Galerkin technique using the bar and beam eigenfunctions as suitable basis functions. The resulting second-order ordinary differential equations were recast in first-order form to make it possible to analyse the system using different tools, as will be discussed in the following chapters.

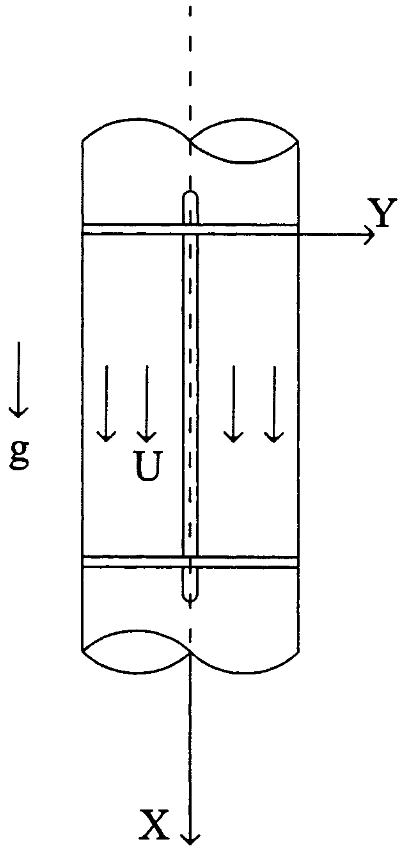

Figure 2-1 Diagrammatic view of a vertical slender flexible and extensible cylinder subjected to axial flow, in the test-section of a circulation system.

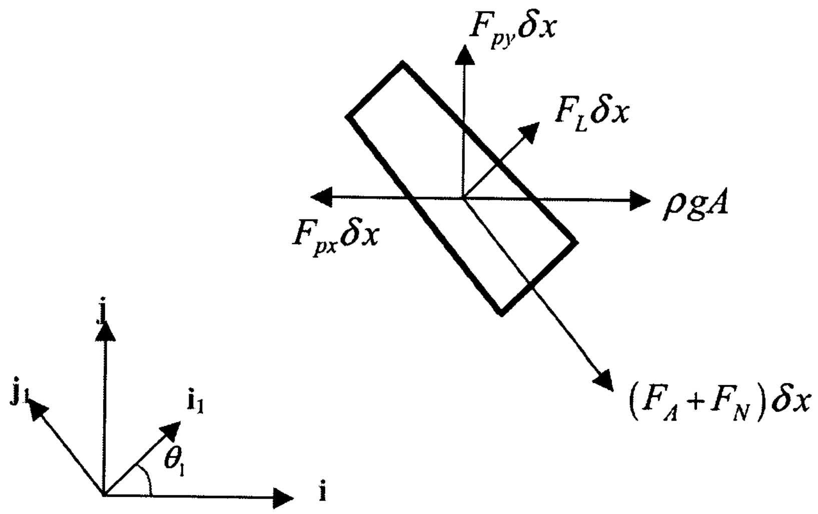

Figure 2-2 An element δx of the cylinder, showing the forces acting on it.

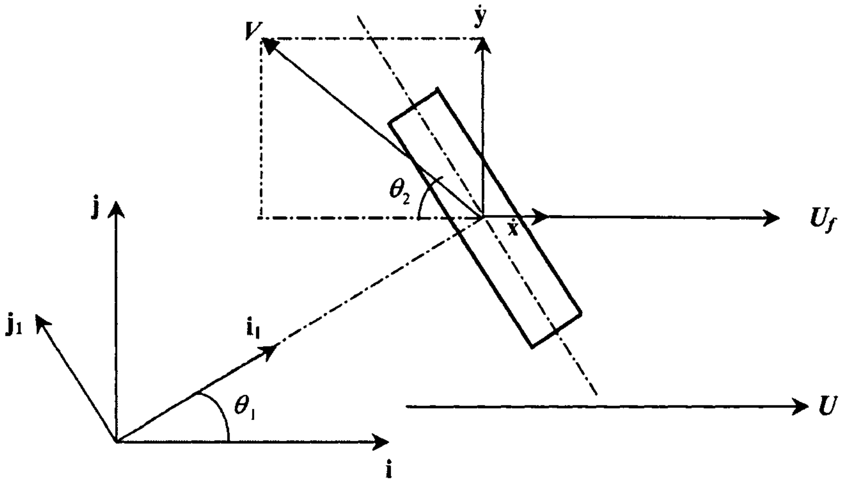

Figure 2-3 An element of the cylinder used for the determination of the relative fluid-cylinder velocity V and of the angles θ_1 and θ_2; V is the vectorial sum of $\dot{y}$ and $-U_f + \dot{x}$.

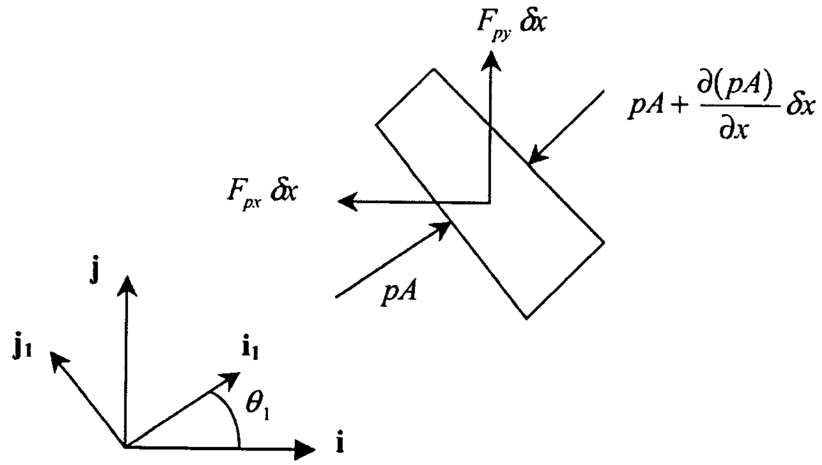

Figure 2-4 A rigid element of the cylinder surrounded by fluid.

3. Methods of Solution

3.1. Introduction

In this chapter, the methods used in this thesis to analyse the behaviour of slender flexible cylinders subjected to axial flow are presented. The equations of motion of this system are two coupled nonlinear partial differential equations (Equations (2-64) and (2-65)), which can be discretized by Galerkin's technique to give a set of second-order implicit nonlinear ordinary differential equations, of the type

$$\mathbf{M}\ddot{\mathbf{x}} + \mathbf{C}\dot{\mathbf{x}} + \mathbf{K}\mathbf{x} = \mathbf{F}\left(\mathbf{x}, \dot{\mathbf{x}}, \ddot{\mathbf{x}}, t\right), \tag{3-1}$$

with appropriate initial conditions $\mathbf{x}(0)$ and $\dot{\mathbf{x}}(0)$, in which $\mathbf{x}$ contains all the generalized coordinates used in the discretization. **M**, **C** and **K** are the mass, damping and stiffness matrices associated with the linear part of the system; if $N_t = N_u + N_v$ is the total number of degrees of freedom (N_u and N_v are the umber of modes in the axial and the transverse directions, respectively, as explained in Section 2.6), these matrices will be of order $N_t \times N_t$; and **F**, an $N_t \times 1$ vector, includes all the nonlinear terms. Equation (3-1) is said to be implicit because of the presence of the *nonlinear* inertial terms $\ddot{\mathbf{x}}$ in **F**; see the nonlinear inertial terms in (2-68) and (2-69).

The first method discussed in this chapter is Houbolt's finite difference method (FDM), which is an initial value problem solver and is used to solve the second-order ordinary differential equation (3-1), directly without any need to recast it in first-order form.

Equation (3-1) can also be expressed as an explicit relation, or in vector form

$$\dot{\mathbf{y}} = \mathbf{G}\left(\mathbf{y}, t\right), \qquad \mathbf{y}(0) = \mathbf{y}_0 \tag{3-2}$$

where **y** has the size of $2N_t$. Equation (2-74) is the first-order form of the equations of motion of a slender flexible cylinder subjected to axial flow. In this thesis, AUTO, which is a package for continuation and bifurcation problems in ordinary differential equations, is used to analyse the first-order form of the equations of motion for this system.

The analytical method of centre manifold reduction, which is used to study the behaviour of the system in the neighbourhood of the critical points, is also discussed in this chapter, especially to examine the behaviour of the system in the vicinity of the pitchfork bifurcation point. In this method, the essential behaviour of the system in the neighbourhood of the pitchfork bifurcation point can be studied by restricting attention to a one-dimensional invariant subspace, which is called the centre manifold.

3.2. Houbolt's Finite Difference Method (FDM)

Houbolt's finite difference method is an initial-value problem solver in which the system of equations is integrated numerically for one initial condition at a particular time, and the state of the system at any time thereafter can be reproduced. It has been shown that Houbolt's method is probably the most efficient time integrator for elastic-plastic structural dynamical problems (Tillerson and Stricklin, 1970; Wu and Witmer, 1973). It introduces some numerical damping, as well as some frequency distortion (Park, 1975), which is also the case for other popular schemes. Nath and Sandeep (1994) showed that Houbolt's scheme became unstable for their problem if the time step Δt was smaller than a critical value that depended upon the physical parameters. Semler et al. (1996) showed that this method could be used to solve equations of the form of Equation (3-1) directly, without re-writing them in the first-order form of Equation (3-2). They studied three specific methods, which were candidate numerical schemes to solve the second-order implicit nonlinear differential equations (3-1). According to their findings, the Picard iteration method using Chebychev series is not valid for solving implicit equations containing nonlinear inertial terms. They found that the Incremental Harmonic Balance method yields accurate periodic solutions, and also the frequency of oscillations and the dynamical stability of the system may be assessed very easily, but it cannot compute non-periodic (chaotic) solutions (Païdoussis, 1998, p. 376). Semler et al. (1996) showed that Houbolt's 4th order finite difference method can be used to compute time histories of initial value problems, if the time step is properly chosen. It was shown that when the time step is sufficiently small, e.g., 250 time steps per cycle, FDM yields accurate results. The only deficiency in Houbolt's scheme is that it introduces some very small numerical damping together with a phase shift, which might be negligible when dealing with dissipative systems. It is also noted that FDM finds only stable orbits, which nevertheless may be periodic, quasiperiodic or chaotic.

In Houbolt's finite difference method, the second-order and the first-order time derivatives are approximated in terms of the previously calculated values of the unknown by

$$\ddot{x}_{j,n+1} = \left[2x_{j,n+1} - 5x_{j,n} + 4x_{j,n-1} - x_{j,n-2}\right] / (\Delta t)^2, \tag{3-3}$$

$$\dot{x}_{j,n+1} = \left[11x_{j,n+1} - 18x_{j,n} + 9x_{j,n-1} - 2x_{j,n-2}\right] / (6\Delta t), \tag{3-4}$$

where $x_{j,n} = x_j(n\Delta t)$; Δt is the time step; x_j is the j^{th} element of the vector of unknowns $\mathbf{x}$; n is the step of calculations in which $x_{j,n}$, $x_{j,n-1}$ and $x_{j,n-2}$ have already been calculated in the previous steps, and $x_{j,n+1}$ is the unknown, to be found in this step.

Using Equations (3-3) and (3-4), we transform the N_t-dimensional second-order ordinary differential equation (3-1) to a set of nonlinear algebraic equations:

$$\mathbf{f}(\mathbf{x}_{n+1}) = \mathbf{0}, \tag{3-5}$$

where $\mathbf{f}$ is an N_t-dimensional nonlinear function of $\mathbf{x}_{n+1}$ that has to be solved numerically; $\mathbf{x}_n$, $\mathbf{x}_{n-1}$ and $\mathbf{x}_{n-2}$ are known from the previous steps.

The Newton-Raphson method is used to solve Equation (3-5) and is known to converge very rapidly: in less than 10 iterations usually. In the Newton-Raphson method, one has to start with an initial guess for $\mathbf{x}_{n+1}$. Because the time step, Δt in (3-3) and (3-4), is assumed to be small, a good initial guess is $\mathbf{x}_{n+1} = \mathbf{x}_n$. The next step in this method is to evaluate $\mathbf{f}$ and its Jacobian,

$$\mathbf{J} = \left(\partial f_i / \partial x_{j,n+1}\right), \tag{3-6}$$

at $\mathbf{x}_{n+1}$, numerically. The Jacobian may generally be obtained either analytically or numerically. In most vibration problems, and in the cases considered in this thesis, it is assumed that the Jacobian may be obtained analytically, and in the FDM program we provide the Jacobian analytically. Solving the linear system of equations,

$$\mathbf{J}(\mathbf{x}_{n+1})\mathbf{y} = -\mathbf{f}(\mathbf{x}_{n+1}), \tag{3-7}$$

for y, one can write

$$\mathbf{x}_{n+1} = \mathbf{x}_{n+1} + \mathbf{y}, \tag{3-8}$$

and repeat these steps until y is negligible to find the converged value of $\mathbf{x}_{n+1}$, which is the solution sought.

Figure 3-1 shows the flowchart of the FDM program, in which, basically, after reading the general physical parameters of the system, the program repeats all the above-mentioned steps for each flow velocity to find the time series. The resulting time series is then analysed to study the behaviour of the system at each flow velocity.

3.3. AUTO

Continuation methods are a very powerful numerical tool, which have been developed based on the concept of bifurcation theory. These methods follow a particular type of solution as it evolves in phase space as a result of varying one or more independent parameter(s). By considering the stability of the solutions, they detect the onset of new types of solutions, which bifurcate from a given solution branch. These methods are very useful in constructing bifurcation diagrams, which summarize the dynamical behaviour as an independent parameter is varied.

AUTO is a software for continuation and bifurcation problems in ordinary differential equations (Doedel and Kernéves, 1986). It can do a limited bifurcation analysis of algebraic systems of the form

$$\mathbf{f}(\mathbf{y}, p) = 0, \quad \mathbf{f} \text{ and } \mathbf{y} \text{ in } \mathbb{R}^n, \tag{3-9}$$

and of systems of ordinary differential equations of the form

$$\dot{\mathbf{y}}(t) = \mathbf{f}(\mathbf{y}(t), p), \quad \mathbf{f} \text{ and } \mathbf{y}(t) \text{ in } \mathbb{R}^n, \tag{3-10}$$

subject to initial conditions, boundary conditions, and integral constraints. Here y is the vector of variables and p denotes one or more parameters. AUTO can also do certain continuation and evolution computations for parabolic partial differential equations. In this thesis, we concentrate on the applications of AUTO for the system of ordinary differential equations (3-10). AUTO cannot handle second-order equations in the form of (3-1) directly, but it is extremely powerful in following stable and unstable solution branches if the equations can be transformed into first-order form as in (3-2). To use AUTO, one has to have the solution of the system for some particular set of parameters, e.g., the *initial configuration* of the system. Then by varying a parameter, one can follow the solution and detect the possible bifurcation points, from which new solution branches emerge. As these new solution branches themselves become new *initial configurations*, and as AUTO can switch from one solution to another at the bifurcation point, the new solution branches can also be followed in search for other possible bifurcation points. Furthermore, AUTO can follow the stable and unstable solutions, which can be static or periodic; but it cannot follow quasiperiodic and chaotic solutions. Usually, for the range of parameters where quasiperiodic and chaotic oscillations are expected, AUTO finds a group of unstable solutions. This, together with the overall behaviour of the system, may be a sign of the existence of chaos, which must be proved by other methods (e.g., by using FDM in this thesis).

AUTO determines the stability of static solutions by computing the eigenvalues of the linearized form of (3-10) along the static branches. When detecting a branch point, AUTO follows the same branch, which changes stability afterward, and it also switches branches and follows the new solutions. AUTO also computes branches of stable and unstable periodic solutions and the corresponding Floquet multipliers, which determine stability along these branches. Starting data for the computation of periodic orbits are generated automatically at Hopf bifurcation points. It can also locate folds, regular bifurcations, period doubling bifurcations, and bifurcations to tori along branches of periodic solutions. Branch switching is possible at regular and period doubling bifurcations, but not at torus bifurcations, as the emerging solution is no longer periodic.

In this thesis, we introduce to AUTO the equations of motion in their first-order form (Equation (2-74)) in a subroutine. AUTO calculates the Jacobian of the equations, numerically; therefore, there is no need to provide AUTO with the Jacobian, analytically. Varying the flow velocity as the independent parameter, AUTO follows the solutions and finds the values of $\mathbf{x}$ at every flow velocity. Using variable step sizes, it can locate the bifurcation points and construct the bifurcation diagram, very accurately and fairly rapidly, except for the ranges of flow velocity where quasiperiodic and chaotic oscillations might exist. For these ranges of flow, we use FDM to find the stable solutions and to complete the bifurcation diagram.

3.4. Centre manifold reduction for pitchfork bifurcation

The idea of the centre manifold reduction is to use the eigenvalues and eigenvectors of the linearized system and to reduce the dimension of the original nonlinear system in the vicinity of an equilibrium (degenerate) point. In general, the eigenvalues of the linearized system at the degenerate point have negative, positive and zero real parts, whose corresponding eigenvectors span three subspaces: the stable (E^s), unstable (E^u) and centre (E^c) subspaces, respectively, onto which the solution space of the linearized system can be decomposed. The three invariant subspaces tangent to the above-mentioned subspaces are called stable (W^s), unstable (W^u) and centre (W^c) manifold. The idea here is to find the centre manifold subspace first, and then to find a sub-system on the centre manifold whose dimensions are definitely smaller than those of the original system, such that it contains the essential behaviour of the original system, including the existence and the stability of all the solutions around the equilibrium point. It can be shown that the idea of centre manifold is useful only when the unstable subspace is null, i.e. the linearized system has eigenvalues with negative and zero real parts only. In the case of existence of a positive-real-part eigenvalue, the centre manifold will not be attractive.[1]

To find the equations of motion on the centre manifold, the first step is to write the equations in their so-called *standard form*. Here the standard form is formulated for the pitchfork bifurcation. In general the governing equations of motion can be written as

$$\dot{\mathbf{x}} = \mathbf{A}\mathbf{x} + \mathbf{f}(\mathbf{x}), \tag{3-11}$$

in which $\mathbf{x}$ is the vector containing the unknowns, $\mathbf{A}$ is a matrix representing the linear part of the equations of motion and $\mathbf{f}$ contains all nonlinear terms of the equations of motion. Here, $\mathcal{U}$ is considered as the only parameter to be varied, in the neighbourhood of the critical flow, $\mathcal{U}_{\mathrm{BP}}$, at which a pitchfork bifurcation occurs.

---

[1] Carr (1981), Guckenheimer and Holmes (1983), and Païdoussis (1998, appendix F) give a very comprehensive explanation on the centre manifold reduction theory.

At $\mathcal{U} = \mathcal{U}_{\text{BP}}$, matrix **A** has one zero eigenvalue and all the other eigenvalues have negative real parts. One can construct a modal matrix **P** consisting of the real and imaginary parts of the eigenvectors, such that, by letting $\mathbf{x} = \mathbf{P}\mathbf{y}$, the system equation (3-11), may be brought into the standard form

$$\dot{\mathbf{y}} = \mathbf{P}^{-1}\mathbf{A}\mathbf{P}\mathbf{y} + \mathbf{P}^{-1}\mathbf{f}(\mathbf{P}\mathbf{y}), \tag{3-12}$$

where $\mathbf{P}^{-1}\mathbf{A}\mathbf{P}$ contains the eigenvalues of A. For a pitchfork bifurcation, and for the case when **x** has four elements,

$$\boldsymbol{\Lambda} = \mathbf{P}^{-1}\mathbf{A}\mathbf{P} = \begin{bmatrix} 0 & 0 & 0 & 0 \\ 1 & \sigma_1 & 0 & 0 \\ 0 & 0 & \sigma_2 & -\omega_2 \\ 0 & 0 & \omega_2 & \sigma_2 \end{bmatrix}, \tag{3-13}$$

where the eigenvalues of **A** are $\lambda_1 = 0$, $\lambda_2 = \sigma_1$, $\lambda_{3,4} = \sigma_2 \pm i\omega_2$.

After transforming the system into the standard form (3-12), we can compute the centre manifold and the corresponding sub-system. Separating the centre components from the stable ones, we obtain

$$\dot{\mathbf{y}}_1 = \mathbf{A}_0\mathbf{y}_1 + \mathbf{f}_0(\mathbf{y}_1, \mathbf{y}_2), \tag{3-14}$$

$$\dot{\mathbf{y}}_2 = \mathbf{B}_0\mathbf{y}_2 + \mathbf{g}_0(\mathbf{y}_1, \mathbf{y}_2), \tag{3-15}$$

where $\mathbf{y}_1 \in \mathbb{R}^n$, $\mathbf{y}_2 \in \mathbb{R}^m$, and $\mathbf{A}_0$ and $\mathbf{B}_0$ are constant matrices such that all the eigenvalues of $\mathbf{A}_0$ (of dimension *n*) have zero real parts while all the eigenvalues of $\mathbf{B}_0$ (of dimension *m*) have negative real parts. It is also assumed that $\mathbf{f}_0(0,0) = \mathbf{f}_0'(0,0) = \mathbf{g}_0(0,0) = \mathbf{g}_0'(0,0) = \mathbf{0}$ (here $\mathbf{f}_0'$ and $\mathbf{g}_0'$ are the Jacobian matrices of $\mathbf{f}_0$ and $\mathbf{g}_0$, respectively).

We introduce the centre manifold for (3-14), **h** as

$$\mathbf{y}_2 = \mathbf{h}(\mathbf{y}_1), \tag{3-16}$$

with

$$\mathbf{h}(\mathbf{0}) = \mathbf{0}, \qquad \mathrm{D}\mathbf{h}(\mathbf{0}) = \mathbf{0},$$

Differentiating (3-16) with respect to time,

$$\dot{\mathbf{y}}_2 = \mathrm{D}\mathbf{h}(\mathbf{y}_1)\dot{\mathbf{y}}_1, \tag{3-17}$$

and substituting (3-16) into (3-14) and (3-15),

$$\dot{\mathbf{y}}_1 = \mathbf{A}_0\mathbf{y}_1 + \mathbf{f}_0\left(\mathbf{y}_1, \mathbf{h}(\mathbf{y}_1)\right), \tag{3-18}$$

$$\dot{\mathbf{y}}_2 = \mathbf{B}_0\mathbf{h}(\mathbf{y}_1) + \mathbf{g}_0\left(\mathbf{y}_1, \mathbf{h}(\mathbf{y}_1)\right). \tag{3-19}$$

Then, substituting (3-18) and (3-19) into (3-17) gives

$$\mathrm{D}\mathbf{h}(\mathbf{y}_1)\left[\mathbf{A}_0\mathbf{y}_1 + \mathbf{f}_0\left(\mathbf{y}_1, \mathbf{h}(\mathbf{y}_1)\right)\right] = \mathbf{B}_0\mathbf{h}(\mathbf{y}_1) + \mathbf{g}_0\left(\mathbf{y}_1, \mathbf{h}(\mathbf{y}_1)\right). \tag{3-20}$$

Equation (3-18) captures the essential dynamics of (3-11), and (3-20) represents a partial differential equation that $\mathbf{h}(\mathbf{y}_1)$ must satisfy. To find a centre manifold it is necessary to solve (3-20) for $\mathbf{h}(\mathbf{y}_1)$, which cannot, of course, be solved exactly in most cases (to do so would imply that a solution of the original equation had been found!), but its solution can be approximated arbitrarily closely as a Taylor series at $\mathbf{y}_1=\mathbf{0}$. Equation (3-18) is the sub-system of the original nonlinear system on the centre manifold $\mathbf{h}(\mathbf{y}_1)$. The dynamics of the original nonlinear system around the pitchfork bifurcation can therefore be studied by studying the simple equation (3-18).

3.5. Summary

In this chapter, the three different methods used in this thesis to deal with the nonlinear equations of motion of slender flexible cylinders subjected to axial flow have been presented. Houbolt's fourth-order finite difference method (FDM) was introduced as a suitable scheme to solve the discretized nonlinear second-order ordinary differential equations, directly. Using Houbolt's assumptions, one can transform the nonlinear ordinary differential equations to a set of nonlinear algebraic equations, which can be solved by the Newton-Raphson method.

AUTO uses the first-order form of the nonlinear ordinary differential equations and, using continuation and bifurcation theories, constructs the bifurcation diagram of the system by varying a particular parameter, e.g., the flow velocity. As AUTO is not able to find quasiperiodic and chaotic oscillations, we use FDM to complete the bifurcation diagrams in the ranges where the possibility of quasiperiodic and chaotic oscillations exists. Therefore, by a combination of AUTO and FDM, bifurcation diagrams may be constructed for any desired range of flow velocity.

Analytical centre manifold theory was presented as a modern tool to study the behaviour of the system in the vicinity of the pitchfork bifurcation point. In this method one can reduce the dimensions of the system in the neighbourhood of the pitchfork bifurcation to one, and study analytically the behaviour of the system by considering the resulting simple one-dimensional system, instead of the original multi-dimensional one.

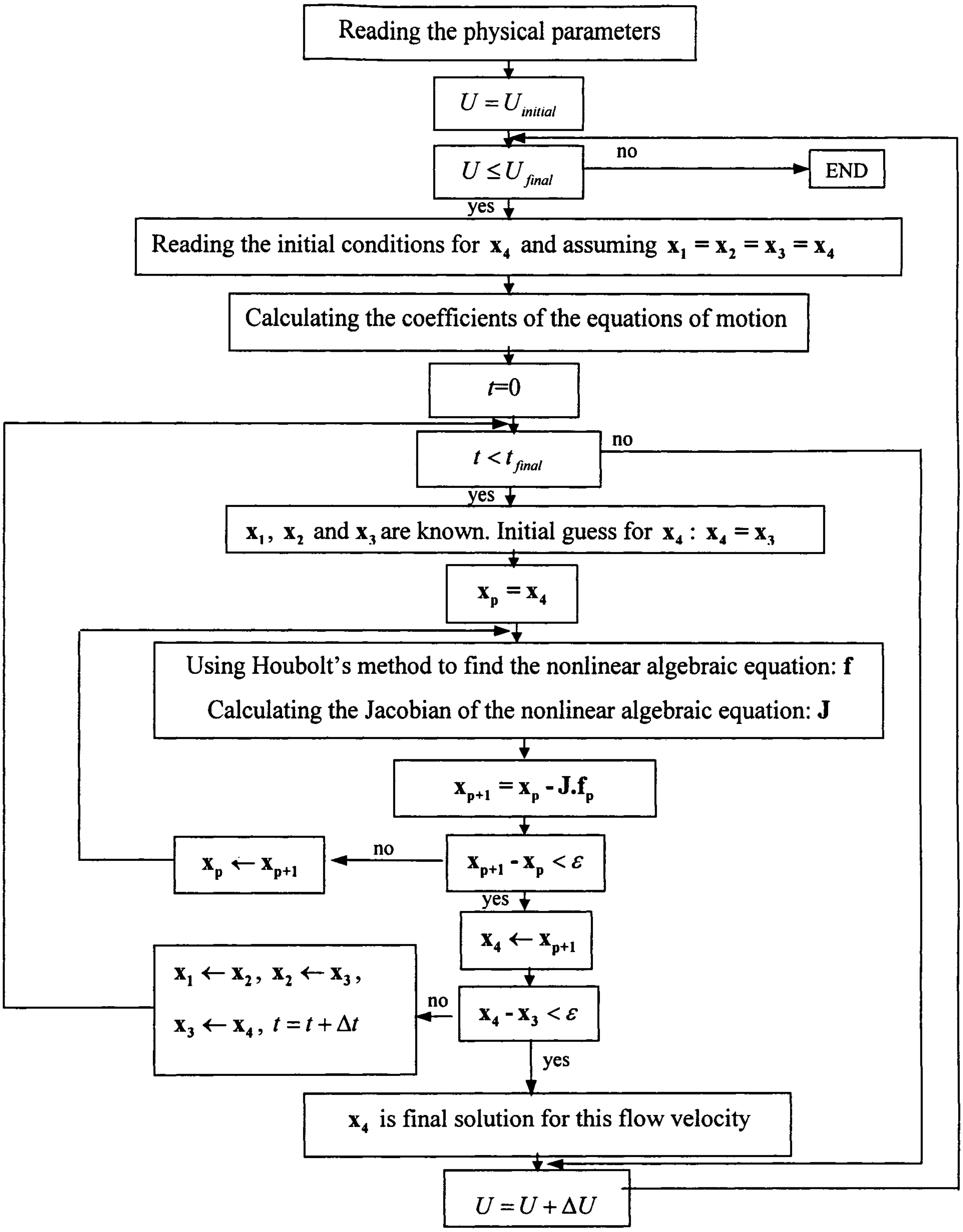

Figure 3-1 Flowchart of the FDM program.

4. Nonlinear Dynamics of a Simply Supported Cylinder Subjected to Axial Flow

4.1 Introduction

In this chapter, the dynamical behaviour of a simply supported cylinder subjected to axial flow is studied. Figure 4-1 shows the system under consideration: the cylinder is vertical and the flow direction is the same as the direction of gravity, i.e., downward. As discussed in Chapter 1 (Section 1.2.1), the linear results for this system were presented by Païdoussis (1973), showing that the cylinder undergoes a first-mode divergence, followed by a second-mode divergence and a so-called "Païdoussis-type" coupled-mode flutter at higher flow. These results will be reproduced and discussed in Section 4.2. It should be noted that the linear results are reliable only up to the first point of instability, and the existence of post-divergence instabilities as predicted by linear analysis needs to be validated by using a nonlinear model. This is what is done in this chapter, using the nonlinear equations of motion derived in Chapter 2. The nonlinear behaviour of the system is presented in the form of bifurcation diagrams where the cylinder amplitude is plotted versus the flow velocity, which is the varying (independent) parameter. Time histories, phase plane plots, power spectral density plots and Poincaré maps are also presented at different flow velocities.

The effect of different physical parameters (i.e., frictional coefficients, externally imposed uniform tension and dimensionless axial rigidity) on the behaviour of the system is studied. Also, the effect of the number of Galerkin modes used in discretizing the partial differential equations on the stability of the results is studied, to find the number of modes necessary for reliable results.

The case when the fluid-related forces are linear while the structure is assumed to be nonlinear is also studied, to judge the importance of including the nonlinear fluid forces into the equations of motion derived in Chapter 2. The results will show whether one can neglect all the nonlinear terms due to the fluid forces in the equations of motion and still get acceptable results or not.

Centre manifold reduction theory is used to study analytically the behaviour of the system in the neighbourhood of the first pitchfork bifurcation point. This is done to validate the numerical results in this neighbourhood in terms of both the nature of the pitchfork bifurcation (subcritical or supercritical) and the amplitude of the buckled solution.

4.2 Linear analysis

The linear equation of motion for this system was presented by Païdoussis (1966b) and in its corrected and more general form by Païdoussis (1973). In this section, a reproduction of some of the linear results of Païdoussis (1973), also found in Païdoussis (2004), is presented to give a flavour of the results found by using a linear model.

The dimensionless linear equation of motion is

$$\begin{aligned}&\left(1+(\chi-1)\beta\right)\ddot{\eta}+2\chi\mathcal{U}\sqrt{\beta}\,\dot{\eta}'+\chi\mathcal{U}^2\eta''-\left[\tfrac{1}{2}\mathcal{U}^2c_b(1-\delta)\right]\eta''+\left[\bar{\Gamma}\delta+(1-2\nu)\bar{\Pi}\delta\right](-\eta'')\\&+v^{(4)}+\tfrac{1}{2}\varepsilon\mathcal{U}^2c_t(1+h)\Big\{\left[\zeta-\zeta(1)(1-\delta)\right]\eta''-\left(1-\tfrac{1}{2}\delta-\xi\right)\eta''\Big\}\\&+\tfrac{1}{2}\varepsilon\,\mathcal{U}^2\left(c_n+c_th\right)\eta'+\tfrac{1}{2}\varepsilon\,\mathcal{U}c_n\sqrt{\beta}\dot{\eta}+\left(1-\tfrac{1}{2}\delta-\xi\right)\left(-\eta''\right)\Big\}+O\!\left(\epsilon^2\right)=0,\end{aligned}\qquad(4\text{-}1)$$

in which the nondimensional parameters are the same as those presented in Chapter 2 after Equation (2-65). To study the dynamical behaviour of the system, the flow velocity is varied starting from zero; the eigenvalues of this linear equation are calculated at each step and the stability of the system is examined. Here, we study the case of a simply supported cylinder subjected to axial flow with the following dimensionless parameters: $\beta=0.1$, $\gamma=0.84$, $c_n=c_t=0.025$, $c_b=0$, $\varepsilon=15.81$, $\chi=1$, $\delta=1$, $\bar{\Pi}=\bar{\Gamma}=0$.

Figure 4-2 shows the real and imaginary components of eigenvalues as functions of the dimensionless flow velocity, $\mathcal{U}$, for the first two modes. These results show that the cylinder is stable for $0<\mathcal{U}<\pi$, i.e. at its original equilibrium position; at $\mathcal{U}=\mathcal{U}_{\mathrm{BP}}=\pi$ the eigenvalue of the first mode becomes zero, and therefore the system loses stability in its first mode by divergence, via a pitchfork bifurcation. The post–divergence dynamical behaviour of this system, i.e. for $\mathcal{U}>\mathcal{U}_{BP}$, strictly cannot be predicted by linear theory. Linear theory is applicable only up to the fist loss of stability and cannot provide any definitive prediction of post-critical behaviour. The reason for this is that, in the linear equation of motion, it is required that motions be small so that the system remains in the vicinity of the equilibrium state, while for $\mathcal{U}>\mathcal{U}_{BP}$ the system has diverged away from that state. Nevertheless, it is of interest to see what the linear theory predicts for $\mathcal{U}>\mathcal{U}_{BP}$. It is found that the cylinder develops divergence in the second mode at $\mathcal{U}\simeq 2\pi$; and immediately after, at $\mathcal{U}=6.45$, the first- and the second-mode eigenvalues coalesce to give rise to so-called "Païdoussis-type" coupled-mode flutter (see Done and Simpson (1977)).

Figure 4-3 shows the same graphs as Figure 4-2, but for $\beta=0.48$ and $\varepsilon=10$. The first-mode divergence occurs at $\mathcal{U}\simeq\pi$. The second divergence is associated with the hitherto stable branch of the first mode, followed immediately by a coupled-mode flutter via re-coalescence of the two bifurcated branches of the first mode.

More details on the methods of linear analysis for such systems and a very complete study of the dynamics of the system, from a linear point of view, can be found in Païdoussis (2004, Chapter 8). What is of interest in this thesis is the fact that, according to the linear results, the cylinder loses stability by divergence, followed by coupled-mode flutter at higher flow velocities. The nonlinear model must be able to find the first point of instability (the onset of divergence) at exactly the same point as predicted by the linear model (in fact, by assuming small displacements and neglecting all the nonlinear terms in the nonlinear equations of motion, one can retrieve the linear equation (4-1)). The question here is whether or not the post-divergence instability (flutter) *exists* according to the nonlinear analysis.

In order to investigate the validity of the post-critical behaviour of the system as predicted by linear theory, and also to determine the amplitude of buckling, as well as the amplitude and the frequency of oscillatory motion if flutter does exist, the system needs to be examined via nonlinear analysis. This will be conducted next, by using the nonlinear model of Chapter 2.

4.3 Nonlinear analysis: basic concepts

As for the linear system, the first task is to discretize the equations of motion via the Galerkin method, but because there are two equations involved, one in the axial and one in the transverse direction, two sets of comparison functions must be utilized. In the case of a simply supported cylinder, the eigenfunctions of a both-ends-fixed bar in the axial vibration, $\psi_j(\xi)$, and those of a simply supported beam in the transverse vibration, $\phi_j(\xi)$, are used as basis functions, because they satisfy the same boundary conditions as the problem at hand. These eigenfunctions are identical; i.e.,

$$\psi_j(\xi) = \sqrt{2}\sin(j\pi\xi), \tag{4-2}$$

$$\phi_j(\xi) = \sqrt{2}\sin(j\pi\xi). \tag{4-3}$$

One can then evaluate the coefficients of the tensor form equations (2-68) and (2-69).

AUTO and FDM, as explained in Chapter 3, are used to solve equations (2-68) and (2-69) for $q_1, q_2, \ldots, q_{N_u+N_v}$ for different values of the flow velocity, $\mathcal{U}$. The number of modes used in the axial and the transverse direction are N_u and N_v, respectively. As will be seen, the results found using AUTO and FDM are in perfect agreement for all the static results and also for the dynamic results before the point at which a torus bifurcation occurs; this limitation is because AUTO cannot follow the *stable* solutions after a torus, and only FDM can be used for finding solutions when the system performs quasiperiodic and chaotic motions.

The information gained from a nonlinear analysis of the system is summarized in bifurcation diagrams in which, typically, the amplitude of motion is plotted as a function of one parameter of the system; in this thesis, the first generalized coordinate in the transverse direction, q_1, is plotted as a function of the dimensionless flow velocity, $\mathcal{U}$, unless otherwise mentioned. It has been verified that dynamical behaviour of q_1 is representative of that of the full system. In the bifurcation diagrams, a solution on the *x*-axis represents the original configuration, i.e. the inert cylinder in its equilibrium position. A nonzero solution can represent either a non-trivial static equilibrium position (representing a buckled stationary cylinder) or the amplitude of oscillation for flutter, depending on the context.

Figure 4-4 shows a typical bifurcation diagram for this system, found by AUTO and FDM to show that the results obtained with these two methods match perfectly. The continuous and dotted lines show the stable and unstable solutions, respectively, obtained by AUTO, and the asterisks are the results obtained by FDM. Only two Galerkin modes have been used to discretize the partial differential equations. This bifurcation diagram shows that at low flow velocities, the system is in its original equilibrium position and with increasing flow, the system undergoes a pitchfork bifurcation (the onset of divergence) at $\mathcal{U} \simeq 3.14$ (BP1) and with further increase of the flow, the amplitude of buckling increases. It is noted that AUTO can follow even *unstable* solutions (dotted lines in Figure 4-4), which do not materialize physically, e.g. in the experiments, while FDM can only find the stable solutions. The second bifurcation point (BP2) and the branches coming out of it (the nonzero dotted lines) are unstable. AUTO finds both possible solutions for the cylinder: the upper branch and the lower branch in Figure 4-4; while using FDM only one solution (on one of the branches) at a time can be obtained, depending on the initial conditions. For example, in Figure 4-4, only the solutions on the upper branch are found by FDM; however, the lower branch could be obtained simply by using opposite initial conditions.

4.4 The influence of different parameters on the stability and the amplitude of the buckled solution

In this section, the influence of different parameters on the stability and the amplitude of the buckled solution of the system is examined for the following physical parameters: $D = 0.0254$ m, $\rho = 1000$ kg/m^3, $m = 0.5817$ kg/m, $M = 0.507$ kg/m and $E = 2.76$ MPa; leading to the following dimensionless values: $\mathcal{U} \simeq 3\,UL$, $\beta = 0.47$, $\gamma = 12.996L^3$ and $\tau = 0.27t/L^2$, where U is in m/s, L in m and t in s. Here $\mathcal{U}$ is used as the independent parameter, which is varied. It is assumed that $\chi = 1$ and $h = 0$, which correspond to a cylinder in unconfined flow, and that the coefficient of form drag is zero, $c_d = 0$. The cylinder is not allowed to slide at the downstream end; hence, $\delta = 1$ and $c_b = 0$. The damping ratio, ς, is assumed to be 0.01 in all modes.

4.4.1 Influence of frictional coefficients

In this study, the frictional coefficients in the normal and tangential directions are assumed to be equal, $c_n = c_t$ (Païdoussis, 2004, Appendix Q). Also, since in the equations of motion they always appear as εc_n and εc_t, the effect of varying $\varepsilon c_n = \varepsilon c_t$ is the same as varying $c_n = c_t$. Figure 4-5(a) shows the bifurcation diagram of the system for different values of $\varepsilon c_n = \varepsilon c_t$. Here it is assumed that $\Pi_0 = 10\ 000$, corresponding to L=64 cm and $\varepsilon = 25$, and $\bar{\Gamma} = \bar{\Pi} = 0$. It is seen that, with increasing εc_n and εc_t, the first bifurcation point (divergence) occurs at progressively lower flow velocities; also, at a fixed flow velocity, the amplitude of buckling is increased with larger values of these coefficients. These two effects could be explained by noting that larger εc_t (for δ=1) implies that half the cylinder is subjected to an increasing compressive load.

4.4.2 Influence of externally imposed uniform tension

An externally imposed uniform tension $\left(\bar{\Gamma} = \bar{T}L^2/EI\right)$ represents a pre-strain in the longitudinal direction of the cylinder. Figure 4-5(b) shows the bifurcation diagrams of the system with varying $\bar{\Gamma}$ for $\Pi_0 = 10\ 000$, $\bar{\Pi} = 0$ and $c_n = c_t = 0.025$. When a larger tension is applied on a cylinder, higher flow velocities are needed to cause instability; hence, the critical flow velocity (for divergence) increases. With increasing $\bar{\Gamma}$ at a fixed flow velocity, the amplitude of bucking decreases. This is because the resistance to a lateral displacement in a tensioned cylinder will be larger. One would expect the same influence on the behaviour of the system for the coefficient of pressurization ($\bar{\Pi}$), which also represents a pre-strain in the longitudinal direction of the cylinder.

4.4.3 Influence of dimensionless axial flexibility

The dimensionless axial flexibility, $\Pi_0 = EAL^2/EI$, is a measure of the axial rigidity as compared with the transverse rigidity of the system. For a full cylinder (not hollow), $\Pi_0 = \left(4L/D\right)^2$; this implies that, for a fixed D, increasing the value of Π_0 means a larger

L; therefore, a larger amplitude of buckling should be expected. Figure 4-5(c) shows the bifurcation diagrams of the system for different values of Π_0 for $c_n = c_t = 0.025$ and $\bar{\Gamma} = \bar{\Pi} = 0$. It is seen that, the larger the value of Π_0 is, the *smaller* the amplitude of buckling becomes, which seems to be contrary to what was expected! The answer to this paradox lies in the fact that the dimensionless flow velocity and the dimensionless transverse displacement both depend on the length of the cylinder ($\mathcal{U} = \sqrt{\rho A/EI}\, UL$, $\eta = v/L$). Once this is taken into account, the results are as one would expect: a longer cylinder buckles at lower flow and when buckled, for a given dimensional flow velocity, its amplitude is larger compared with a shorter cylinder (Figure 4-5(d)). It has also to be noticed that Π_0 has no influence on the critical dimensionless flow velocity for the first bifurcation point.

4.5 Nonlinear post-divergence behaviour of a simply supported cylinder

In the previous two sections, the behaviour of a simply supported cylinder was studied in its static state (pre-buckling and buckling positions). Here, this system is studied over a wider range of flow velocities in order to study its dynamical behaviour (if it exists at all) at higher flow velocities. Figure 4-6 shows the bifurcation diagram for a simply supported cylinder with a length of L=40 cm and a diameter of D=2.54 cm and therefore $\varepsilon = 15.81$. Young's modulus of the cylinder is $E = 2.76$ MPa and the mass of the cylinder per unit length is $m = 0.5817$ kg/m. The axially flowing fluid is water with density of $1000\,\text{kg/m}^3$. The corresponding dimensionless axial flexibility is $\Pi_0 = 4000$. It is also assumed that $c_n = c_t = 0.025$ and $\bar{\Gamma} = \bar{\Pi} = 0$.

As is well known, bifurcations are determined mathematically by the eigenvalues in the case of a fixed point, and by the Floquet multipliers in the case of a periodic solution. If all the generally complex eigenvalues have negative real parts, the system is stable; if one of the complex eigenvalues becomes zero, a pitchfork bifurcation (static divergence) occurs, and when a set of complex conjugate eigenvalues crosses the imaginary axis (the real components become zero) a Hopf bifurcation occurs. If all the Floquet multipliers are inside the unit circle, the oscillatory solution is stable. If two complex conjugate Floquet multipliers cross the unit circle, a torus bifurcation occurs; further, if one of the Floquet multipliers crosses the unit circle at -1, a period doubling bifurcation occurs, and if it crosses the unit circle at $+1$, a saddle-node bifurcation takes place.

To construct the bifurcation diagram (Figure 4-6), at least 6 Galerkin modes have been used in both the axial and the transverse directions (the convergence of the results is studied in Section 4.7). It has been confirmed that the first generalized coordinate in the transverse direction, q_1, is representative of the qualitative behaviour of the system.

As expected, the system is stable at very low flow velocities and remains in its original equilibrium state, up to where it loses stability via a supercritical pitchfork bifurcation (one eigenvalue becomes zero) at a nondimensional flow velocity $\mathcal{U} \simeq \pi$ (BP1) in conformity with linear theory; this leads to a buckled state (stable nonzero static solution or fixed point). Subsequently, q_1 increases with $\mathcal{U}$. The resulting static solution eventually loses stability, and the system develops flutter via a supercritical Hopf bifurcation (two complex-conjugate eigenvalues with zero real parts) at $\mathcal{U} \simeq 14.15$ (HB1), corresponding to periodic solutions around the buckled state. Figure 4-7 shows the time history, phase plane plot, power spectral density plot and Poincaré map of the periodic response of the system at $\mathcal{U}=14.6$, where the system is subject to flutter. The system oscillates around the static equilibrium point, where $q_1 \simeq 0.082$ and the PSD plot (Figure 4-7(c)) shows that the frequency of oscillation is $f \simeq 9.5\ \text{Hz}$. The Poincaré map (Figure 4-7(d)) gives a qualitative picture of the type of dynamical behaviour that occurs. Thus when the solution is periodic, the phase plane plot is a limit cycle and the Poincaré map, which is a section through the limit cycle, has a finite number of points (4 in this case). In this thesis, the Poincaré maps have been obtained by plotting $\dot{q}_1$ versus q_1 when $\dot{q}_2 = 0$, unless otherwise mentioned. It ought to be remarked that the precise number of points in the Poincaré map depends on the section one takes. Figure 4-7(d), a map with four points, was obtained by plotting $\dot{q}_1$ versus q_1 when $\dot{q}_2 = 0$; if the condition is altered to $\dot{q}_2 = 0.1$, one obtains only two points in the Poincaré map. These figures are constructed using 1,000,000 sample points in 100 nondimensional time units.

With increasing flow, the limit cycle becomes unstable via a torus bifurcation (two complex-conjugate Floquet multipliers cross the unit circle) at $\mathcal{U} \simeq 14.73$. This bifurcation corresponds to the appearance of a second frequency in the response, indicating that quasiperiodic solutions are possible thereafter. Figure 4-8 shows the time history, phase plane plot, power spectral density plot and Poincaré map of the system at $\mathcal{U}=14.8$, which all display a quasiperiodic-two oscillation, meaning that the solution involves two fundamental frequencies. These two dominant frequencies are $f_3 = 4.19$ and $f_7 = 9.76$; all the other peaks in the PSD plot may be written as $f = mf_3 \pm nf_7$, with m and n integers. For example the first peak in the PSD plot is $f_1 = -2f_3 + f_7$, while the second one is $f_2 = 3f_3 - f_7$. Table 4-1 shows how all the peaks shown in Figure 4-8(c) can be written in terms of the two fundamental frequencies, f_3 and f_7.

It has been confirmed that for $\mathcal{U}$=14.9 and $\mathcal{U}$=15.0 the system undergoes quasiperiodic-2 motions also. Time histories, phase plane plots, PSD plots and Poincaré maps for these latter two cases are shown in Figure 4-9 and Figure 4-10. In the PSD plots, all the peaks can be written as the linear combination of the two fundamental frequencies as shown in Table 4-1. For $\mathcal{U}=14.9$, the fundamental frequencies are $f_4 = 4.23$ and $f_9 = 9.82$; and for $\mathcal{U} = 15.0$, they are $f_4 = 4.31$ and $f_9 = 9.88$.

If one uses 7 modes in both the axial and the transverse directions, after periodic solutions, a period-doubling bifurcation occurs at $\mathcal{U} = 14.53$ (one of the Floquet multipliers crosses the unit circle at −1). This is not observed when using 6 modes in each direction, but the results with 8 modes in each direction display a period-doubling bifurcation at almost the same critical flow velocity. The fact that by using more modes one can observe the period-doubling bifurcation confirms its existence, at least theoretically; thus 6 modes in each direction are not enough to capture this detail in the dynamics. [An alternative explanation is that the period-doubling bifurcation is incidental, as it is not a key to the dynamics at higher flow velocities (cf. Table 4-3, the columns BP, HP and TR). In this interpretation of the dynamical behaviour, one can conclude that even with 3 modes one captions the essential dynamics of the system.]

The period-2 oscillation becomes unstable by a torus at $\mathcal{U} = 14.73$, which corresponds exactly to the critical value of the torus bifurcation when using 6 modes in each direction. The time history, phase plane and power spectral density plots and Poincaré map for $\mathcal{U}=14.6$ found using 7 modes in each direction (Figure 4-11) show the period-2 motion of the system: as compared to Figure 4-7, we clearly see the subharmonic to the main frequency of $f \simeq 9.5$ in the PSD plot. It is also obvious from the time history and the phase plane plot (Figure 4-11(a) and (b)) that the period of oscillation is twice as much as that for the periodic oscillation of Figure 4-7. The number of points in the Poincaré map is also twice as many as those in the map for the periodic oscillation. After the critical point for the torus bifurcation, the system displays the same behaviour whether analysed using 6 or 7 modes in each direction. To save computational time, the analysis of the system henceforth is based on 6 modes in each direction.

Chaotic oscillations start at $\mathcal{U}=15.1$. The time history, phase plane plot, power spectral density plot and Poincaré map of the system at $\mathcal{U}=16$ are shown in Figure 4-12. The oscillation here is clearly chaotic. In the PSD plot, as expected, chaotic oscillation is associated with a wide frequency band. Notice that, at $\mathcal{U}=16$, although the main frequency $(f \simeq 11)$ and its main subharmonic $(f \simeq 5.5)$ and harmonics are still prominent, the overall subharmonic background is of high amplitude compared with the periodic and quasiperiodic states in the previous figures. As the dynamics is chaotic, the Poincaré map becomes more complex, but nevertheless retains a definite structure with a limited subspace, in contrast to that for a random process.

As mentioned before, AUTO is unable to switch at a torus bifurcation and follow the stable branches thereafter, because the emerging solution is not periodic but quasiperiodic. However, some useful information can still be obtained. According to the results by AUTO, there exist many unstable branches in the bifurcation diagram for the range of flow velocity where chaotic solutions are found by FDM. As observed in the upper half of the bifurcation diagram of Figure 4-13, which is produced by AUTO, there are 6 unstable branches:

- four nonzero *static* solutions emanating from the unstable pitchfork bifurcation points occurring at $\mathcal{U}=6.3$, $\mathcal{U}=9.4$, $\mathcal{U}=12.6$ and $\mathcal{U}=15.7$, which, according to linear theory, correspond to the instability of the cylinder in its second to fourth mode, respectively;

- one nonzero *static* solution which becomes unstable through the Hopf bifurcation (HB); and
- one *dynamic* solution that becomes unstable via the torus bifurcation (TR).

Furthermore, the unstable branches, symmetric to those shown, exist on the lower part of the bifurcation diagram (not shown here), corresponding to negative q_1. There is also the unstable branch of the original trivial solution, after the first pitchfork bifurcation point. Thus, for this particular system, in total there exist 13 unstable branches over the range of flow where chaotic oscillations have been observed.* Although, the existence of *many* unstable branches in the bifurcation diagram made by AUTO gives a first clue of the existence of chaos, it is not a *proof*, and the chaotic oscillations must be observed using other methods of solutions, e.g., FDM.

There is a range of flow velocities $(16.88 < \mathcal{U} < 17.2)$ where two different stable attractors co-exist: a stable nonzero static solution and a chaotic solution (strange attractor) (see Figure 4-14). Using AUTO, we are able to find the whole range of the stable static solution very precisely, from $\mathcal{U}$=16.88 to $\mathcal{U}$=18.73. The nonzero static branch in the bifurcation diagram loses stability by a Hopf bifurcation at $\mathcal{U} = 18.73$ (HB2 in Figure 4-13) and a high frequency periodic motion arises. The frequency of oscillation is around 30 Hz (nondimensional), while the frequency of the periodic motion after the first Hopf bifurcation, at $\mathcal{U} = 14.4$ for example, is around 10 Hz. Figure 4-15 shows the dynamical behaviour of the system at $\mathcal{U} = 19$. The resulting high-frequency oscillatory motion becomes unstable via a torus bifurcation at $\mathcal{U} = 19.60$ (TR2 in Figure 4-13), leading to a quasiperiodic motion. A time history, a phase plane plot, a power spectral density plot and a Poincaré map of the system for $\mathcal{U} = 20.5$ (Figure 4-16) confirm quasiperiodic-two motion (again, all the frequencies in PSD can be written in terms of two main frequencies, which are $f_1 \simeq 10$ and $f_2 \simeq 38$). For flow velocities larger than $\mathcal{U} = 21$, the program does not converge, although different initial conditions were tried.

---

* Note that we did not attempt to find the periodic unstable solution, which would emanate from the Hopf bifurcation at $\mathcal{U} = 15.3$.

Figure 4-17 shows the spatial shape of the cylinder for different flow velocities. Figure 4-17(a) shows the cylinder in its buckled state at $\mathcal{U} = 12$, at which the deformation is a deformed half sinusoid (the classical first-mode shape). Figure 4-17(b) shows the cylinder motion over one period of oscillations ($\Delta\tau = 0.1$) at $\mathcal{U} = 14.6$, where it undergoes a periodic oscillation around its buckled position. The cylinder position at every one tenth of the period of oscillation (i.e. at every $\Delta\tau = 0.01$) is shown in Figure 4-18(a). It should be noted that the amplitude of oscillations is very small compared with the amplitude of the buckled state; if the static component of the cylinder motion is removed, the oscillatory motions are more obvious (Figure 4-18(b)). Figure 4-17(c) and (d) show the cylinder performing quasiperiodic and chaotic oscillations around its buckled position at $\mathcal{U} = 14.8$ and $\mathcal{U} = 16$, respectively. These two figures show the cylinder motion over a time interval of $\Delta\tau = 0.3$. In all these cases, the maximum displacement of the cylinder is not at the mid-point, but rather at a point in the lower half of the cylinder, due to the tension-compression induced by gravity and friction. Figure 4-17(e) shows the static deformation of the cylinder at $\mathcal{U} = 18$. Surprisingly, it is basically of first-mode shape, with the maximum displacement in the upper half of the cylinder! It should be mentioned that, this solution belongs to a different branch in the bifurcation diagram (another family of solutions) and this may perhaps justify, mathematically, the difference in the behaviour (the occurrence of the maximum amplitude on the upper half, instead of the lower one) compared with the other cases shown in this figure.

4.6 The behaviour of cylinders with different lengths

In Section 4.5, the dynamics of a simply supported cylinder with L = 40 cm $(\Pi_0 = 4000)$ was discussed in detail. Here, the effect of the cylinder length on the behaviour of the system is studied to ascertain whether the results predicted in Section 4.5 are particular to that cylinder length or are broadly generic. In Section 4.4.3 this study was conducted for the critical value for the onset of divergence and the amplitude of buckling. Now, after discussing dynamic instabilities of the cylinder for a particular length in Section 4.5, we are in a position to extend our study of dynamic instabilities to simply supported cylinders of varying lengths. Cylinders with the lengths of L = 0.2, 0.3, 0.4 and 0.52 m are studied. Changing the length of the cylinder changes the nondimensional axial rigidity (Π_0) as well as the nondimensional gravity parameter (γ), both of them being functions of the length (see Table 4-2). It is observed in Table 4-2 that, qualitatively, the behaviour of the system is the same as that for $\Pi_0 = 4000$: a pitchfork bifurcation destabilizes the initial position of the cylinder, followed by a Hopf bifurcation and a torus at higher flow velocities. It should be mentioned that for all the cases studied here, except for L=0.2 m, the cylinder undergoes a period-doubling bifurcation before the torus. Chaotic oscillations are observed, together with the co-existence of the static nonzero deformation and chaotic oscillations in a range of high flow velocities. The static nonzero solution undergoes a Hopf bifurcation followed by a torus. The difference, as one expects, is in the critical values: by changing the cylinder length, the critical values of flow velocity for different bifurcation points are changed.

Table 4-2 also shows the critical flow velocities and the frequency of oscillations at the Hopf bifurcation point for the four different cylinder lengths. For each case, the critical value is given in dimensionless form (upper entry) and in dimensional form (lower entry), using the relation for the dimensionless flow velocity in terms of the dimensional flow velocity: $\mathcal{U} = 3UL$. As the cylinder length increases, the nondimensional flow velocities for the bifurcation points increase, while the corresponding dimensional values decrease. Following the discussion of Section 4.4.3 on the apparently paradoxical results for different values of Π_0, these results are as expected: a longer cylinder is more susceptible to losing stability than a shorter cylinder. It is observed that by increasing the cylinder length, the frequency of oscillation at the Hopf bifurcation point is increased, mainly due to the effect of L^2 in the dimensionless frequency.

4.7 Convergence tests

As mentioned in Chapter 2, the dimensionless partial differential equations of motion describing the motion of a simply supported cylinder subjected to axial flow are discretized by Galerkin's technique with the eigenfunctions of a beam and those of a bar as basis functions. A very important issue, while using Galerkin's technique, is to make sure that a sufficient number of modes (N_u and N_v, respectively in the axial and the transverse directions) are used in the discretization to obtain reliable results. Solutions of the equations of motion need to be found for increasing values of N_u and N_v till the solution does not change anymore, both qualitatively and quantitatively. It was shown that the necessary number of modes is dependent on the system parameters, the major one being the flow velocity. Table 4-3 shows the critical values of flow velocity for $\mathit{\Pi}_0 = 4000$, $\beta = 0.1$, $\gamma = 0.84$, $c_n = c_n = 0.025$, $c_b = c_d = 0$, $\varepsilon = 15.81$, $\delta = 1$, $\nu = 0.47$, $\chi = 1$, $\bar{\Pi} = \bar{\Gamma} = 0$, found by AUTO using different number of modes. The first column gives the number of modes used in the *X*- and *Y*-direction: for example, "2-2" means that 2 modes in the *X*-direction ($N_u = 2$) and 2 modes in the *Y*-direction ($N_v = 2$) have been used. For the first instability point (pitchfork bifurcation) to converge, a very small number of modes (2 each in the axial and in the transverse directions) is enough, while for the post-divergence critical points (Hopf bifurcation, period doubling and torus) more modes are necessary. This illustrates that, as the flow velocity increases, more modes are needed to obtain convergent results. It is observed (Figure 4-19) that the critical flow velocities for the Hopf and the torus bifurcations converge asymptotically to the final values, which can be considered to be $\mathcal{U}_{\mathrm{HB}} = 14.2$ and $\mathcal{U}_{\mathrm{TR}} = 14.8$. Period-doubling bifurcation is not observed if 6 modes or less are used in each direction, except for the 3-3 case, which perhaps surprisingly detects the period-doubling bifurcation; however, its corresponding value is far from the values found by 7-7 and 8-8 cases. The critical value for the period-doubling bifurcation can be considered to be at $\mathcal{U}_{\mathrm{PD}} = 14.3$. One can finally conclude that, except for the range of flow velocities where period-2 oscillations exist, for which one must use at least 7 modes, using 6 modes in each direction is reliable for studying the behaviour of this system. Furthermore, as remarked in Section 4.5, the occurrence of period-doubling is not of fundamental importance in the subsequent dynamics; thus it is not part of a period-doubling cascade leading to chaos. Hence, not too much importance should be attached to its absence for some ranges of N_u and N_v.

It may strike the reader as peculiar that in all the calculations in Table 4-3, $N_u = N_v$. In fact, there was an earlier series of convergence tests, in which N_u and N_v were varied independently; but unfortunately the damping (dissipative) model used was incorrect. Bearing in mind the relatively small influence of damping on the dynamics, the effect of varying N_u and N_v on convergence for the correct damping model would be little different. It was found that convergence with $N_u = N_v$ was representative of convergence with N_u a little different from N_v; hence, in the calculations discussed above $N_u = N_v$ was taken throughout.

Modarres-Sadeghi et al. (2003) studied the dynamics of this system, using only two modes in each direction. They showed that if one imposes a very large initial value for the first generalized coordinate, large-amplitude high-frequency flutter-like motion of the cylinder is predicted; this unrealistic motion disappears when the number of modes used in the solution is increased sufficiently.

4.8 The behaviour of the system for the case of linear fluid dynamics and a nonlinear structural model

As discussed in Chapter 2, the fluid-related forces acting on the cylinder are considered to be nonlinear. In this section, we study the dynamics when the fluid-related forces are considered to be linear, while for the structure the same nonlinear model as before is used, to see if it is possible to assume a linear fluid-dynamics model and still predict the behaviour of the system correctly. It ought to be mentioned here that, the advantage of this assumption, if at all correct, is that the resulting equations of motion are much simpler (Equations (4-4) and (4-5) in what follows) as compared to those derived for the nonlinear fluid-related forces (Equations (2-64) and (2-65)). Then, of course, it would be much simpler to study the system by using these equations and also, in the future, to derive the three-dimensional equations of motion for a slender cylinder subjected to axial flow, as an extension to these two-dimensional equations of motion.

The dimensionless equations of motion for the case where the fluid-related forces are assumed to be linear are

$$
\begin{aligned}
&(1-\beta)\ddot{\zeta}-\Pi_0\left(\zeta''+\eta'\eta''\right)-\left(\eta''\eta'''+\eta'\eta^{(4)}\right)\\
&+\tfrac{1}{2}\varepsilon\,\mathcal{U}^2c_t(1+h)\zeta'+\left[\tfrac{1}{2}\mathcal{U}^2c_b(1-\delta)+\bar{\Gamma}\delta+(1-2\nu)\bar{\Pi}\delta\right]\eta'\eta''+O\left(\epsilon^5\right)=0,
\end{aligned}
\tag{4-4}
$$

$$
\begin{aligned}
&\bigl(1+(\chi-1)\beta\bigr)\ddot{\eta}+2\chi\mathcal{U}\sqrt{\beta}\,\dot{\eta}'+\chi\mathcal{U}^2\eta''\\
&-\left[\tfrac{1}{2}\mathcal{U}^2c_b(1-\delta)\right]\eta''+\left[\bar{\Gamma}\delta+(1-2\nu)\bar{\Pi}\delta\right]\left(-\eta''+\eta'\zeta''+\eta''\zeta'+\tfrac{3}{2}\eta'^2\eta''\right)-\Pi_0\left(\zeta''\eta'+\zeta'\eta''+\tfrac{3}{2}\eta'^2\eta''\right)\\
&+\nu^{(4)}-\left(8\eta'\eta''\eta'''+\eta'\zeta^{(4)}+2\eta'^2\eta^{(4)}+2\eta''^3+2\zeta'\eta^{(4)}+4\zeta''\eta'''+3\zeta'''\eta''\right)\\
&+\tfrac{1}{2}\varepsilon\mathcal{U}^2c_t(1+h)\Bigl\{\bigl[\zeta-\zeta(1)(1-\delta)\bigr]\eta''-\left(1-\tfrac{1}{2}\delta-\xi\right)\eta'\Bigr\}+\tfrac{1}{2}\varepsilon\,\mathcal{U}^2\left(c_n+c_th\right)\eta'+\tfrac{1}{2}\varepsilon\,\mathcal{U}c_n\sqrt{\beta}\dot{\eta}\\
&+\left(1-\tfrac{1}{2}\delta-\xi\right)\left(-\eta''+\eta'\zeta''+\eta''\zeta'+\tfrac{3}{2}\eta'^2\eta''\right)\Bigr\}+O\left(\epsilon^5\right)=0.
\end{aligned}
\tag{4-5}
$$

These equations have been found by neglecting all the nonlinear fluid-dynamic terms in the general form of the equations of motion, Equations (2-64) and (2-65). The dimensionless parameters are the same as those introduced in Chapter 2, Equation (2-63). The same numerical methods of analysis as those presented earlier for the complete equations of motion (AUTO and FDM) are used here also.

Figure 4-20(a) shows the bifurcation diagram for the system found by AUTO, in which q_1 is plotted versus the dimensionless flow velocity. Initially, the cylinder is at its original stable equilibrium position and by increasing the flow velocity, it loses stability by a pitchfork bifurcation at $\mathcal{U} \simeq \pi$ (the first circle in Figure 4-20(a)), the same as for the original case discussed in Section 4.5. This, of course, is not surprising. The amplitude of the buckling increases with flow, but unlike the original case, no secondary bifurcation is obtained. Figure 4-20(b) compares the amplitude of buckling of the system found by the full theory and the linear fluid dynamics theory. It is observed that when the lateral displacements are small (i.e., $\nu < 0.07$) the two models are in perfect agreement. This indicates that for such very small amplitudes, the fluid-related nonlinear effects are still negligible and the linear model works very well. However, with increasing flow, the amplitude predicted by the linear fluid model becomes larger than that predicted by the full theory. The bifurcation diagram (Figure 4-20(a)) shows some more pitchfork bifurcations at $\mathcal{U} = 2\pi$, 3π, … in the range of flow shown; these static instabilities, together with the coupled mode flutter [which was predicted by the linear theory (not shown in the bifurcation diagram)], happen where the solution is already unstable (dotted lines in the bifurcation diagram) and therefore do not materialize.

It ought to be remarked here very briefly that the behaviour of the cylinder in this case is similar to that of a simply supported pipe conveying fluid (internal flow), in which there exists no secondary bifurcation, after the pitchfork bifurcation at $\mathcal{U} = \pi$. There is one major difference, however: the pipe was studied by using the most general nonlinear equations of motion (nonlinear structure and nonlinear fluid-related forces) and the results in that case are physically justifiable, while in the case studied in this section, the model is incomplete and the results are therefore not physically correct. The dynamics of the pipe problem (internal flow) has been shown to be independent of frictional forces, since they are exactly counterbalanced by the pressure-loss forces along the pipe. As a result, both pressure-loss and frictional forces vanish from the equation of motion [see Modarres-Sadeghi et al. (2006) for more details about the internal flow case].

The results of this section show that to study the nonlinear behaviour of the system, one must take into account the nonlinear fluid-related forces together with the nonlinear structure. The linearized fluid-related forces in combination with the nonlinear structure, as discussed here, give erroneous results for the behaviour of the system.

4.9 The behaviour of a simply supported cylinder around the pitchfork bifurcation point via centre manifold reduction

The aim of this section is to apply the modern dynamical system theory of centre manifold reduction to the problem of a simply supported cylinder subjected to axial flow and, by reducing the system to a one-dimensional one, so as to extract some of its key features in the neighbourhood of the pitchfork bifurcation.

To begin with, the first-order form of the equations of motion, presented in Chapter 2, Equation (2-74), is rewritten in compact form as

$$\dot{\mathbf{x}} = \mathbf{A}\mathbf{x} + \mathbf{f}(\mathbf{x}) \tag{4-6}$$

in which,

$$\mathbf{x} = \{x\}_{2N_r\times 1} = \begin{Bmatrix} X \\ Y \end{Bmatrix}_{2N_r\times 1}.$$

We consider the system already analysed by the numerical methods in Section 4.5 with the same parameters. Here, to make it simpler to understand the procedure, we use only one mode in each direction in Galerkin's technique, leading us to a system of 4 first-order ordinary differential equations.

From the linear analysis, and also confirmed by the nonlinear results of the previous sections, the critical flow velocity for buckling is $\mathcal{U}_{\mathrm{BP}} \simeq \pi$, where all the elements of $\mathbf{x}$ are zero $(p_1 = q_1 = \dot{p}_1 = \dot{q}_1 = 0)$. The eigenvalues of the linearized matrix evaluated at the critical point are

$\lambda_1 = 0,$

$\lambda_2 = \sigma_1 = -0.623068,$

$\lambda_{3,4} = \sigma_2 \pm \mathrm{i}\omega_2 = -3.7489 \pm \mathrm{i}272.908.$

One can construct a modal matrix **P** consisting of **V**$_1$, **V**$_2$ and the real and imaginary parts of **V**$_3$, where **V**$_1$, **V**$_2$ and **V**$_3$ are the eigenvectors of the linearized matrix,

$$\mathbf{P} = \begin{bmatrix} \mathbf{V}_1 & \mathbf{V}_2 & \mathrm{Re}(\mathbf{V}_3) & \mathrm{Im}(\mathbf{V}_3) \end{bmatrix}$$
$$= \begin{bmatrix} 0 & 0 & 0 & 0.0037 \\ 1 & -0.85 & 0 & 0 \\ 0 & 0 & 1 & 0 \\ 0 & 0.53 & 0 & 0 \end{bmatrix}.$$

Letting $\mathbf{x} = \mathbf{P}\mathbf{y}$, one can write the standard form of the equations in the neighbourhood of the pitchfork bifurcation point as

$$\begin{aligned}\dot{y}_1 =& \left(99.53\mu+15.84\mu^2\right)y_1-\left(84.59\mu+13.44\mu^2\right)y_2+\left(0.16+0.05\mu\right)y_2y_4\\ &-\left(467742+924.23\mu+147.1\mu^2\right)y_1^3\\ &+\left(1190964+2353\mu+374.536\mu^2\right)y_1^2y_2\\ &-\left(1010810+1996.85\mu+317.88\mu^2\right)y_1y_2^2\\ &+\left(285968+564.87\mu+89.93\mu^2+0.0113/\left(\mu+\pi\right)\right)y_2^3+O(4),\end{aligned}$$

$$\begin{aligned}\dot{y}_2 =& \left(117.27\mu+18.66\mu^2\right)y_1-\left(0.62+99.66\mu+15.84\mu^2\right)y_2+\left(0.19+0.06\mu\right)y_2y_4\\ &-\left(551105+1088.95\mu+173.31\mu^2\right)y_1^3\\ &+\left(1403224+2352.74\mu+441.29\mu^2\right)y_1^2y_2\\ &-\left(1190961+2352.74\mu+374.54\mu^2\right)y_1y_2^2\\ &+\left(336935+665.54\mu+105.96\mu^2+0.0113/\left(\mu+\pi\right)\right)y_2^3+O(4),\end{aligned}$$

$$\dot{y}_3 = -7.5y_3-\left(272.9+0.0086\mu+0.0014\mu^2\right)y_4+O(4),$$

$$\dot{y}_4 = 272.96y_3+O(4), \tag{4-7}$$

where $\mu=\mathcal{U}-\mathcal{U}_{\mathrm{BP}}$ and $O(4)$ means terms of order four, or higher.

To find the centre manifold, we substitute $y_2=h_2(y_1,\mu)$, $y_3=h_3(y_1,\mu)$ and $y_4=h_4(y_1,\mu)$ into the second, third and fourth equations of the standard form, Equation (4-7), and then using the chain rule and following the notation of Equations (3-18) and (3-19), we obtain

$$\begin{aligned}\dot{y}_i &= \frac{\partial h_i}{\partial y_1}\frac{\partial y_1}{\partial t}=\frac{\partial h_i}{\partial y_1}\left(\mathbf{A}_0\mathbf{x}+\mathbf{f}_0\left(y_1,h_2(y_1,\mu),h_3(y_1,\mu),h_4(y_1,\mu)\right)\right)\\ &=\mathbf{B}_0\mathbf{x}+\mathbf{g}_0\left(y_1,h_2(y_1,\mu),h_3(y_1,\mu),h_4(y_1,\mu)\right),\end{aligned} \tag{4-8}$$

with boundary conditions

$$h_i(0,0)=\frac{\partial h_i}{\partial y_1}(0,0)=0, \qquad i=1\text{-}4.$$

In this case, the centre eigenspace, E^c, is one-dimensional and the stable eigenspace, E^s, is three-dimensional. To approximate the centre manifold, we set

$$h_i(y_1) = a_i y_1^2 + b_i y_1^3 + O(4), \qquad i = 2-4, \tag{4-9}$$

which satisfies the boundary conditions of the centre manifold. Now we substitute (4-9) into (4-8) and equate the powers of y_1^2 and y_1^3 to find the unknown coefficients, a_2, b_2, a_3, b_3, a_4, b_4. Doing so, for this set of parameters, we obtain

$$a_2 = a_3 = a_4 = b_3 = b_4 = 0,\ b_2 = \frac{8697.81 + 17.1864\mu + 2.73529\mu^2}{-0.00983357 - 6.28532\mu - \mu^2}, \tag{4-10}$$

which suggests that the centre manifold is the surface defined by

$$y_2(y_1) = \frac{8697.81 + 17.1864\mu + 2.73529\mu^2}{-0.00983357 - 6.28532\mu - \mu^2} y_1^2,\ \ y_3(y_1) = y_4(y_1) = 0. \tag{4-11}$$

Moreover, the first equation of the standard form which captures the essential behaviour of the system, becomes

$$\dot{y}_1 = (0.9787\mu) y_1 - \left(4599.57 + 2204190\mu^2\right) y_1^3. \tag{4-12}$$

This is the governing equation on the centre manifold and is in its normal form already. It is clear that the bifurcation occurring at the critical parameter is a supercritical pitchfork bifurcation: when $\mu < 0$ $(\mathcal{U} < \mathcal{U}_{\mathrm{BP}})$, the origin is stable and when $\mu > 0$ $(\mathcal{U} > \mathcal{U}_{\mathrm{BP}})$, the origin becomes unstable and two symmetric equilibrium positions appear. The solutions diverge to one of the stable equilibria, depending on the initial condition. This was also found through the numerical integration of the equations in Section 4.5.

Moreover, the equilibrium position can be evaluated very easily from Equation (4-12); letting $\dot{y}_1 = 0$ yields

$$y_1 = \sqrt{\frac{0.9787\mu}{4599.57 + 2204190\mu^2}}. \tag{4-13}$$

Using the modal matrix **P**, one can reconstruct the stationary solution through the transformation **x=Py** and find the values for p_1 and q_1. Figure 4-21 shows the bifurcation diagram in the neighbourhood of the critical point, where centre manifold theory is valid. The continuous line shows the result found by the centre manifold theory, and the dots show the results by AUTO using one mode in each direction. Centre manifold theory, in agreement with the numerical results, has predicted a supercritical pitchfork bifurcation; also, a parabolic shape for q_1 versus μ is obtained. As μ is increased the difference between the amplitudes predicted by the centre manifold theory and those predicted by AUTO increases, because the centre manifold theory is valid only in the neighbourhood of the equilibrium point (in this particular case, for very small values of μ).

4.10 Summary

Based on the nonlinear equations of motion derived in Chapter 2, the dynamics of a simply supported cylinder in axial flow was studied from a nonlinear point of view, and the existence of post-divergence instabilities of the cylinder was proved. In general, the system was found to be stable at low flow velocities until the critical value for the onset of divergence, at which point the initial equilibrium position of the cylinder becomes unstable, giving rise to a new stable buckled static state. The amplitude of the buckled solution increases with flow velocity. At higher flow, the buckled stationary cylinder loses stability by a Hopf bifurcation, after which a periodic solution *does* arise; this proves the prediction of linear theory about the existence of post-divergence dynamic instability. The periodic solution is then followed by a period-doubling bifurcation giving rise to period-2 oscillations, which lose stability by a torus bifurcation afterward, followed by quasiperiodic and chaotic oscillations at higher flow velocities. At still higher flow velocities, there is a range of flow velocities in which chaotic and static solutions co-exist. This new nonzero static solution itself loses stability by a Hopf bifurcation and the resulting high-frequency periodic solution becomes quasiperiodic via a torus bifurcation at higher flow.

The effect of some of the key parameters affecting the critical flow velocities and the amplitude of the resultant motions were explored. It was observed that the simply supported cylinders with different parameters studied here have qualitatively similar dynamical behaviour, and the main difference for varying parameters is in the values of the critical flow velocities. Also, the effect of the number of modes used in Galerkin's technique was studied. It was shown that at least 6 modes each in the axial and the transverse direction are necessary to obtain reliable results.

It was shown that, by assuming a nonlinear structure and linear fluid-related forces, the cylinder buckles and the amplitude of buckling increases with flow, but no secondary bifurcation is obtained. This is not physically the case (Chapter 6) and it is not in agreement with the results of the general nonlinear model, implying that one must use nonlinear fluid-related forces as well as a nonlinear structural model to predict correctly the overall dynamical behaviour of the system.

The system behaviour was also analysed by centre manifold reduction in the vicinity of the pitchfork bifurcation point. The analytical results confirmed the numerical ones by showing that the pitchfork bifurcation *is* supercritical. Also, the amplitude of the results found using the numerical and analytical methods were in very good quantitative agreement in the small neighbourhood of the critical point, where centre manifold theory is applicable.

	$\mathcal{U}=14.8$	$\mathcal{U}=14.9$	$\mathcal{U}=15.0$
f_1	$-2f_3+f_7$	$-2f_4+f_9$	$-2f_4+f_9$
f_2	$3f_3-f_7$	$-4f_4+2f_9$	$-4f_4+2f_9$
f_3	4.19	$3f_4-f_9$	$3f_4-f_9$
f_4	$-f_3+f_7$	4.23	4.31
f_5	$-3f_3+2f_7$	$-f_4+f_9$	$-f_4+f_9$
f_6	$2f_3$	$-3f_4+2f_9$	$-3f_4+2f_9$
f_7	9.76	$4f_4-f_9$	$4f_4-f_9$
f_8	$-2f_3+2f_7$	$2f_4$	$2f_4$
f_9	$3f_3$	9.82	9.88
f_{10}	f_3+f_7	$-2f_4+f_9$	$-2f_4+f_9$
f_{11}	$-f_3+2f_7$	$-4f_4+3f_9$	$-4f_4+3f_9$
f_{12}	$-3f_3+3f_7$	$3f_4$	$3f_4$
f_{13}	$2f_3+f_7$	f_4+f_9	f_4+f_9
f_{14}	$2f_7$	$-f_4+2f_9$	$-f_4+2f_9$
f_{15}		$-3f_4+3f_9$	$-3f_4+3f_9$
f_{16}		$2f_4+f_9$	$2f_4+f_9$
f_{17}		$2f_9$	$2f_9$

Table 4-1 All the peaks in the PSD plots of the system can be written as the linear combinations of the fundamental frequencies when the system has quasiperiodic oscillations. These results are for the system with parameters defined in Section 4.5 and correspond to Figure 4-8 to Figure 4-10.

L (m)	Π_0 (-)	γ (-)	PB	HB	PD	TR	CH	ST	HB2	QP2	Frequency
0.20	1000	0.1	3.14	9.64	-	10.37	10.5	11.02	11.91	12.34	6.52
			5.23	16.10	-	17.28	17.5	18.37	19.81	20.57	
0.30	2000	0.35	3.14	11.54	12.06	12.28	12.5	13.73	14.97	15.43	7.81
			3.49	12.82	13.40	13.64	13.89	15.26	16.63	17.14	
0.40	4000	0.84	3.14	14.23	14.53	14.76	15.1	16.88	18.73	19.60	9.79
			2.61	11.86	12.10	12.3	12.58	14.10	15.60	16.30	
0.52	6707	1.83	3.14	17.68	17.96	18.01	21.5	21.2	23.65	24.63	19.42
			2.01	11.33	11.51	11.54	13.78	13.59	15.16	15.79	

Table 4-2 The critical flow velocities and the frequency at the Hopf bifurcation point for a cylinder of different lengths for the system with parameters $\beta = 0.47$, $c_n = c_t = 0.025$, $\delta = 1$, $\nu = 0.47$, $\chi = 1$, $\bar{\Pi} = \bar{\Gamma} = 0$, $c_b = c_d = 0$, showing the onset of the first buckling (BP), periodic oscillations (HB), quasiperiodic oscillations (TR), chaotic oscillations (CH), nonzero static solution (ST), high frequency periodic oscillations (HB2) and the subsequent quasiperiodic oscillations (QP2); upper entries: nondimensional; lower entries: dimensional (m/s). The frequency is in nondimensional Hz

Number of modes	BP	HB	PD	TR
2-2	3.14	29.63	-	>40
3-3	3.14	14.57	15.22	15.35
4-4	3.14	14.31	-	15.07
5-5	3.14	14.78	-	15.05
6-6	3.14	14.23	-	14.76
7-7	3.14	14.16	14.53	14.73
8-8	3.14	14.11	14.35	14.65

Table 4-3 The effect of number of bar and beam modes (N_u and N_v, respectively) on the critical flow velocities for pitchfork bifurcation, Hopf bifurcation, period doubling and torus for a simply supported cylinder with parameters $\beta = 0.47$, $\gamma = 0.838$, $c_n = c_t = 0.025$, $\varepsilon = 15.81$, $\delta = 1$, $\nu = 0.47$, $\Pi_0 = 4000$, $\chi = 1$, $\bar{\Pi} = \bar{\Gamma} = c_b = c_d = 0$, taking $N_u = N_v$

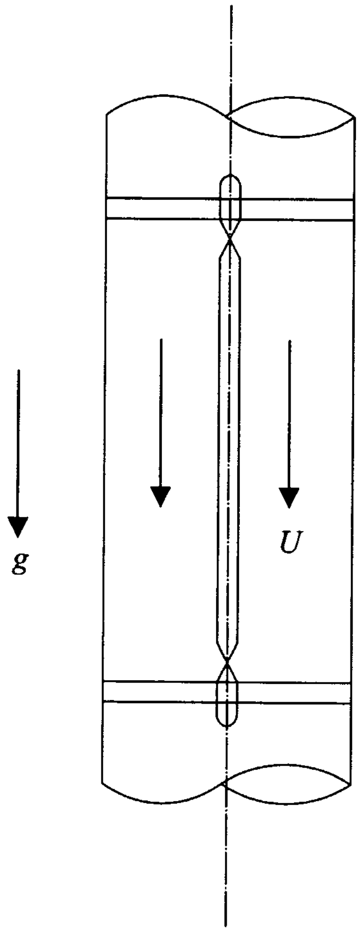

Figure 4-1 A vertical simply supported cylinder subjected to axial flow.

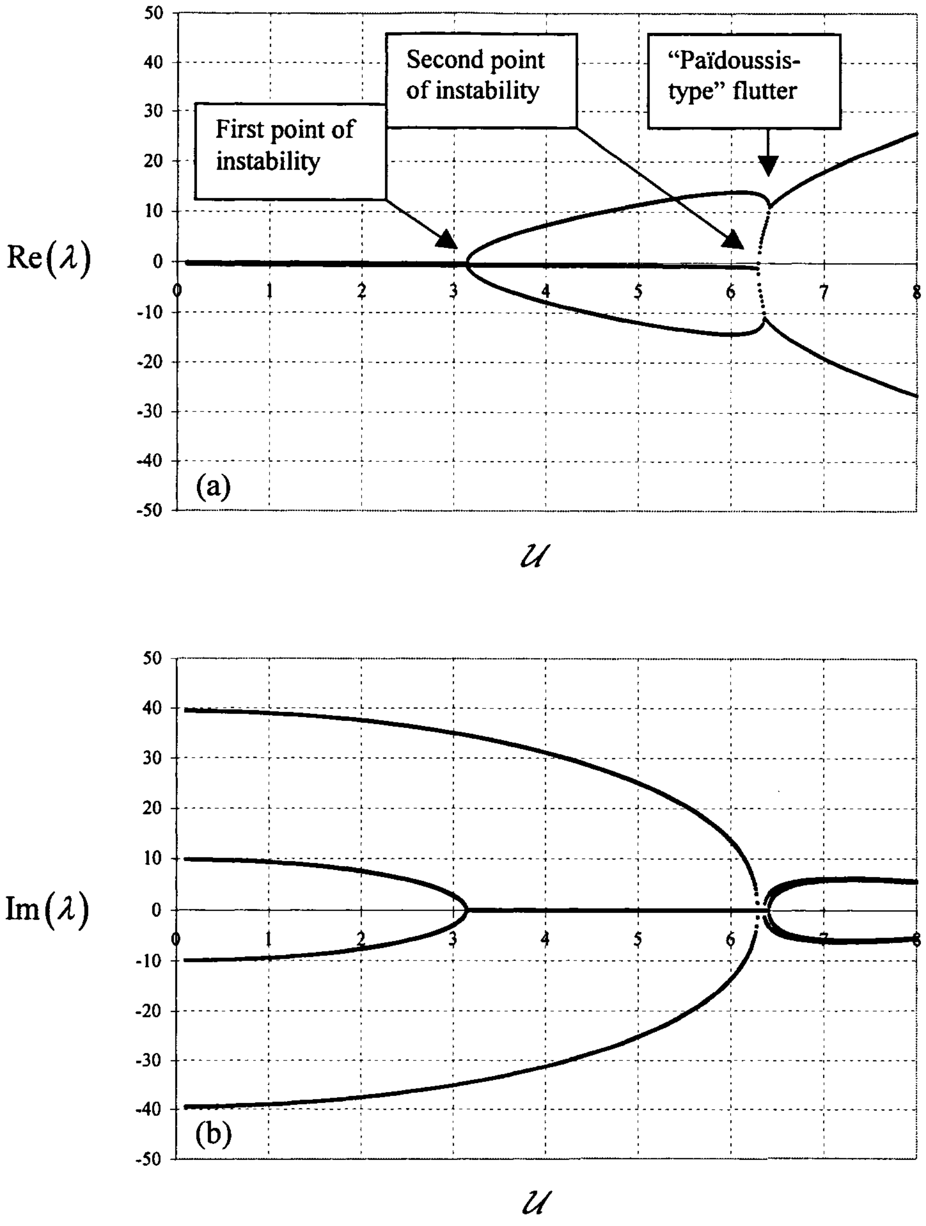

Figure 4-2 (a) Real and (b) imaginary parts of the eigenvalues of a simply supported beam subjected to axial flow versus flow velocity with the following system parameters: $\beta = 0.1$, $\gamma = 0.838$, $c_n = c_t = 0.025$, $\varepsilon = 15.81$, $\delta = 1$, $\overline{\Pi} = \overline{\Gamma} = 0$.

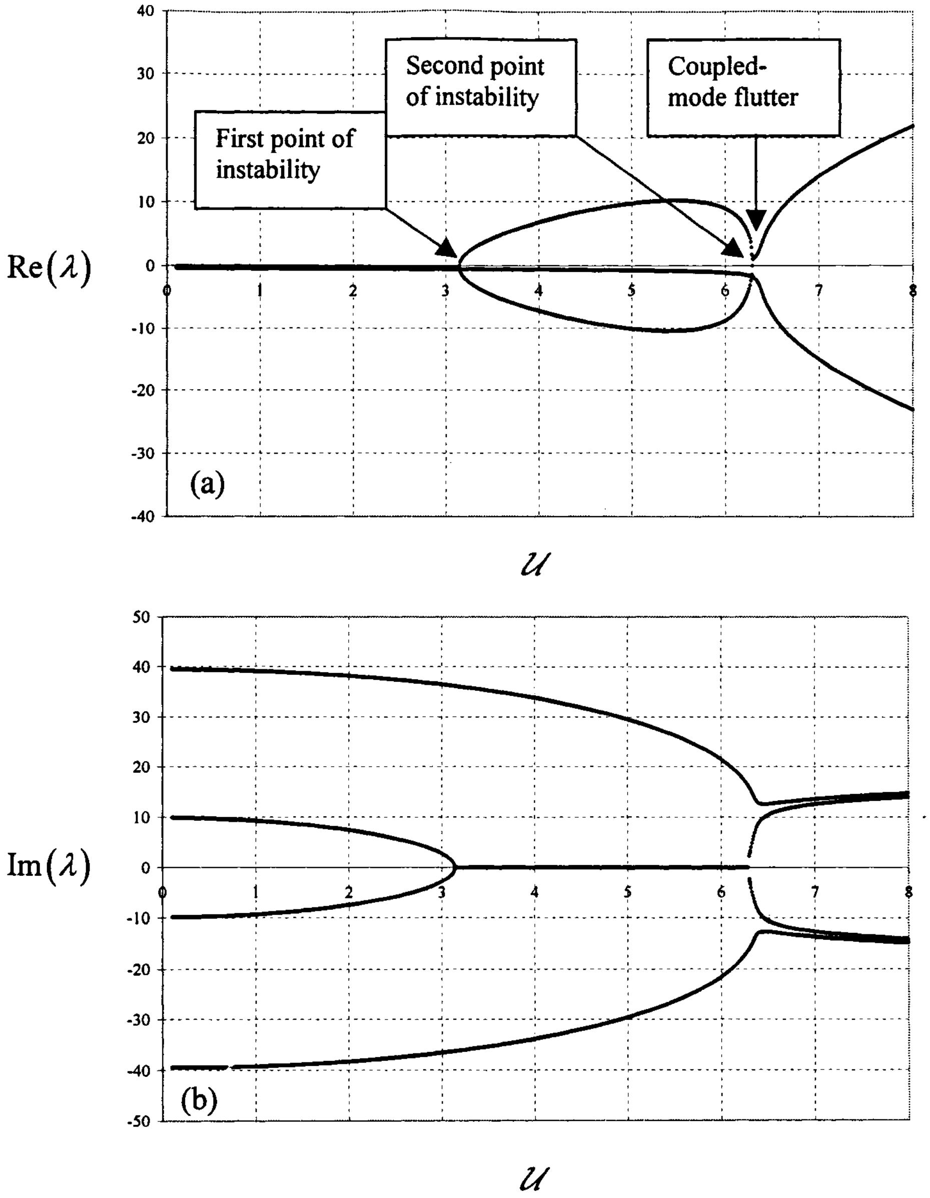

Figure 4-3 (a) Real and (b) imaginary parts of the eigenvalues of a simply supported beam subjected to axial flow versus flow velocity with the following system parameters: $\beta = 0.48$, $\gamma = 0.838$, $c_n = c_t = 0.025$, $\varepsilon = 10.0$, $\delta = 1$, $\overline{\Pi} = \overline{\Gamma} = 0$.

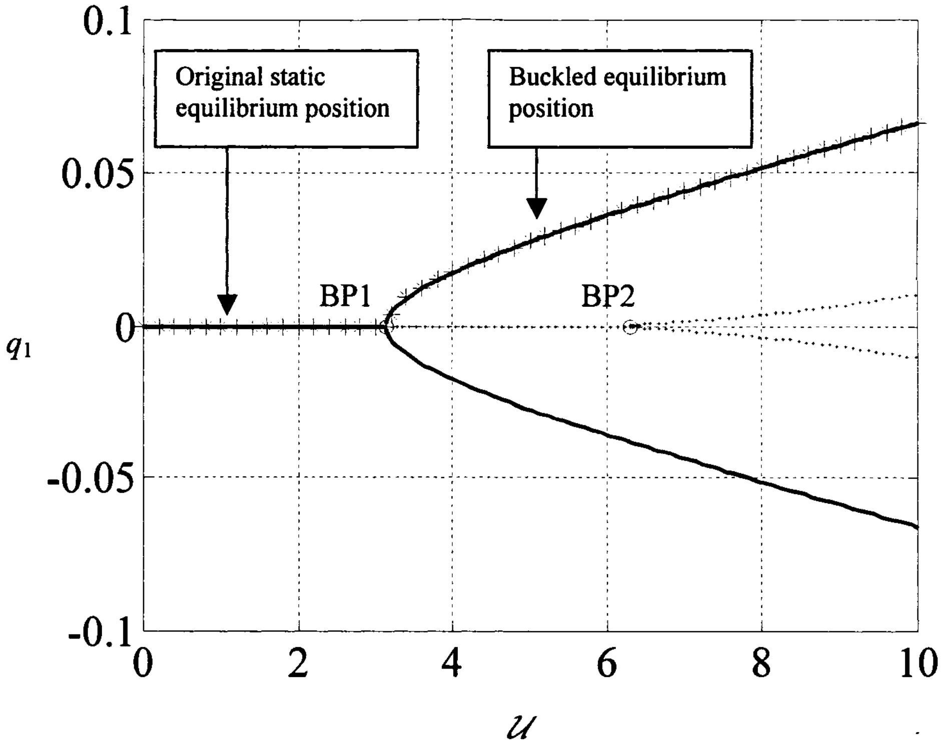

Figure 4-4 A typical bifurcation diagram for a simply supported cylinder subjected to axial flow, obtained by AUTO (continuous and dotted lines) and by FDM (asterisks).

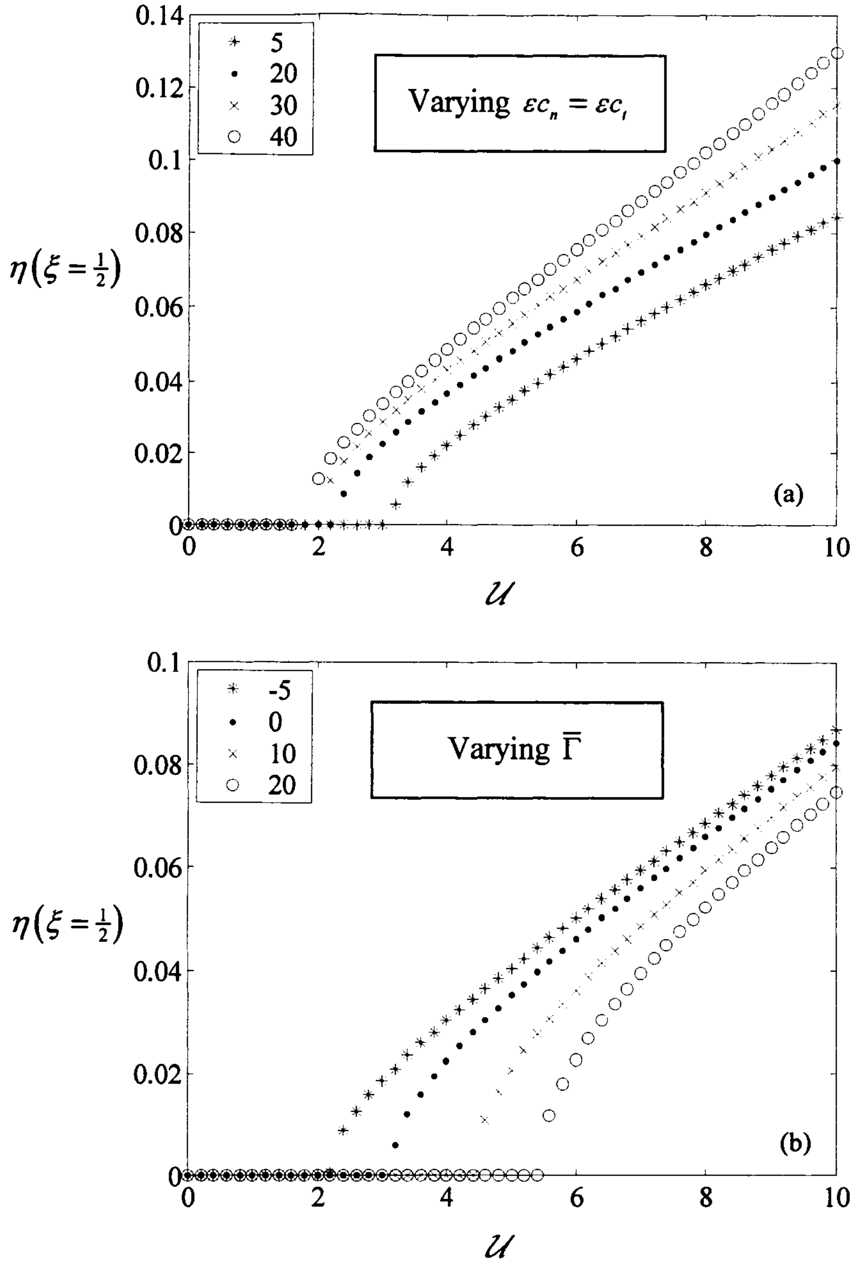

Figure 4-5(a,b); see next page.

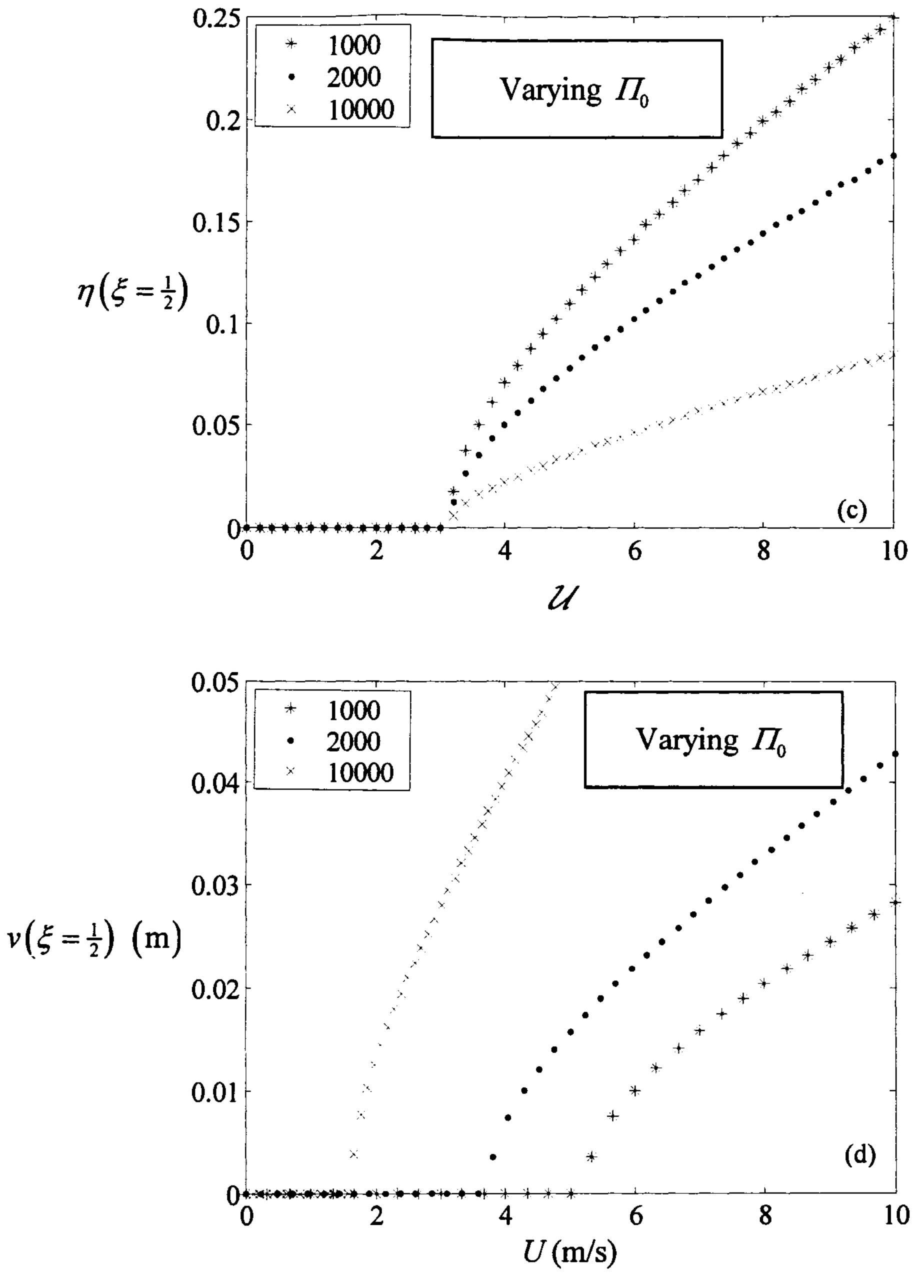

Figure 4-5 Bifurcation diagrams of a simply-supported cylinder obtained with $N_u = N_v = 2$ and with (a) different values of $\varepsilon c_n = \varepsilon c_t$, ranging from 5 to 40, (b) different values of $\overline{\Gamma}$, ranging from –5 to 20, (c) different values of Π_0, ranging from 1000 to 10 000, and (d) different values of Π_0, ranging from 1000 to 10 000 with dimensional values for the transverse displacement and the flow velocity.

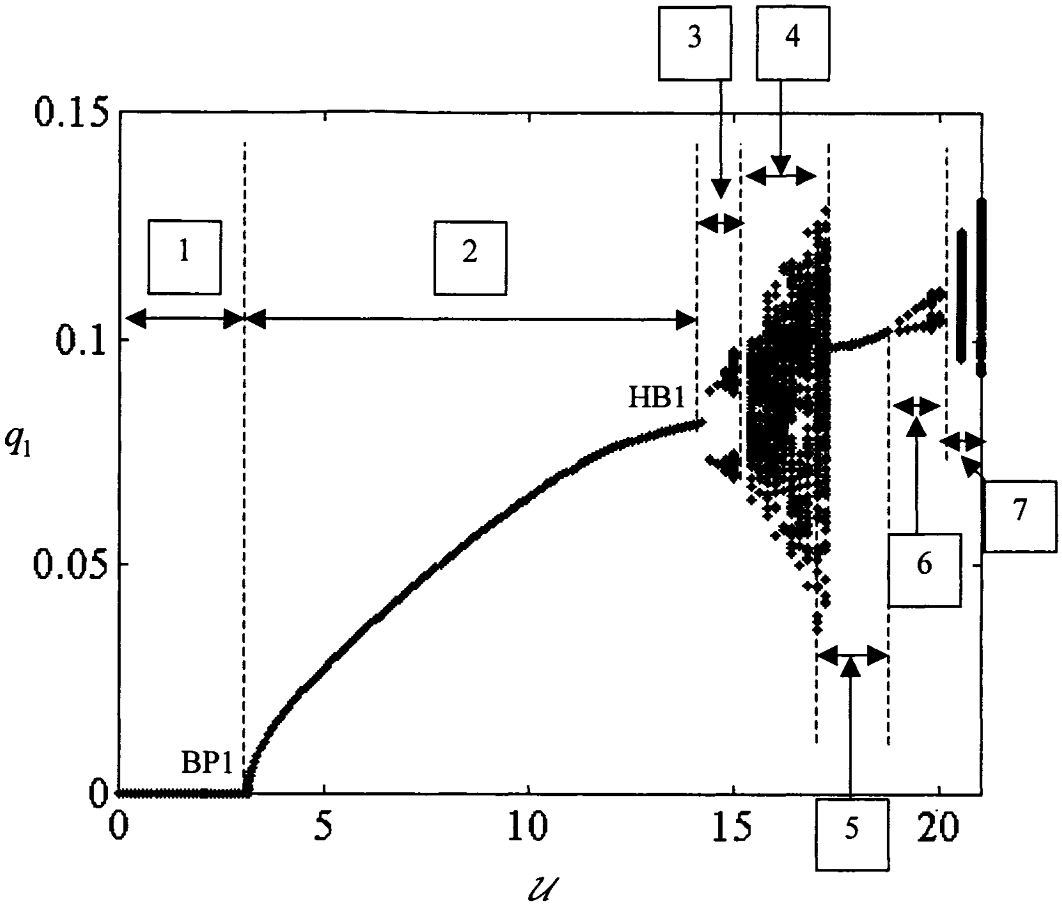

Figure 4-6 Bifurcation diagram of a simply supported cylinder with $\beta = 0.47$, $\gamma = 0.838$, $c_n = c_t = 0.025$, $\varepsilon = 15.81$, $\delta = 1$, $\nu = 0.47$, $\Pi_0 = 4000$, $\chi = 1$, $\bar{\Pi} = \bar{\Gamma} = 0$, $c_b = c_d = 0$, obtained with $N_u = N_v = 6$, showing different states of the system: 1: original equilibrium position; 2: buckled state; 3: periodic oscillations; 4: quasiperiodic and chaotic oscillations; 5: nonzero static solution; 6: high-frequency periodic oscillations; 7: quasiperiodic oscillations.

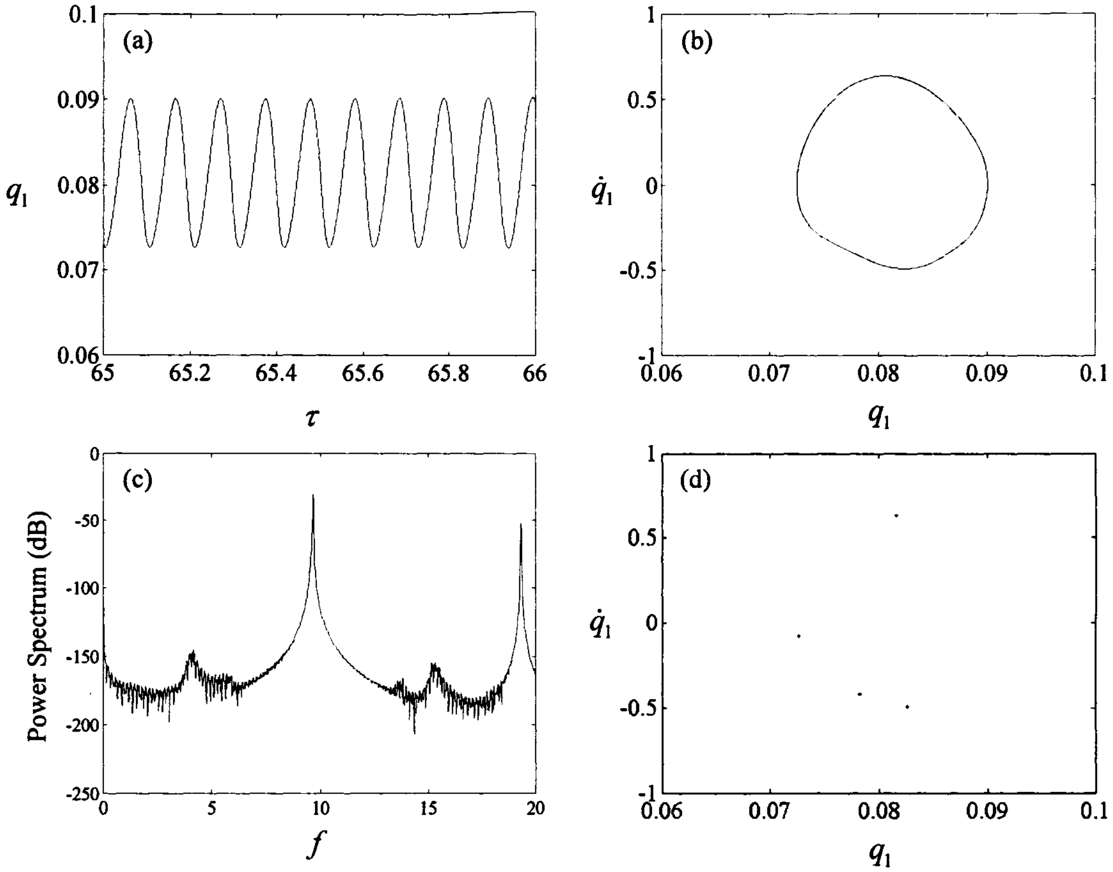

Figure 4-7 (a) Time history, (b) phase plane plot, (c) power spectral density plot and (d) Poincaré map for the system of Figure 4-6 for $\mathcal{U}=14.6$, obtained with $N_u = N_v = 6$ (periodic motion).

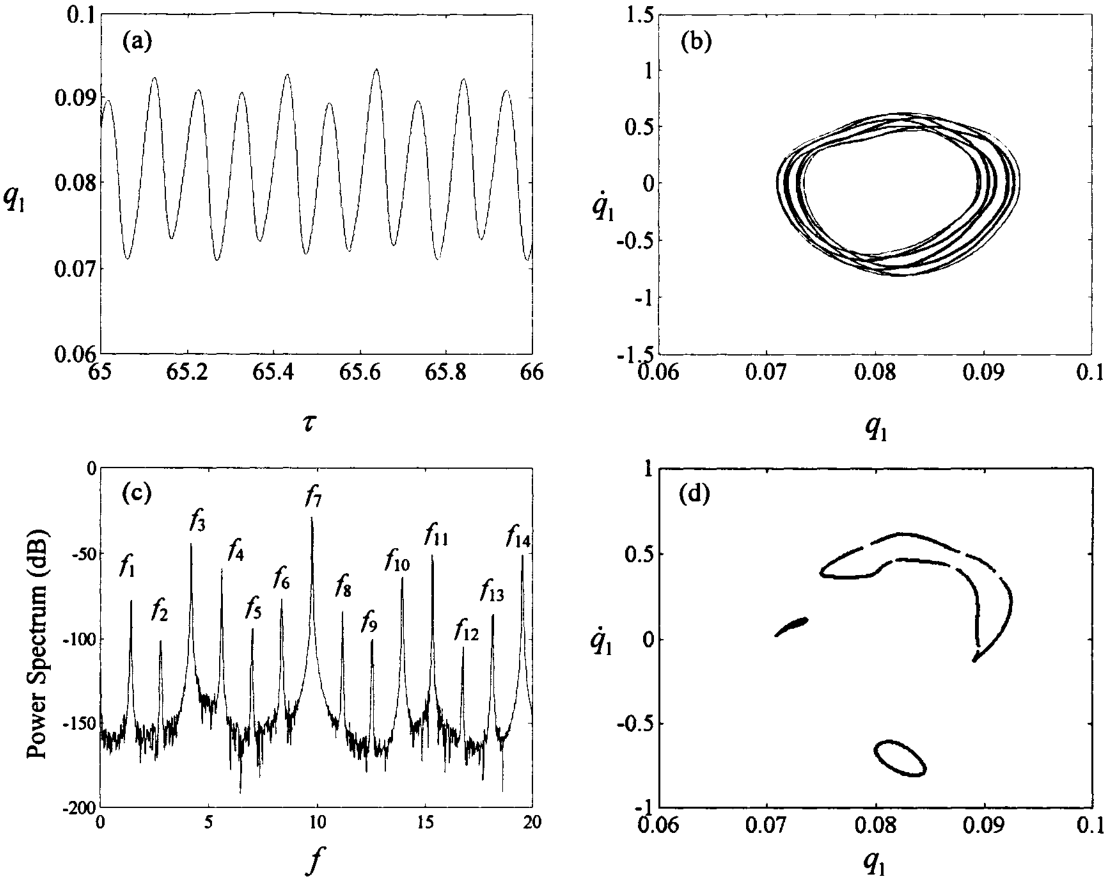

Figure 4-8 (a) Time history, (b) phase plane plot, (c) power spectral density plot and (d) Poincaré map for the system of Figure 4-6 for $\mathcal{U} = 14.8$, obtained with $N_u = N_v = 6$ (quasiperiodic oscillation).

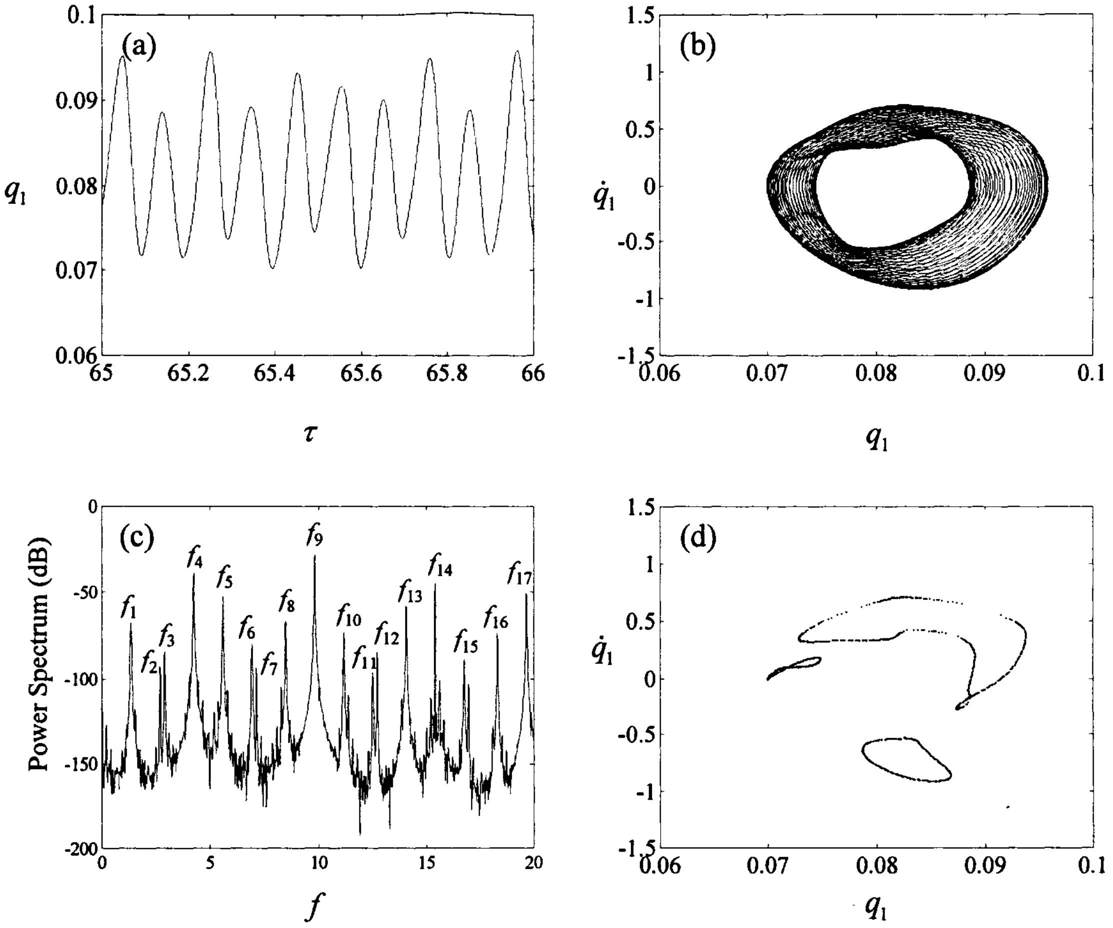

Figure 4-9 (a) Time history, (b) phase plane plot, (c) power spectral density plot and (d) Poincaré map for the system of Figure 4-6 for $\mathcal{U}=14.9$, obtained with $N_u = N_v = 6$ (quasiperiodic oscillation).

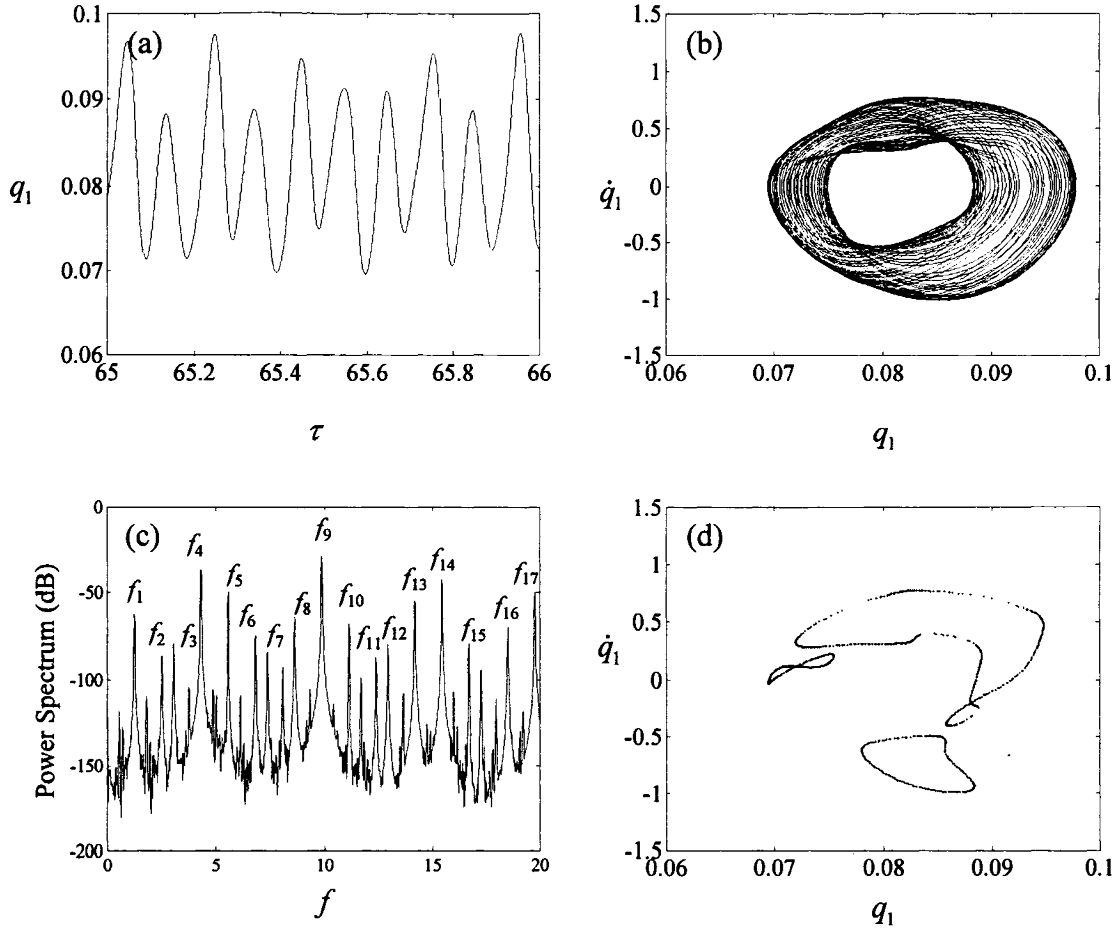

Figure 4-10 (a) Time history, (b) phase plane plot, (c) power spectral density plot and (d) Poincaré map for the system of Figure 4-6 for $\mathcal{U} = 15.0$, obtained with $N_u = N_v = 6$ (quasiperiodic oscillation).

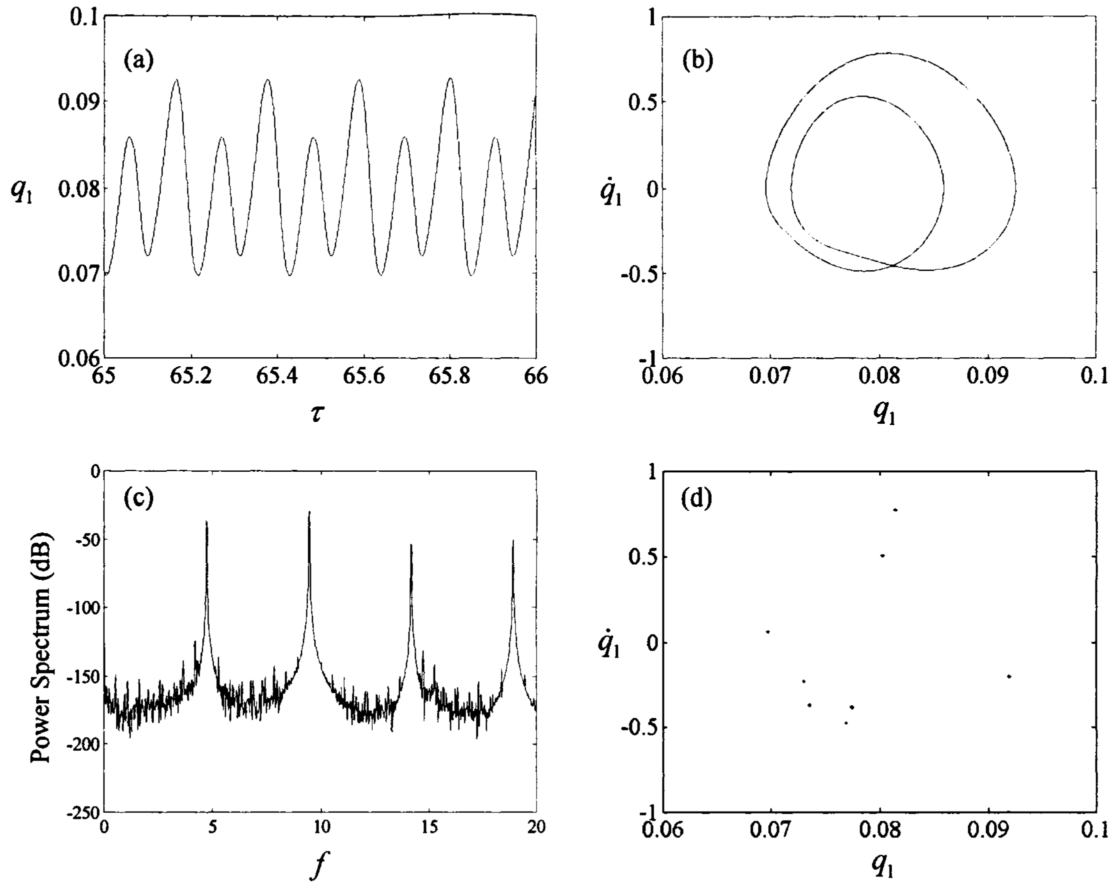

Figure 4-11 (a) Time history, (b) phase plane plot, (c) power spectral density plot and (d) Poincaré map for the system of Figure 4-6 for $\mathcal{U} = 14.6$, obtained with $N_u = N_v = 7$ (period-2 oscillation).

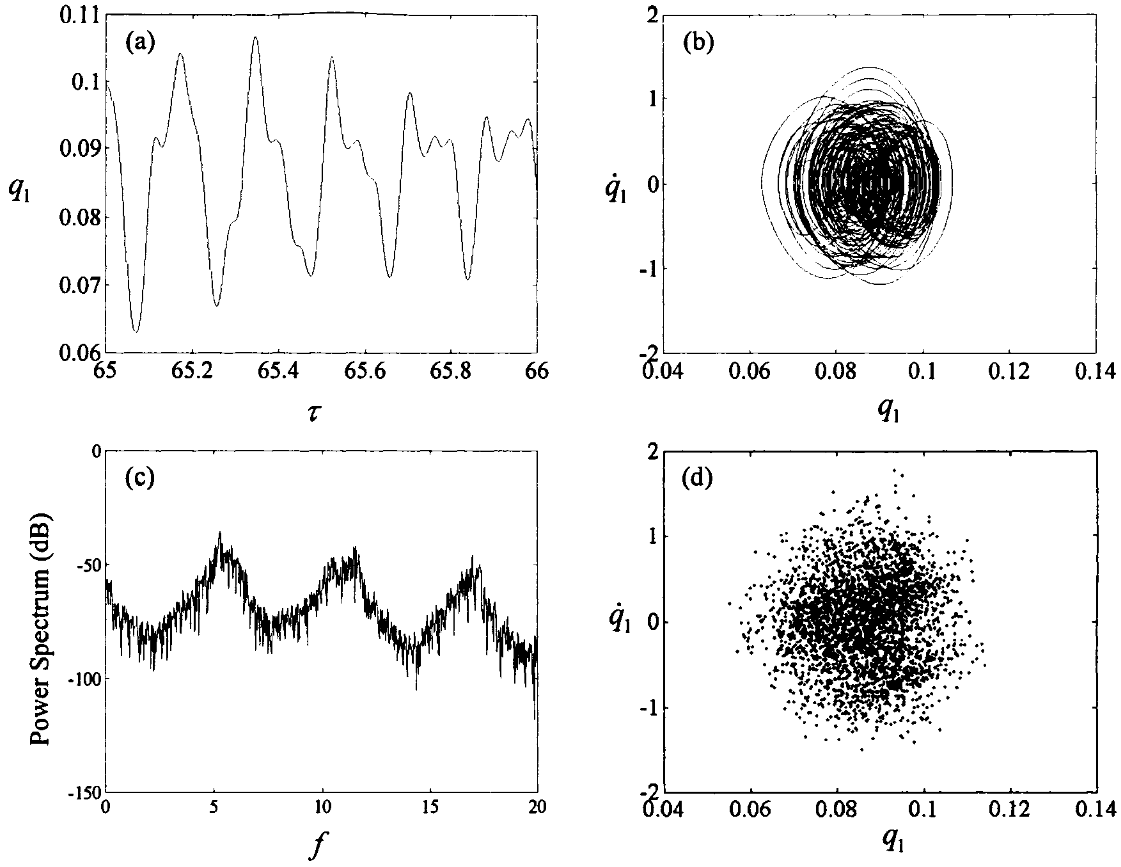

Figure 4-12 (a) Time history, (b) phase plane plot, (c) power spectral density plot and (d) Poincaré map for the system of Figure 4-6 for $\mathcal{U} = 16$, obtained with $N_u = N_v = 6$ (chaotic oscillation).

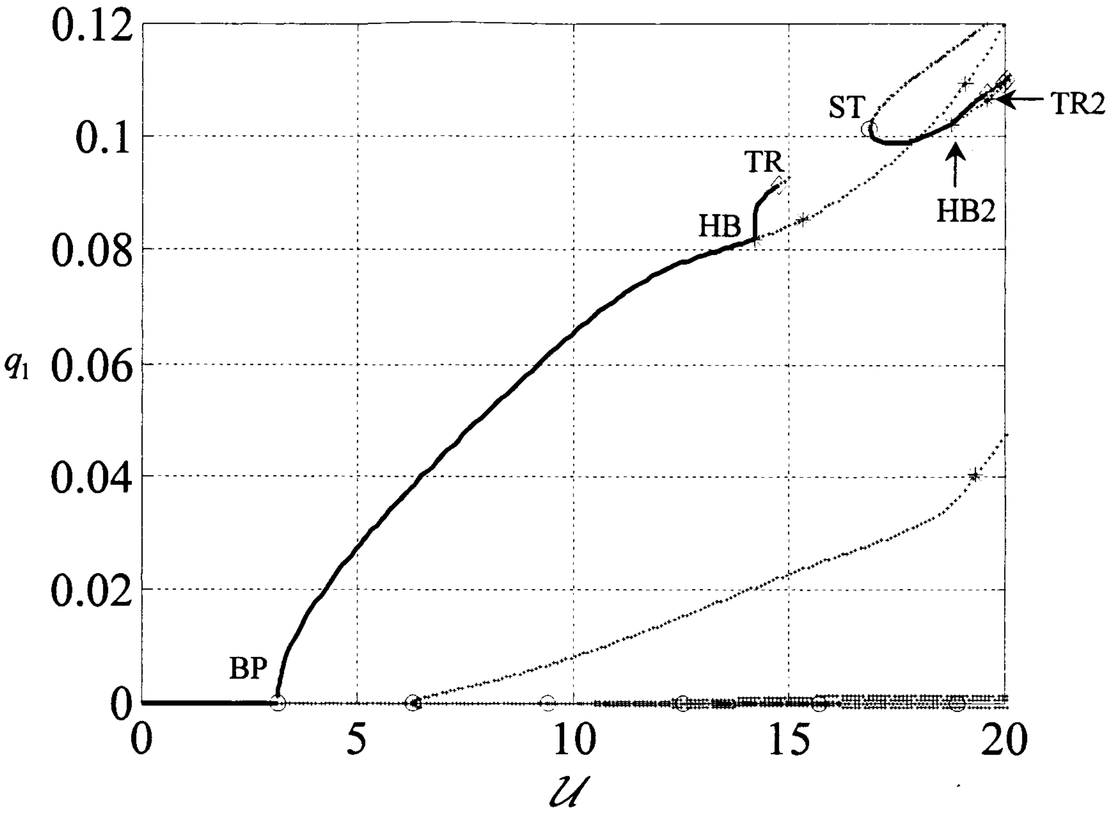

Figure 4-13 Bifurcation diagram found by AUTO for the system of Figure 4-6, obtained with $N_u = N_v = 6$; continuous lines: stable solutions; dotted lines: unstable solutions.

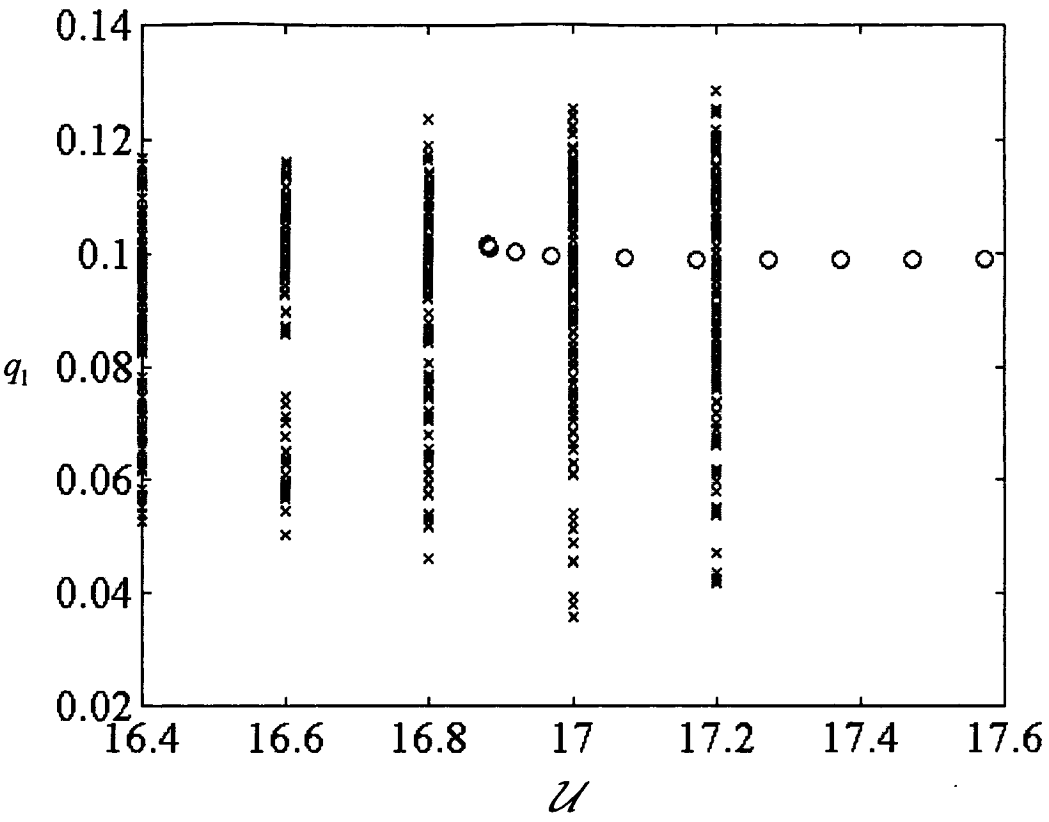

Figure 4-14 A zoomed view of the bifurcation diagram of Figure 4-6, obtained with $N_u = N_v = 6$, showing the co-existence of chaotic and static solutions over a range of flow velocity.

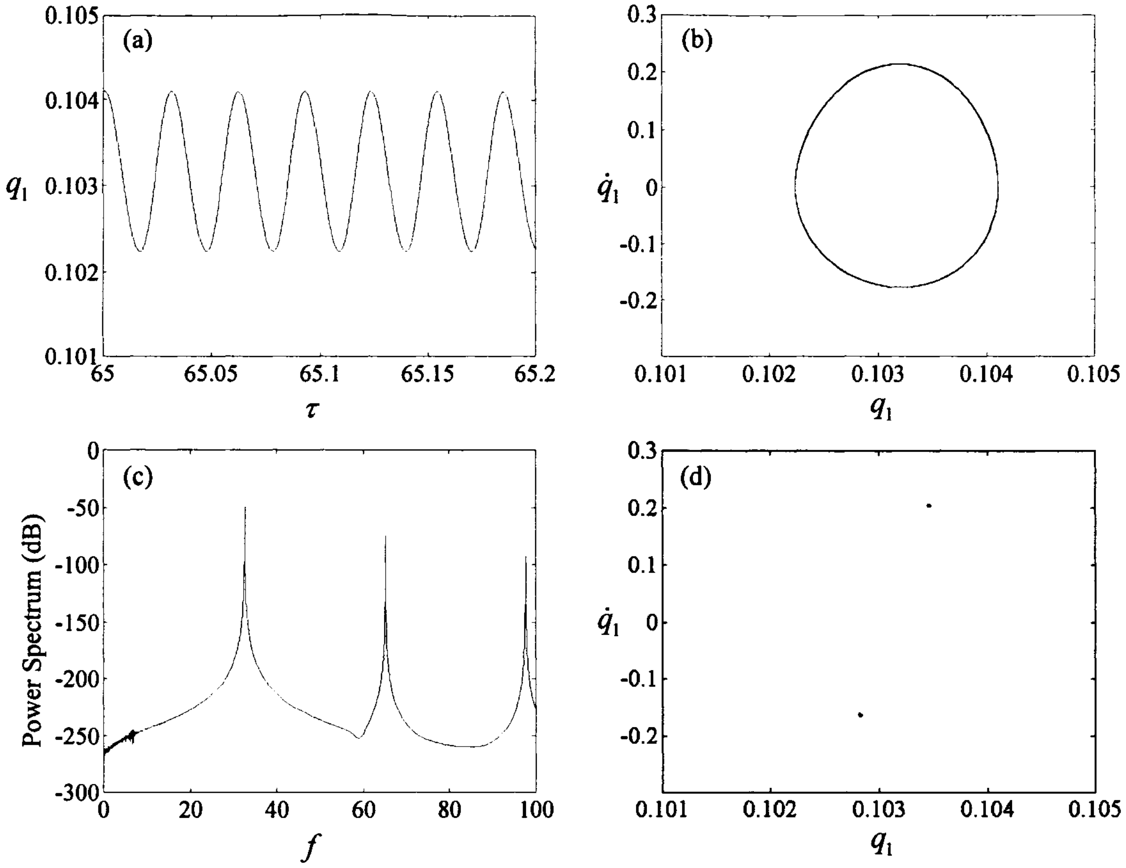

Figure 4-15 (a) Time history, (b) phase plane plot, (c) power spectral density plot and (d) Poincaré map for the system of Figure 4-6 for $\mathcal{U}=19$, obtained with $N_u = N_v = 6$ (high-frequency oscillation).

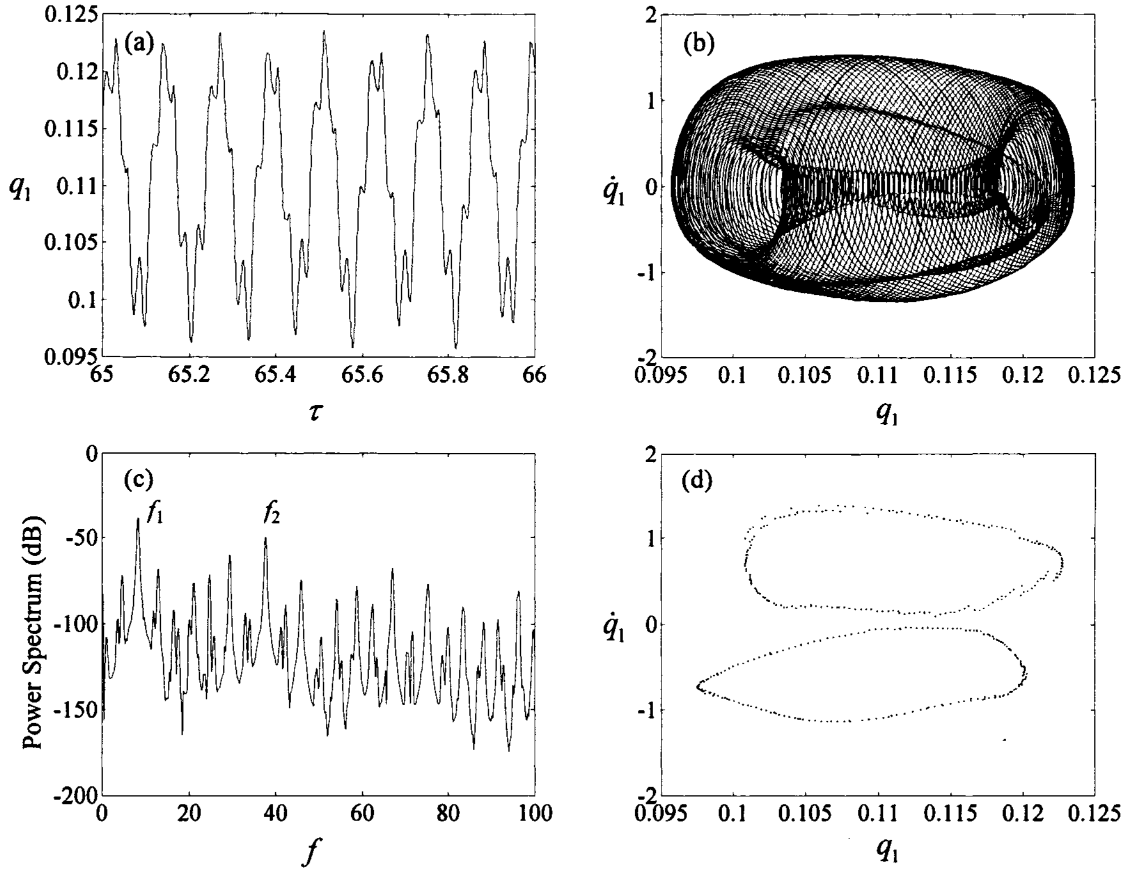

Figure 4-16 (a) Time history, (b) phase plane plot, (c) power spectral density plot and (d) Poincaré map for the system of Figure 4-6 for $\mathcal{U} = 20.5$, obtained with $N_u = N_v = 6$ (quasiperiodic oscillation).

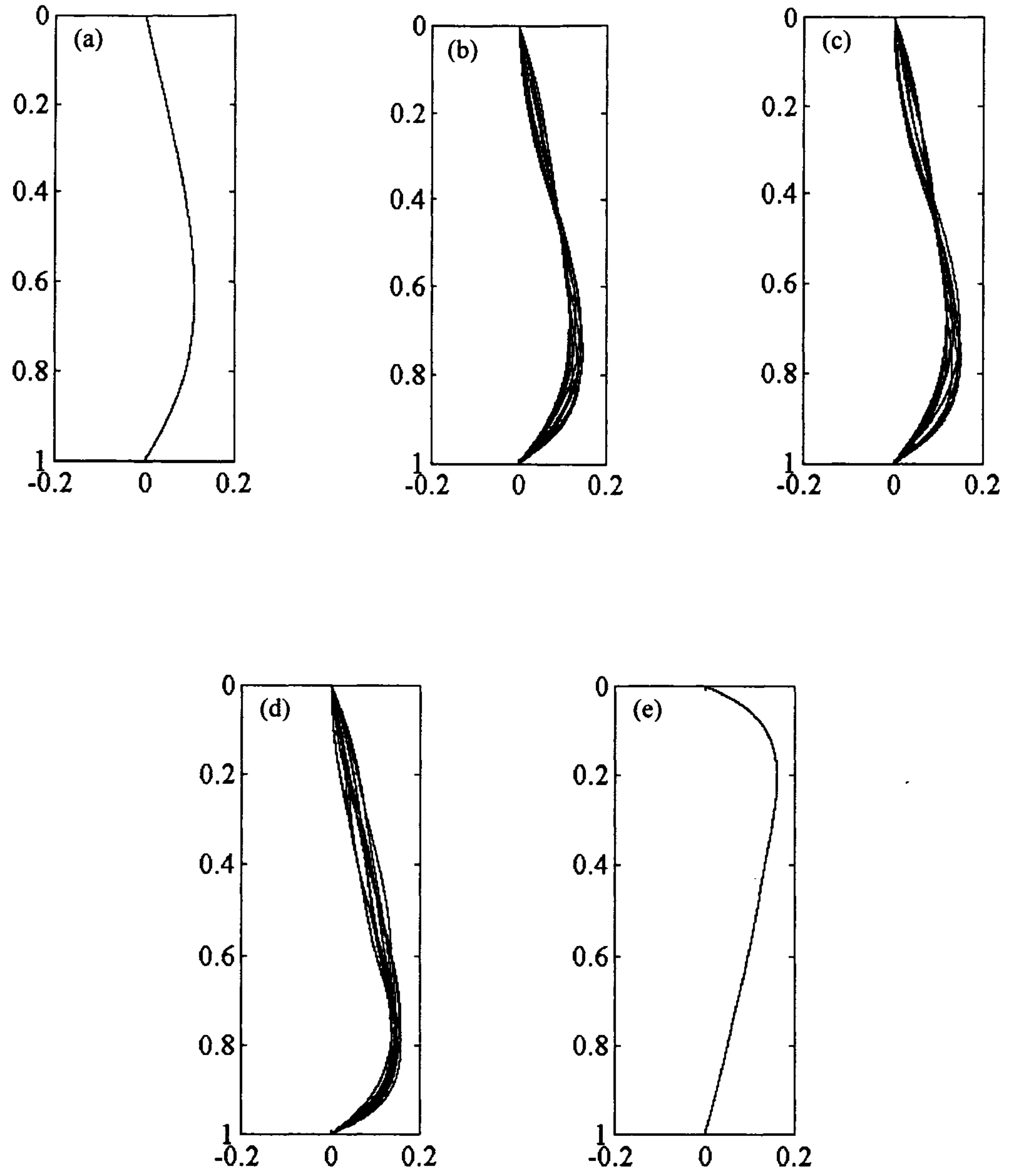

Figure 4-17 Spatial shape of the cylinder of Figure 4-6 at different flow velocities: (a) $\mathcal{U}$=12, buckled position, (b) $\mathcal{U}$=14.6, periodic oscillation, (c) $\mathcal{U}$=14.8, quasiperiodic oscillation, (d) $\mathcal{U}$=16, chaotic oscillation, and (e) $\mathcal{U}$=18, static deformation co-existing with chaotic oscillation.

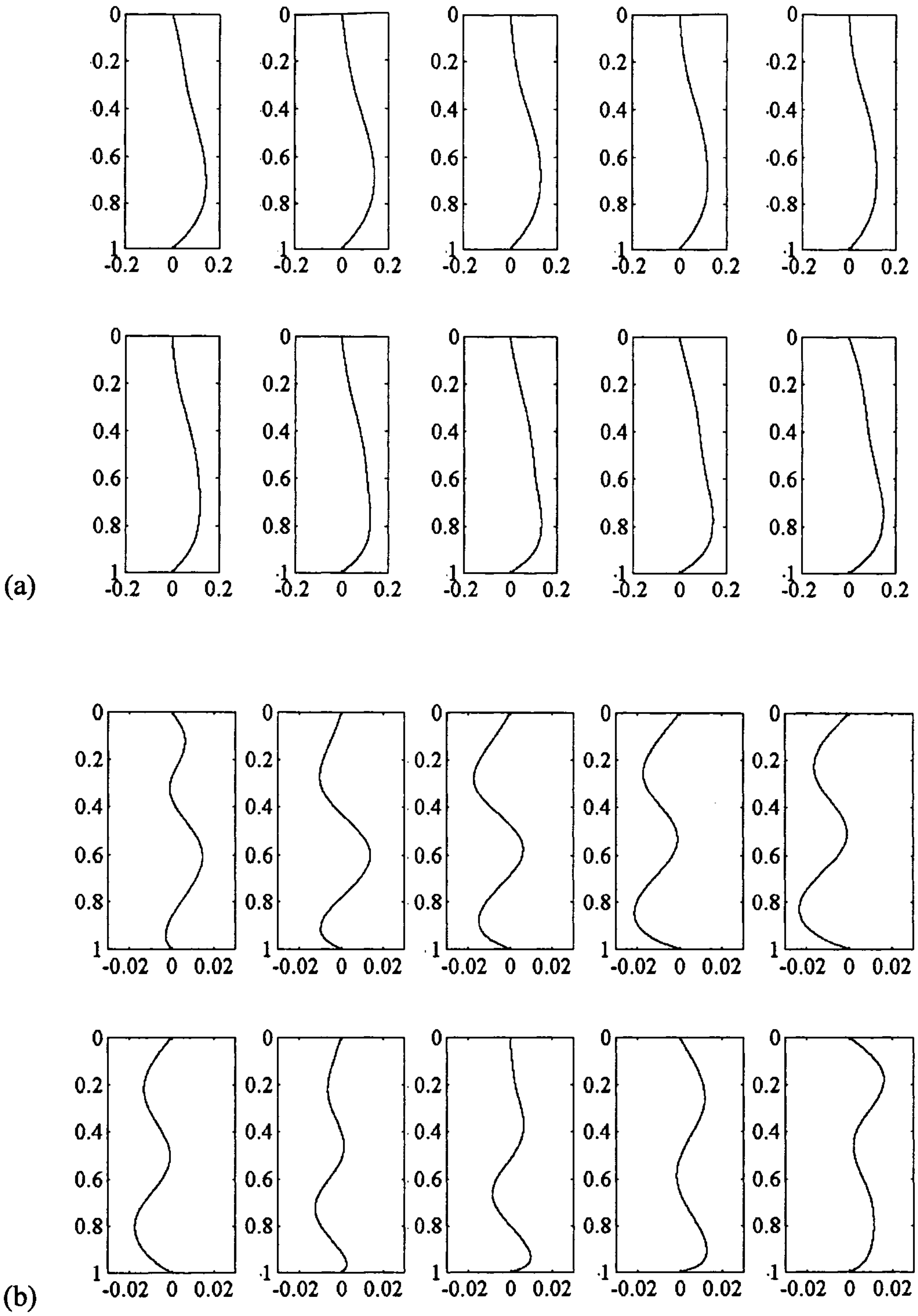

Figure 4-18 Spatial shape of the cylinder of Figure 4-6 at $\mathcal{U}=14.6$, periodic oscillation (see also Figure 4-17(b)): (a) total displacement, (b) vibrations around the buckled position.

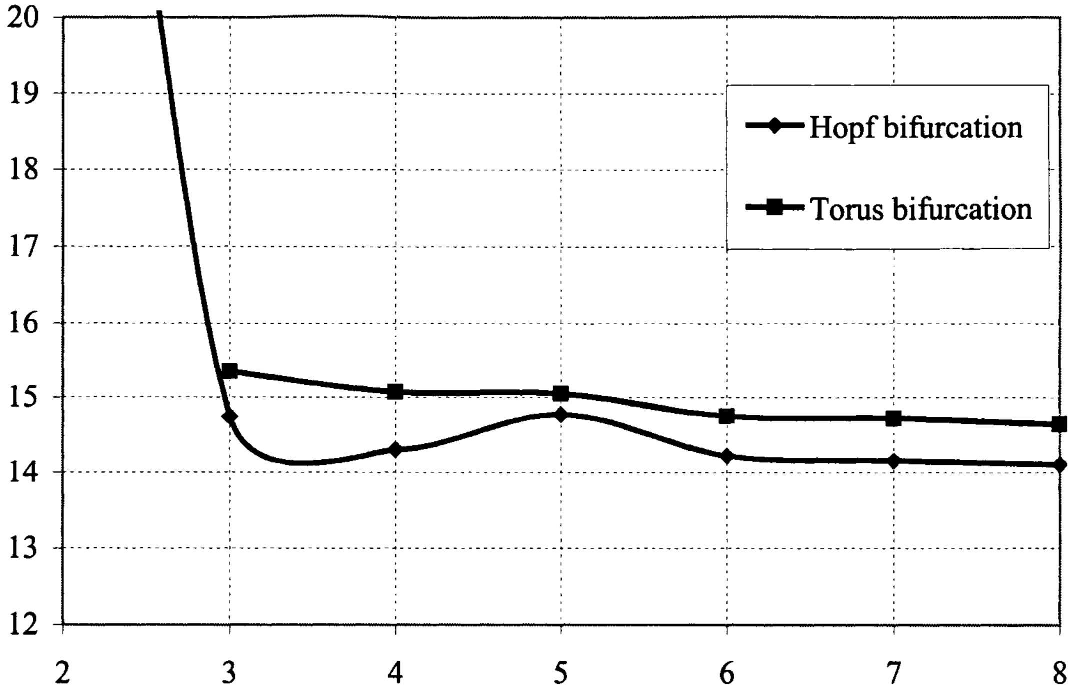

Figure 4-19 The critical flow velocities for the Hopf (HB) and torus (TR) bifurcations of the simply supported cylinder of Figure 4-6, versus the number of modes used in discretization.

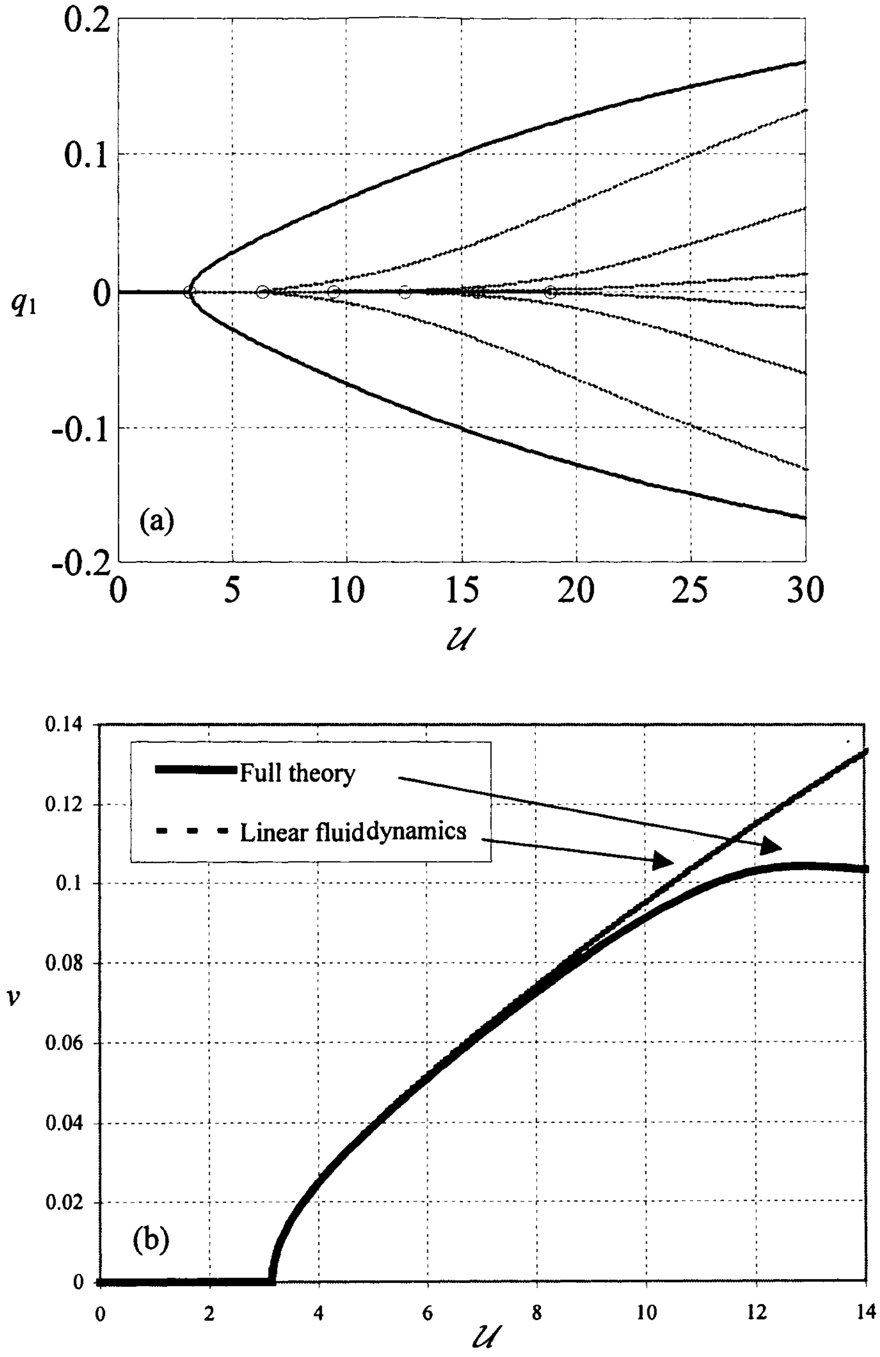

Figure 4-20 (a) Bifurcation diagram for a simply supported cylinder subjected to axial flow using a nonlinear structural model but linear fluid-related forces, for $\beta = 0.47$, $\delta = 1$, $\gamma = 0$, $c_n = c_t = 0.025$; showing no secondary instabilities; (b) comparison between the results found using the full model and the one with linear fluid-dynamic forces.

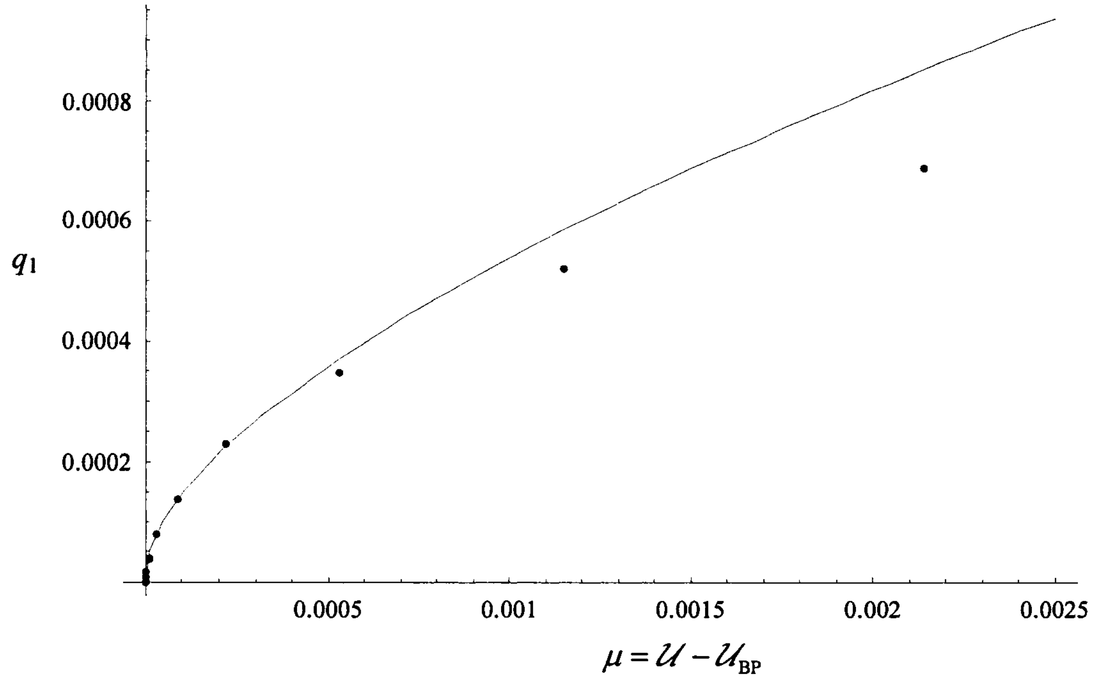

Figure 4-21 Bifurcation diagram for a simply supported cylinder subjected to axial flow of Figure 4-6 obtained with N_u=N_v=1 using centre manifold reduction (continuous line) and AUTO (dots).

5. Nonlinear Dynamics of Clamped-Clamped, Clamped-Hinged and Hinged-Clamped Cylinders Subjected to Axial Flow

5.1. Introduction

The focus of this chapter is to extend the study of the dynamical behaviour of a slender flexible cylinder subjected to axial flow to various other boundary conditions. The main motivations are: (i) to discuss and study the physical behaviour of this system under various possible boundary conditions, because, to the best of our knowledge, the nonlinear analysis of such systems has never been conducted before; (ii) to examine in more depth the possibilities and the limitations (if any) of the nonlinear model of Chapter 2 and of the numerical and analytical methods of Chapter 3.

Three different boundary conditions are considered for the cylinder. First, a vertical cylinder with clamped-clamped boundary conditions is investigated (Figure 5-1(a)). From an experimental point of view, as will be discussed in Chapter 6 where the results of some experiments conducted on clamped-clamped cylinders will be compared with the theoretical ones, this is the simplest set of boundary conditions to realize. In this chapter, however, only the theoretical results are presented. After analysing a clamped-clamped cylinder, the cylinders with mixed support conditions are studied: a cylinder clamped at the upper end and hinged at the lower one (referred to as a *clamped-hinged cylinder*, see Figure 5-1(b)); or hinged at the upper end and clamped at the lower end (referred to as a *hinged-clamped cylinder*, see Figure 5-1(c)). In all the cases studied in this chapter, it is assumed that the downstream end of the cylinder is fixed and no axial sliding is permitted (δ=1 in the equations of motion).

The nonlinear equations of motion derived in Chapter 2, which are the general governing equations for a cylinder with any boundary conditions, are used in all cases. The equations are discretized by using the proper comparison functions satisfying the cylinder boundary conditions (given in Table 5-1), and the resulting set of ordinary differential equations is solved either by numerical (FDM and AUTO) or analytical (centre manifold reduction) methods, as presented in Chapter 3 and used in Chapter 4 for a simply supported cylinder. The results are presented in the form of bifurcation diagrams, as well as time series, phase plane plots, power spectral densities and Poincaré maps, together with the spatial shapes of the cylinder at different flow velocities.

5.2. A clamped-clamped cylinder

In this section, the dynamical behaviour of a clamped-clamped cylinder subjected to axial flow is studied for the dimensional and nondimensional physical parameters listed in Table 5-2. As shown in Figure 5-1(a), the cylinder is assumed to be vertical and the flow direction is downward. To use the nonlinear model of Chapter 2, one has to first calculate the coefficients of the tensor-form equations (Equations (2-68) and (2-69)). To this end, the eigenfunctions of a both-ends-fixed bar for axial deformations, $\psi_j(\xi)$, and those of a clamped-clamped dry beam for transverse deformations, $\phi_j(\xi)$, are used. For convenience, these eigenfunctions are given in Table 5-1. Initially, the numerical methods of AUTO and FDM are used to analyse the system, and then the analytical centre manifold reduction is applied to study the behaviour of the system in the vicinity of the first point of instability.

Figure 5-2(a) shows the bifurcation diagram of the system found by AUTO, where q_1 is plotted versus nondimensional flow velocity, $\mathcal{U}$. The cylinder is at its original equilibrium state at low flow velocities. With increasing flow, it loses stability via a supercritical pitchfork bifurcation at a nondimensional flow velocity $\mathcal{U} \simeq 2\pi$ (the first circle in Figure 5-2(a), BP) leading to divergence (a buckled state, i.e., a stable non-zero static solution or fixed point). The original equilibrium state (the continuous line on the horizontal axis until $\mathcal{U} \simeq 2\pi$) becomes unstable for $\mathcal{U} > 2\pi$. The dotted line on the horizontal axis corresponds to this unstable state. It is interesting to observe that this unstable solution itself undergoes some additional pitchfork bifurcations as the flow velocity is increased (the circles on the horizontal axis) and some new unstable branches emanate from these bifurcation points. However, because they are all unstable, they are not solutions that could materialize physically. The continuous line coming out from the first pitchfork bifurcation point (BP) in Figure 5-2(a) corresponds to the stable buckled state of the cylinder. The amplitude of buckling (q_1) increases with the flow ($\mathcal{U}$).

The static solution eventually loses stability, and the system develops flutter via a supercritical Hopf bifurcation at $\mathcal{U} = 21.60$ (the asterisk in Figure 5-2(b), HB) giving rise to periodic solutions with the frequency of $f = 10.8$ Hz. The system oscillates around the static equilibrium point, where $q_1 \approx 0.085$. Time history, phase plane and power spectral density (PSD) plots and a Poincaré map for the system at $\mathcal{U} = 21.8$ are shown in Figure 5-3. The phase plane is a closed curve and the Poincaré map displays two dots, where the trigger is $\dot{q}_2 = 0$.

The oscillatory motion loses stability via a period-doubling bifurcation at $\mathcal{U} = 21.92$ (the square in Figure 5-2 (b), PD) and the system develops period-2 motions afterward. Figure 5-4 shows the same plots as Figure 5-3 at $\mathcal{U} = 21.95$, for period-2 oscillation: it takes for the cylinder motion two cycles to close the curve in the phase plane; the PSD plot shows that the main frequency is $f = 10.4$ Hz, but a subharmonic exists at $f = 5.2$ Hz; and the Poincaré map shows 4 points (instead of 2 in the periodic case).

Quasiperiodic oscillations are observed for flow velocities greater than $\mathcal{U} = 22.03$ (the diamond in Figure 5-2 (b), TR), where a torus bifurcation occurs. Figure 5-5 indicates that the motion at $\mathcal{U} = 22.5$ is quasiperiodic-2, i.e. all the frequency peaks observed in the PSD plot can be expressed as the linear combination of the two "fundamental frequencies": $f_1 = 0.76$ Hz and $f_2 = 10.7$ Hz. [It is of course obvious that all the peaks can be expressed as linear combinations of *any* two of them. Here we have chosen as one of them the peak that is clearly the descendant of the peak dominating the period-1 and period-2 motions (see Figure 5-3 and Figure 5-4), namely f_2. As the second fundamental frequency, we took the lowest, which clearly corresponds to the beat frequency of the envelope of the oscillation in Figure 5-5(a), namely f_1.] Also, it is noted that the structure of a period-2 oscillation is obvious in the PSD plot, while the contribution of the first fundamental frequency, f_1, has altered that structure to a quasiperiodic one. The phase plane plot and the Poincaré map (a closed curve) confirm a quasiperiodic oscillation, as well.

The quasiperiodic oscillations become chaotic at $\mathcal{U} \simeq 23$ and remain chaotic thereafter for the flow range studied here ($\mathcal{U} < 27$). Figure 5-6 shows the chaotic behaviour of the system at $\mathcal{U} = 25$, where the time history shows a complex motion with no visible pattern or periodicity; the phase plane plot shows orbits that never close or repeat and their trajectories tend to fill up a section of the phase plane with time; the PSD plot shows a broad band; and the Poincaré map does not consist of either a finite set of points or a closed orbit.

Figure 5-7 shows the spatial shape of the cylinder at different dynamical states found by FDM, where the flow direction is downward. In Figure 5-7(a), the cylinder is buckled mainly in its first mode at $\mathcal{U} = 15.0$. The clamped condition is obvious at both the upstream and the downstream ends of the cylinder. At higher flow, as already discussed, the cylinder undergoes a dynamic instability and oscillates around its buckled state. Figure 5-7(b) shows this oscillation at $\mathcal{U} = 21.8$. The amplitude of oscillation is relatively small compared with the amplitude of the buckled state. This figure shows ten configurations of the cylinder (every 0.01 of nondimensional second) in one period of oscillation ($\Delta\tau \simeq 0.1$). These configurations are shown in Figure 5-8(a) in a separate sequence of plots. Figure 5-8(b) shows the oscillations of the cylinder at this flow velocity if the static buckled state is removed. These predominantly third-beam-mode shape oscillations are not obvious in Figure 5-8(a) because the amplitude of buckling is very large compared with the amplitude of oscillations. Period-2 oscillation of the cylinder at $\mathcal{U} = 21.95$ is shown in Figure 5-7(c) for one period of period-2 oscillations ($\Delta\tau \simeq 0.2$), which is in fact equal to two periods of the period-1 oscillations. The cylinder performs oscillations around its buckled position and the maximum amplitude of these oscillations is larger than that of the period-1 oscillations. Quasiperiodic oscillations of the cylinder at $\mathcal{U} = 22.5$ are shown in Figure 5-7(d) for an arbitrary time interval of $\Delta\tau = 0.3$, showing even larger maximum amplitude of oscillations. At $\mathcal{U} = 25.0$, the cylinder undergoes chaotic oscillations and, as is observed in Figure 5-7(e), the range of oscillations in the upper half of the cylinder is much wider than that at the lower flow velocities.

The critical flow velocities for this system, found using various numbers of modes in Galerkin's technique are given in Table 5-3. From these results, it is obvious that by using 5 modes in each direction, the critical flow velocity for the pitchfork bifurcation can be obtained accurately, i.e., $\mathcal{U}_{\mathrm{BP}} = 6.25$. However, the results with even 3 modes only in each direction suggest $\mathcal{U}_{\mathrm{BP}} = 6.26$, which can be considered accurate enough. By increasing the number of modes, the corresponding critical values for the Hopf bifurcation oscillate around a value which can be thought of as the *converged* critical value for the Hopf bifurcation: $\mathcal{U}_{\mathrm{HB}} \simeq 21.6$. This is more obvious in Figure 5-9. The case of 4 modes in each direction appears to be a weird one, where there is a sudden jump in the critical flow velocity. This jump can be said to be due to an insufficient number of modes (4 in each direction, 4-4) and will not affect the final *converged* critical flow velocity for the Hopf bifurcation, i.e. $\mathcal{U}_{\mathrm{HB}} \simeq 21.6$. No explanation was found for the fact that only the 4-4 case displays a pathologically large value for the Hopf bifurcation, while results with even a fewer number of modes do not result in such large values. The oscillatory convergence of the critical values also arises for the critical flow velocities for the period-doubling (PD) and torus (TR) bifurcations (see Figure 5-9). Due to the fact that the dynamic runs of AUTO (which was the method used in this thesis to obtain the critical flow velocities) for a large number of modes are very time consuming for the present problem, the critical values of the period-doubling and torus bifurcations are found using up to 7 modes in each direction only. From the results of Table 5-3 and Figure 5-9, the critical flow velocities for the period-doubling and torus bifurcations can be considered to be $\mathcal{U}_{\mathrm{PD}} \simeq 21.9$ and $\mathcal{U}_{\mathrm{TR}} \simeq 22.4$. To save a lot of computational time, the graphs presented in this section are found by using 6 modes in each direction, unless otherwise mentioned.

The behaviour of the system in the neighbourhood of the pitchfork bifurcation can be studied by centre manifold reduction theory for the clamped-clamped cylinder with the properties given in Table 5-2. The idea is to compare the results of this analytical study with the numerical ones. Keeping in mind that the analytical calculations for this system with many modes will be computationally very expensive, the results are found using one mode in each direction. Following the steps discussed in Section 4.9, the centre manifold for this system can be found to be the surface defined by

$$y_2(y_1)=\frac{156626+24969.5\mu+74.0\mu^2}{0.224+80.77\mu+19.1\mu^2}y_1^2,\quad y_3(y_1)=y_4(y_1)=0, \tag{5-1}$$

and the dynamics of the clamped-clamped cylinder on this manifold is governed by

$$\dot{y}_1=\frac{751.62\mu+177.5\mu^2}{6.35+\mu}y_1-\frac{792000+2.14\times10^8\mu+8.5\times10^7\mu^2}{1.42+513.3\mu+201.86\mu^2}y_1^3, \tag{5-2}$$

indicating a supercritical pitchfork bifurcation. Figure 5-10 shows the bifurcation diagrams of this system found by centre manifold reduction and by AUTO with one mode in each direction. The amplitudes found by the two methods are in very good agreement for small μ, e.g., $\mu<0.0025$. By increasing μ beyond the range of applicability of the centre manifold reduction, the difference between the results of numerical and analytical methods becomes larger.

5.3. A clamped-hinged cylinder

In the studies presented in Chapter 4 and Section 5.2, the cylinder was assumed to be under the same support conditions at both ends: either hinged (simply supported) or clamped. In this section and the following one, the dynamical behaviour of "mixed" support conditions is studied, i.e., a vertical cylinder clamped at the upper end and hinged at the lower one (clamped-hinged) or vice versa (hinged-clamped). The case of a clamped-hinged cylinder (Figure 5-1(b)) with the same physical properties as in Section 5.2 (given in Table 5-2) is studied in this section.

Again, the nonlinear model of Chapter 2 is used and the coefficients of the equations in tensor form (Equations (2-68) and (2-69)) are calculated by using the appropriate comparison functions (given in Table 5-1). It should be noted that for a clamped-hinged cylinder, one must use very accurate eigenvalues. By using only up to 6 significant figures, some unrealistic results were found: the cylinder lost its original stability by a Hopf bifurcation! This behaviour was not observed when more accurate eigenvalues were used: i.e., accurate to twelve significant figures. The sensitivity of the results to the accuracy of the eigenvalues has also been observed for clamped-hinged shells in axial flow by Païdoussis (2004, Chapter 7). The results are not as sensitive for the case of clamped-clamped and even hinged-clamped cylinders (discussed in Section 5.4).

Figure 5-11(a) shows the bifurcation diagram of the clamped-hinged cylinder. Qualitatively, the cylinder behaves similarly to the clamped-clamped one. It is at its original equilibrium state, up to where it loses stability via a supercritical pitchfork bifurcation at a nondimensional flow velocity $\mathcal{U} \simeq 4.37$ (the first circle in Figure 5-11(a), BP) leading to divergence. The amplitude of divergence increases with the flow, and then the static solution loses stability via a supercritical Hopf bifurcation at $\mathcal{U} = 17.60$ (the asterisk in Figure 5-11(b), HB), and the system develops flutter around its buckled state. The frequency of these periodic oscillations is almost twice as high as the frequency of oscillations for a clamped-clamped cylinder ($f_{\text{C-H}} = 22.0$ Hz compared to $f_{\text{C-C}} = 10.8$ Hz). It ought to be mentioned that the frequency of oscillation at the Hopf bifurcation for a simply supported cylinder with the same length as the cylinders studied in this chapter is $f_{\text{S-S}} = 19.4$ Hz, which is comparable with that of the clamped-hinged cylinder. In both the clamped-hinged and the simply supported cases, at the Hopf bifurcation, the third mode of the system loses stability, and as a result the cylinder performs high-frequency oscillations, while in the clamped-clamped case, the second mode becomes unstable. The high-frequency oscillation of the clamped-hinged cylinder at $\mathcal{U} = 18.0$ is obvious in the time history and the PSD plot of Figure 5-12. A phase plane plot and a Poincaré map of the system (Figure 5-12) also confirm the periodic nature of the oscillations at $\mathcal{U} = 18.0$.

The periodic oscillations of the cylinder are followed by period-2 oscillations via a period-doubling bifurcation at $\mathcal{U} = 18.76$ (the square in Figure 5-11(b), PD), followed immediately by a torus bifurcation at $\mathcal{U} = 19.13$ (the diamond in Figure 5-11(b), TR). Figure 5-13 shows very clearly that the cylinder has undergone a period-2 oscillation at $\mathcal{U} = 18.8$. The main frequency is still $f = 22$ Hz, and its subharmonic is observed at $f = 11$ Hz in the PSD plot. Figure 5-14 shows the quasiperiodic behaviour of the system at $\mathcal{U} = 19.5$. The high-frequency oscillation as well as the low frequency envelope signal are obvious, in the time history. The Poincaré map displays two closed curves, indicating that the oscillation is quasiperiodic and the PSD plot shows that the fundamental frequencies are $f_1 = 1.8$ Hz and $f_2 = 22.5$ Hz.

The system undergoes chaotic oscillations for $\mathcal{U} > 19.7$. Figure 5-15 shows time history, phase plane plot, PSD plot and Poincaré map of the cylinder at $\mathcal{U} = 20$. The time history shows that the oscillation is not periodic or quasiperiodic and this is the first sign of chaotic oscillation. The trajectory of the orbit in the PSD plot fills up a section of the phase space and the PSD plot displays a broad spectrum, both indicating a chaotic oscillation. The Poincaré map of this chaotic oscillation contains a cloud of points; however, it displays four black clusters of points (marked by the arrows), indicating the possibility of existence of some *local attractors* at these points.

Figure 5-16 shows the spatial shape of the clamped-hinged cylinder for the flow velocities discussed above. Figure 5-16(a) shows the cylinder in its buckled state at $\mathcal{U} = 14$, which resembles mainly first-mode buckling, and the maximum amplitude occurs at a point lower than the midpoint. Also the clamped and hinged conditions of the cylinder at the boundaries are obvious. The periodic oscillations of the cylinder at $\mathcal{U} = 18.0$ are observed in Figure 5-16(b) for a period of oscillation ($\Delta\tau \simeq 0.05$) where similarly to the clamped-clamped case, the cylinder oscillates around its buckled position with relatively small amplitude of oscillations. However, in this case, it is more obvious than for the clamped-clamped cylinder that the cylinder oscillates mainly with a third-mode shape and there are two nodes noticeable at $\xi \simeq 0.4$ and $\xi \simeq 0.7$. These two nodes are observed also in the case of the period-2 oscillations at $\mathcal{U} = 18.8$ (Figure 5-16(c)), showing still mainly third-mode oscillations. Here, the maximum amplitude of oscillation is larger than that of the period-1 case. When the cylinder undergoes quasiperiodic oscillation at $\mathcal{U} = 19.5$ (Figure 5-16(d)), the two nodes are not clearly visible anymore, but still exist, and the oscillations are of even larger maximum amplitude. The chaotic oscillations of the cylinder at $\mathcal{U} = 20.0$ (Figure 5-16(e)) do not show any nodes (suggesting spatio-temporal chaos) and the amplitude of oscillations is comparable with the amplitude of the buckled state of the cylinder.

Table 5-4 shows the effect of the number of modes used in Galerkin's technique to discretize the partial differential equations of motion on the critical flow velocities of a clamped-hinged cylinder. It is obvious that by using only 3 modes in each direction, one can find the exact value of the critical flow velocity for divergence, i.e., $\mathcal{U}_{\mathrm{BP}} = 4.37$. The results for the critical flow velocities for the Hopf and period-doubling bifurcations display oscillatory convergence, similarly to the case of a clamped-clamped cylinder, while the critical values for the torus converge monotonically (see also Figure 5-17). The critical values, therefore, can be considered to be $\mathcal{U}_{\mathrm{HB}} \simeq 17.9$, $\mathcal{U}_{\mathrm{PD}} \simeq 18.4$ and $\mathcal{U}_{\mathrm{TR}} \simeq 19.0$. The graphs presented in this section have been produced using 6 modes in each direction, unless otherwise mentioned.

Using the centre manifold theory, one can find that the centre manifold surface for a system discretized using one mode in each direction is

$$y_2(y_1) = \frac{21821.4 + 35.76\mu + 4.02\mu^2}{0.0201 + 8.90\mu + \mu^2} y_1^2, \quad y_3(y_1) = y_4(y_1) = 0, \tag{5-3}$$

and the governing equation of motion on the centre manifold is

$$\dot{y}_1 = \left(108.03\mu + 12.15\mu^2\right) y_1 - \frac{67954.2 + 2.25\times10^7\mu + 7.62\times10^6\mu^2}{0.09 + 39.58\mu + 13.34\mu^2} y_1^3. \tag{5-4}$$

Figure 5-18 shows the bifurcation diagrams of the system by AUTO and the centre manifold theory with qualitative agreement (supercritical pitchfork bifurcation) and very good quantitative agreement for the transverse amplitude for small values of μ.

5.4. A hinged-clamped cylinder

After studying the behaviour of a mixed supported cylinder with a clamped upstream end and a hinged downstream one, in this section the other possible case of a mixed supported cylinder is studied: a cylinder with the hinged upstream end and clamped downstream one, called a hinged-clamped cylinder (Figure 5-1(c)). Obviously, because the direction of the flow and gravity is fixed (downward) in both the clamped-hinged and the hinged-clamped cylinders, the dynamical behaviour of these two systems is not expected to be the same. Païdoussis (2005) discusses the dynamics of fluid-conveying shells with mixed supports (clamped-hinged and hinged-clamped).

The cylinder studied in this section has the same physical properties as in the two previous sections (Table 5-2). The nonlinear model of Chapter 2 is used, with the eigenfunctions for the Galerkin technique as given in Table 5-1.

Figure 5-19(a) shows the bifurcation diagram of this system. The system behaves very similarly to the case of a cylinder with clamped-clamped or clamped-hinged boundary conditions. The original equilibrium position of the cylinder loses stability by a supercritical pitchfork bifurcation at $\mathcal{U} = 4.61$ (the first circle in Figure 5-19(a), BP) and the amplitude of the resulting buckled state increases with the flow and then this stable state loses stability by a Hopf bifurcation at $\mathcal{U} = 21.23$ (the asterisks in Figure 5-19(b), HB) leading to periodic oscillations. The frequency of oscillation at the Hopf bifurcation is $f_{\text{H-C}} = 8.7$ Hz, which is close to the frequency of oscillation for the clamped-clamped cylinder; the relatively high-frequency oscillation of the clamped-hinged or simply supported cylinder is not observed in this case, because it is the second mode that becomes unstable at the Hopf bifurcation. Figure 5-20 gives the time history, phase plane and PSD plots, as well as a Poincaré map of the system at $\mathcal{U} = 22$, all of them showing periodic oscillation.

The periodic oscillation undergoes a period-doubling bifurcation at $\mathcal{U} = 22.5$ (not shown in Figure 5-19). This is obtained when 9 modes in each direction are used. By using 8 modes or less in each direction, no period-doubling bifurcation is obtained (see Table 5-5). Similarly to the previous cases, the resulting period-2 oscillations become quasiperiodic at $\mathcal{U} = 22.93$ (the diamond in Figure 5-19(b), TR), when a torus bifurcation occurs. Figure 5-21 shows the system graphs at $\mathcal{U} = 24$ when the cylinder undergoes a quasiperiodic oscillation. As can be observed in the time history and also in the PSD plot, the two fundamental frequencies of oscillation are taken to be $f_1 = 1.3$ and $f_2 = 12.1$. With increasing flow, chaotic oscillations are observed from $\mathcal{U} = 25$ on, and the system behaviour remains chaotic thereafter until the maximum flow velocity studied here, $\mathcal{U} = 30$. Figure 5-22 shows the plots of the chaotic oscillation of the system at

$\mathcal{U} = 26$. A complex motion with no visible pattern or periodicity in the time history, partially filled phase plane, broad spectrum PSD plot and a cloud of points in the Poincaré map, all indicate the existence of chaos at this flow velocity.

Figure 5-23 shows the spatial shapes of the cylinder in various dynamical states. At $\mathcal{U} = 20.0$, the cylinder has buckled (Figure 5-23(a)) and the maximum of its transverse amplitude is on the lower half of the cylinder, as one would expect. The very small-amplitude periodic oscillation of the cylinder around its buckled position is shown in Figure 5-23(b) for $\mathcal{U} = 22.0$. At higher flow, the cylinder performs quasiperiodic and chaotic oscillations as are shown in Figure 5-23(c, d) for $\mathcal{U} = 24.0$ and $\mathcal{U} = 26.0$, respectively.

In Table 5-5, the effect of the number of modes used in the discretization on the system critical flow velocities is tabulated. Obviously, to find the converged value for the pitchfork bifurcation point, at least 3 modes in each direction are necessary. The critical values for the Hopf and the period-doubling bifurcation points converge monotonically, as the number of modes is increased (Figure 5-24), instead of showing oscillatory convergence, as for the other boundary conditions. These results also show that unlike the two previous cases, in this case one should use at least 8 modes in each direction to study reliably the system behaviour. By using 9 modes in each direction, one can see that the system undergoes a period-doubling bifurcation at $\mathcal{U} = 22.49$, followed by a torus at $\mathcal{U} = 22.75$. Otherwise, the system behaviour does not change whether 8 or 9 modes are used, and the results found with 8 modes in each direction are reliable. The graphs presented in this section are found using 8 modes in each direction, unless otherwise mentioned.

The governing equation of motion on the centre manifold can be found to be

$$\dot{y}_1 = \left(85.55\mu + 9.2\mu^2\right) y_1 - \frac{217098 + 4.62\times 10^7 \mu + 2.49\times 10^7 \mu^2}{0.71 + 200.97\mu + 108.0\mu^2} y_1^3, \tag{5-5}$$

where, the centre manifold surface is defined as

$$y_2(y_1)=\frac{60660.3+13152.2\mu+30.81\mu^2}{0.15+43.2\mu+13.94\mu^2}y_1^2,\quad y_3(y_1)=y_4(y_1)=0, \tag{5-6}$$

The bifurcation diagrams for this system at small post-divergence values of the flow velocity are presented in Figure 5-25, showing, similarly to the previous two cases, qualitative and very good quantitative agreement between the numerical (AUTO) and analytical (the centre manifold) results.

5.5. The axial displacement and the strain in a clamped-clamped cylinder

In this section, some calculations are conducted on a clamped-clamped cylinder as a sample of the systems studied in this thesis to validate some of the assumptions made in the derivation of the equations of motion in Chapter 2.* In the results presented so far, in all the bifurcation diagrams, the transverse displacement of the cylinder was plotted versus the flow velocity. In this section, a typical bifurcation diagram with the axial displacement versus the flow velocity is presented and also the assumption of the second-order axial displacement being $u=O(\epsilon^2)$ and the first order transverse displacement being $v=O(\epsilon)$ is investigated. Also, the importance of the extensibility of the centreline for both-ends-supported cylinders is examined. In the derivation of the equations of motion in Chapter 2, it is assumed that the cylinder centreline is extensible, i.e., the axial strain along the centreline, ε, is not negligible. On the other hand, the inextensible model of Lopes et al. (2002) assumes $\varepsilon=0$ for a cantilevered cylinder, which is acceptable for that case. The axial strain along the centreline of a cylinder can be found by using Equation (2-4).

The transverse (v) and the axial displacements (u) of the cylinder at ξ = 0.8 (80 percent of the length from the upstream end) versus the flow velocity are shown in Figure 5-26(a,b). The transverse displacement behaves similarly to q_1 in Figure 5-2, as expected. The axial displacement, which is zero before the onset of buckling, becomes negative for the flow velocities immediately after the critical flow for the pitchfork

---

* Of course, this study can be conducted for any boundary condition.

bifurcation, indicating that this point of the cylinder moves upwards to accommodate the lateral deflection. With increasing flow, the axial displacement vanishes, and then increases exponentially (compared to the transverse displacement, which increases parabolically). It is observed that for all flow velocities, $v = O(0.01)$, while $u = O(0.001)$, which is in agreement with the assumption made in the derivation of the model: the axial displacement is one order of magnitude smaller than the transverse displacement. Figure 5-27(a) shows the cylinder axial displacement along its length at $\mathcal{U} = 15$. It is observed that the axial displacement is a fourth-mode (string-mode): on the upper half of the cylinder, it has a maximum at $\xi \simeq 0.18$ and becomes zero at $\xi \simeq 0.4$, but no negative axial displacement is observed in the upper half, which is physically correct: the upper half of a vertical cylinder subjected to downward flow stretches downwards. The maximum axial displacement occurs at $\xi \simeq 0.65$, which is almost equivalent to the point of maximum total displacement (see Figure 5-7(a)). For $\xi > 0.82$, the axial displacement becomes negative indicating an upward motion for this part of the cylinder.

Figure 5-26(c) shows the axial strain of the cylinder in its buckled state at $\xi = 0.8$ versus the flow velocity. It is observed that the axial strain increases from zero at $\mathcal{U} = \mathcal{U}_{\mathrm{BP}}$, to its maximum ($\varepsilon = 0.06$) before the onset of oscillatory motions. This is the maximum strain at this particular point on the cylinder. Figure 5-27(b) shows the axial strain along the cylinder length at $\mathcal{U} = 15$. The strain changes in a sinusoidal pattern (with twice the number of spatial cycles as u), and its maximum ($\varepsilon = 0.031$) at this flow occurs on the lower part of the cylinder, at $\xi \simeq 0.78$. It has been found that the maximum strain in the cylinder at $\mathcal{U} \simeq 21.6$, right before the onset of periodic oscillations, is $\varepsilon \simeq 0.083$, occurring at $\xi \simeq 0.82$. It can be concluded that in general, for the both-ends-supported cylinders in axial flow, the axial strains, though small, are not negligible and therefore one cannot use the equations based on the inextensibility assumption to accurately predict the dynamics of such systems. However, for particular cases where $\varepsilon \simeq 0.1$ is deemed to be negligible, the inextensibility assumption can be used.

5.6. Summary

In this chapter, the nonlinear behaviour of a slender flexible cylinder with various boundary conditions (clamped-clamped, clamped-hinged and hinged-clamped) and subjected to axial flow was studied. The general equations of motion presented in Chapter 2 were used as the governing equations and the numerical and analytical methods discussed in Chapter 3 were used to analyse the system.

For all the boundary conditions, it was found that the system behaviour is qualitatively similar to that of a simply supported cylinder. The system is stable at low flow velocities until the critical flow for divergence, at which point the initial equilibrium position of the cylinder becomes unstable, giving rise to a new stable buckled solution. The amplitude of the buckled solution increases with flow velocity. At higher flow, the stationary buckled cylinder loses stability by a Hopf bifurcation, followed by periodic oscillations, which are destabilized at higher flow by a period-doubling bifurcation, giving rise to period-2 oscillations. A torus bifurcation occurs thereafter, followed by quasiperiodic and chaotic oscillations at higher flow velocities, showing a quasiperiodic route to chaos.

In the case of a simply supported cylinder (discussed in Chapter 4), at still higher flow velocities, there is a range of flow velocities in which chaotic and static solutions co-exist. This new nonzero static solution itself loses stability by a Hopf bifurcation and the resulting high-frequency periodic oscillation becomes unstable by a torus bifurcation at higher flow giving rise to quasiperiodic oscillations. The co-existence of chaotic and static solutions is not observed for clamped-clamped, clamped-hinged and hinged-clamped cylinders (at least for the parameters used in these calculations). However, to find these co-existing solutions one must try many different initial conditions in the FDM program. Such a comprehensive search was not conducted but, for the initial conditions considered here, a co-existing static solution was not obtained.

It was found that the frequency of oscillations at the Hopf bifurcation point, in the case of a simply supported or a clamped-hinged cylinder is almost twice as high as the frequency of oscillations for the other two cases. This is due to the fact that, where high frequency oscillations are observed, the third mode of the system becomes dynamically unstable (the real part of the corresponding eigenvalue becomes zero) at the Hopf bifurcation point, and the cylinder undergoes mainly third-mode oscillations (with two nodes in the spatial shapes). On the other hand, for a clamped-clamped or a hinged-clamped cylinder, the cylinder loses stability in its second mode, even though the form of these oscillations around the buckled solution is mainly of third-beam-mode shape. One can conclude from this discussion that, for a cylinder with fixed physical parameters, the downstream boundary condition plays a key role in high- or low-frequency oscillations: a hinged lower support results in high-frequency oscillations, while a clamped lower end results in low-frequency oscillations.

A summary of the critical flow velocities for the cylinder with the physical properties of Table 5-2 for various boundary conditions together with the corresponding frequency at the Hopf bifurcation point are given in Table 5-6. In general, the critical flow velocities for the simply supported cylinders are smaller than those for the clamped-hinged cylinders, which themselves are smaller than those for the hinged-clamped cylinders. [The reason for $\mathcal{U}_{\mathrm{BP}}$ being lower for clamped-hinged than for hinged-clamped cylinders is that the lower half in the former case, which is subjected to compression (weakening the flexural restoring force), is also close to a point where free rotation is permitted.] There is, however, one exception: the Hopf bifurcation (first dynamic instability) for the clamped-hinged cylinder occurs at lower flow velocity than for a simply supported cylinder. This could be related to differences in the divergence-induced tension in the two cases. In general, clamped-clamped and simply supported boundary conditions are, respectively, the most and the least stable boundary conditions.

Although the critical flow velocity for the pitchfork bifurcation for the clamped-clamped cylinder is larger than that for a hinged-clamped cylinder, the critical flow velocity for dynamic instabilities (Hopf bifurcation, period doubling and torus) in these two cases are almost the same. This implies that the hinged-clamped cylinder remains buckled for a wider range of flow velocities compared to the clamped-clamped cylinder and loses stability by a Hopf bifurcation at almost the same flow velocity as the clamped-clamped cylinder.

Figure 5-28(a) shows the bifurcation diagrams of a cylinder with various boundary conditions in the range of static deflection only. In these diagrams, the maximum nondimensional midpoint displacement of the cylinder is plotted versus the nondimensional flow velocity. The simply supported cylinder buckles at a lowest flow velocity, and at any given flow velocity its amplitude is larger than that of the other three boundary conditions for $\mathcal{U} < 17$. It ought to be noted that the maximum midpoint displacement is not representative for the maximum displacement of the cylinder. As can be observed in Figure 5-28(b), where the spatial shape of the buckled state of a cylinder with various boundary conditions are shown at $\mathcal{U} = \mathcal{U}_{\text{HB}} - 1$, the maximum transverse amplitude for the cases with the hinged lower end is lower than that for the cases of clamped lower end. Therefore, what we observe in Figure 5-28(a) is not the maximum transverse displacement. It is interesting to notice that, again, the boundary condition at the lower end is responsible for the difference in the system behaviour (the place of the maximum transverse displacement), similar to the difference in the frequency of oscillations, due to the different lower-end boundary.

A convergence test showed that, except for the case of a hinged-clamped cylinder, where one has to use at least 8 modes in each direction to obtain reliable results, in the other cases, 6 modes in each direction are sufficient.

The analytical centre manifold theory was used to study the behaviour of the cylinder in the vicinity of the first point of instability for all the boundary conditions. In all cases, a supercritical pitchfork bifurcation is found using the centre manifold theory, in qualitative agreement with the numerical methods. Also, the amplitude of the buckled state in this neighbourhood was found by the centre manifold method and very good quantitative agreement with the numerical results was obtained.

Boundary conditions	Eigenfunctions		Eigenvalues
Clamped-clamped	$\phi_j(\xi)=\cosh(\lambda_j\xi)-\cos(\lambda_j\xi)$ $+\beta_j\left[\sinh(\lambda_j\xi)-\sin(\lambda_j\xi)\right]$	$\beta_j=-\dfrac{\cos\lambda_j-\cosh\lambda_j}{\sin\lambda_j-\sinh\lambda_j}$	$\lambda_1=4.730040744862704$ $\lambda_2=7.853204624095838$ $\lambda_3=10.99560783800167$ $\lambda_4=14.13716549125746$ $\lambda_5=17.27875965739948$ $\lambda_j=(2j+1)\pi/2$
Clamped-hinged	$\phi_j(\xi)=\cosh(\lambda_j\xi)-\cos(\lambda_j\xi)$ $-\beta_j\left[\sinh(\lambda_j\xi)-\sin(\lambda_j\xi)\right]$	$\beta_j=\cot\lambda_j$	$\lambda_1=3.926602312047919$ $\lambda_2=7.068582745628732$ $\lambda_3=10.21017612281303$ $\lambda_4=13.35176877775409$ $\lambda_5=16.49336143134641$ $\lambda_j=(4j+1)\pi/4$
Hinged-clamped	$\phi_j(\xi)=\sin(\lambda_j\xi)+\beta_j\sinh(\lambda_j\xi)$	$\beta_j=-\dfrac{\sin\lambda_j}{\sinh\lambda_j}$	$\lambda_1=3.926602312047919$ $\lambda_2=7.068582745628732$ $\lambda_3=10.21017612281303$ $\lambda_4=13.35176877775409$ $\lambda_5=16.49336143134641$ $\lambda_j=(4j+1)\pi/4$
Bar	$\psi_j(\xi)=\sqrt{2}\sin(\lambda_j\xi),$	-	$\lambda_j=j\pi$

Table 5-1 Eigenfunctions and eigenvalues of a dry beam with various boundary conditions for the transverse deformation and those of a bar with both ends fixed, used as comparison functions in the Galerkin discretization

Dimensional parameters		Nondimensional parameters	
L (m)	0.52	Π_0	6707
D (m)	0.0254	ε	20.47
ρ $\left(\text{kg/m}^3\right)$	1000	β	0.47
m $\left(\text{kg/m}\right)$	0.5817	γ	1.83
E $\left(\text{Pa}\right)$	2.76×10^6	χ	1
$\bar{P}$	0	$\bar{\Pi}$	0
$\bar{T}$	0	$\bar{\Gamma}$	0
		c_n	0.025
		c_t	0.025
		c_d	0
		δ	1
		c_b	0

Table 5-2 Dimensional and nondimensional parameters of the cylinder subjected to axial flow

Number of modes	BP	HB	PD	TR
2-2	6.35	22.67	>40	>40
3-3	6.26	20.12	29.60	30.12
4-4	6.26	39.12	>40	>40
5-5	6.25	23.29	25.29	25.51
6-6	6.25	21.60	21.92	22.03
7-7	6.25	22.02	22.60	22.63
8-8	6.25	20.95	Not calculated	Not calculated
9-9	6.25	21.31	Not calculated	Not calculated
10-10	6.25	21.71	Not calculated	Not calculated
11-11	6.25	22.45	Not calculated	Not calculated

Table 5-3 Critical flow velocities for a clamped-clamped cylinder with the physical parameters of Table 5-2 using different numbers of modes. BP: pitchfork bifurcation; HP: Hopf bifurcation; PD: period doubling; TR: torus

Number of modes	BP	HB	PD	TR
2-2	4.38	20.00	25.60	26.60
3-3	4.37	18.47	19.32	23.58
4-4	4.37	16.51	17.99	21.43
5-5	4.37	19.10	-	19.28
6-6	4.37	17.60	18.76	19.13
7-7	4.37	18.27	Not calculated	Not calculated
8-8	4.37	17.87	Not calculated	Not calculated

Table 5-4 Critical flow velocities for a clamped-hinged cylinder with the physical parameters of Table 5-2 using different numbers of modes. BP: pitchfork bifurcation; HP: Hopf bifurcation; PD: period doubling; TR: torus

Number of modes	BP	HB	PD	TR
2-2	4.62	38.80	-	39.12
3-3	4.61	33.33	-	34.14
4-4	4.61	29.87	-	32.28
5-5	4.61	26.77	-	27.61
6-6	4.61	25.61	-	28.05
7-7	4.61	22.39	-	23.85
8-8	4.61	21.23	-	22.93
9-9	4.61	21.11	22.49	22.75

Table 5-5 Critical flow velocities for a hinged-clamped cylinder with the physical parameters of Table 5-2 using different numbers of modes. BP: pitchfork bifurcation; HP: Hopf bifurcation; PD: period doubling; TR: torus

	BP	HB	Frequency at the HB	PD	TR
Simply supported	3.14	17.68	19.4	17.96	18.01
Clamped-hinged	4.37	17.6	22.0	18.76	19.13
Hinged-clamped	4.61	21.23	8.7	22.49	22.93
Clamped-clamped	6.25	21.60	10.8	21.92	22.03

Table 5-6 Critical flow velocities and frequencies at the Hopf bifurcation point for the cylinder of Table 5-2 subjected to axial flow, with various boundary conditions. BP: pitchfork bifurcation; HP: Hopf bifurcation; PD: period doubling; TR: torus

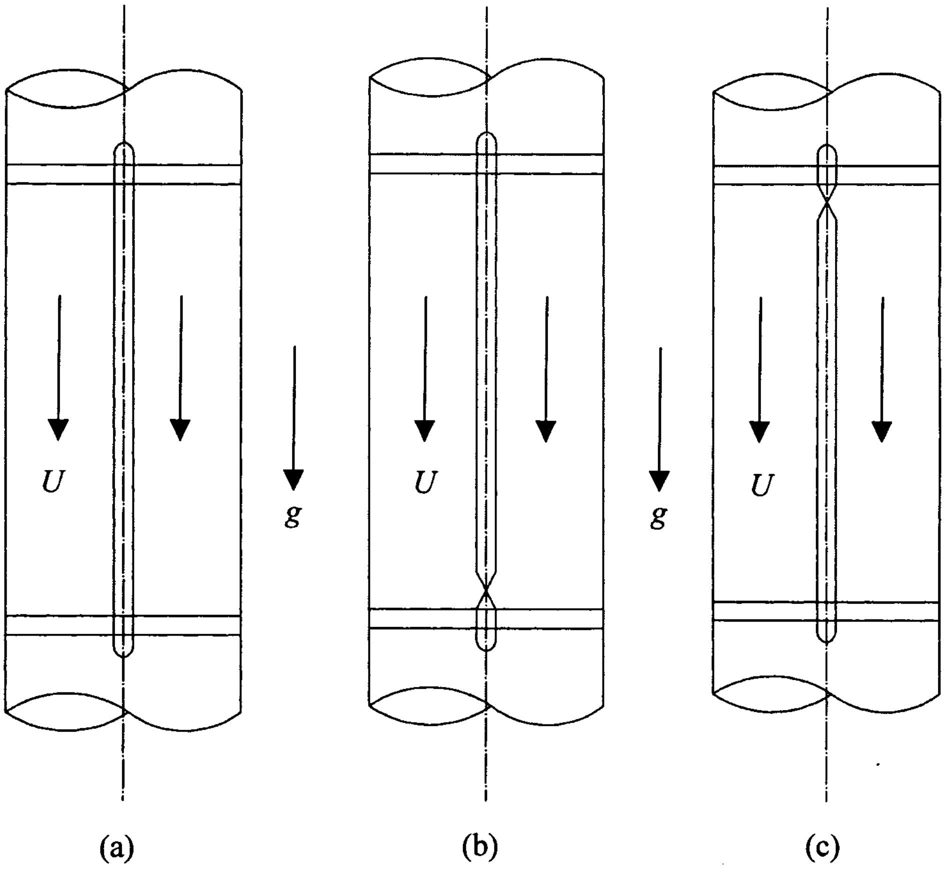

Figure 5-1 A vertical slender flexible cylinder with various boundary conditions subjected to axial flow: (a) clamped-clamped, (b) clamped-hinged, and (c) hinged-clamped boundary conditions.

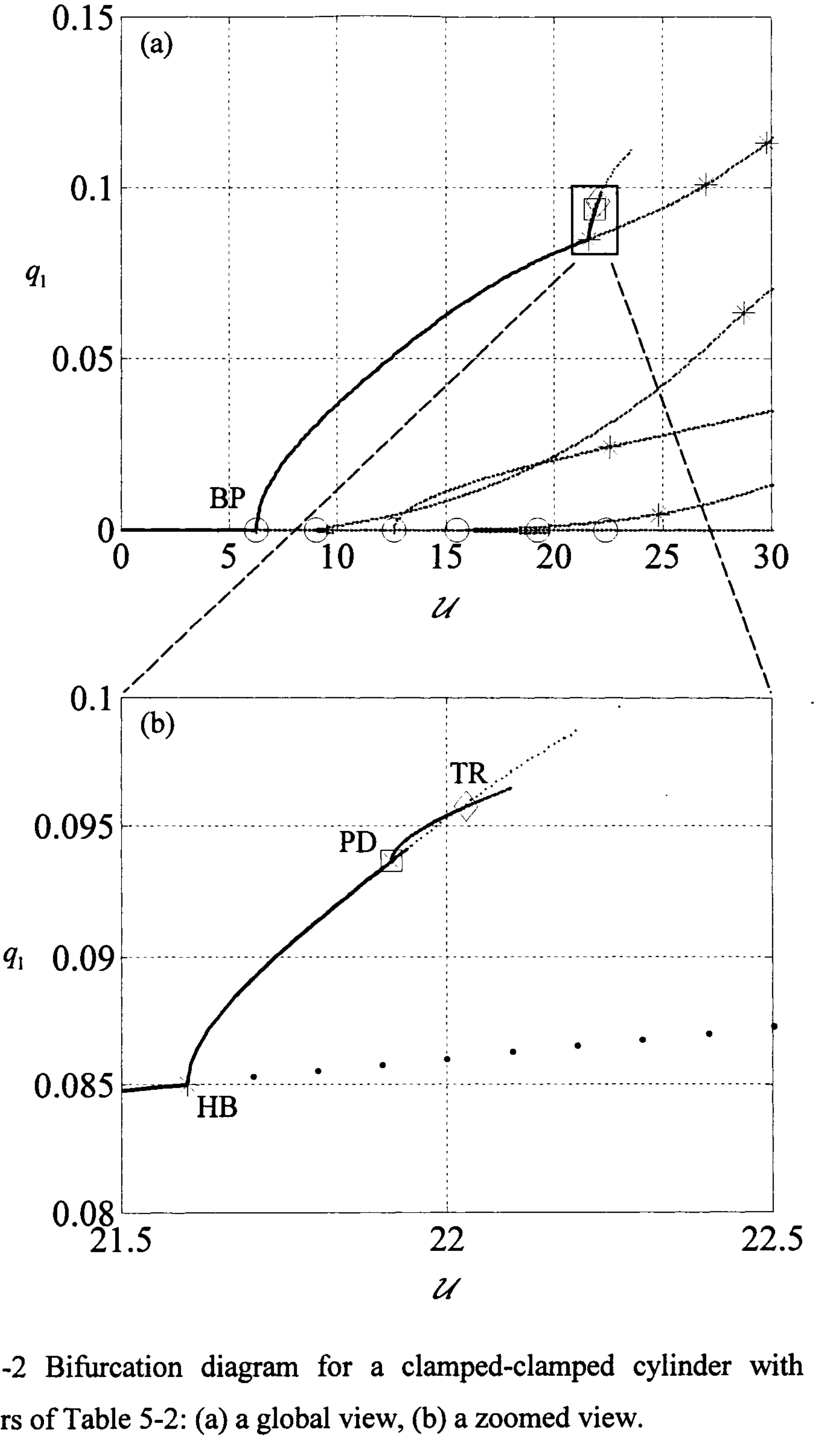

Figure 5-2 Bifurcation diagram for a clamped-clamped cylinder with the physical parameters of Table 5-2: (a) a global view, (b) a zoomed view.

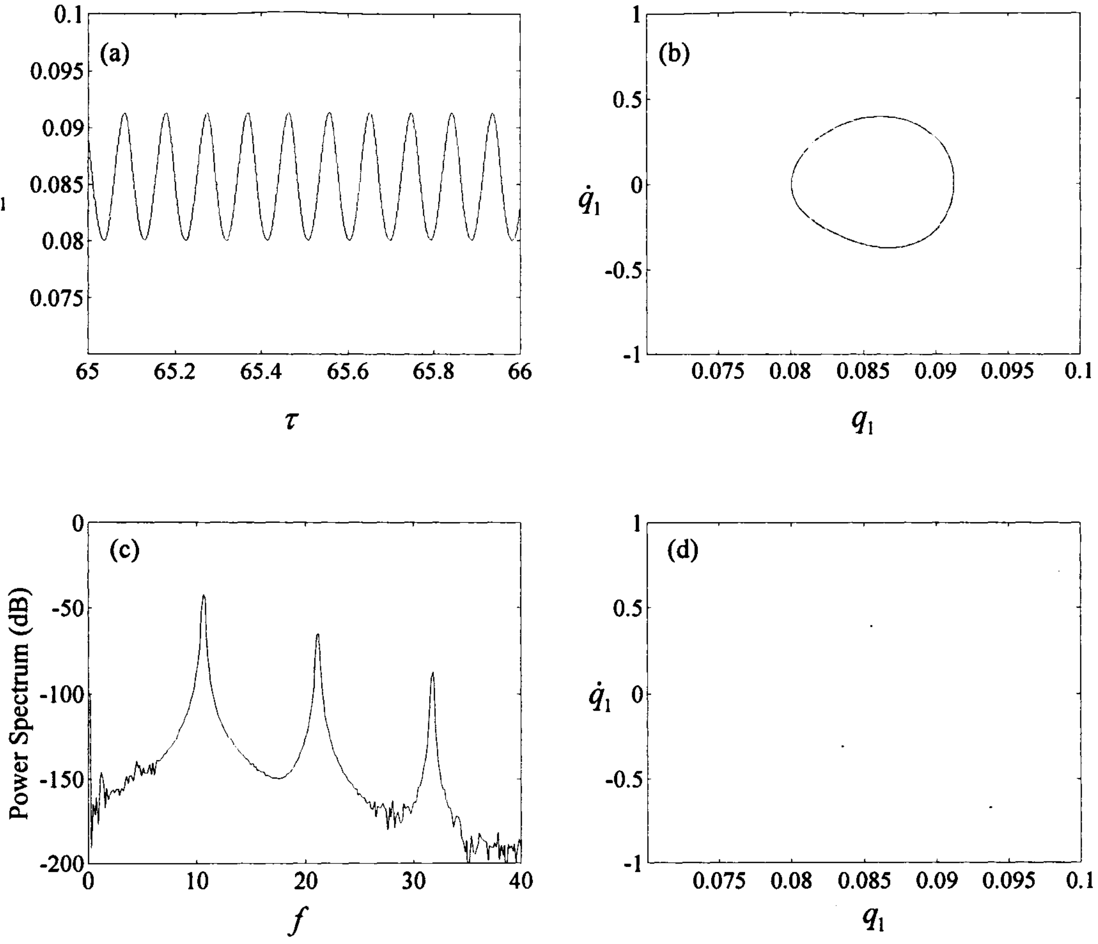

Figure 5-3 (a) Time history, (b) phase plane plot, (c) power spectral density plot and (d) Poincaré map for the system of Figure 5-2 (clamped-clamped cylinder) for $\mathcal{U} = 21.8$, obtained with $N_u = N_v = 6$ (periodic oscillation).

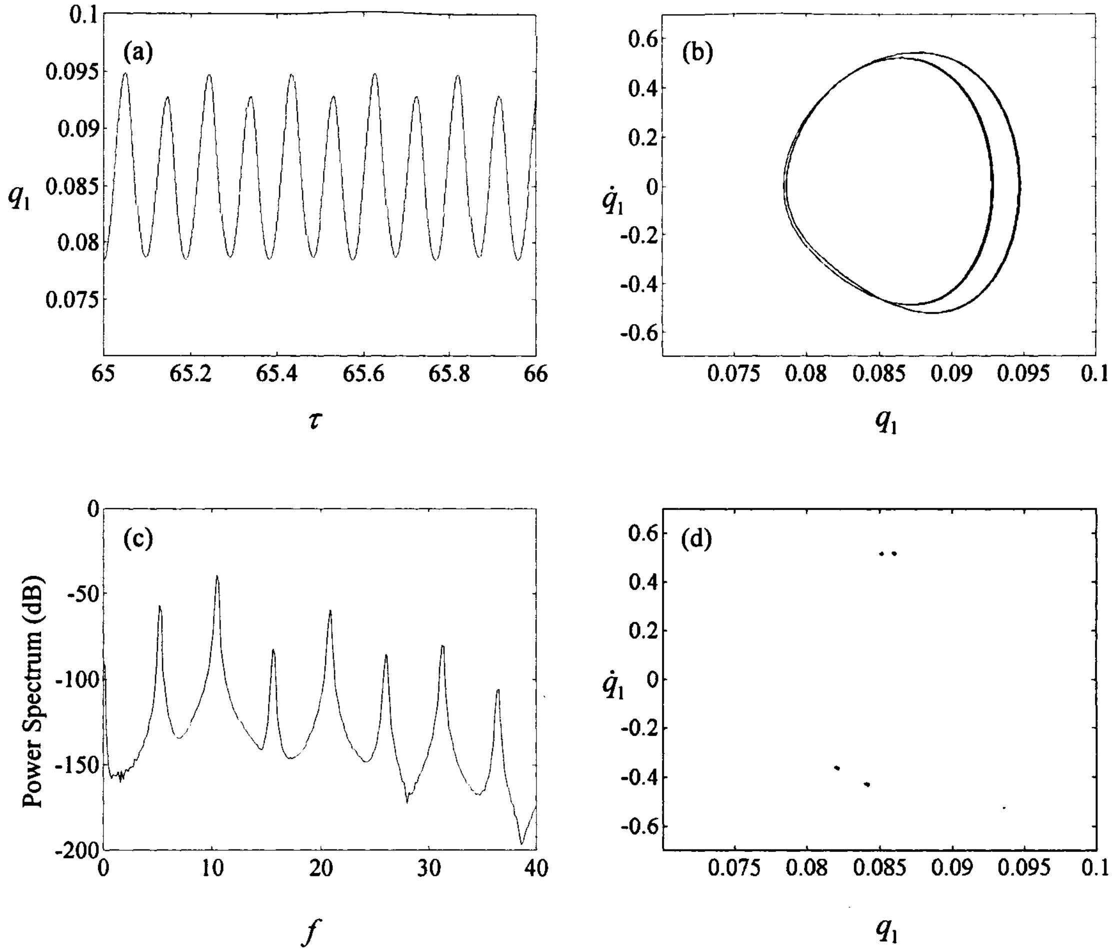

Figure 5-4 (a) Time history, (b) phase plane plot, (c) power spectral density plot and (d) Poincaré map for the system of Figure 5-2 (clamped-clamped cylinder) for $\mathcal{U} = 21.95$, obtained with $N_u = N_v = 6$ (period-2 oscillation).

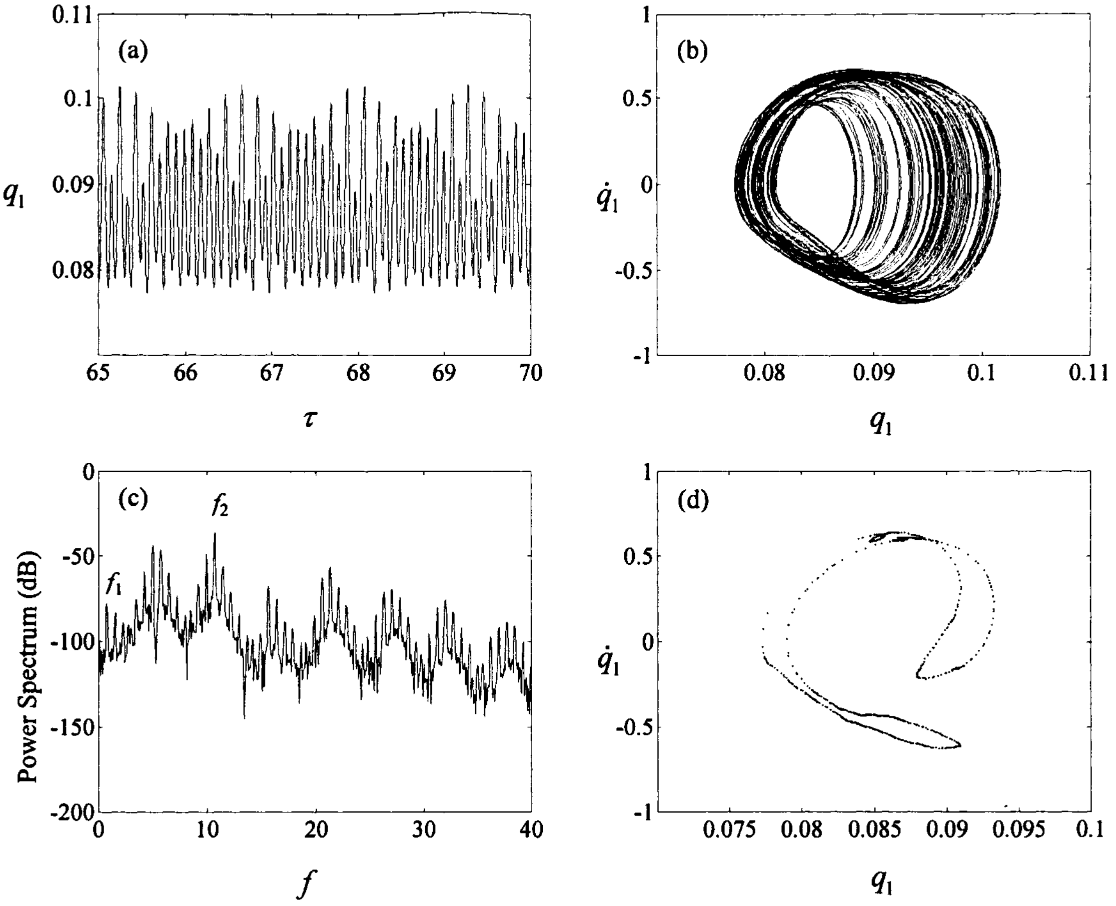

Figure 5-5 (a) Time history, (b) phase plane plot, (c) power spectral density plot and (d) Poincaré map for the system of Figure 5-2 (clamped-clamped cylinder) for $\mathcal{U} = 22.5$, obtained with $N_u = N_v = 6$ (quasiperiodic oscillation).

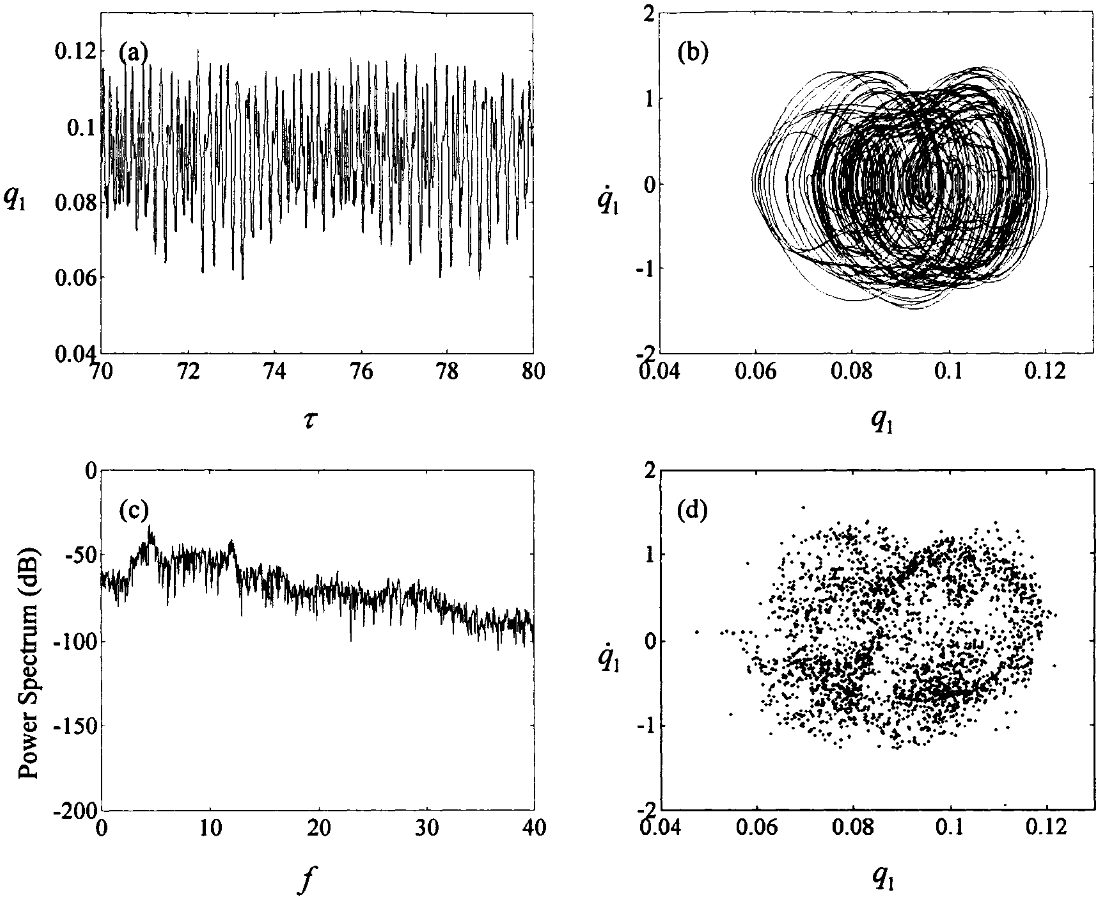

Figure 5-6 (a) Time history, (b) phase plane plot, (c) power spectral density plot and (d) Poincaré map for the system of Figure 5-2 (clamped-clamped cylinder) for $\mathcal{U} = 25.0$, obtained with $N_u = N_v = 6$ (chaotic oscillation).

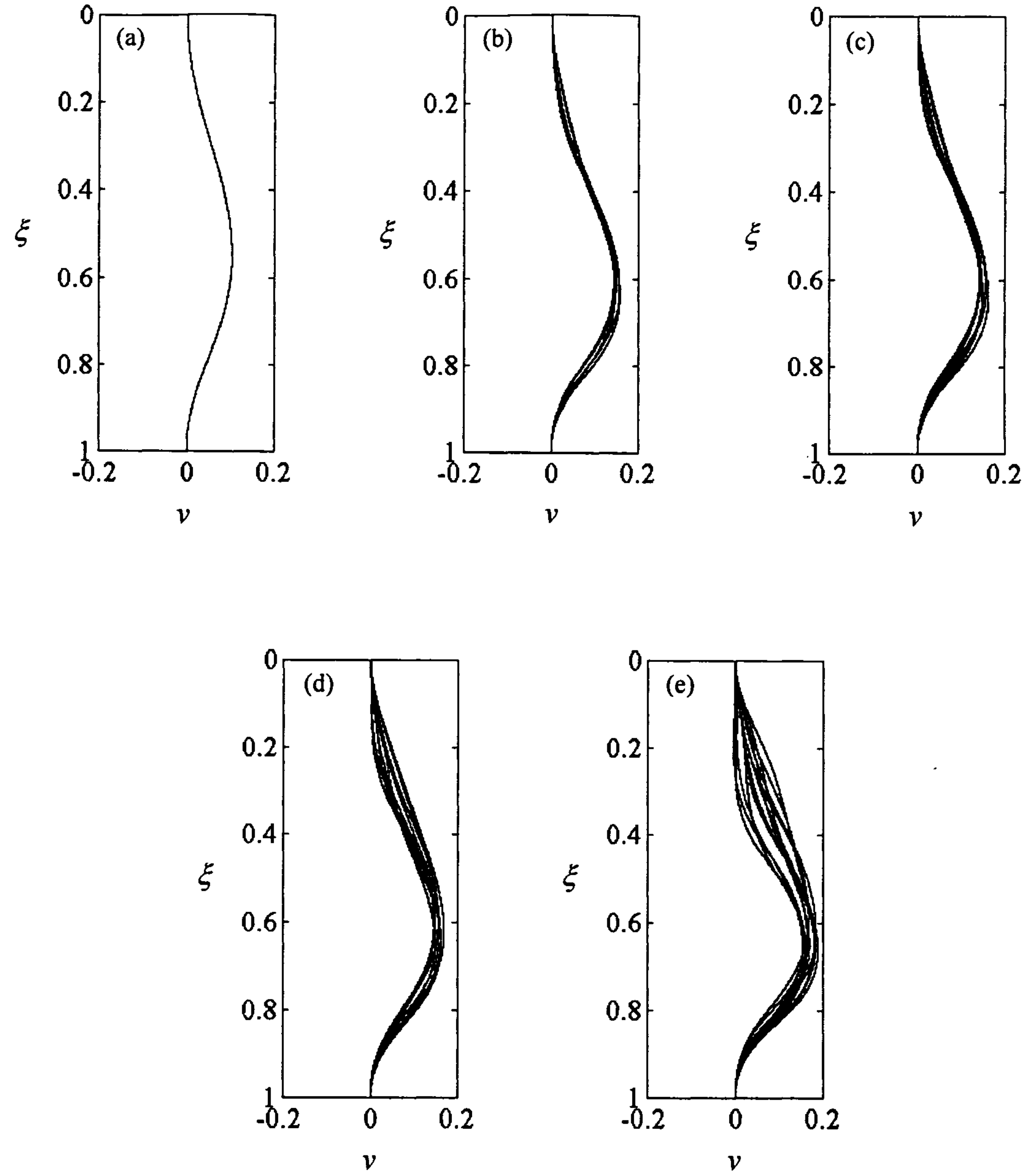

Figure 5-7 Spatial shape of the clamped-clamped cylinder of Figure 5-2(a) at different flow velocities: (a) $\mathcal{U}=15$, buckled position, (b) $\mathcal{U}=21.8$, periodic oscillation, (c) $\mathcal{U}=21.95$, period-2 oscillation and (d) $\mathcal{U}=22.5$, quasiperiodic oscillation, (e) $\mathcal{U}=25.0$, chaotic oscillation.

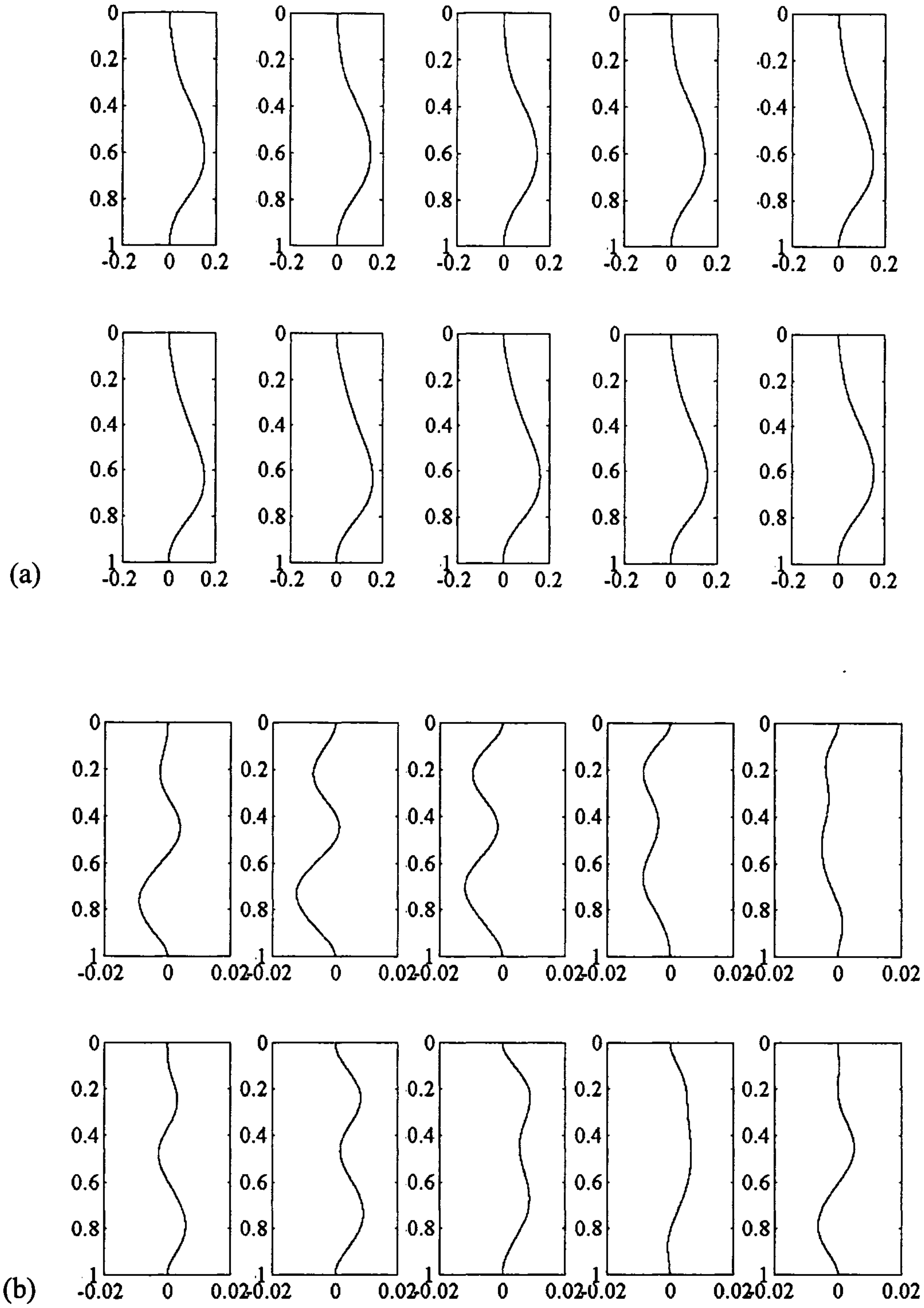

Figure 5-8 Oscillations of the clamped-clamped cylinder, plotted at every 1/10th of the period: (a) the total oscillations; (b) the oscillations around the buckled state.

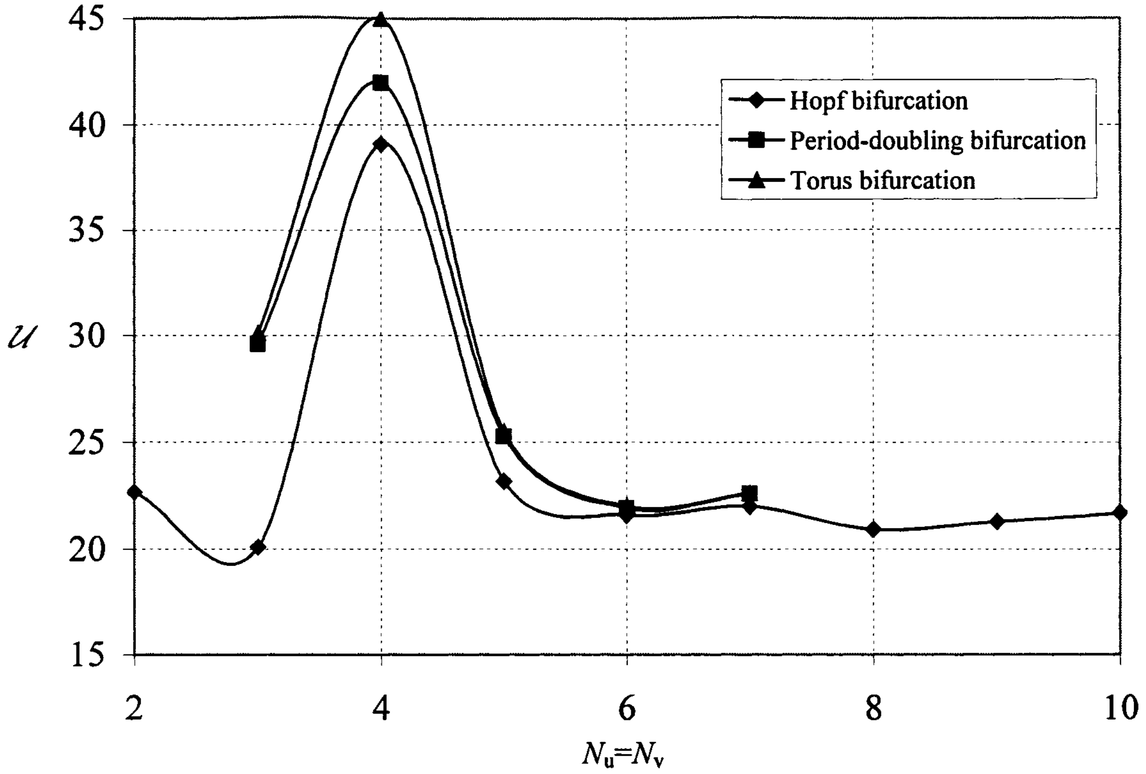

Figure 5-9 Critical values for the Hopf (HB), period-doubling (PD) and torus (TR) bifurcations of the clamped-clamped cylinder with the physical parameters of Table 5-2 versus the number of modes used in the calculations.

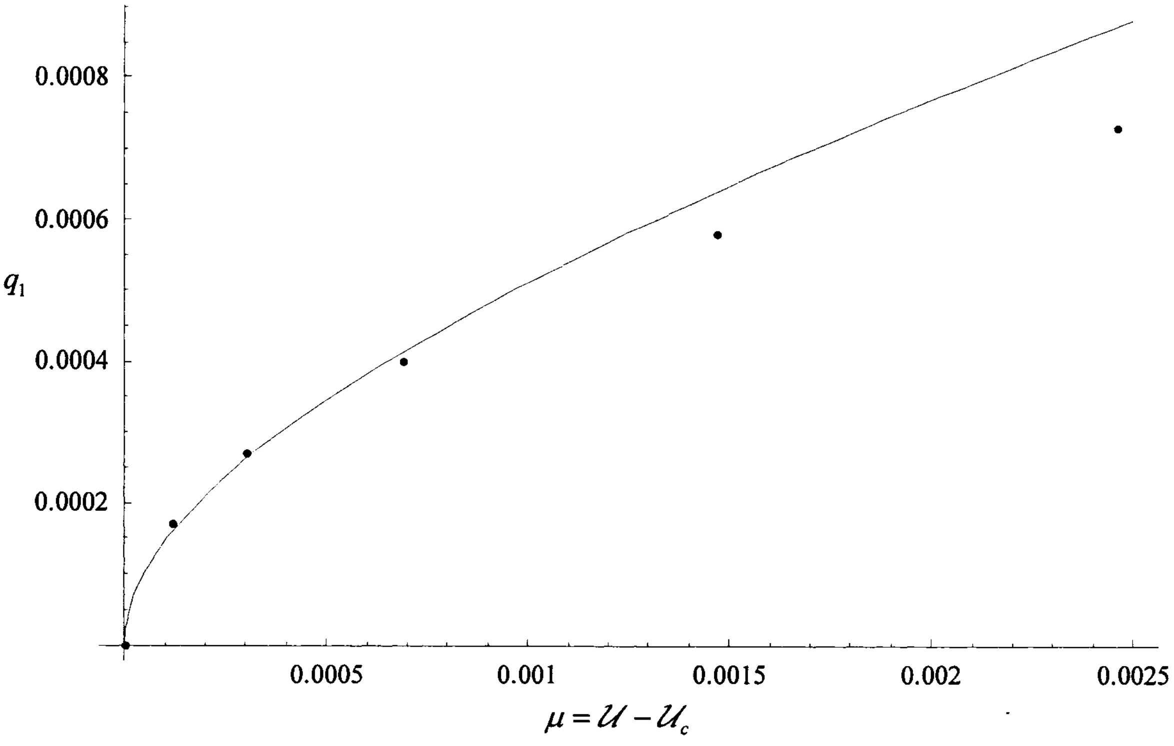

Figure 5-10 Bifurcation diagram for the clamped-clamped cylinder with the physical parameters of Table 5-2 in the vicinity of the pitchfork bifurcation point, obtained with $N_u = N_v = 1$ using centre manifold reduction (continuous line) and AUTO (dots).

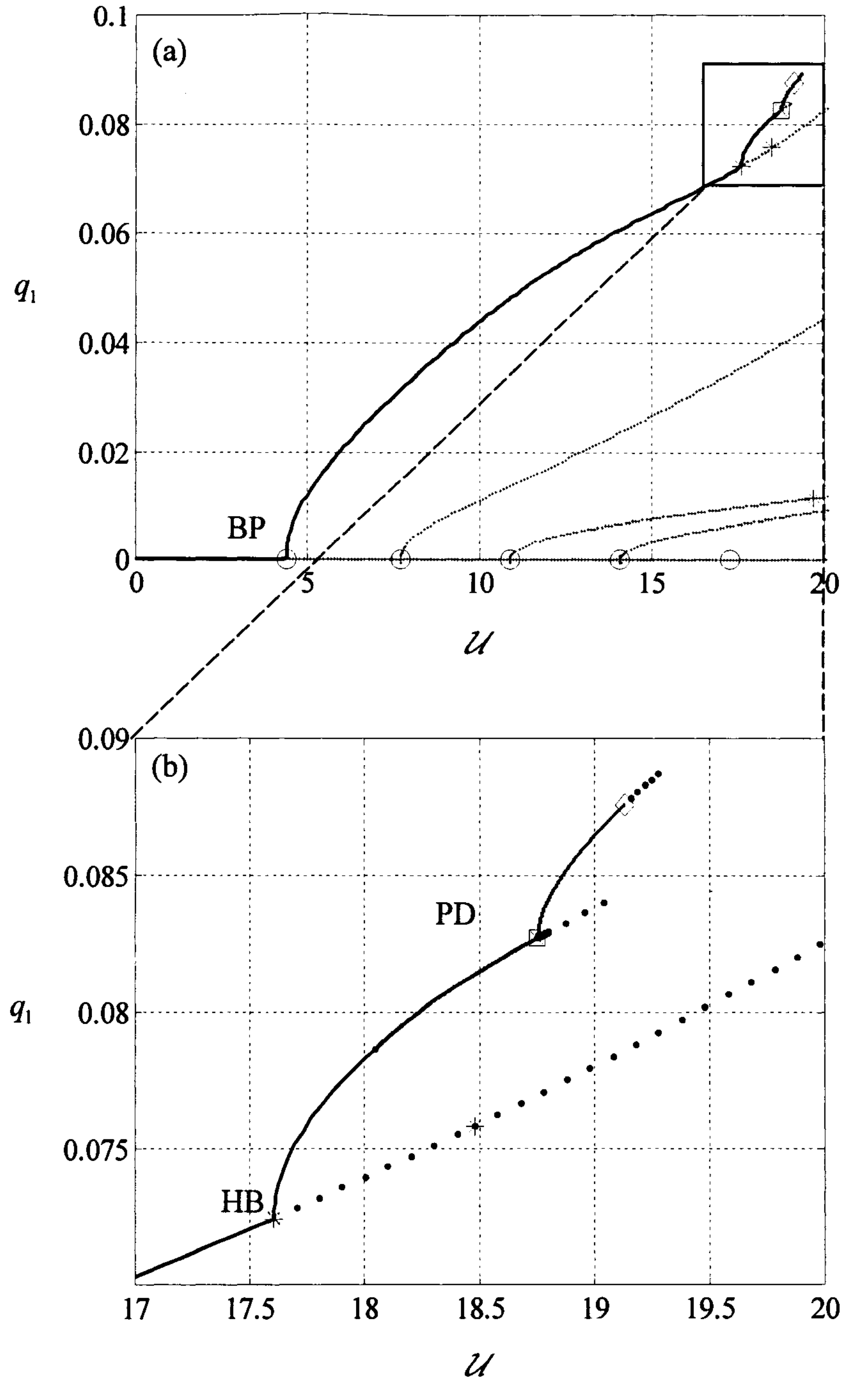

Figure 5-11 Bifurcation diagram for a clamped-hinged cylinder with the physical parameters of Table 5-2: (a) a global view, (b) a zoomed view.

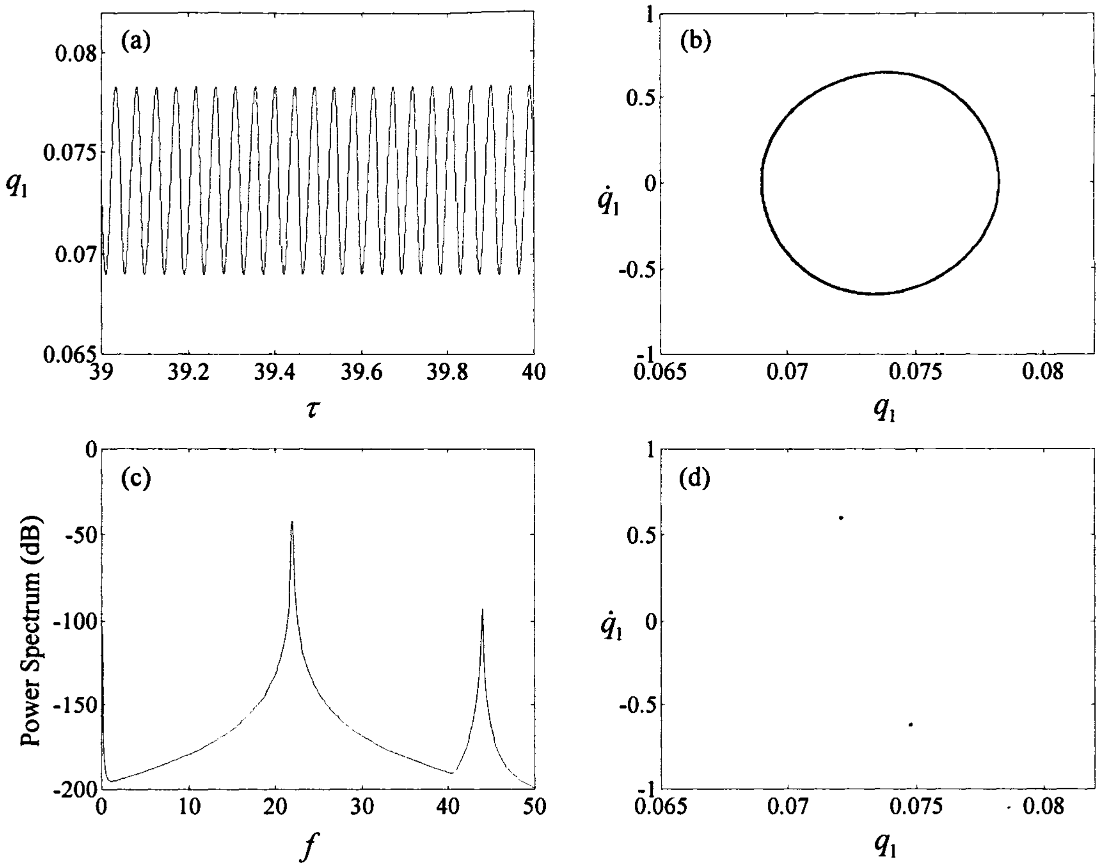

Figure 5-12 (a) Time history, (b) phase plane plot, (c) power spectral density plot and (d) Poincaré map for the system of Figure 5-11 (clamped-hinged cylinder) for $\mathcal{U}=18.0$, obtained with $N_u = N_v = 6$ (periodic oscillation).

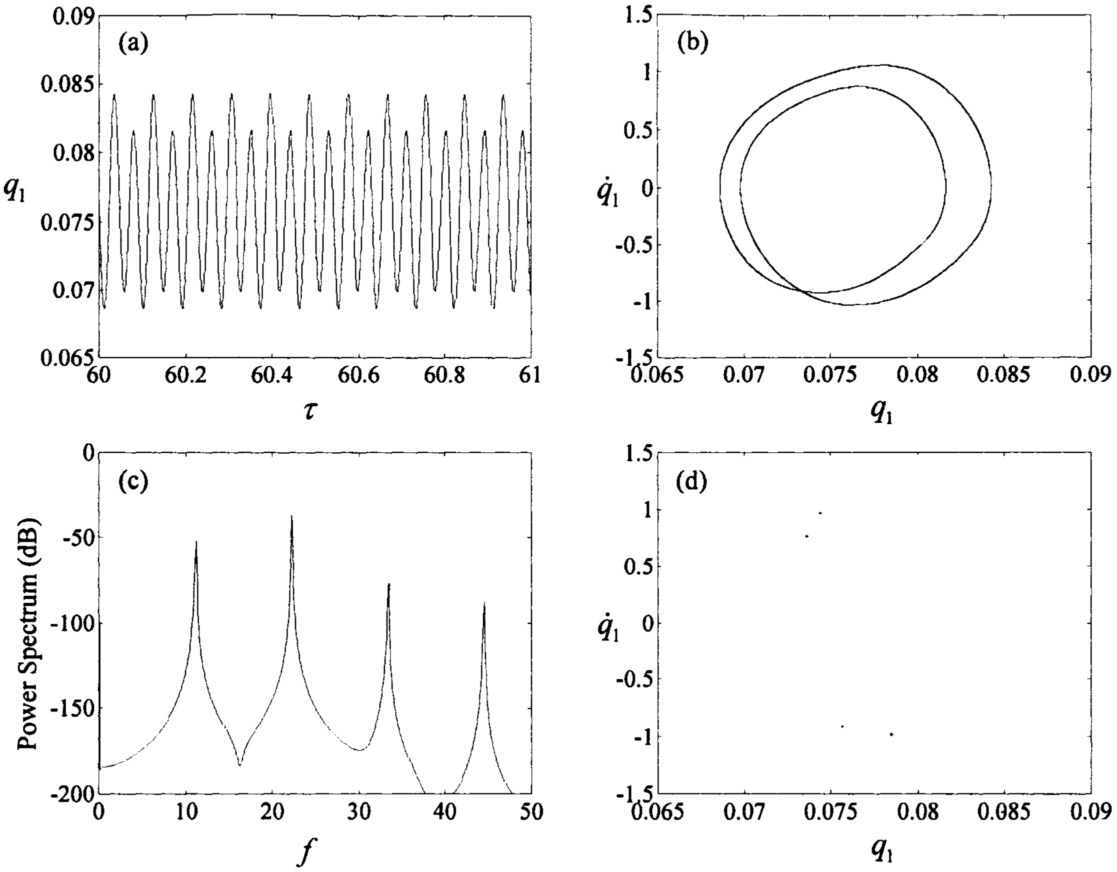

Figure 5-13 (a) Time history, (b) phase plane plot, (c) power spectral density plot and (d) Poincaré map for the system of Figure 5-11 (clamped-hinged cylinder) for $\mathcal{U}=18.8$, obtained with $N_u = N_v = 6$ (period-2 oscillation).

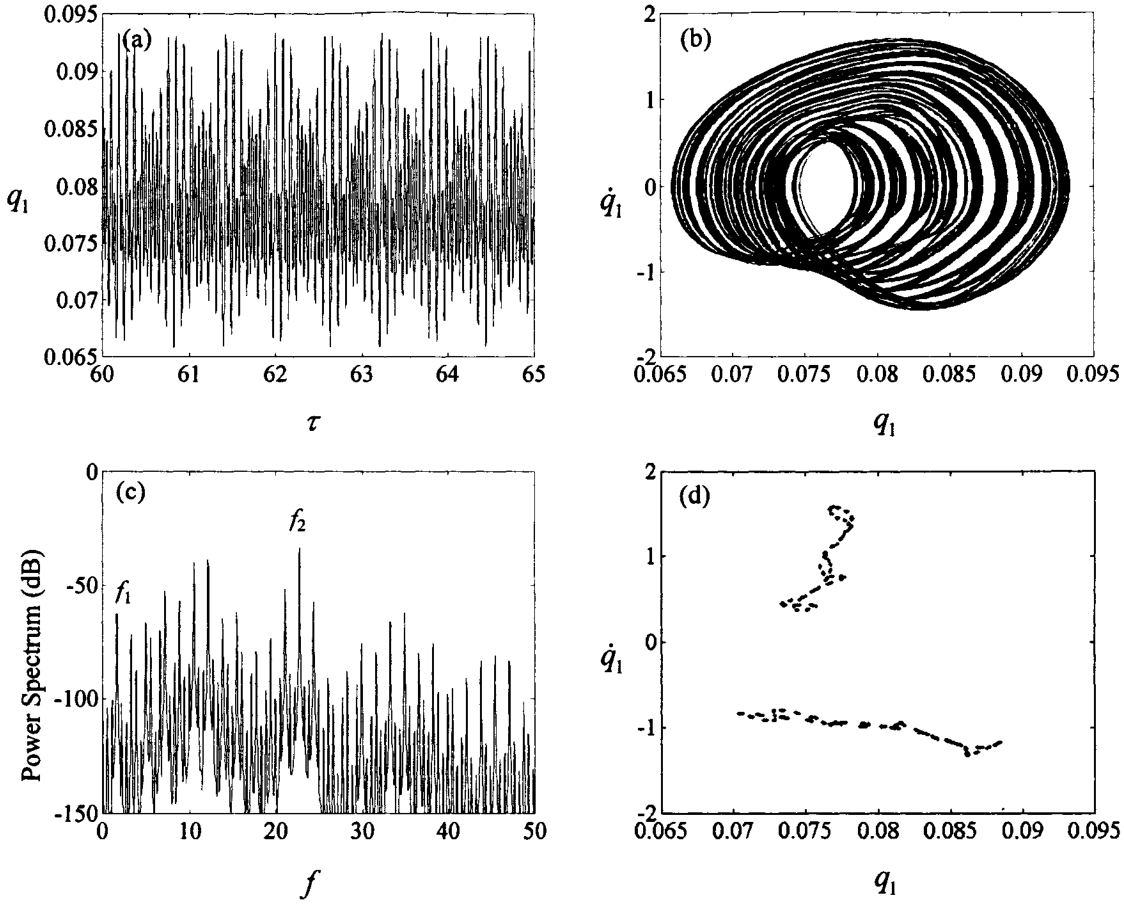

Figure 5-14 (a) Time history, (b) phase plane plot, (c) power spectral density plot and (d) Poincaré map for the system of Figure 5-11 (clamped-hinged cylinder) for $\mathcal{U}=19.5$, obtained with $N_u = N_v = 6$ (quasiperiodic oscillation).

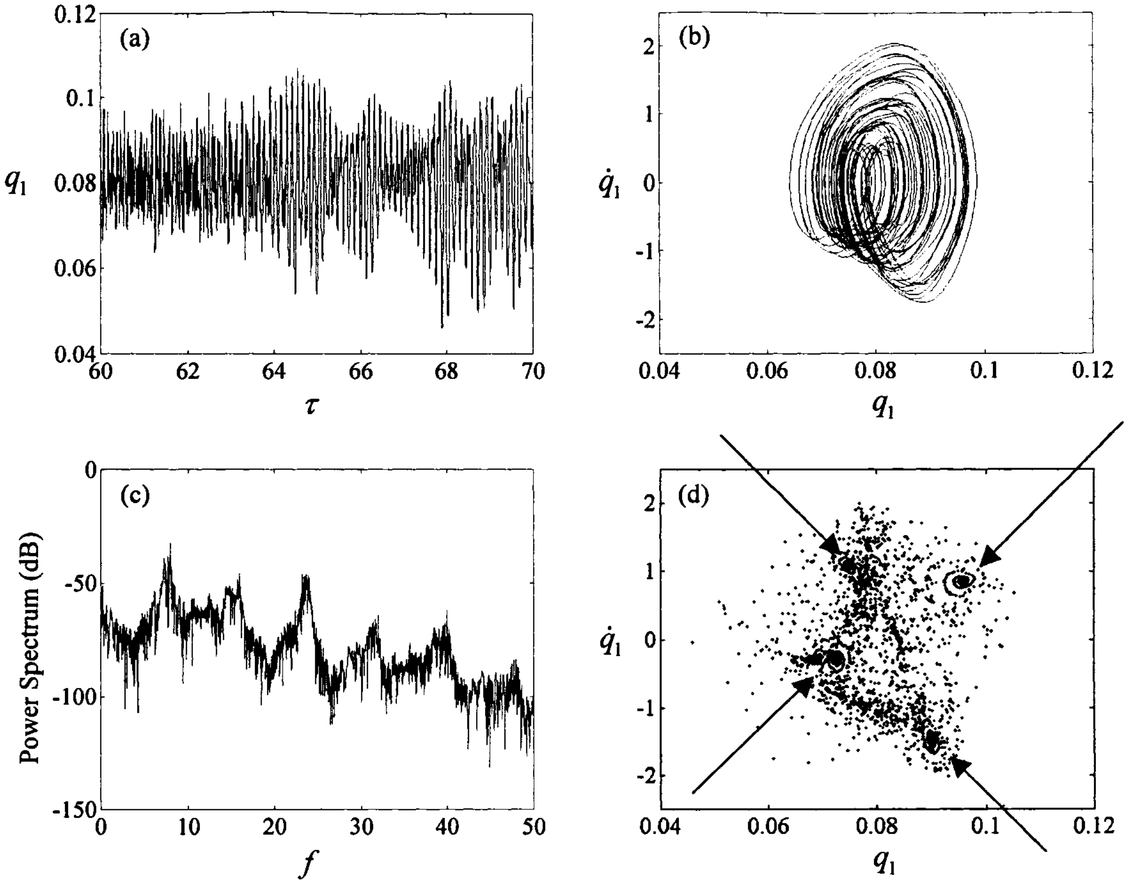

Figure 5-15 (a) Time history, (b) phase plane plot, (c) power spectral density plot and (d) Poincaré map for the system of Figure 5-11 (clamped-hinged cylinder) for $\mathcal{U} = 20.0$, obtained with $N_u = N_v = 6$ (chaotic oscillation).

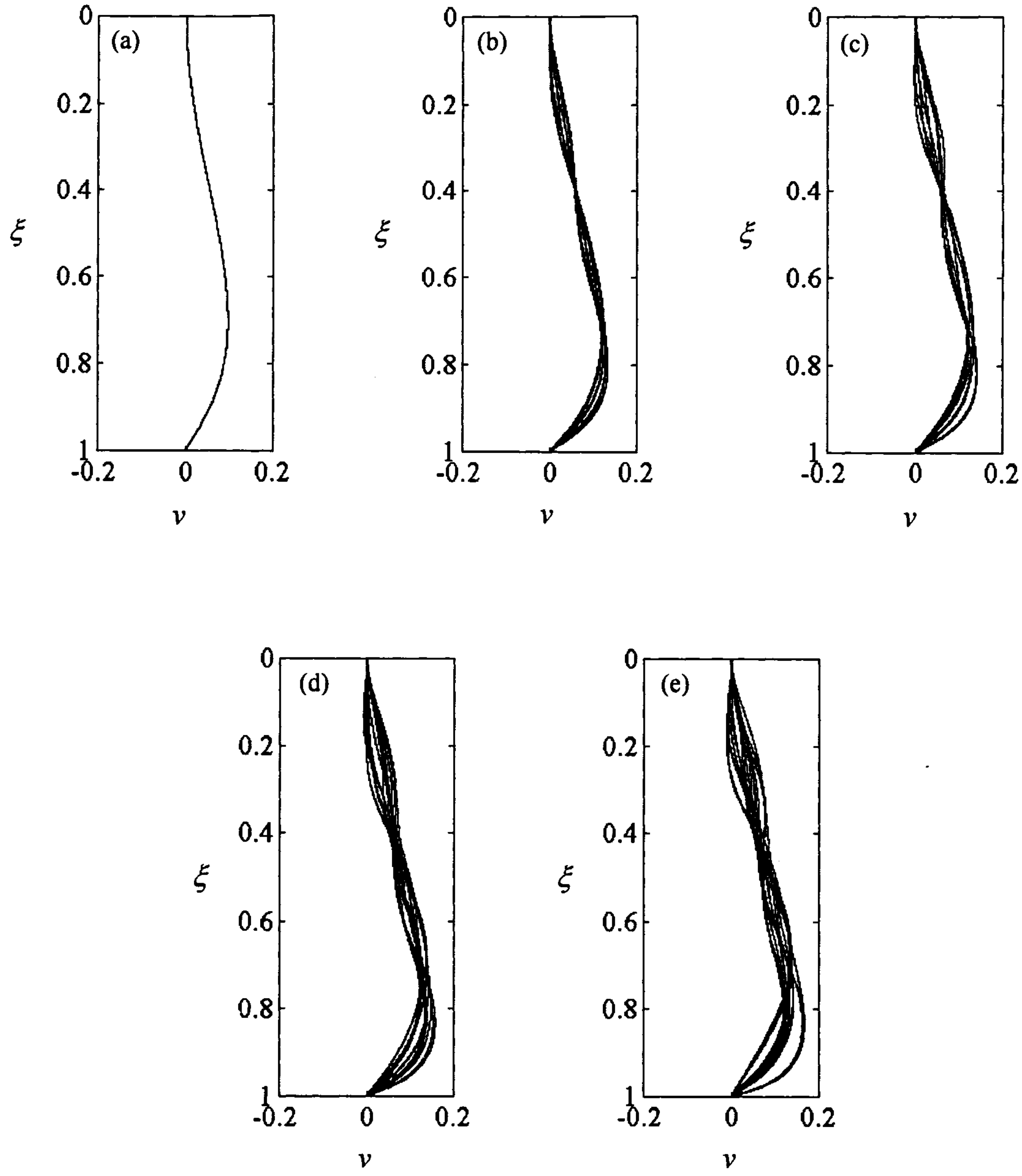

Figure 5-16 Spatial shape of the clamped-hinged cylinder at different flow velocities: (a) $\mathcal{U}$ =14.0, buckled position, (b) $\mathcal{U}$ =18.0, periodic oscillation, (c) $\mathcal{U}$ =18.8, period-2 oscillation and (d) $\mathcal{U}$ =19.5, quasiperiodic oscillation, (e) $\mathcal{U}$ =20.0, chaotic oscillation.

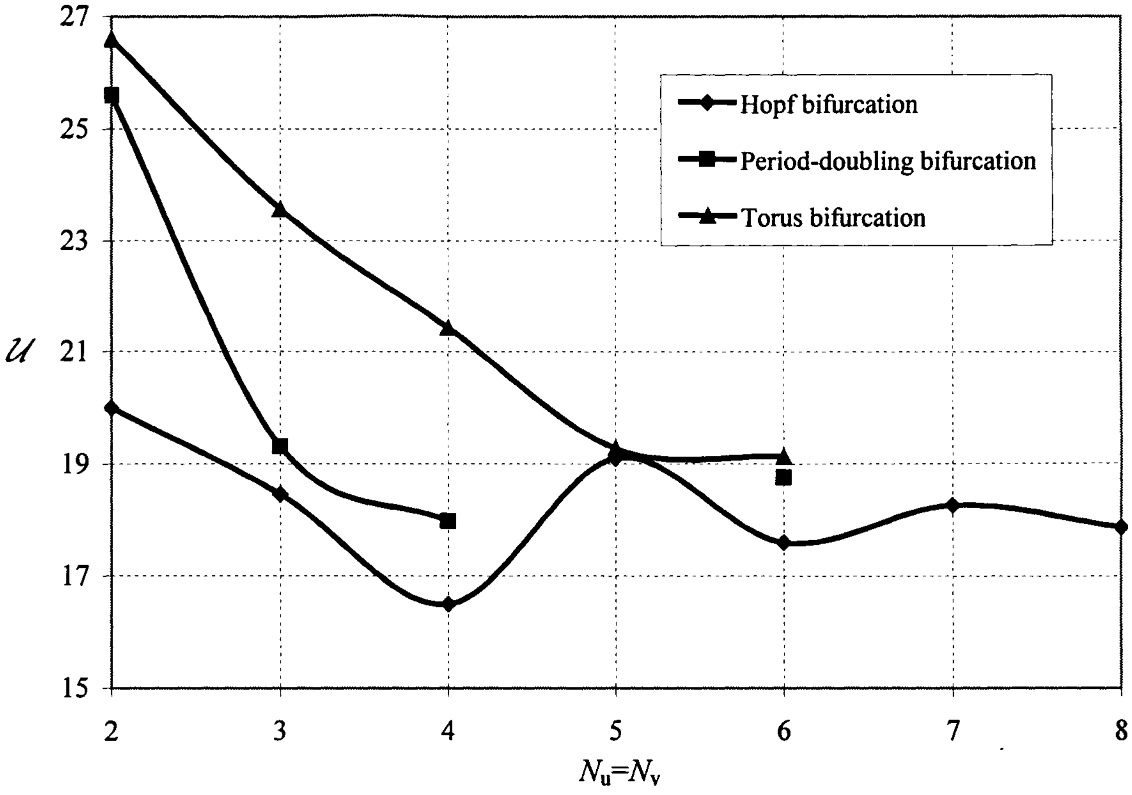

Figure 5-17 Critical values of $\mathcal{U}$ for the Hopf (HB), period-doubling (PD) and torus (TR) bifurcations of the clamped-hinged cylinder with the physical parameters of Table 5-2 versus the number of modes, $N_u=N_v$.

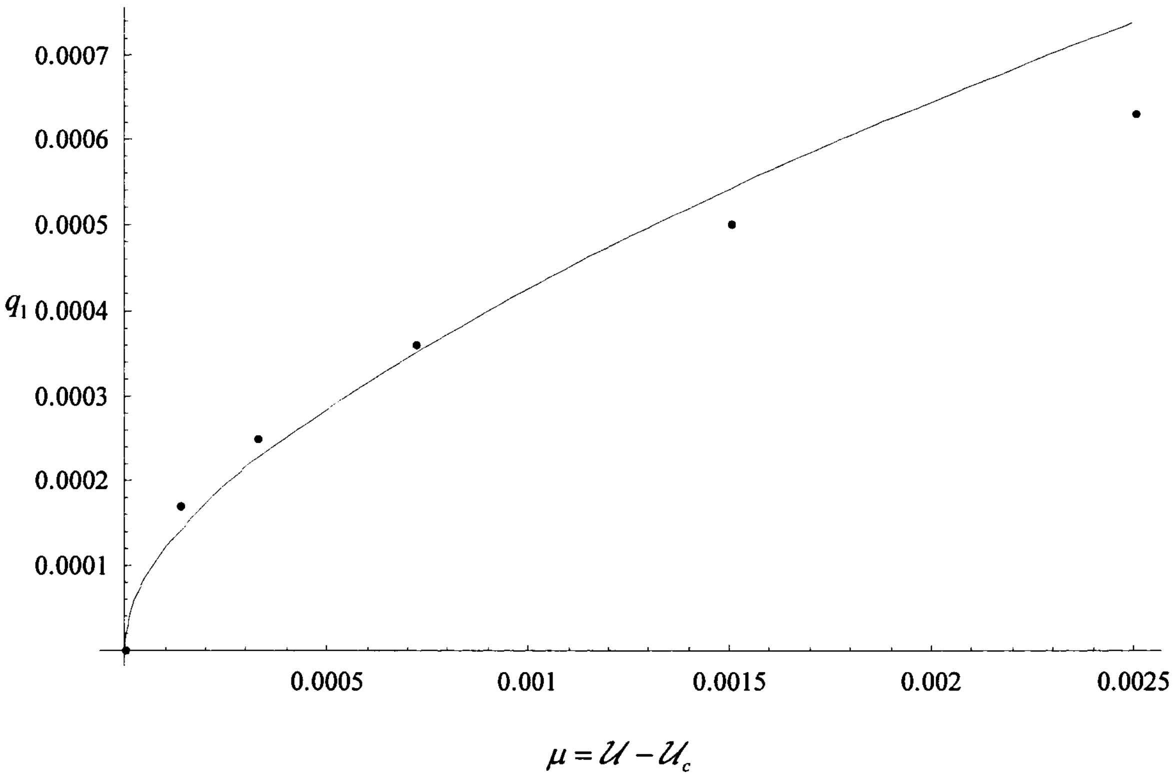

Figure 5-18 Bifurcation diagram for the clamped-hinged cylinder with the physical parameters of Table 5-2 in the vicinity of the pitchfork bifurcation point, obtained with $N_u = N_v = 1$ using centre manifold reduction (continuous line) and AUTO (dots).

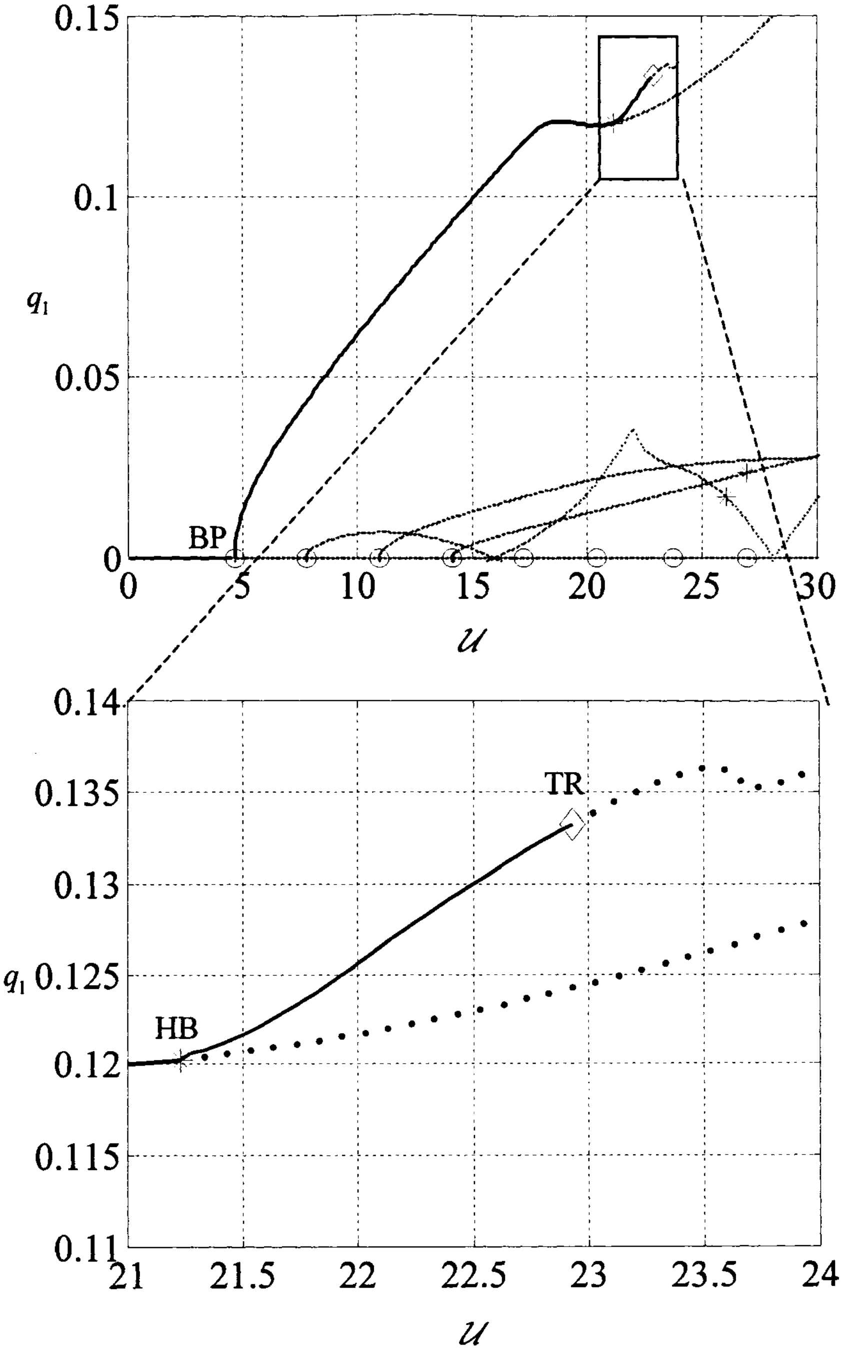

Figure 5-19 Bifurcation diagram for a hinged-clamped cylinder with the physical parameters of Table 5-2 found by AUTO with $N_u = N_v = 8$.

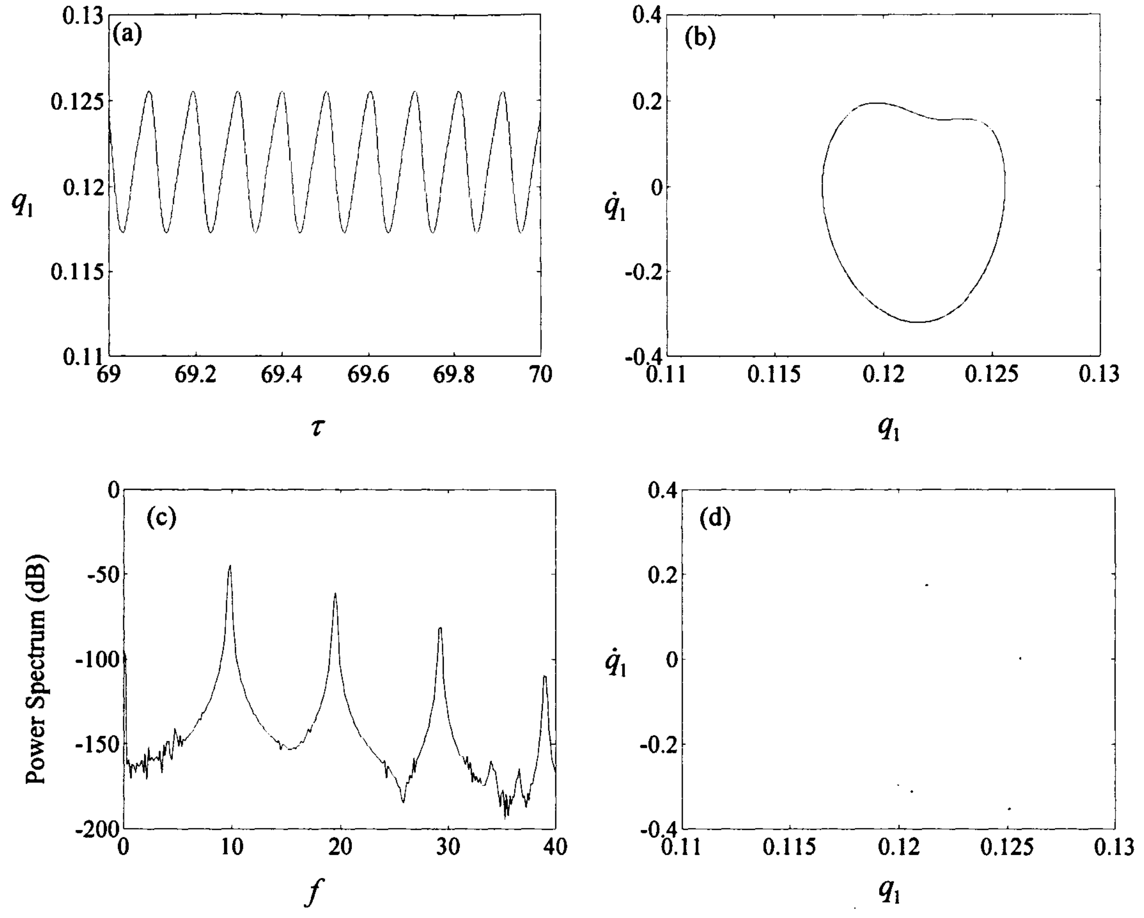

Figure 5-20 (a) Time history, (b) phase plane plot, (c) power spectral density plot and (d) Poincaré map for the system of Figure 5-19 (hinged-clamped cylinder) for $\mathcal{U}=22$, obtained with $N_u = N_v = 8$ (periodic oscillation).

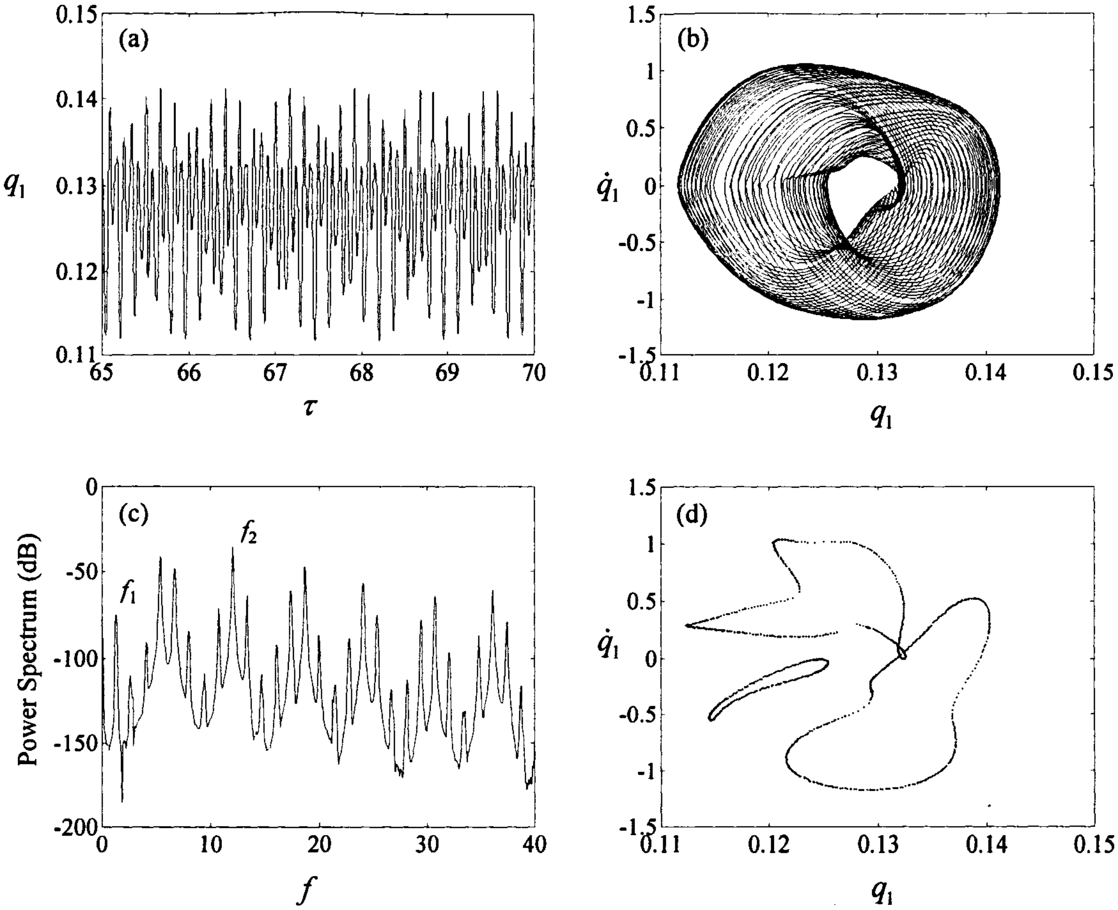

Figure 5-21 (a) Time history, (b) phase plane plot, (c) power spectral density plot and (d) Poincaré map for the system of Figure 5-19 (hinged-clamped cylinder) for $\mathcal{U}=24$, obtained with $N_u = N_v = 8$ (quasiperiodic oscillation).

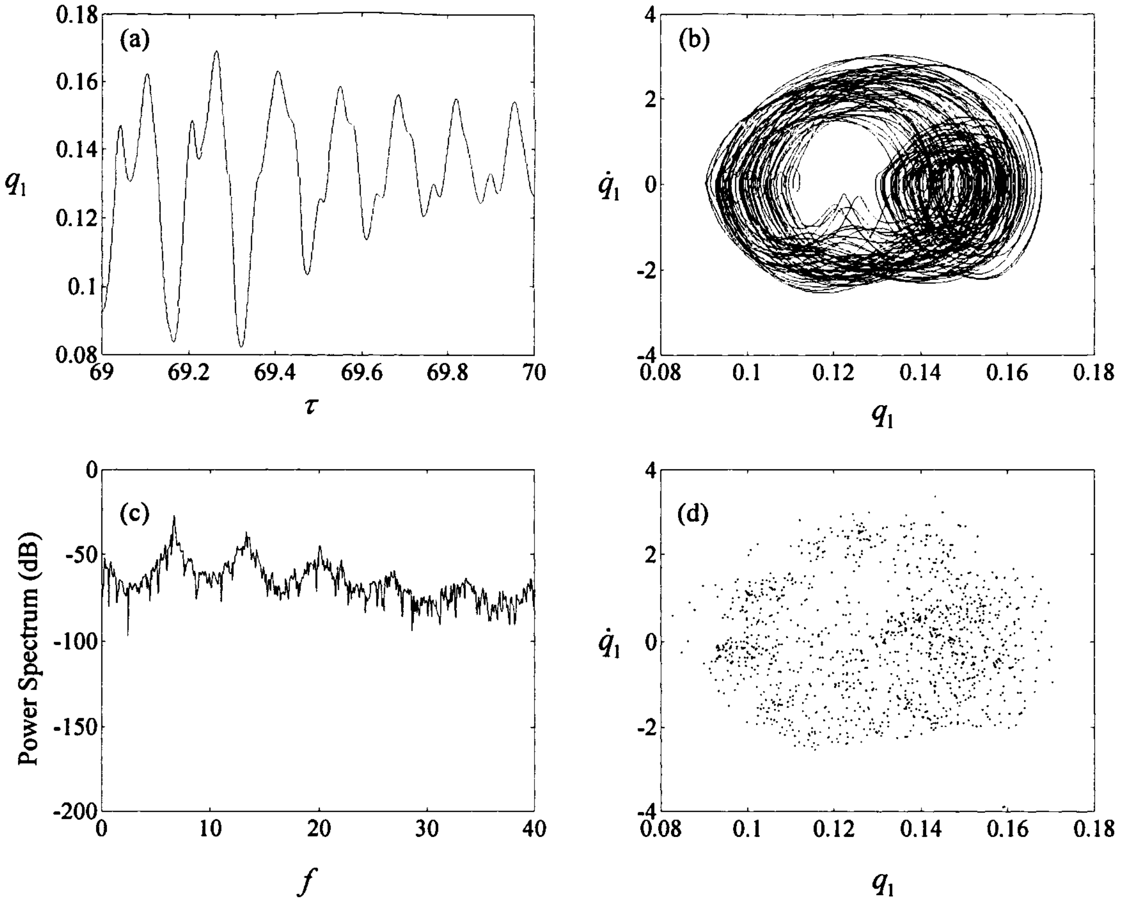

Figure 5-22 (a) Time history, (b) phase plane plot, (c) power spectral density plot and (d) Poincaré map for the system of Figure 5-19 (hinged-clamped cylinder) for $\mathcal{U}=26$, obtained with $N_u = N_v = 8$ (chaotic oscillation).

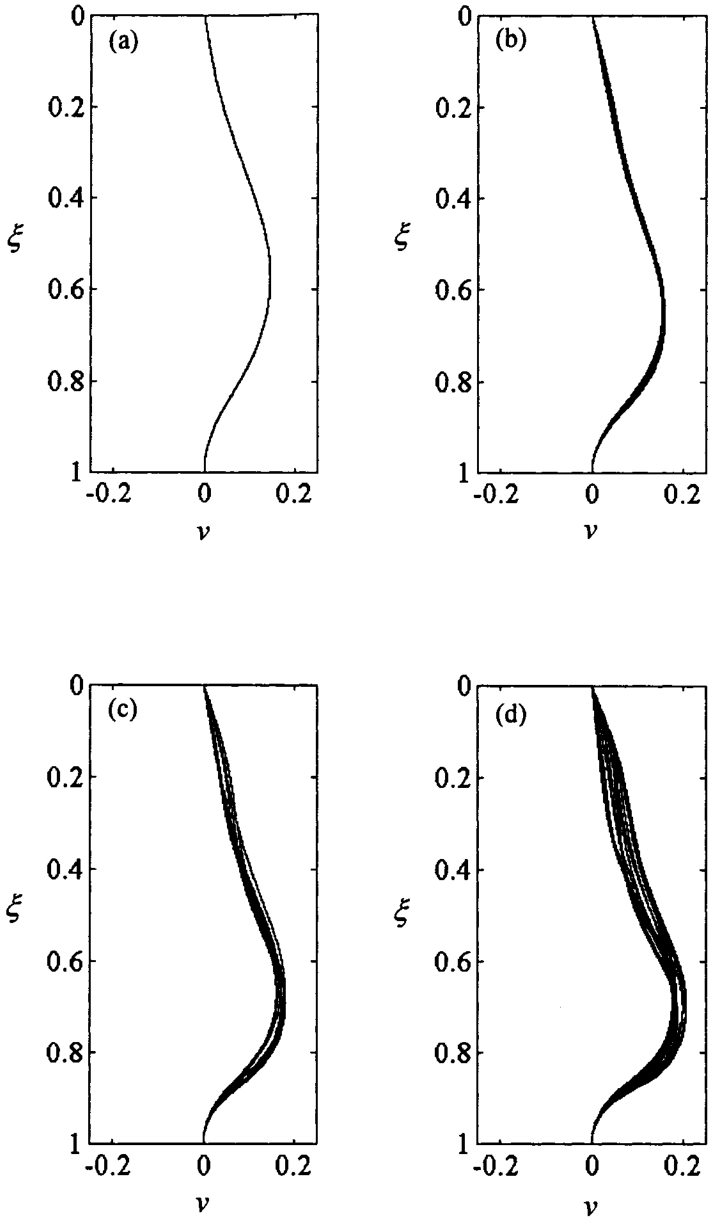

Figure 5-23 Spatial shape of the hinged-clamped cylinder of Figure 5-19 at different flow velocities: (a) $\mathcal{U}$ =20, buckled position, (b) $\mathcal{U}$ =22.0, periodic oscillation, (c) $\mathcal{U}$ =24.0, quasiperiodic oscillation, (d) $\mathcal{U}$ =26.0, chaotic oscillation.

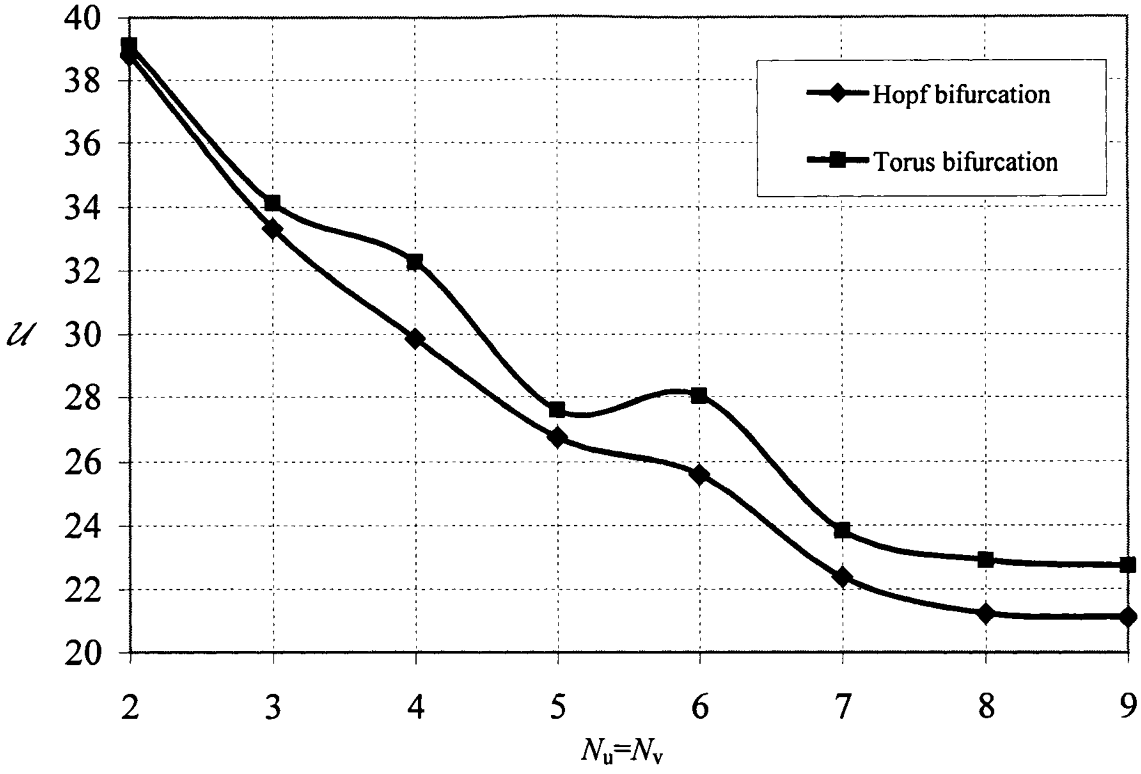

Figure 5-24 Critical values for the Hopf (HB) and torus (TR) bifurcations of the hinged-clamped cylinder with the physical parameters of Table 5-2 versus the number of modes.

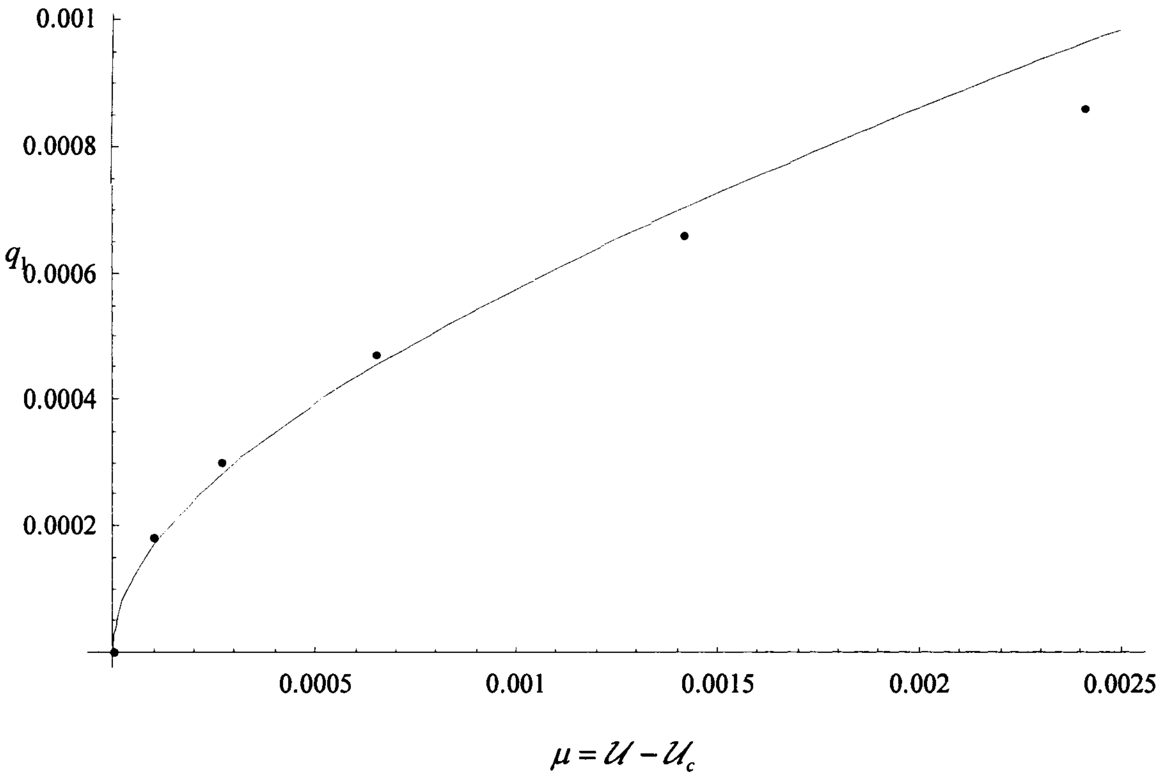

Figure 5-25 Bifurcation diagram for the hinged-clamped cylinder with the physical parameters of Table 5-2 in the vicinity of the pitchfork bifurcation point, obtained with $N_u = N_v = 1$ using centre manifold reduction (continuous line) and AUTO (dots).

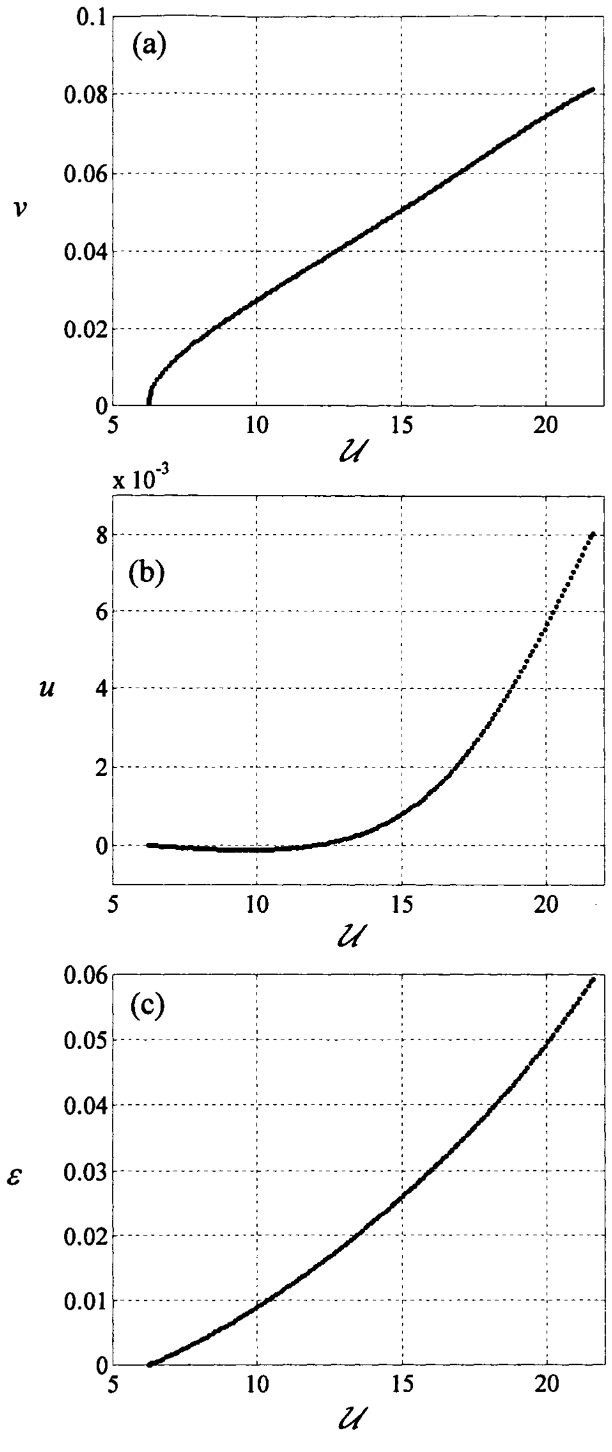

Figure 5-26 (a) Transverse displacement, (b) axial displacement and (c) axial strain versus $\mathcal{U}$ for a clamped-clamped cylinder with the physical parameters of Table 5-2 in the bucked state at $\xi = 0.8$.

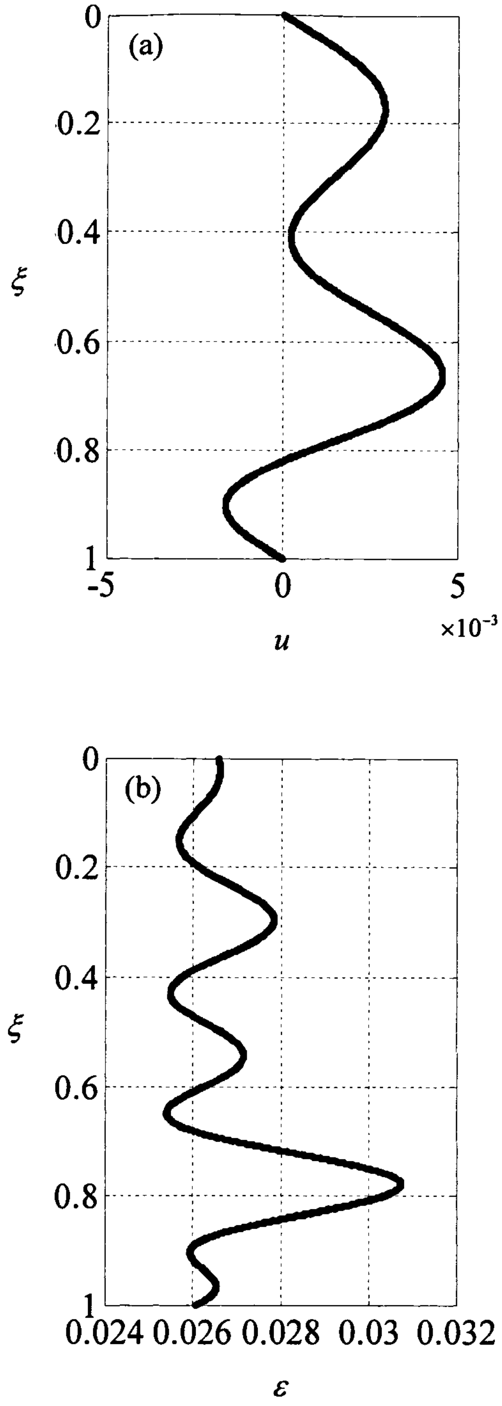

Figure 5-27 (a) The axial displacement and (b) the strain along the length of the clamped-clamped cylinder of Figure 5-26 for $\mathcal{U} = 15$.

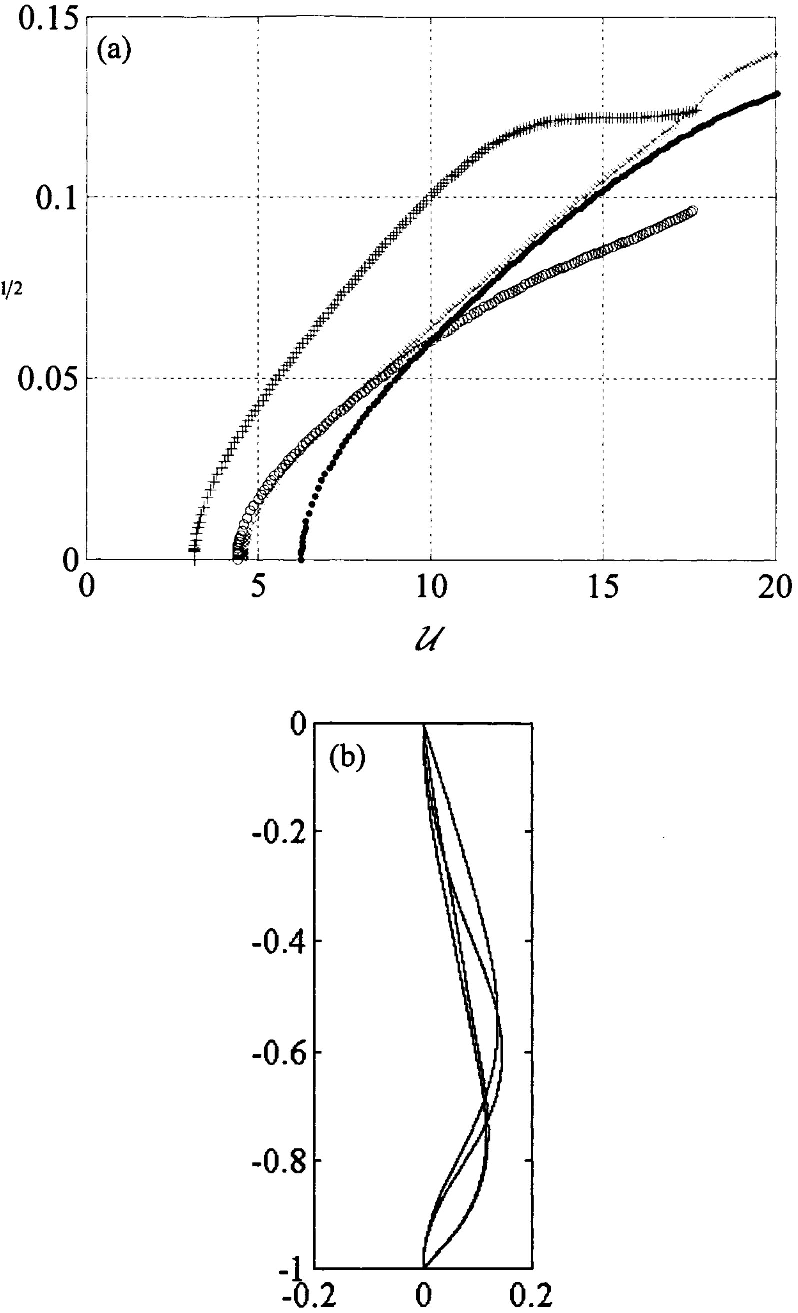

Figure 5-28 (a) The bifurcation diagrams of the midpoint deflection versus nondimensional flow velocity for various boundary conditions: +: simply supported, o: clamped-hinged, x: hinged-clamped, ... clamped-clamped; (b) Spatial shape of the buckled state of a cylinder for the four boundary conditions investigated at $\mathcal{U} = \mathcal{U}_{\mathrm{HB}} - 1$.

6. Experiments on Vertical Slender Flexible Cylinders Clamped at both Ends and Subjected to Axial flow

6.1. Introduction

The experimental behaviour of slender flexible cylinders subjected to axial flow is discussed in this chapter. A vertical elastomer cylinder, clamped at both ends and placed in the middle of the test-section of a water tunnel was used in the experiments. The downstream end of the cylinder could be fixed or free to slide axially. This is the second experimental study on such a system; the first one, by Païdoussis (1966c), as discussed in detail in Chapter 1, was conducted on horizontal cylinders and its results were compared with the linear theoretical results. According to the nonlinear theory discussed in Chapter 5, with increasing flow, the cylinder buckles at a certain flow velocity and the amplitude of buckling increases thereafter. At higher flow the statically deformed cylinder undergoes a Hopf bifurcation, which gives rise to periodic oscillations, followed by quasiperiodic and chaotic oscillations. The idea here is (i) to observe the post-divergence behaviour of the system and measure the corresponding data (the amplitude of buckling, as well as the amplitude and the frequency of oscillations in case of dynamic motions, if at all exist) and (ii) to compare the experimental observations with the results of nonlinear theory, both qualitatively and quantitatively, in order to validate the theoretical model, and hopefully to observe experimentally the same sequence of dynamical states as predicted by the nonlinear model.

First, experiments with a cylinder clamped at both ends, but free to slide axially in its downstream end are discussed. Then, the results for clamped-clamped cylinders with no axial sliding are presented. The influence of axial compression is also studied experimentally for this case. Because no dynamic instability was observed in these two series of experiments due to flow limitations in the water tunnel, another series of experiments were conducted on a more flexible cylinder. These experiments, in which flutter *was* observed, are also discussed. In all the experiments, graphs of the frequency versus nondimensional flow velocity are presented for pre-buckling turbulence-induced vibrations of the cylinders. Also, in each case, bifurcation diagrams of the system are presented in which the maximum midpoint amplitude of the cylinders is plotted versus nondimensional flow velocity. Three different methods are used to approximate the onset of divergence, all of which give comparable results. Also, the influence of different parameters on the onset of periodic motions is discussed.

6.2. Experimental set-up

The experiments were conducted with flexible cylinders, which were made of silicone rubber by casting in special moulds. Each cylinder was fitted with metal discs, which could be screwed onto different support assemblies at the upper and the lower ends to provide clamped boundary conditions (see Figure 6-1).* The upper end support was well streamlined. The cylinder was mounted vertically in the test-section of the water tunnel, which is shown schematically in Figure 6-2. The test-section ("channel") diameter was $D_{\mathrm{ch}} = 0.20$ m and its length was $L_{\mathrm{ch}} = 0.75$ m. Flow straighteners, screens, and a large flow-area reduction were utilized to ensure an axial, uniform flow stream in the test-section. The velocity profile was flat and uniform over the central portion of the test-section, covering at least 15 cm in diameter. The highest attainable flow velocity in the water tunnel was 5 m/s [see Païdoussis (2004, Chapter 8), for a complete description of the water tunnel].

To measure the midpoint displacement of the cylinder, two non-contacting optical motion-followers were used, measuring the displacements in two perpendicular directions to guarantee that the plane and the value of the maximum displacement were measured. Figure 6-3(a) shows schematically how the two motion-followers were placed relative to the cylinder. The first measuring device measured the displacements of the cylinder perpendicular to the axis of the device, while the second device measured the displacements in the direction of its axis. The output of these two motion-followers was saved in a computer for later analysis by the LabView© software. The resultant of these two measurements, as shown in Figure 6-3(b), gives the plane and the value of the maximum displacement, which is the value plotted in the theoretical results. In each

---

* For details about the method of making these cylinders, see Païdoussis (1998, Appendix D).

experiment, the flow velocity was increased gradually from zero, and at each step the midpoint displacement of the cylinder was measured.

6.3. First series of experiments: clamped-sliding cylinder

In the first series of experiments, the cylinder with the physical parameters given in Table 6-1 was used (the corresponding dimensionless parameters are given in Table 6-2). In this case, the lower end could slide axially in its support. The maximum attainable nondimensional flow velocity for this system was $\mathcal{U} = 7$.

The cylinder was at its original equilibrium position at zero flow velocity. At small flow velocities, turbulence-induced vibrations were damped. With increasing flow, the cylinder buckled mainly in its first mode; i.e. its amplitude at that point increased dramatically. This, however, occurred at almost the maximum attainable flow. Therefore, the cylinder behaviour substantially beyond the onset of divergence could not be observed. The PSD plots of the vibrations of the cylinder were produced at each flow velocity to construct the frequency-versus-flow graph and to obtain the critical value for divergence. Figure 6-4 shows the PSDs of the vibrations of the cylinder measured at its midpoint at two different flow velocities before the onset of divergence. The dominant frequency of vibration is at $f_1 \simeq 3.5$ Hz for $\mathcal{U} = 2.2$ (Figure 6-4(a)), which can be identified with the first eigenfrequency of the system at this flow. At $\mathcal{U} = 5.6$, two peaks are noticeable in the PSD plot: $f_1 \simeq 2$ Hz and $f_2 \simeq 8$ Hz, which correspond respectively to the first and the second eigenfrequencies of the system.[†] It is observed that the eigenfrequencies of the system vary with the flow velocity.

Figure 6-5(a) shows how the dominant frequency ($\omega_1 = 2\pi f_1$) varies with the nondimensional flow velocity for this system. The asterisks are the experimental results and the full dots are the theoretical ones. Theoretically, the first-mode frequency varies with $\mathcal{U}$ parabolically, and at the onset of divergence the first-mode frequency vanishes: $\omega_1 = 0$. The experimental values follow very closely the theoretical parabola, showing good agreement between theory and experiment. To approximate the critical flow

---

[†] Although the deformation was sensed at the midpoint of the cylinder, the second mode was still picked up, since, with flow, the midpoint is not a stationary node.

velocity for divergence, one should fit a parabola to the experimental results (the continuous line in Figure 6-5(a)) and extend it to cross the flow-velocity axis at a point which is considered as the critical flow velocity for divergence. This is called "the first method" to determine the critical point for divergence in this thesis. Doing so, it was found that the critical flow velocity for divergence is $\mathcal{U}_{\mathrm{BP}}^{(1)} = 6.5$, as shown in Figure 6-5(a).

Figure 6-5(b) shows the experimental results in the form of a bifurcation diagram. In this diagram, the midpoint displacement of the cylinder is plotted versus the nondimensional flow velocity. The crosses and the circles are the values measured by the two motion-follower devices in two perpendicular directions. The resultant (maximum) midpoint displacements are shown by asterisks. There is a smooth increase in the amplitude in the direction measured by the first motion-follower device ($\times$), while there is a sudden jump in the amplitude measured by the second one ($\circ$). This jump corresponds to a change in the direction of the plane of maximum displacement, due to flow irregularities or imperfections in the cylinder itself. However, we concentrate on the resultant displacement, which is the maximum midpoint amplitude of the cylinder, and this will be used as the experimental result that follows. The sudden jump in the amplitude measured by the second device has no effect on the resultant value, because the change in the plane of buckling does not change the maximum amplitude.

Figure 6-5(c) shows the comparison between experimental and theoretical bifurcation diagrams, for the whole range of attainable flow velocities in the water tunnel. Theoretically, the displacement should be zero, from $\mathcal{U} = 0$ to the critical flow velocity for divergence, $\mathcal{U}_{\mathrm{BP}}$, when the amplitude should increase precipitously with flow. In the experiments, however, one obtains nonzero η for all $0 < \mathcal{U} < \mathcal{U}_{\mathrm{BP}}$, as seen in Figure 6-5(c) for the experimental results ($*$). This is called the first zone in the experimental bifurcation diagram, where nonzero amplitudes are observed due to the growth of initial geometric and structural imperfections of the cylinder. The second zone is for $\mathcal{U} > \mathcal{U}_{\mathrm{BP}}$ where η increases much more rapidly with $\mathcal{U}$, showing the occurrence of divergence. To find the critical flow for divergence, one can fit the results in the two above-mentioned zones by two straight lines and consider the flow velocity at the intersection as the critical flow for divergence (see Figure 6-5(c)). We call this "the second method" for determining the critical flow velocity for divergence. According to this method, the critical flow velocity for divergence is $\mathcal{U}_{\text{BP}}^{(2)} = 5.8$, as shown in Figure 6-5(c).

Another, pragmatic criterion used to find the critical values for divergence is to set $\eta = 0.01 \equiv y/D = 0.2$ as the threshold of divergence. If the cylinder amplitude goes beyond this threshold, the cylinder will be considered buckled. This is called "the third method" to find the critical flow velocity for divergence in this thesis and it yields $\mathcal{U}_{\text{BP}}^{(3)} = 6.2$ for the system studied here (see Figure 6-5(c)). Table 6-3 shows the critical values for divergence found by the three methods discussed above together with the corresponding theoretical value. The first method is in very good agreement with the theoretical result, with only 2.9 percent error; this does not necessarily mean, however, that the first method is superior to, say, the second.

To find the theoretical results, the nondimensional parameters given in Table 6-2 have been used, where Π_0, β, γ and ε are calculated using the physical parameters of the cylinder given in Table 6-1, $h = D/D_{\text{ch}}$ and

$$\chi = \left(D_{\text{ch}}^2 + D^2\right)/\left(D_{\text{ch}}^2 - D^2\right), \tag{6-1}$$

according to Païdoussis (2004, p. 796). The coefficient of transverse form drag, c_d, can also be calculated, following Païdoussis (2004, Appendix Q)[‡]:

$$c_d = 8\sqrt{2\Omega\nu^*}, \tag{6-2}$$

where, Ω is radian frequency and ν^* is the kinematic viscosity; for water flow $\nu^* = 10^{-6}\,\text{m}^2/\text{s}$. One can take $c_n/c_t = 1$ and the tangential frictional coefficient to be $c_t = 0.025$.

[‡] In Appendix Q of Païdoussis (2004), the following relations are given: $c_d = (4/\pi)(\mathcal{U}/U)C_D$, where $C_D = (\pi/2)D\Omega C_d$ and $C_d = 2\sqrt{2}/\sqrt{S}$, in which $S = \Omega R^2/\nu^*$. Now substituting these relations backward, one finds $C_d = 4\sqrt{2}/D\sqrt{\Omega/\nu^*}$, and therefore $C_D = 2\pi\sqrt{2\Omega\nu^*}$, and assuming $\mathcal{U}/U \simeq O(1)$, it can be found that $c_d = 8\sqrt{2\Omega\nu^*}$.

The indicial-form equations of motion (2-68) and (2-69) are used. The eigenfunctions of a clamped-clamped cylinder for the transverse deformation (see Table 5-1) are used as the basis functions for the transverse displacement; moreover the eigenfunctions of a fixed-sliding bar undergoing axial motion,

$$\psi_j(\xi) = \sqrt{2}\sin\left(\frac{2j-1}{2}\pi\xi\right), \tag{6-3}$$

are used as the basis functions for the axial displacement. These eigenfunctions are used to reflect the fact that axial displacement at the lower end of the cylinder can occur freely. Only 2 modes in each direction are used to discretize the partial differential equations, because the maximum flow studied here is not very high, and two modes in each direction are enough to get converged results.

6.4. Second series of experiments: clamped-clamped cylinder with no sliding

In this series of experiments, the same cylinder, clamped at both ends was used, but no end-sliding was permitted. Similarly to the first series of experiments, the midpoint displacement of the cylinder was measured at each flow velocity and the corresponding PSD plots were produced. Figure 6-6 shows the PSD plots of the vibrations at a pre-buckling flow velocity ($\mathcal{U}=3.2$) and a post-buckling flow velocity ($\mathcal{U}=6.1$). The dominant frequency, at $f_1 \simeq 3$ Hz for $\mathcal{U}=3.2$, can be identified with the first eigenfrequency of thc system. The PSD plot at $\mathcal{U}=6.1$ shows three peaks: at $f_1 \simeq 2$ Hz, $f_2 \simeq 8$ Hz and $f_3 \simeq 17$ Hz in Figure 6-6(b), which correspond to the first, second and third eigenfrequencies of the system, respectively. The dominant peak in Figure 6-6(a) corresponds to the first-mode eigenfrequency. In Figure 6-6(b), this frequency peak has migrated further towards zero, but it is not zero. In contrast to linear theory, nonlinear theory does not imply zero net rigidity in the buckled state, and the first, second and third mode frequencies seen in Figure 6-6(b) are those of the buckled cylinder. All modes respond to the wide-band turbulence spectrum.

Figure 6-7(a) shows how the frequency of vibrations varies with the nondimensional flow velocity for this system. The asterisks are the experimental results and the continuous line represents the theoretical ones, calculated using the dimensionless parameters of Table 6-2. For relatively small flow velocities $(\mathcal{U} < 5)$, the experimental values for the frequency of vibrations follow the theoretical curve very closely. But for higher flow velocities, the experimental values deviate from the theoretical ones and it seems that they are tending toward a constant value: $\omega_1 \simeq 10$ rad/s, in contrast to the theoretical curve, which goes toward zero parabolically. This deviation is due to the fact that in the experiments, because axial sliding is prevented, increased deflection generates an increase in tension and therefore the frequency never becomes zero (Figure 6-7(b) shows the nonzero pre-buckling deflection of the cylinder). But, the theory assumes that there is no pre-buckling deflection and vibration, and therefore that there is no tension in the cylinder before the onset of buckling. It ought to be noted that in fitting the parabola to estimate the critical flow velocity for divergence by "the first method", only the sampling points which resemble a parabola have been taken into account and the almost-constant-frequency points have been neglected. The fitted parabola is shown in Figure 6-7(a) and the corresponding critical flow velocity is at $\mathcal{U}_{\mathrm{BP}}^{(1)} \simeq 6.8$.

Figure 6-7(b) shows the bifurcation diagram of the system for this case. The asterisks are the experimental values for the maximum midpoint displacement of the cylinder and the continuous line is the theoretical result. The post-buckling range in the bifurcation diagram is very limited $(6.3 < \mathcal{U} < 7)$, making it difficult to study the behaviour of the system in this range. However, for the existing range of buckling, the experimental amplitude of buckling is in good agreement with the theoretical ones. The first row in Table 6-4 gives the critical values for the pitchfork bifurcation found using the three methods previously discussed, together with the corresponding theoretical results. Relatively good agreement is obtained between the theoretical and experimental results. The second method gives the closest value to the theoretical prediction for the critical flow velocity for divergence, in this case.

Because in both cases discussed so far, divergence occurred at a flow velocity very close to the maximum flow attainable in the water tunnel, it was not possible to study the post-divergence behaviour of the system, either in terms of the amplitude of buckling or with respect to the possible existence of a post-divergence dynamic instability. Therefore, in what follows we discuss:

- the experiments with the same cylinder under axial compression, and
- the experiments with a more flexible cylinder.

In both cases, the critical nondimensional flow velocity for divergence is lower than in the present case, making it possible to observe the post-divergence behaviour of the cylinder over a wider flow range. Also, in the case of a more flexible cylinder, the theoretical nondimensional flow velocity for flutter is lower and, as we shall see in Section 6.5, dynamic instability can be observed.

6.4.1. Influence of axial compression

In order to study the influence of axial compression on the system and also to make it possible to study the post-divergence behaviour of the system over a wider range of flow velocity by decreasing the critical flow velocity of divergence, experiments were conducted with the same cylinder, but under an externally applied compression. To apply this axial compression, rings of varying thickness and with the same outer diameter as the cylinder ($D_{\mathrm{r,o}} = D = 0.0254\ \mathrm{m}$) and with the inner diameter of $D_{\mathrm{r,i}} = 0.0067\ \mathrm{m}$ were inserted between the lower end of the cylinder and the lower support assembly (see Figure 6-8). The inserted ring, depending on its thickness, results in pre-straining (shortening) the cylinder and therefore applies a pre-stress (an axial compression) on the cylinder with no flow.

To relate the applied axial pre-shortening to the nondimensional compression, we start from one of the relations in Equation (2-63), namely

$$\bar{\Gamma} = \frac{\bar{T}L^2}{EI}, \tag{6-4}$$

where $\bar{T} = \sigma A = E\varepsilon A$. Therefore,

$$\bar{\Gamma} = \frac{\Delta A L}{I}, \tag{6-5}$$

where, Δ is the pre-shortening, L is the cylinder length, $I = (\pi/64)D^4$ is the moment of inertia of the cylinder, and A is the cylinder cross-sectional area. Therefore, for the cylinder used in the present experiments, $\bar{\Gamma} = 1.29\times10^4\,\Delta$.

The procedure, measurements and the nomenclature of the figures are the same as previously described. Figure 6-9 shows how the frequency of turbulence-induced vibrations of the cylinder varies with the flow velocity for different axial compressions. In all cases, similar to the case of no axial compression, the frequencies decrease in a more or less parabolic form with flow for small flow velocities. From a certain flow velocity on, the frequencies do not follow the theoretical parabola and tend to an almost constant asymptote instead of going toward zero. By increasing the axial compression, the corresponding frequency of turbulence-induced vibration decreases, as expected. In the experimental observations (Figure 6-9) the frequency for $\mathcal{U}=0$ varies from $\omega_1 = 21.0$ rad/s to $\omega_1 \simeq 19.5$ rad/s when the nondimensional axial compression is varied from $\bar{\Gamma}=-12.9$ to $\bar{\Gamma}=-29.7$. Theoretical results, however, show much more significant changes in the corresponding first-mode frequency. This implies that by increasing the axial compression, the deviation of the experimental results from the theoretical curve starts at lower flow velocities. This becomes more significant for higher axial compressions. The main reason for this disagreement lies in the fact that the original position of the cylinder in the experiment, even before turning on the flow, was not totally straight anymore, because of the relatively large applied initial compression. A fairly large bow existed at zero flow, which was not considered in the theory; the theory is for initially straight cylinders. As the axial compression increases, the initial bow becomes larger and the initial position of the cylinder in the experiment diverges farther from the assumption of the straight initial position. This deviation from the theoretical assumptions affects the pre-buckling behaviour of the system much more than the post-buckling behaviour[§] as will be discussed in what follows, using the corresponding bifurcation diagrams.

Figure 6-10 shows the bifurcation diagrams for the system with different axial compressions. The above-mentioned initial bow is not obvious in the bifurcation diagrams, because the measurements were conducted relative to the initially bowed cylinder.[**] The same three "divergence criteria" are used here to find the critical flow velocities for divergence in the presence of an axial compressive load. The corresponding

---

[§] The reason is that the theory assumes a straight cylinder, while in the experiment the cylinder is not straight before buckling. After buckling, both theory and experiment say the cylinder is no longer straight.

[**] The occurrence of the bow of course means that the cylinder has developed buckling due to compression a great deal sooner (for smaller compression) than theoretically predicted, because of imperfections.

results are given in Table 6-4 and plotted in Figure 6-11 and compared with theory. The theoretical result (continuous line) shows that, as expected, by increasing the axial compression, the critical flow velocity for divergence decreases, and there is a certain value of axial compression for which the cylinder buckles, even with no flow. This occurs at $\bar{\Gamma} \simeq 41$, which is slightly different from the critical value of the Euler problem for a clamped-clamped column, $\bar{\Gamma} = 4\pi^2$, due to the effect of gravity, which increases the critical value for divergence. It is noted that, by increasing the axial compression, the experimental values follow the theoretical curve less closely. It is also noted that for large axial compressions the cylinder amplitude has an immediate parabolic increase with flow, making the approximations of the critical flow velocity for divergence much less accurate (e.g., Figure 6-10(c)).

In all these cases, the cylinder midpoint amplitude increases with flow as shown in Figure 6-10. As the axial compression increases, the range of flow velocity in which the cylinder is buckled becomes wider (by decreasing the critical flow velocity for divergence, while the maximum attainable flow remains the same) and, therefore, the amplitude of buckling can be compared with the theoretical results. Fairly good quantitative agreement between the theoretical and experimental results is observed. Similar to the case of a clamped-sliding or clamped-clamped cylinder with no end-sliding and no axial compression, the main qualitative difference is that in the experimental results the amplitude of the buckled cylinder increases with flow exponentially, while the theory predicts a parabolic increase in the amplitude. The imperfections and the deformation-induced tension in the cylinder can be thought of as the main source for the difference.

For all the cases studied in this series of experiments, the cylinder did not undergo any dynamic instability before the maximum attainable flow velocity was reached, encouraging us to conduct another series of experiments with a more flexible clamped-clamped cylinder, as will be discussed in the next section, in order to hopefully observe the post-divergence dynamic instability predicted by theory.

6.5. Third series of experiments: a more flexible cylinder with no end-sliding

In this series of experiments a more slender and more flexible hollow clamped-clamped cylinder was used. This results in a decreased dimensional flow velocity for any given nondimensional one; in this way, it was hoped that the maximum attainable flow velocity could exceed that necessary to give rise to post-divergence flutter (presuming that it exists). Table 6-5 gives the physical parameters of the cylinder used in this case. The same set-up as for the previous series of experiments was used.

Similarly to the previous experiments, at small flow velocities the cylinder was straight and the turbulence-induced vibrations were damped (Figure 6-12(a)). With increasing flow, the cylinder buckled mainly in its first mode (Figure 6-12(b)) and the amplitude of buckling increased with flow (Figure 6-12(c)). The flow was increased to almost its maximum, and the cylinder started to oscillate in its second mode around its equilibrium position (Figure 6-12(d)). The experiment was repeated and the oscillatory motions were observed at almost the same flow velocity. In what follows, the observations are discussed quantitatively.

Figure 6-13(a) shows how the frequency of turbulence-induced vibrations varies with the nondimensional flow velocity. Similarly to the cases previously discussed, the experimental frequency of turbulence-induced vibrations tends toward zero parabolically for small flow velocities but never reach zero; instead, they have a more or less constant value over a range of high flows (not shown here). The critical flow velocity for divergence, based on this graph can be approximated as $\mathcal{U}_{\mathrm{BP}}^{(1)} \simeq 7.5$, which is larger than the theoretical value of $\mathcal{U}_{\mathrm{BP}}^{\mathrm{Th.}} = 6.25$.

Figure 6-13(b) shows the bifurcation diagram of the system. For small flow velocities, the cylinder behaviour is similar to the cases previously discussed, in the sense that there is a sudden increase in the rate of change of the cylinder amplitude with flow, corresponding to the onset of divergence. The critical flow velocity for divergence is at $\mathcal{U}_{\mathrm{BP}}^{(3)} \simeq 6.2$, if $\eta = 0.01$ is considered as the threshold for buckling ("the third method"); and at $\mathcal{U}_{\mathrm{BP}}^{(2)} \simeq 5.4$, if the so-called "second method" is used. The cylinder then buckles mainly in its first mode and the amplitude of buckling increases with flow until $\mathcal{U} \simeq 10$, where a sudden decrease in the experimental midpoint amplitude of the cylinder is observed for a short range of flow, after which the cylinder oscillates mainly in its second-mode at $\mathcal{U} \simeq 11.2$. As observed in the bifurcation diagram, the maximum attainable nondimensional flow velocity for this system is $\mathcal{U}_{\max} \simeq 11.5$, and the oscillatory motion of the cylinder starts just before reaching this maximum flow.

Figure 6-14(a-c) shows the PSD plots of this cylinder for pre-buckling ($\mathcal{U}=4.2$), buckling ($\mathcal{U}=6.5$) and oscillatory ($\mathcal{U}=11.2$) states. The three peaks in the PSD plot for $\mathcal{U}=4.2$ ($f_1 \simeq 3$, $f_2 \simeq 8$ and $f_3 \simeq 16$) can be identified with the first, second and third eigenfrequencies of the system. With increasing flow, the peaks move to the left; at $\mathcal{U}=6.5$, they are at $f_1 \simeq 2$, $f_2 \simeq 7$ and $f_3 \simeq 15$. The two peaks in the PSD plot for $\mathcal{U}=11.2$ most probably correspond to the second and the third eigenfrequencies of the system (at $f \simeq 1.8$ and $f \simeq 3.3$), the first mode being the small peak at $f \simeq 0.8$. This ties in with the fact that the observed oscillations were of predominantly second-mode shape, with a sizable third-mode contribution. Figure 6-14(d) shows the time history of the oscillatory motion of the cylinder at $\mathcal{U} = 11.2$, where the displacement measured by the first measuring device is plotted for a time interval of 10 seconds.

6.5.1. *Influence of different parameters on the dynamic instability of the system*

The parameters used in the theoretical calculations to compare the results with the experimental observations are given in Table 6-6. The nondimensional parameters related to the cylinder geometry, and those related to the cylinder material and flow properties, namely Π_0, β, γ, ε, χ and h, are found directly from the physical parameters of the system, given in Table 6-5. Various models can be used for the structural damping in the axial and the transverse directions. The damping in the axial direction is assumed to be of linear viscous type (see Chapter 2), and in the transverse direction the modal structural damping is used. The coefficient of transverse form drag, c_d, can be calculated using Equation (6-2); however, as we shall see, this parameter has a huge effect on the onset of oscillations. On the other hand, the friction-related parameters, c_n and c_t, each can vary over a certain range, depending on the cylinder and flow properties. It is observed that for the system with zero structural damping and when c_d=0, c_n=c_t=0.01, and when there is no external pressurization ($\bar{\Pi}=0$), the critical flow velocity is at $\mathcal{U}_{\mathrm{HB}} = 21.8$. In what follows, the influence of these parameters on the critical flow velocity for the Hopf bifurcation is investigated.

6.5.1.1 *Structural damping coefficients.* In the model, the structural damping in the axial direction is assumed to be the linear viscous one, i.e. $C_{ij}^{u\text{-}st} = \alpha \times 2\zeta\lambda_i^u \sqrt{\Pi_0}\,\delta_{ij}$, where α^u is a coefficient, which can be varied from zero (for the case of no axial structural damping) to 1. With increasing α^u, the corresponding critical flow increases as shown in Figure 6-15(a).

The damping in the transverse direction is assumed to be of modal type: $C_{ij}^{v\text{-}st} = \delta_j \left(\lambda_i^v\right)^2 \delta_{ij}/\pi$, where δ_j are the modal damping coefficients. These damping coefficients were measured experimentally for a vertical cylinder clamped at both ends for the first four modes and were found to be δ_1=0.0718, δ_2=0.1181, δ_3=0.1644 and δ_4=0.2107. It was then assumed that the higher mode coefficients were linearly increasing, i.e., δ_5=0.2570 and δ_6=0.3033, etc. We define a coefficient α^v such that $\delta_j^{\text{considered}} = \alpha^v \delta_j^{\text{measured}}$. Thus, increasing α^v from naught to 1, we can study the influence of modal damping coefficient on the stability of the system. Figure 6-15(b) shows that by increasing the coefficient of modal damping, the critical flow velocity for the Hopf bifurcation increases dramatically, indicating, similarly to the axial case, a stabilizing effect.

6.5.1.2 *Influence of the coefficient of transverse form drag (c_d).* Increasing the coefficient of transverse form drag from naught to 0.1, the critical flow velocity for the Hopf bifurcation increases dramatically as can be seen in Figure 6-15(c). Similarly to the other parameters studied here, increasing this coefficient stabilizes the system. Knowing that the frequency of the resulting oscillatory motion is around 3 Hz, one can use Equation (6-2) to find the corresponding form drag coefficient: c_d =0.06. It is observed (Figure 6-15 (c)) that the corresponding critical flow is $\mathcal{U}_{\text{HB}} = 31.7$, which is very much larger than that observed in the experiments.

6.5.1.3 Influence of the tangential and the normal friction coefficients (c_t and c_n). Païdoussis (2004, Appendix Q) suggests that the reasonable range for c_t and c_n are $0.010 < c_t < 0.025$, and $0.005 < c_n < 0.040$, implying that c_t and c_n should not necessarily be equal, as will be discussed in the next subsection. Here, we assume $c_t = c_n$. Figure 6-15(d) shows that by increasing the friction coefficients, the critical flow velocity for the Hopf bifurcation increases. The same stabilizing effect was observed by Semler et al. (2002), for increasing $c_t = c_n$ for a cantilevered cylinder. It is found (see Figure 6-15 (d)) that the corresponding critical flow velocities for the system studied here is $21.84 < \mathcal{U}_{\text{HB}} < 22.85$ for the above-mentioned range of c_t. Of course, the sensitivity of the critical flow velocity for the Hopf bifurcation to the correct choice of c_t and c_n is small in this range, but still considerable.

6.5.1.4 Influence of the ratio of frictional coefficients (c_n/c_t). Generally, the longitudinal and the normal viscous coefficients are not equal. Ortloff and Ives (1969) suggest that the ratio of c_n/c_t can vary from approximately 0.5 for very rough cylinders to approximately 2 for smooth ones [see Païdoussis (2004, Appendix Q) for more detail]. Figure 6-15(e) shows that the critical flow velocity for the Hopf bifurcation varies from $\mathcal{U}_{\text{HB}} = 8.5$ to $\mathcal{U}_{\text{HB}} = 27.4$ for the system studied here, as the cylinder becomes smoother (with c_n/c_t varying from 0.5 to 2).

6.5.1.5 Comparison with the experimental results and discussion. As observed in the previous subsections, increasing α, δ_j and c_d from zero and $c_t = c_n$ from 0.01 results in higher values of $\mathcal{U}_{\text{HB}}$. It is only by decreasing c_n/c_t that one can find lower values for the critical flow velocity. According to Figure 6-15(e), the critical flow for a rough cylinder ($c_n/c_t = 0.5$) with no structural damping and with $c_d = 0$ is $\mathcal{U}_{\text{HB}} = 8.5$. This is lower than the experimental value for the onset of flutter ($\mathcal{U}_{\text{HB}}^{\text{Exp}} = 11.2$). By adding any damping and by increasing c_d, as discussed in the previous sub-sections, and also by having a smoother cylinder, the critical flow increases. Therefore, it is observed that, the experimental value for the Hopf bifurcation point is inside the range of flow velocities predicted by the theoretical results and depends on the parameters chosen. The assumption of a rough surface for the cylinder used in the experiments is quite reasonable.

According to the theoretical results the cylinder oscillates around its bucked state and the frequency of oscillation is $f^{\text{Th}} \simeq 3$ Hz; in the experiments, on the other hand, the cylinder oscillates around its original equilibrium position with a frequency of $f^{\text{Exp}} \simeq 1.8$ Hz. These two frequencies are of the same order and therefore comparable. The difference in the nature of oscillations (around the buckled state in theory and around the original equilibrium position in experiment) could be due to the fact that the model used in this thesis is correct to third-order magnitude; perhaps, in order to capture the relatively large-amplitude oscillations of the system, one needs to use a model correct to a higher-order (e.g. fifth-order) magnitude.

6.5.2. Dynamic oscillation of the small-diameter cylinder with an external axial compression

To study the influence of the externally applied axial compression on the dynamic instability of the system, experiments were conducted on the small-diameter cylinder of the previous section, with a ring inserted between the lower end of the cylinder and the downstream support, applying an axial compression of $\overline{\Gamma} = -19.0$. Figure 6-16 shows the bifurcation diagram for this system. Similarly to the case of the large-diameter cylinder studied in Section 6.4.1, under axial compression the cylinder buckles at a lower flow velocity, and the amplitude of buckling at a given flow velocity is larger than that of the cylinder with no axial compression. The critical flow velocity for divergence based on the three methods discussed before are $\mathcal{U}_{\text{BP}}^{(1)} = 6.1$, $\mathcal{U}_{\text{BP}}^{(2)} = 5.0$, $\mathcal{U}_{\text{BP}}^{(3)} = 4.3$ and $\mathcal{U}_{\text{BP}}^{\text{Th.}} = 4.5$. Except for the first method, reasonably good agreement between the theoretical and experimental values of the critical flow velocity for the pitchfork bifurcation is observed. What is new in this case and was not observed in the case of the large-diameter cylinder (because no flutter was observed in that case), is that the flutter occurs at almost the same flow velocity as the case with no axial compression! In fact, the cylinder under axial compression buckles at a lower flow velocity $(\mathcal{U} \simeq 4.5)$, and remains buckled for a wider range of flow velocities, until it starts oscillating at $\mathcal{U} \simeq 11$. This is in agreement with what the theoretical nonlinear model predicts. Figure 6-17 shows that by changing the external axial compression from 0 to -150, the critical flow velocity for the Hopf bifurcation increases from $\mathcal{U} = 21.8$ to $\mathcal{U} = 22.3$. The change in the critical flow for varying $\overline{\Gamma}$ from 0 to -19, is almost negligible according to the results shown in this figure. Also, looking at the nonlinear equations of motion of the system (Equations (2-64) and (2-65)), one can see that all the terms involving $\overline{\Gamma}$ (the nondimensional axial compression parameter) are associated with static terms: terms with no time-derivatives of the unknowns. This, however, does not imply that there should be no effect, or negligible effect, on the dynamic behaviour of the system with varying external axial compression; this negligible effect is observed for the critical flow velocity of Hopf bifurcation in Figure 6-17.

6.6. Summary

Three series of experiments have been conducted to study the dynamical behaviour of slender flexible cylinders clamped at both ends and subjected to axial flow. The downstream end of the cylinder could either slide axially or was wholly fixed.

Nonlinear theory predicts that the system loses stability via a pitchfork bifurcation, leading to buckling and that at higher flows a Hopf bifurcation occurs. The second mode of the system becomes unstable at the Hopf bifurcation and the cylinder oscillates about the buckled state. This periodic oscillation is then followed by quasiperiodic and chaotic ones. The existence of the post-divergence dynamic instability had previously been predicted by Païdoussis (1966b) using a linear model and was confirmed with experiments (Païdoussis, 1996c), but as discussed in Chapter 1, the interest in those experiments was confined to the linear realm.

Here, in the first series of experiments, the lower end of the cylinder was free to slide axially, while in the second series, axial sliding was prevented. In all the experiments, small static deflections were observed at small flow velocities, reflecting the growth of the initial structural and geometric imperfections. After a certain flow velocity, the cylinder amplitude increased more rapidly with flow. This flow velocity corresponds to the critical value for divergence. It was observed that, by applying axial compression in the case of fixed ends, the critical flow velocity for divergence decreased, while for a given flow velocity, the amplitude of buckling increased, as one would expect. Good agreement between theoretical and experimental results was observed for both the critical flow velocity for divergence and the amplitude of buckling. No dynamic instabilities were observed in these two series of experiments because the cylinder was rather stiff, and the maximum attainable dimensionless flow velocity was rather low.

The third series of experiments were conducted with a more flexible hollow cylinder, making it possible to reach higher dimensionless flow velocities. Similarly to the previous two series of experiments, the cylinder buckled, and the amplitude of buckling increased with flow. In this case, however, at higher flow, the cylinder developed a dynamic instability and oscillated mainly in its second mode. This proves, experimentally, the existence of flutter, which was previously predicted by linear theory and was confirmed by the nonlinear model. These observations also confirm the experimental results by Païdoussis (1996c). It was observed that the theoretical value for the Hopf bifurcation was largely dependent on system parameters, for which (to the best available knowledge) precise values cannot be assigned. The influence of structural damping in the axial and the transverse direction, friction-related parameters, form drag coefficient and the external compression on the dynamic instability of the system was studied theoretically. It was found that the experimental value of the critical flow velocity for the Hopf bifurcation was within the range of flow velocities obtainable by varying these parameters of the system, within reasonable margins. It was also observed, both experimentally and theoretically, that the influence of externally applied axial compression on the onset of flutter is negligible.

Physical parameter		Value
Diameter	D (mm)	25.4
Length	L (m)	0.52
Mass per unit length	m (kg/m)	0.577
Flexural rigidity	EI (N.m^2)	0.0559

Table 6-1 Physical parameters of the cylinder used in the first two series of experiments (large-diameter cylinder)

Π_0	β	γ	ε	h	χ	c_d	c_t	c_n/c_t
6707	0.47	1.83	20.47	0.125	1.032	0.06	0.025	1

Table 6-2 Dimensionless parameters used in the theoretical calculations for the experiments on the cylinder with the physical parameters of Table 6-1 (the first two series of experiments)

First method, $\mathcal{U}_{\mathrm{BP}}^{(1)}$	Second method, $\mathcal{U}_{\mathrm{BP}}^{(2)}$	Third method, $\mathcal{U}_{\mathrm{BP}}^{(3)}$	Theory, $\mathcal{U}_{\mathrm{BP}}^{\mathrm{th}}$
6.7	5.8	6.2	6.9
2.9	15.9	10.1	Error (%)

Table 6-3 The critical flow velocities for the onset of divergence based on the three methods discussed in Section 6.3, together with the corresponding theoretical result for the clamped-sliding cylinder of the first series of experiments with physical parameters given in Table 6-1 and the corresponding error

Pre-shortening (mm)	Axial compression $\bar{\Gamma}$	Critical value of $\mathcal{U}_{BP}$ (-)			
		Experiment			Theory
		1st method	2nd method	3rd method	
0.0	0	6.8	5.8	5.3	6.25
1.0	-12.9	6.1	5.5	5.0	5.12
1.6	-20.6	5.8	5.4	5.0	4.30
2.3	-29.7	5.3	4.2	4.5	3.10

Table 6-4 The critical flow velocities for the onset of divergence based on the three methods discussed in the text, together with the corresponding theoretical results for the second series of experiments, for the clamped-clamped cylinder with the physical parameters as in Table 6-1, for different externally applied axial compressions

Physical parameter		Value
Outer diameter	D_o (mm)	15.6
Inner diameter	D_i (mm)	9.4
Thickness	t (mm)	3.1
Length	L (m)	0.435
Mass per unit length	m (kg/m)	0.1445
Flexural rigidity	EI (N.m^2)	0.0065

Table 6-5 Physical parameters of the hollow cylinder used in the third series of experiments (small-diameter cylinder)

Π_0	β	γ	ε	h	χ	c_d
9124.2	0.57	-5.78	27.88	0.0768	1.0119	0.060

Table 6-6 Dimensionless parameters used in the theoretical calculations for the experiments on the cylinder with the physical parameters of Table 6-5 (the third series of experiments). The other parameters (α, δ_i, c_t, c_n, c_d and $\bar{\Pi}$) are varied as shown in Figure 6-15.

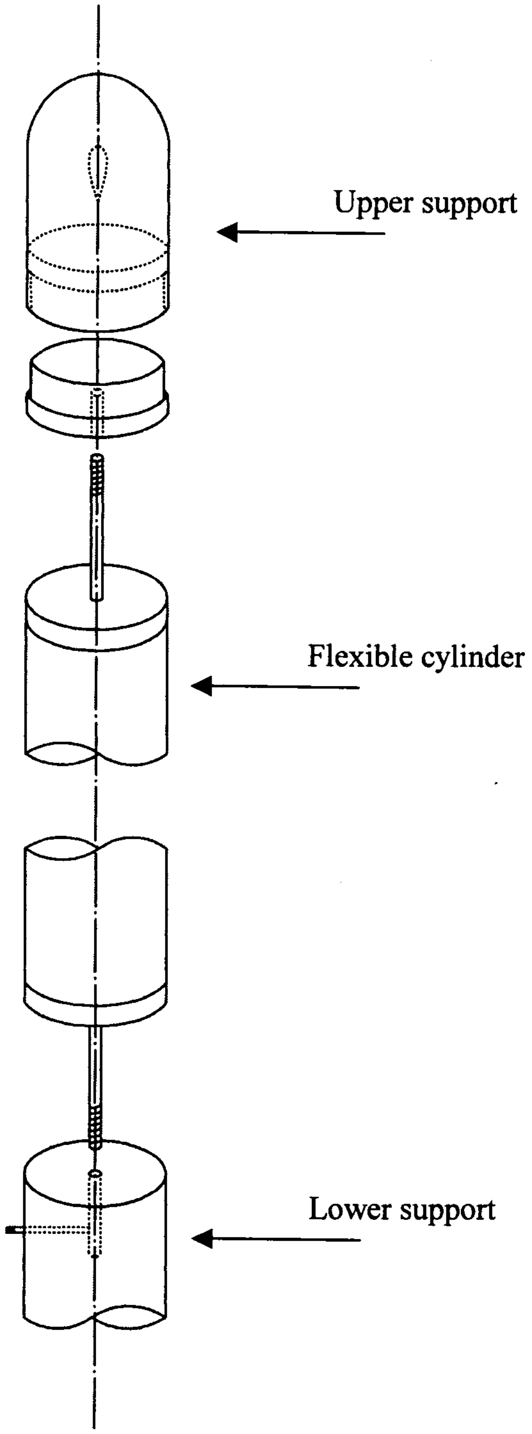

Figure 6-1 A schematic, exploded view of the cylinder and its upstream and downstream ends.

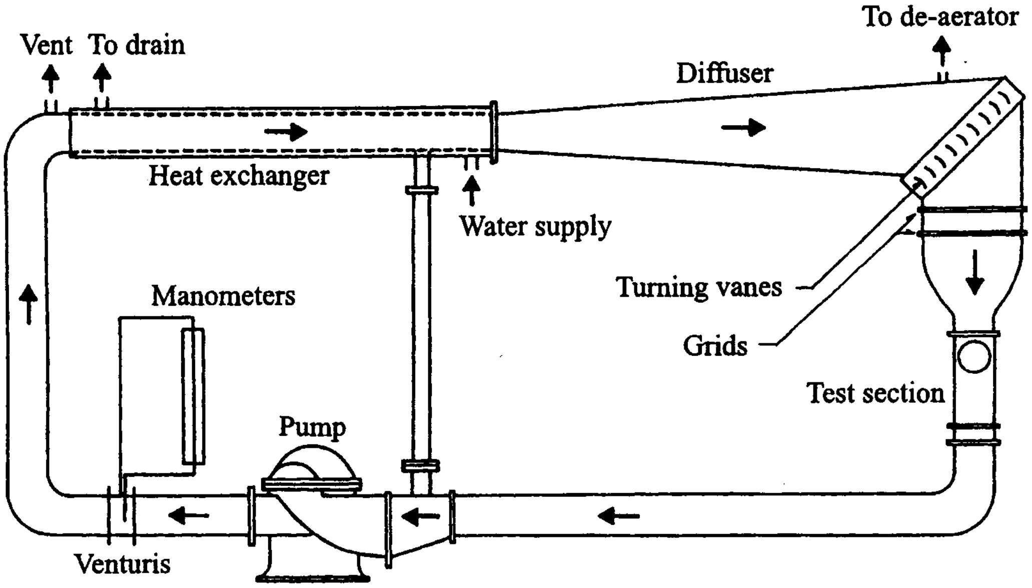

Figure 6-2 Schematic view of the water tunnel [from Païdoussis et al. (2002)].

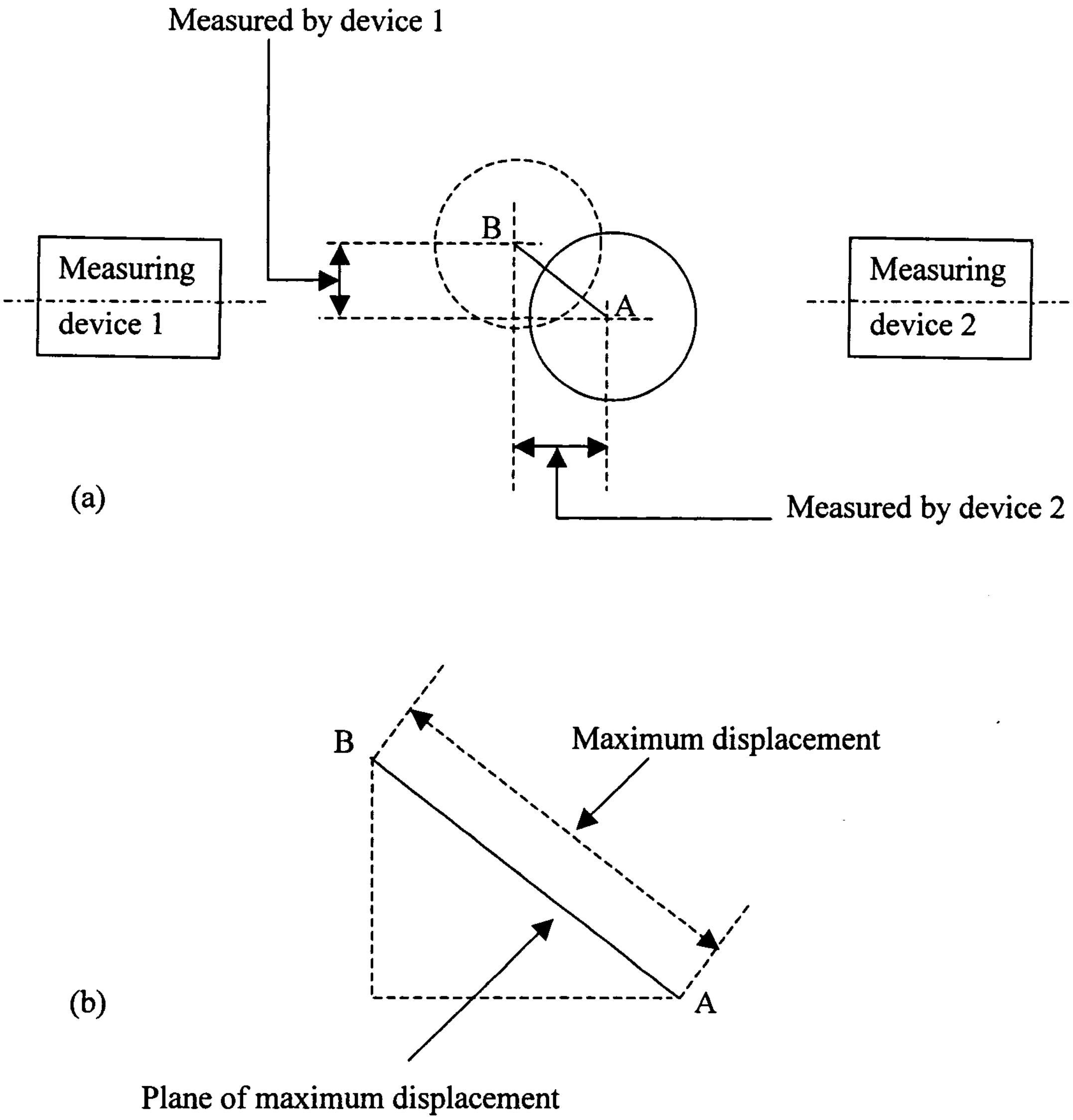

Figure 6-3 (a) Schematic of the motion-followers ("measuring devices") set-up, (b) the plane and the value of the maximum displacement found based on the measurements of the two devices.

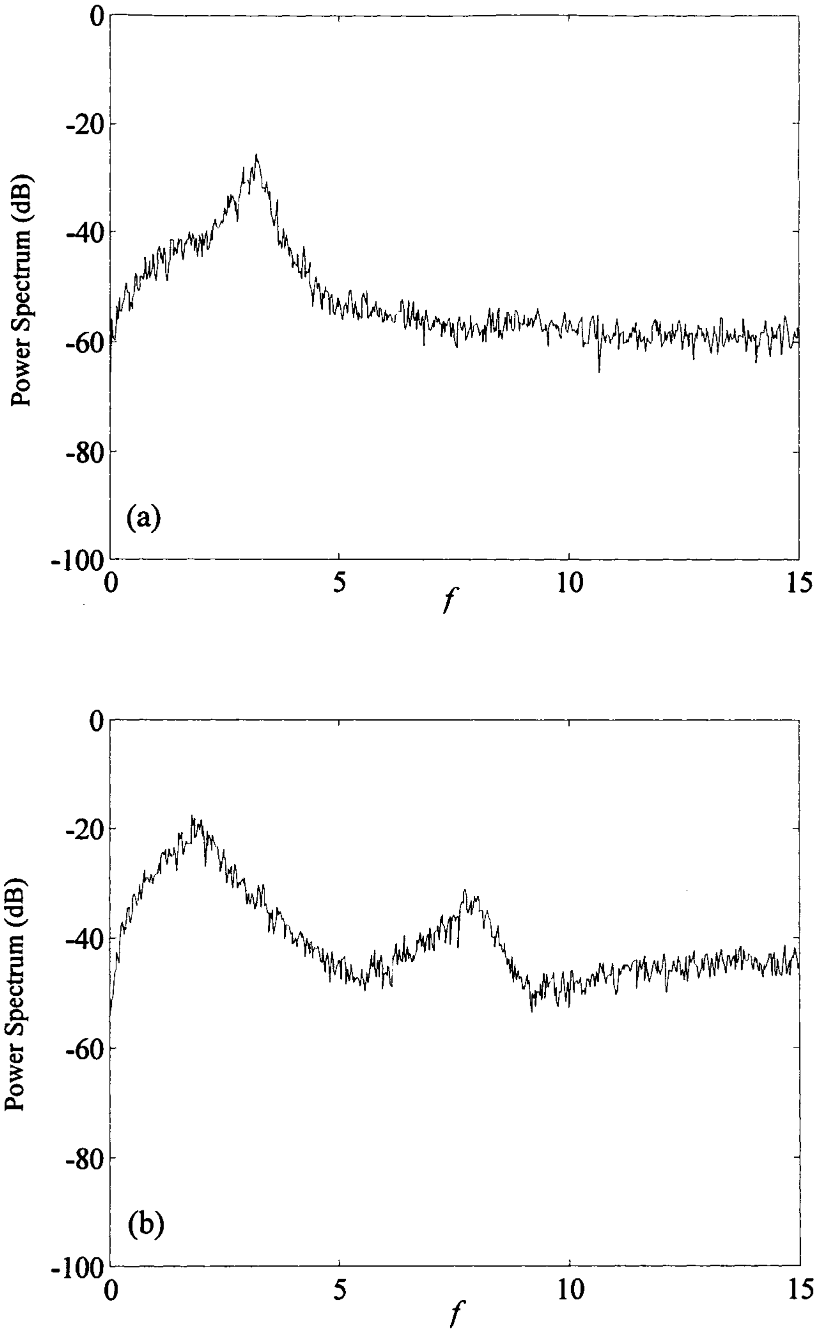

Figure 6-4 PSD plots for the first series of experiments with a clamped-sliding cylinder with parameters given in Table 6-1 at (a) $\mathcal{U} = 2.2$, and (b) $\mathcal{U} = 5.6$.

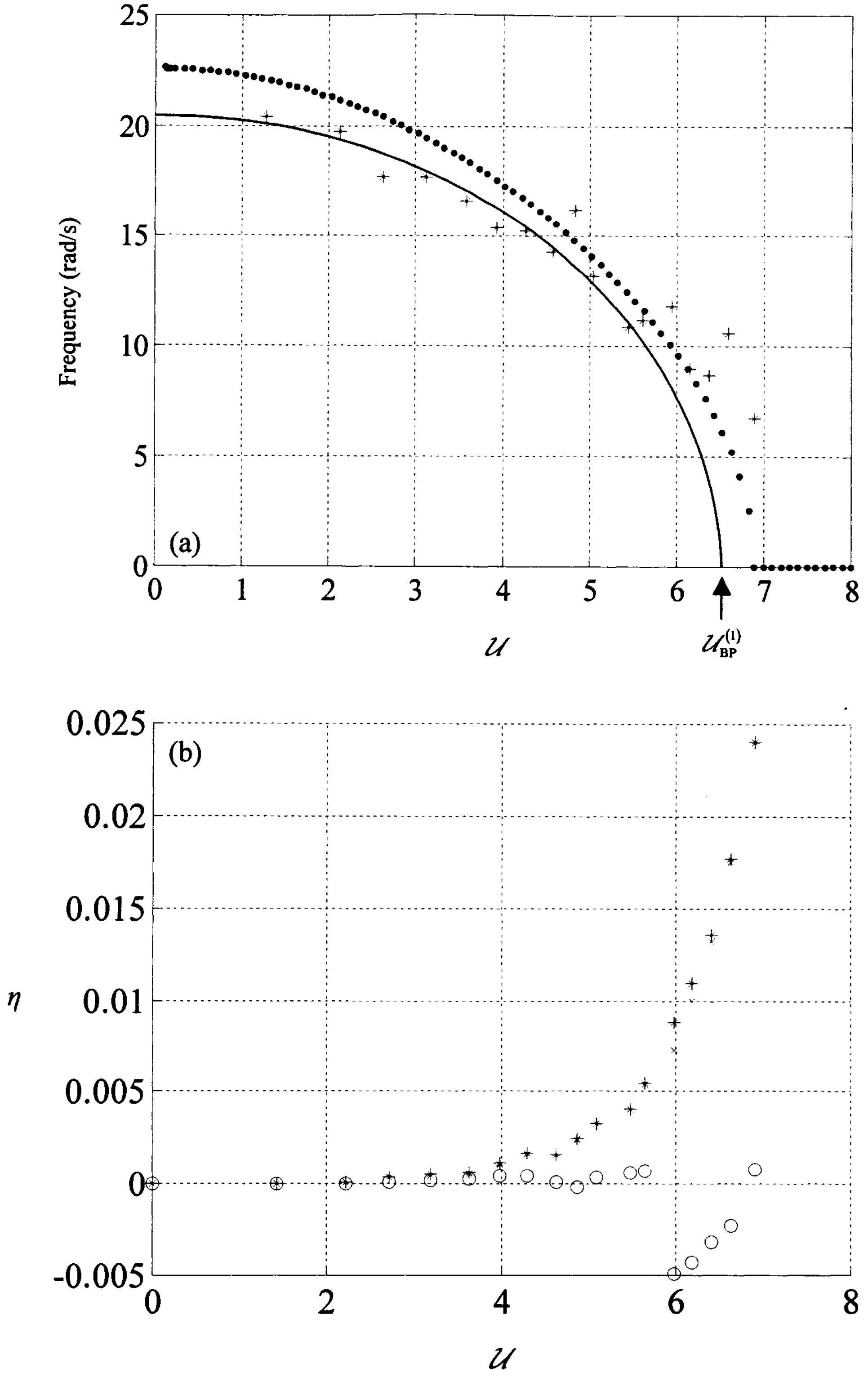

Figure 6-5(a,b); see next page.

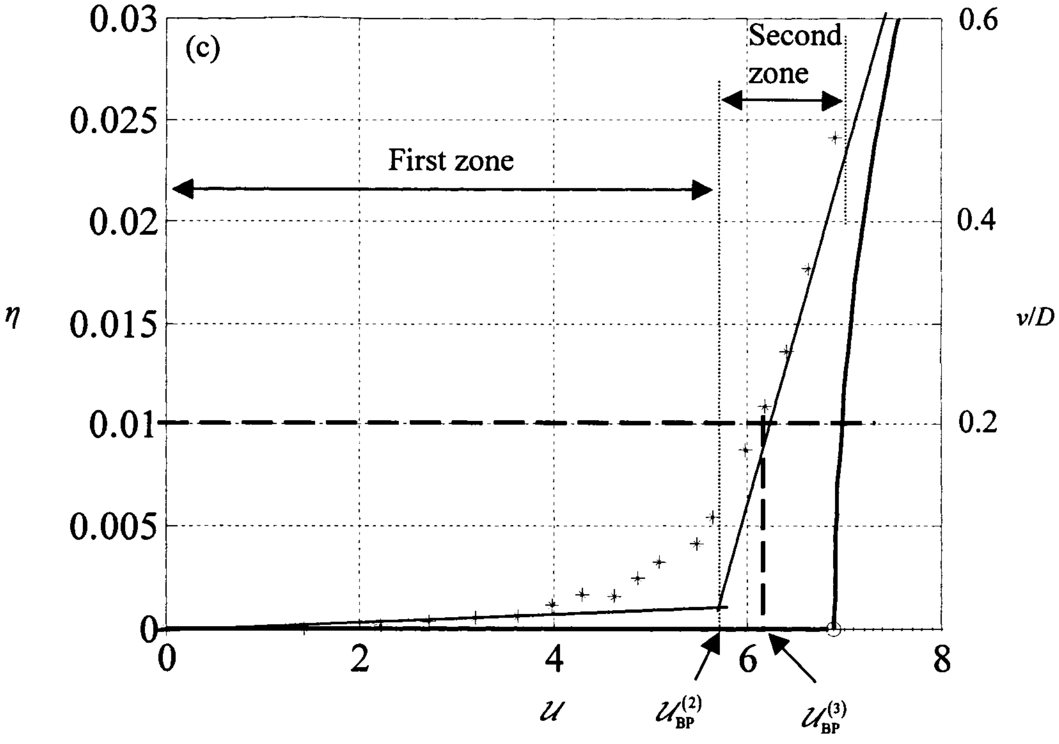

Figure 6-5 (a) Experimental (*) and theoretical (·) graphs of frequency versus dimensionless flow velocity; (b) bifurcation diagram for the first series of experiments with a clamped-sliding cylinder with parameters given in Table 6-1; (c) comparison between theory (continuous line) and experiment (*) in the form of bifurcation diagrams.

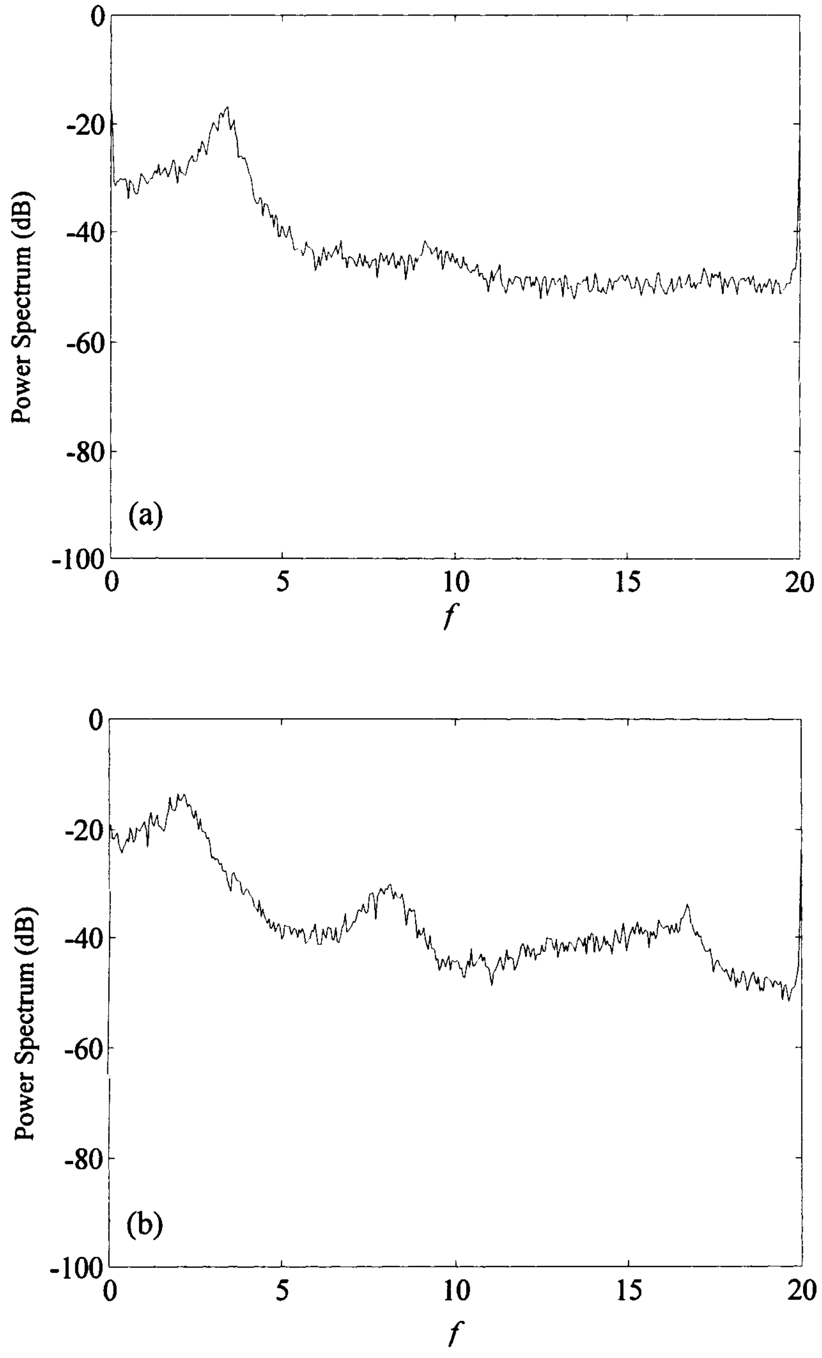

Figure 6-6 PSD plots for the second series of experiments with a clamped-clamped cylinder with no end-sliding and with parameters given in Table 6-1 at (a) $\mathcal{U}=3.2$, and (b) $\mathcal{U}=6.1$.

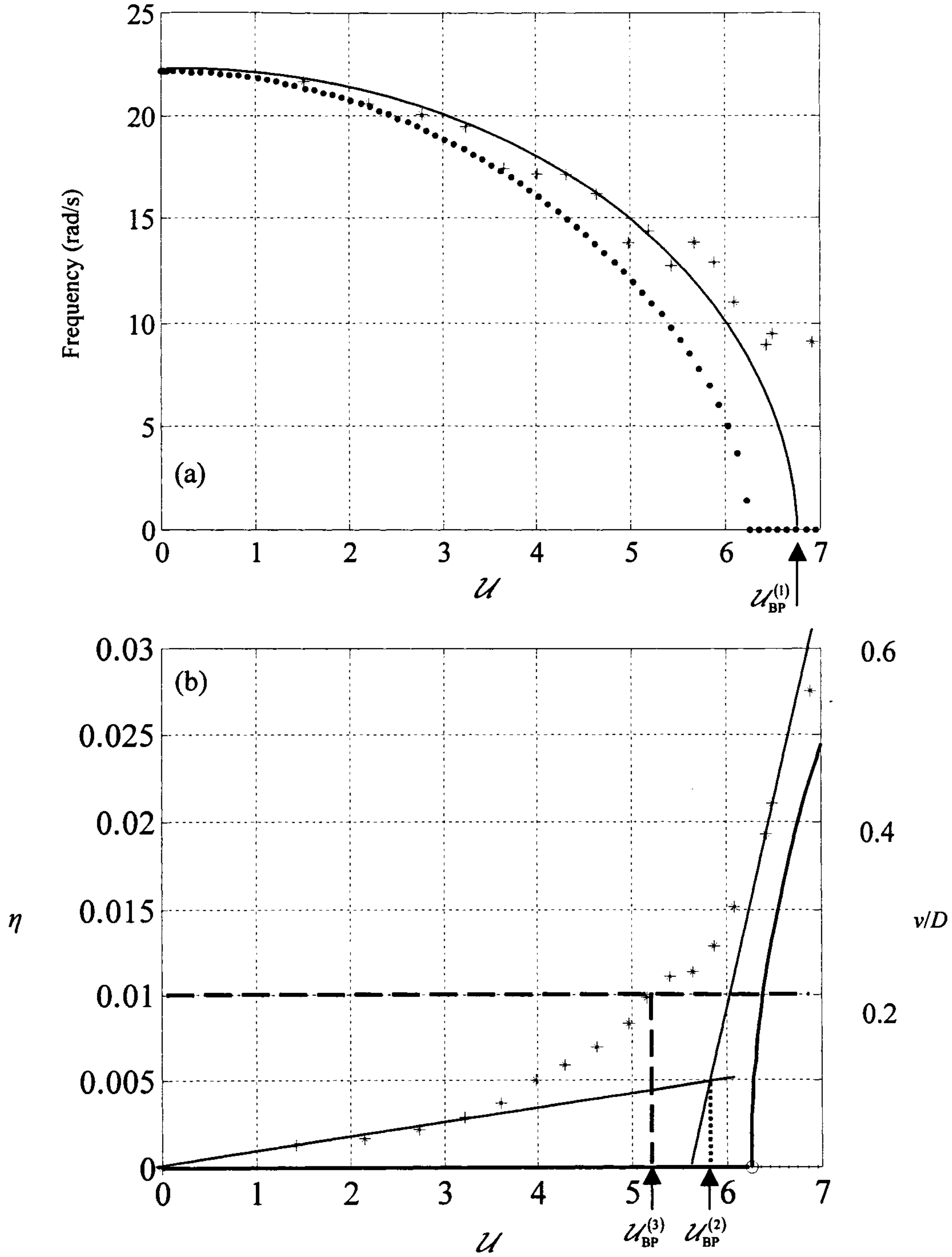

Figure 6-7 Experimental and theoretical results for the second series of experiments with a clamped-clamped cylinder with no end-sliding and with parameters given in Table 6-1. (a) Experimental (*) and theoretical (·) graphs of frequency versus dimensionless flow velocity; (b) comparison between theory (continuous line) and experiment (*) in the form of bifurcation diagrams.

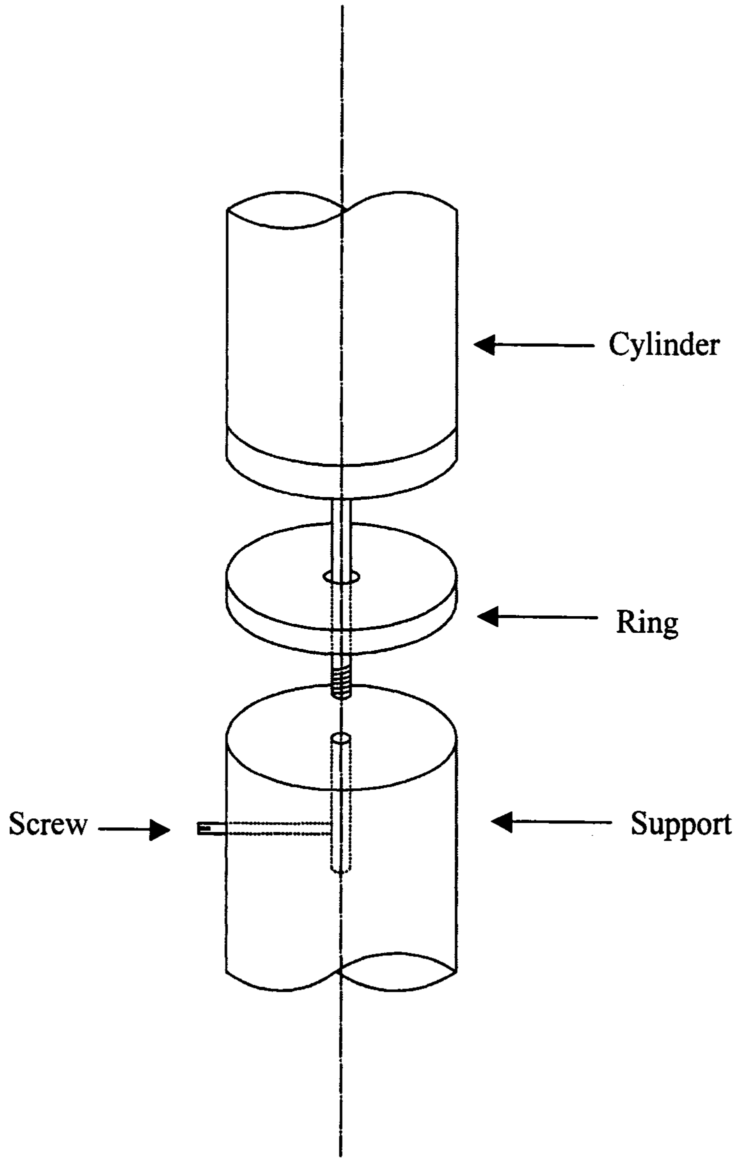

Figure 6-8 A schematic view of the downstream end of the system with a ring inserted between the lower end of the cylinder and the lower support.

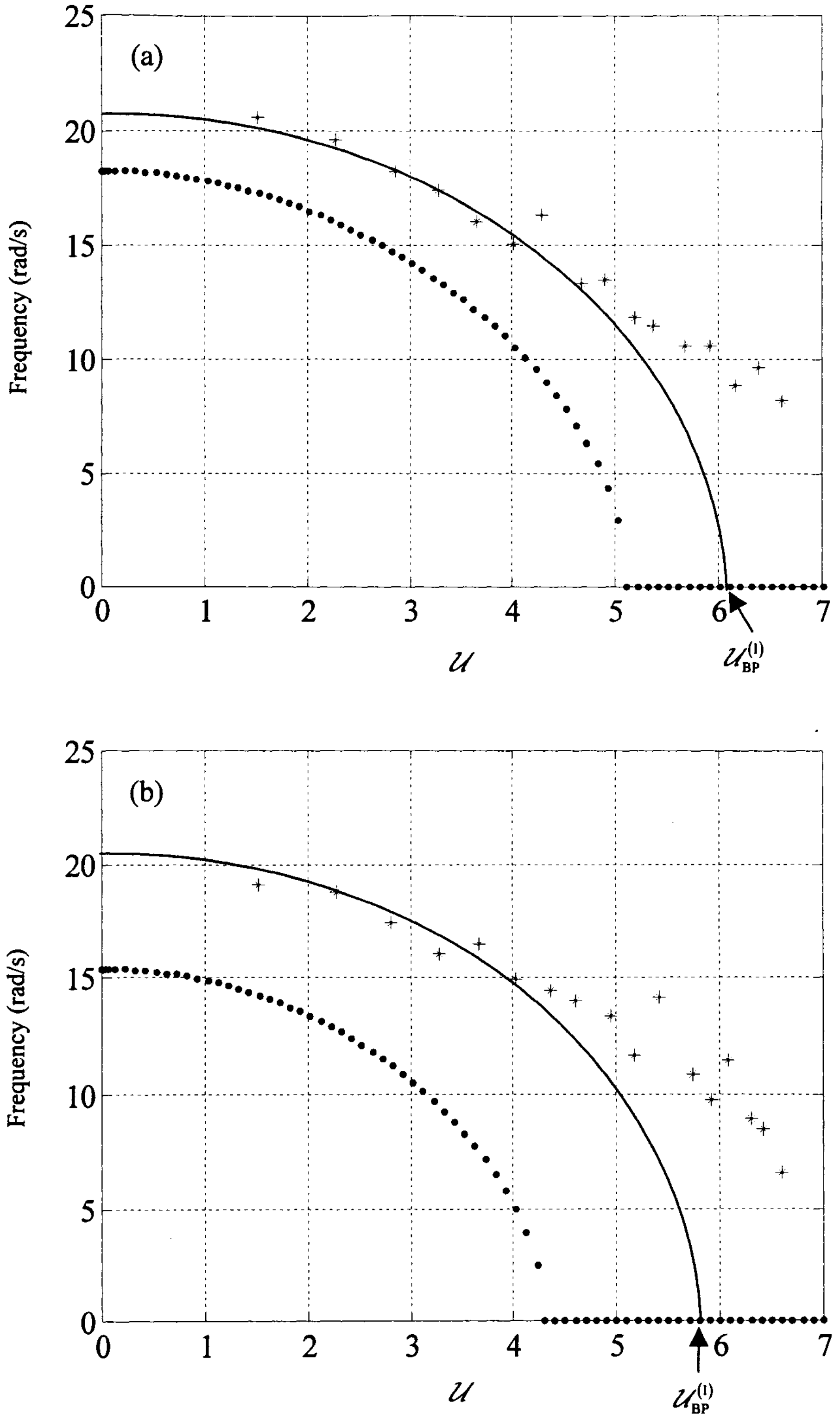

Figure 6-9(a,b); see next page.

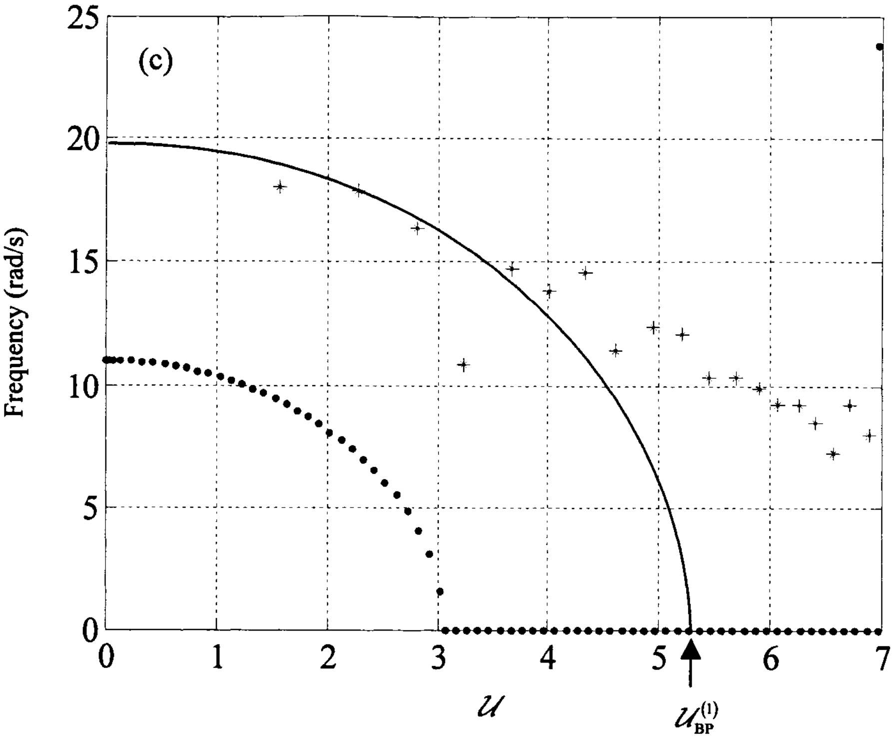

Figure 6-9: Experimental (*) and theoretical (·) values of pre-buckling turbulence-induced frequencies versus flow velocity for the cylinder clamped at both ends and with no end-sliding (parameters given in Table 6-1) for different externally applied axial compressions: (a) $\overline{\Gamma} = -12.9$; (b) $\overline{\Gamma} = -20.6$; (c) $\overline{\Gamma} = -29.7$.

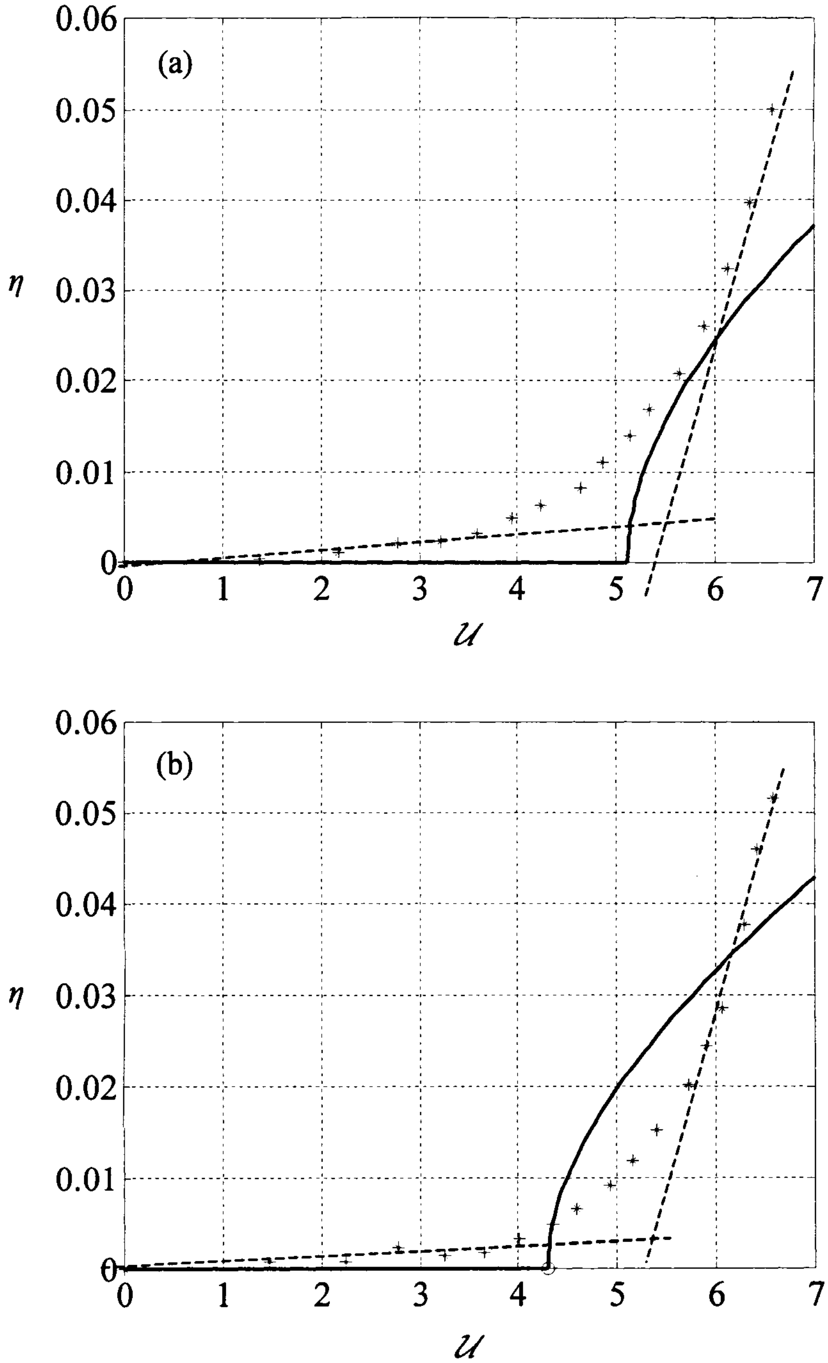

Figure 6-10(a,b); see next page.

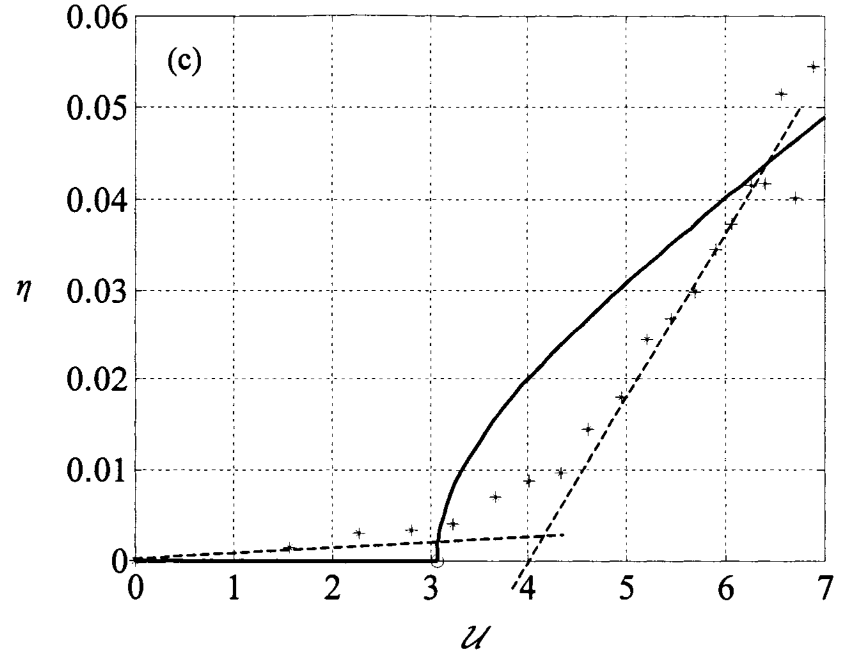

Figure 6-10 Experimental (*) and theoretical (-) bifurcation diagrams for the cylinder clamped at both ends and with no end-sliding (parameters given in Table 6-1) for different externally applied axial compressions: (a) $\bar{\Gamma} = -12.9$; (b) $\bar{\Gamma} = -20.6$; (c) $\bar{\Gamma} = -29.7$.

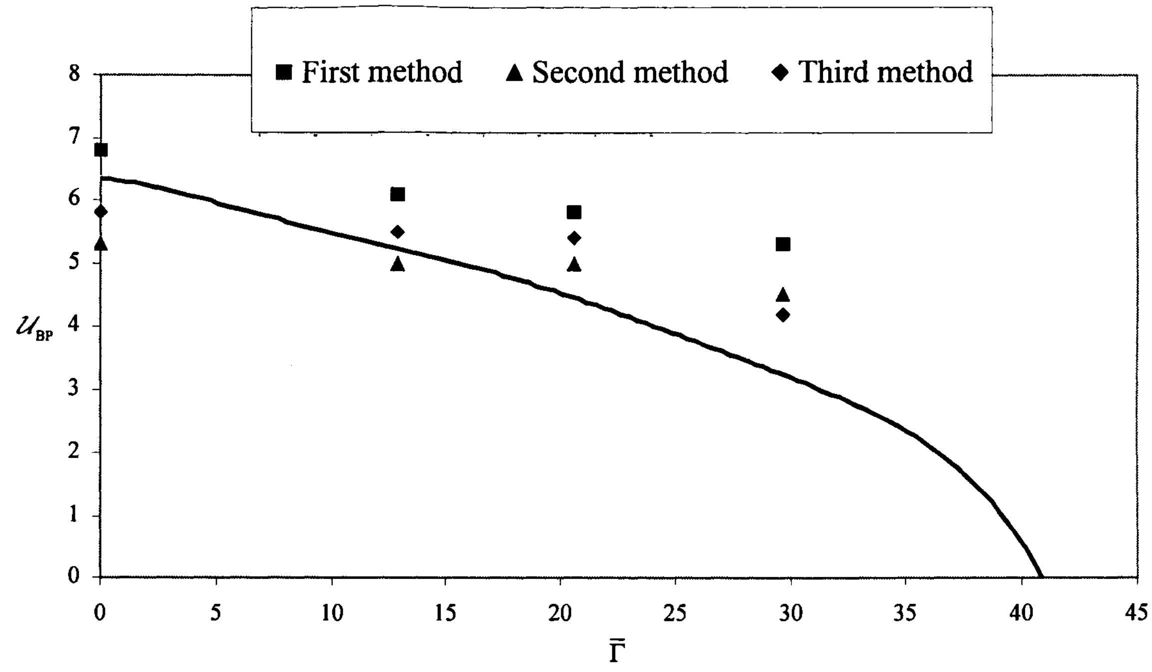

Figure 6-11 Critical flow velocities for divergence the cylinder clamped at both ends and with no end-sliding (parameters given in Table 6-1) for different externally applied axial compressions, found by using the three methods discussed: squares: the first method, triangles: the second method, rotated squares: the third method. The continuous line is the corresponding theoretical curve.

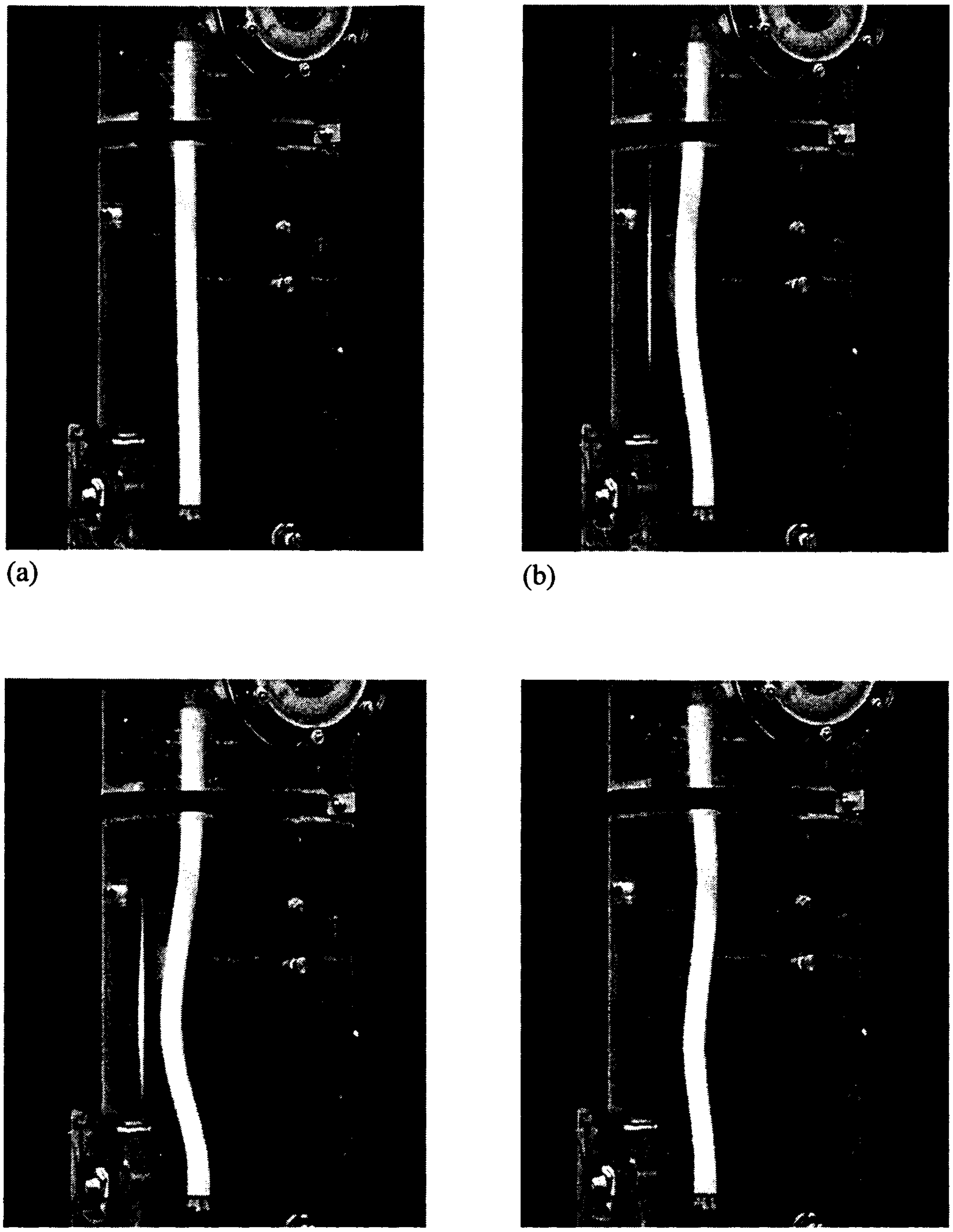
(a) (b) (c) (d)

Figure 6-12 The cylinder of the third series of experiments at different states: (a) pre-buckling, (b) small-amplitude buckling, (c) large-amplitude buckling, (d) oscillatory motions.

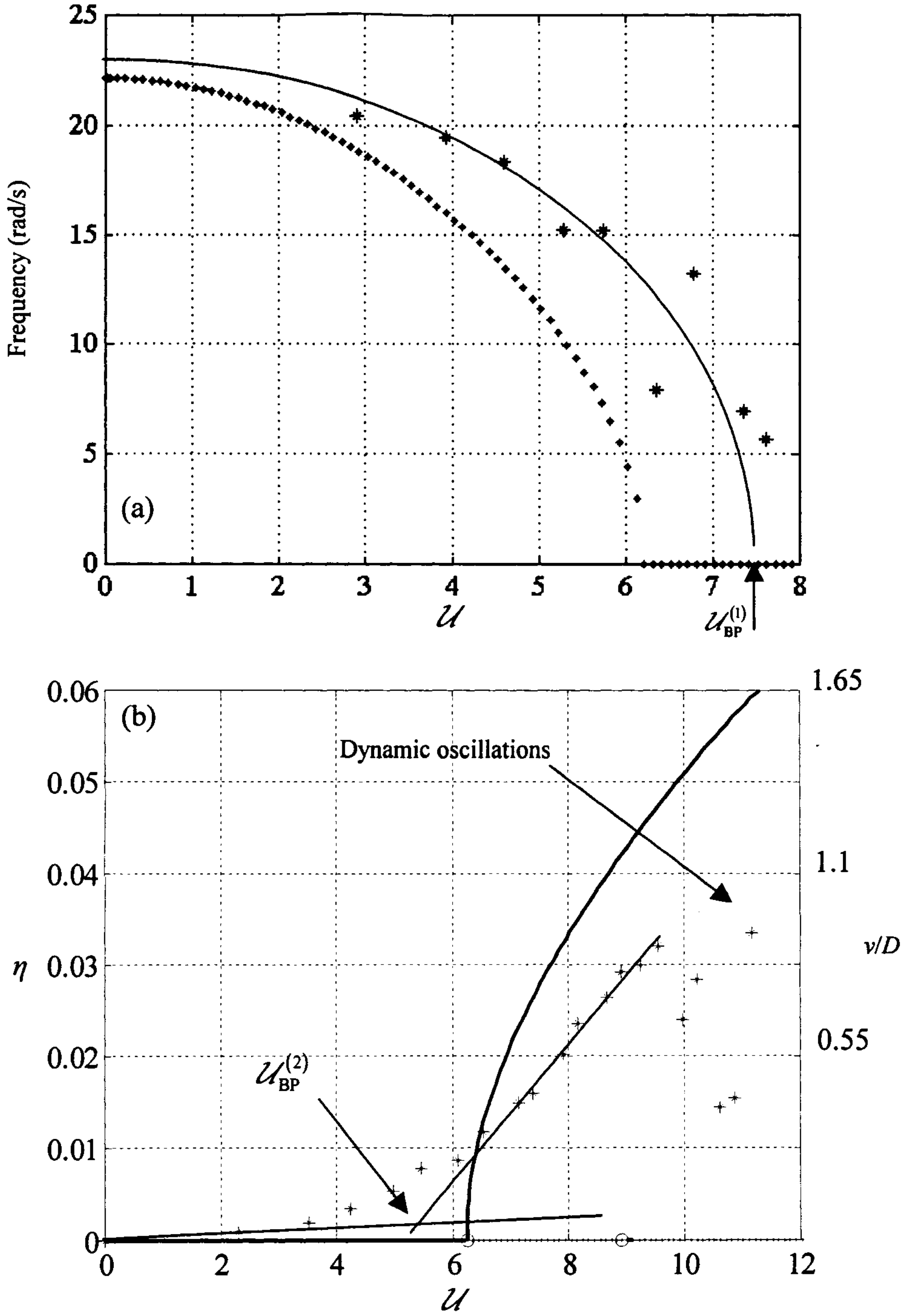

Figure 6-13 Comparison between theory and experiment for the third series of experiments with a small-diameter clamped-clamped cylinder with no end-sliding and with the parameters given in Table 6-5. (a) Experimental (*) and theoretical (·) graphs of frequency versus dimensionless flow velocity; (b) comparison between theory (continuous line) and experiment (*) in the form of bifurcation diagrams.

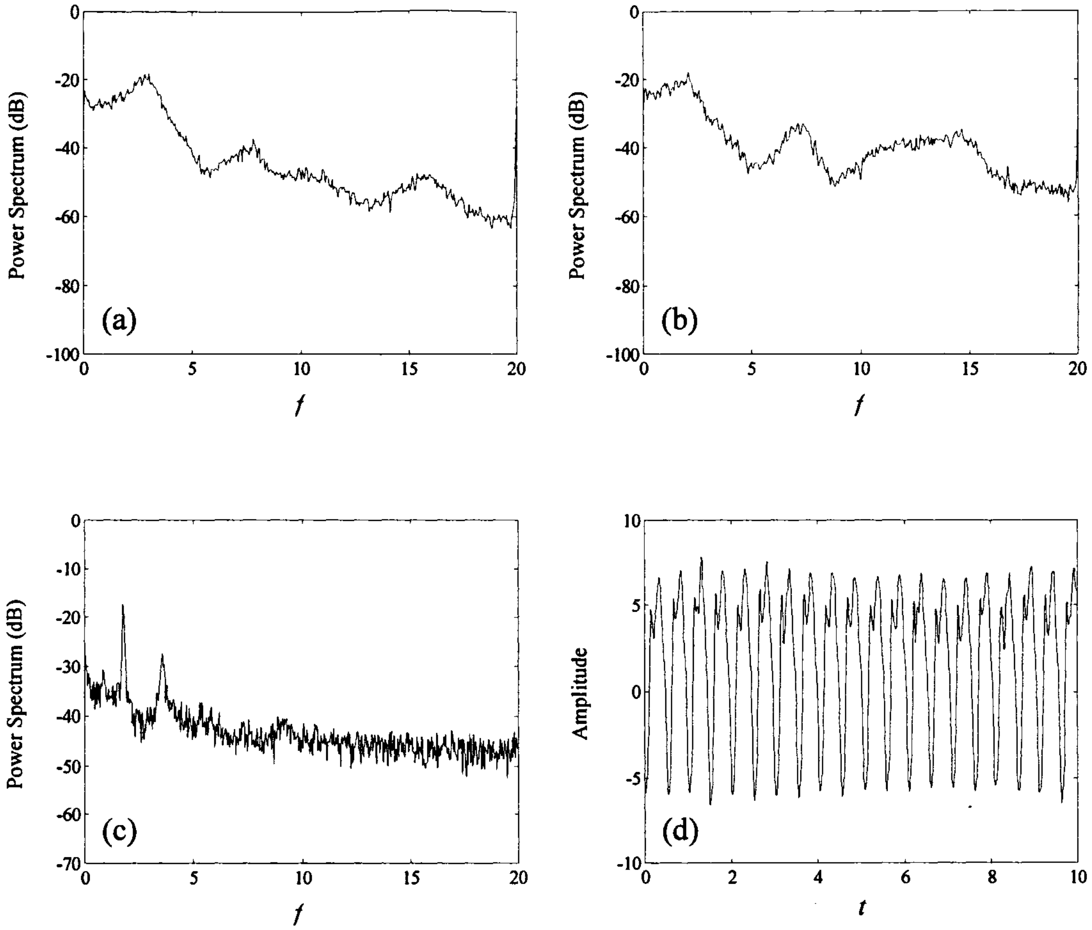

Figure 6-14 PSD plots for the third series of experiments with a small-diameter clamped-clamped cylinder with no end-sliding and with the parameters given in Table 6-5 at (a) $\mathcal{U}=4.2$, (b) $\mathcal{U}=6.5$ and (c) $\mathcal{U}=11.2$, together with (d) the time history at $\mathcal{U}=11.2$.

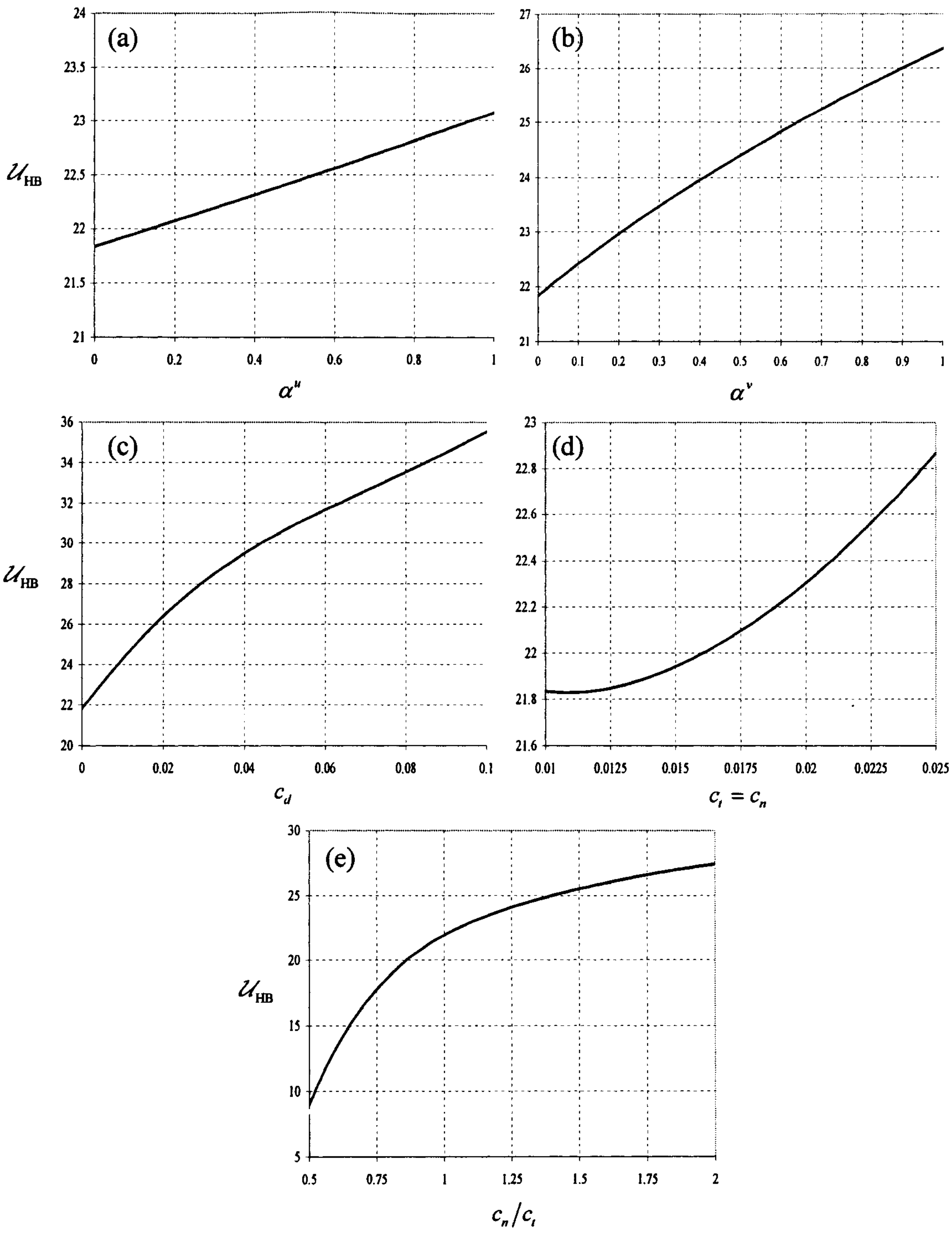

Figure 6-15 Influence of (a) the axial structural damping, (b) the coefficient of the modal damping in transverse direction, (c) the frictional coefficients c_n and c_t, and (d) the ratio of frictional coefficient c_n/c_t and (e) the form drag coefficient on the critical value of Hopf bifurcation for the system with the parameters given in Table 6-6.

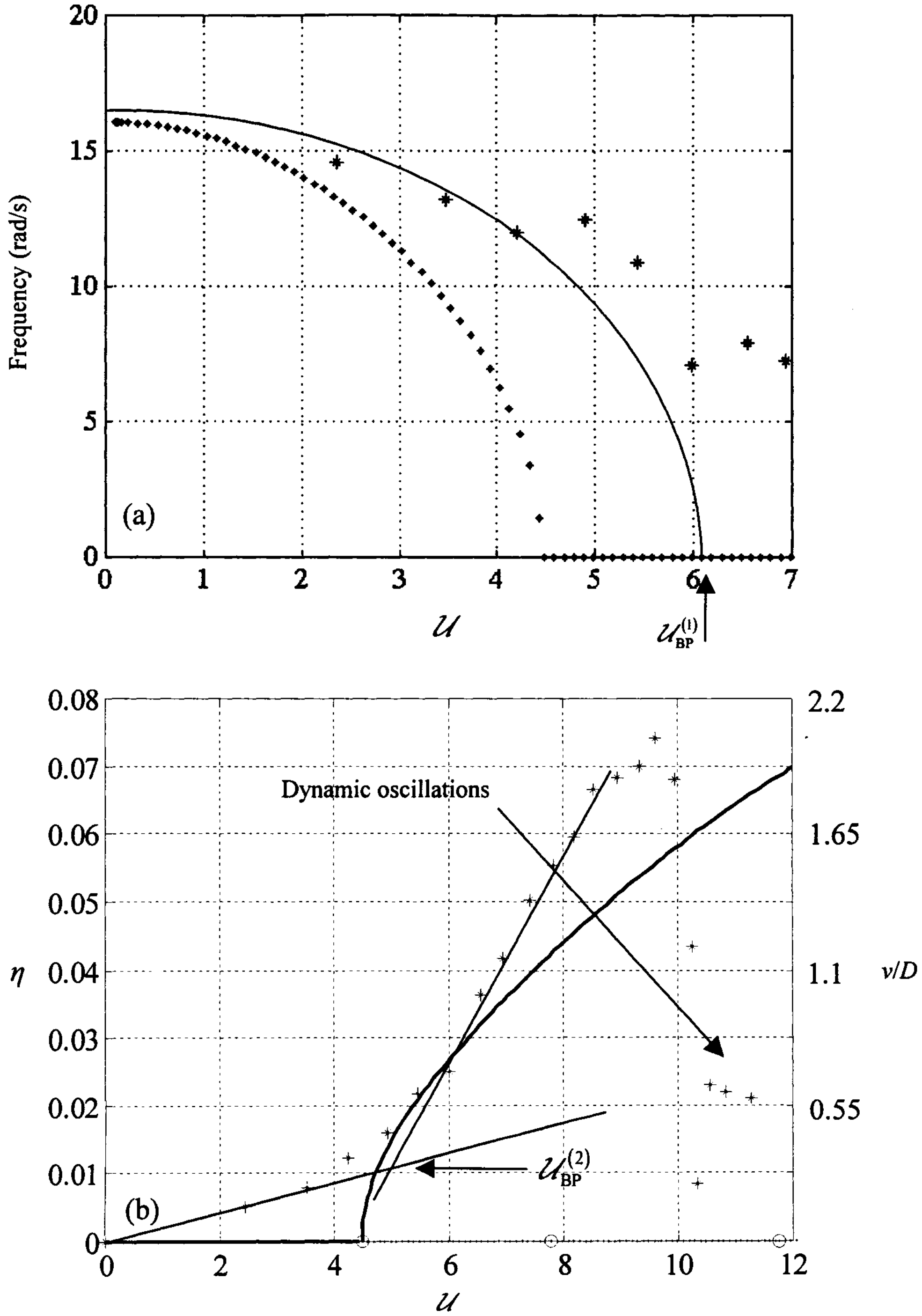

Figure 6-16 comparison between theory and experiment for the third series of experiments with the clamped-clamped cylinder with no end-sliding and (parameters given in Table 6-5) and under axial compression of $\overline{\Gamma} = -19.0$. (a) Experimental (*) and theoretical (·) graphs of frequency versus dimensionless flow velocity; (b) comparison between theory (continuous line) and experiment (*) in the form of bifurcation diagrams.

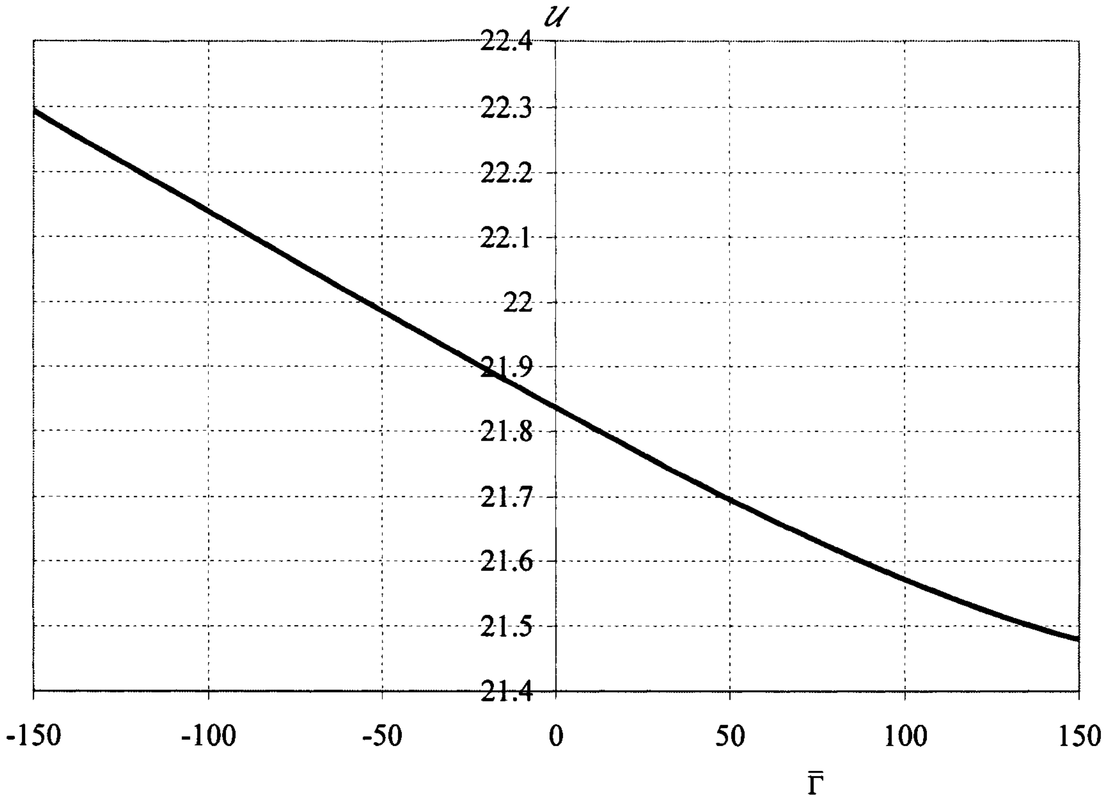

Figure 6-17 Theoretical result for influence of the external axial compression on the critical value of Hopf bifurcation for the system with the parameters given in Table 6-6.

7. Conclusion

7.1 Overview

In this thesis, the nonlinear dynamics of a slender flexible cylinder subjected to axial flow has been studied, both theoretically and experimentally. The linear studies by Païdoussis (1966b,c, 1973, 2004) have shown that, at sufficiently high flow velocity, the system loses stability by divergence, followed by coupled-mode flutter at higher flow velocities. But what has been predicted by the linear theory is reliable only for the first point of instability, and the linear results thereafter need to be validated by a nonlinear theory. Therefore, as mentioned in the Introduction (Chapter 1), the goals of this thesis were

1. to derive the nonlinear equations of motion for a cylinder supported at both ends and subjected to axial flow;
2. to study the post-divergence behaviour of such systems with various boundary conditions;
3. to study the behaviour of the system after the first post-divergence loss of stability and to study the possible route(s) to chaos, if and when it occurs;
4. to conduct a series of experiments to observe the system behaviour experimentally and also to validate the theoretical model.

To achieve the first goal, a nonlinear model was derived by considering various fluid forces, i.e. inviscid hydrodynamic forces, frictional forces and hydrostatic forces acting on a flexible cylinder, which was considered as a nonlinear Euler-Bernoulli beam. This model can be viewed as a nonlinear extension of the linear model of Païdoussis (1973). In fact, the ideas behind the derivation of the equations of motion are the same in these two studies: one from a linear point of view; the other from a nonlinear point of view.

To achieve the second goal, the dynamical behaviour of cylinders with various boundary conditions was investigated using the nonlinear model derived in this thesis. In general, for all the boundary conditions and for the parameters investigated in this thesis, it was found that the cylinder lost stability by a supercritical pitchfork bifurcation, and the amplitude of buckling increased with flow until the cylinder lost stability by a Hopf bifurcation, giving rise to periodic oscillations. Thus, by using a nonlinear theory, it was proved that flutter *does* exist at high flow velocities as had been predicted by the linear theory. In general, the onset of flutter was not very close to that predicted by the linear theory; in fact, flutter manifested itself in a different manner: it occurred when the cylinder had already buckled, while according to linear theory the oscillations start from the original equilibrium position. The important finding, however, was the *existence* of flutter as a post-divergence instability.

To achieve the third goal, the dynamics of the system with various boundary conditions was investigated for flow velocities greater than the critical flow velocity for flutter. This was done by using time histories, phase plane plots, power spectral density plots, and Poincaré maps; and by calculating the eigenvalues and Floquet multipliers. It was shown that, as the flow velocity increased, the periodic oscillations of the cylinder became period-2 oscillations via a period-doubling bifurcation. This was followed immediately (as the flow was further increased) by a torus bifurcation, giving rise to quasiperiodic oscillations. At higher flow velocities, it was shown that chaotic oscillations *do* exist. This trend was almost consistent for all the boundary conditions studied in this thesis, showing a quasiperiodic route to chaos for the system.

To achieve the fourth goal, three series of experiments were conducted on a vertical clamped-clamped flexible cylinder. In these experiments, by increasing flow velocity, the cylinder lost stability by divergence and the amplitude of buckling increased thereafter. At higher flow velocities, the cylinder lost stability by flutter, confirming the existence of a post-divergence oscillatory instability, this time experimentally. Also, good quantitative agreement was obtained between theoretical and experimental results for the amplitude of buckling, and for the critical flow velocities.

7.2 Summary of the work in this thesis

In the previous section, the major results of this thesis work were mentioned, while in this section, a detailed enumeration is presented.

A set of nonlinear equations of motion was derived using Hamilton's principle to describe the cylinder motion with increasing flow velocity. It was assumed that the cylinder centreline was extensible and also that the deflection in the transverse direction was of first-order magnitude, while the axial one of second-order. The final equations of motion were correct to third-order magnitude. The inviscid hydrodynamic forces were modelled by an extension to Lighthill's slender-body work. The frictional forces were formulated essentially as proposed by G.I. Taylor, and hydrostatic pressure forces were in fact the nonlinear extension of Païdoussis' formulation. These forces were determined separately for convenience and were put together in the form of the total virtual work of the fluid forces in Hamilton's principle. The resulting equations of motion were two coupled nonlinear partial differential equations with the cylinder axial and transverse displacements as the unknowns. By defining some dimensionless parameters, the equations of motion were nondimensionalized and the resulting nondimensional set of equations was discretized by Galerkin's technique. The eigenfunctions of a bar for the axial deformation and those of a beam for the transverse deformation were used as the basis functions. Depending on the boundary conditions of the system, the related eigenfunctions could be used. The resulting second-order differential equations were recast in a first-order form to make it possible to analyse the system using different tools.

To solve the set of ordinary differential equations, two numerical methods were used: Houbolt's finite difference method (FDM) and AUTO. In FDM the set of second-order ordinary differential equations were transformed to a set of nonlinear algebraic equations, which could be solved by the Newton-Raphson method. In AUTO the first-order form of the ordinary differential equations were solved, and using continuation and bifurcation theories the bifurcation diagram of the system were constructed very quickly, as compared to FDM; this was continued until the onset of quasiperiodic oscillations, after which only FDM was able to find the solutions. A combination of these two numerical methods was used to study the dynamical behaviour of the system for desired ranges of flow velocity.

The case of simply supported cylinders was studied thoroughly by producing some bifurcation diagrams, time histories, power spectral density and phase plane plots, together with Poincaré maps. It was found that the system lost stability by a pitchfork bifurcation, leading to divergence. The amplitude of buckling increased with flow velocity until the cylinder lost stability by a Hopf bifurcation at a higher flow velocity, leading to flutter. This confirmed the linear prediction of the existence of post-divergence oscillatory motions. With further increase in the flow velocity, a period-doubling bifurcation occurred; the resulting period-2 oscillations were followed at slightly higher flow by a torus bifurcation, giving rise to quasiperiodic oscillations. Chaotic oscillations were observed at still higher flow velocities. There was a range of flow velocities in which chaotic and stable nonzero static solutions co-existed, and the system could have one of these two solutions, depending on the initial conditions. The new nonzero static solution itself lost stability by a Hopf bifurcation and then the resulting periodic oscillations became quasiperiodic via a torus bifurcation. The influence of different parameters on the critical value and the amplitude of buckling was also investigated in the case of a simply supported cylinder.

Analytical centre manifold theory was used to study the behaviour of the system in the vicinity of the pitchfork bifurcation point by reducing the dimensions of the system in this neighbourhood to one. The results of this method confirmed the numerical results, by showing that the pitchfork bifurcation was indeed supercritical.

The study of the dynamics of the system was extended to different boundary conditions, such as clamped-clamped, clamped-hinged and hinged-clamped. It was found that, qualitatively, the cylinder behaviour with any of these boundary conditions was the same as a simply supported cylinder, but the quantitative behaviour changed from one set of boundary conditions to another. In general, the critical flow velocities for the simply supported cylinder were smaller than those for the clamped-hinged cylinders, which themselves were smaller than those for the hinged-clamped cylinders. A clamped-clamped cylinder was found to be the most stable one. Also, it was found that the frequency of oscillations for a simply supported or a clamped-hinged cylinder was almost twice as large as that for the other two boundary conditions.

The effect of number of modes used in Galerkin's technique was studied for all sets of boundary conditions. It was found that for simply supported, clamped-clamped and clamped-hinged cylinders at least 6 modes in each direction (axial and transverse) had to be used to obtain reliable results. For the case of a hinged-clamped cylinder, however, the minimum necessary number of modes in each direction was found to be 8.

Three series of experiments were conducted on a vertical clamped-clamped cylinder to observe experimentally the behaviour of the system, and to compare the results with the theoretical ones, and also to investigate the existence of post-divergence flutter. The flow velocity was increased from zero, and at each step the midpoint displacement of the cylinder was measured. In order to obtain the maximum transverse displacement of the cylinder midpoint, the measurements were conducted in two perpendicular directions, the resultant of which gave the value and the plane of the maximum transverse displacement.

In the first series of experiments, the lower end of the cylinder was free to slide axially, while in the second series of experiments, axial movement was prevented. The critical flow velocity for divergence was defined as the flow velocity at which the rate of change of the transverse displacement increased considerably. It was observed that the frequency of pre-buckling oscillations decreased parabolically with flow velocity, going toward zero at the critical flow velocity for divergence. In the second series of experiments, as an axial compression was applied on the cylinder externally, the critical flow velocity for divergence decreased and the amplitude of divergence for a fixed flow velocity increased, as one would expect. In both of these two series of experiments, no dynamic instabilities were observed, because the maximum attainable flow velocity in the water tunnel was limited.

In order to observe dynamic instabilities in the system, a third series of experiments was conducted on a more flexible cylinder, to make it possible to reach higher dimensionless flow velocities in the water tunnel. With increasing flow, the cylinder buckled and the amplitude of buckling increased thereafter. At higher flow velocities, the cylinder started oscillating mainly in its second mode. This was in agreement with the prediction of existence of flutter as post-divergence instability for a slender cylinder in axial flow. The externally applied axial compression was shown to have negligible effect on the critical flow velocity for dynamic instability; however, as observed also in the second series of experiments, it decreased the critical flow for the onset of buckling. Good agreement was obtained between theoretical and experimental values of the critical flow velocities and of the cylinder amplitude in all three series of experiments.

7.3 Suggestions for future work

The main goal of this thesis work was to introduce a nonlinear model for a slender flexible cylinder subjected to axial flow and then to use this model to study the behaviour of such a cylinder with various boundary conditions. This was also supported by a series of experiments conducted on a vertical cylinder in water flow.

The results of this thesis proved the existence of post-divergence flutter as predicted by linear theory (albeit with a different origination) and also showed a very rich dynamical behaviour of the system, including quasiperiodic and chaotic oscillations. Therefore, it is worth conducting a more comprehensive parametric study for the system using the model derived in this thesis for all the boundary conditions discussed in Chapter 5 to observe more interesting dynamics and possibly other routes to chaos. Also, it has been shown (Modarres-Sadeghi et al., 2006) that, in the very similar problem of a pipe conveying fluid and supported at both ends (internal axial flow), the system undergoes a subcritical pitchfork bifurcation for some particular parameters, when subjected to external axial compression. It is worth conducting a parametric study for the case of a cylinder in external flow to investigate the existence of subcritical pitchfork bifurcations. Also, in Chapter 6 of this thesis, it was shown that the normal and tangential frictional coefficients have a large influence on dynamic instability of the system. A more complete study of the values of these coefficients will be useful in the future to generalize the findings of this thesis to a wider range of cylinder properties.

The case of a cantilever cylinder with extensible centreline can be studied, in principle, by using the model presented in this thesis after taking into account the boundary conditions due to the ogival end of the cantilever cylinder. Some investigation on this case has already been started (Appendix B), showing a subcritical pitchfork bifurcation, but the fold and the stable nonzero solution thereafter could not be observed. On the other hand, the nonlinear study of a cantilever cylinder with inextensible centreline (Semler et al., 2002) has shown a supercritical pitchfork bifurcation. This discrepancy needs to be resolved or explained, in the future. One of the first steps toward resolving it would be to derive a model correct to a higher-order magnitude (e.g. fifth-order).

There are some possible improvements to the model. As an example, the model used in this thesis for structural damping is one of the simplest, which can be replaced by a more sophisticated and maybe even a nonlinear model in the future. Also, the models used for the fluid forces can be improved to bring the model closer to physical reality. For example, it was assumed that the flow velocity was constant all along the cylinder, even when the cylinder buckles or oscillates. The effect of changes in cylinder position on flow velocity can be included in the nonlinear model.

The quasiperiodic and chaotic oscillations of the cylinder in high flow velocities suggest the possibility of three-dimensional motions of the cylinder. A three-dimensional nonlinear model can be derived to investigate the existence of these motions. This seems to be much more complicated than the generalization of a two-dimensional model for a pipe conveying fluid to a three-dimensional one (Wadham-Gagnon et al., 2006), because of the complexity of the flow field around the cylinder compared to that inside a pipe.

A nonlinear finite-element model for the system of a slender flexible cylinder in axial flow can be obtained. Some attempts in this regard have been unsuccessful for the cases of structures (shells or cylinders) in axial flow. Work by Drs A. Lakis and M. Amabili has shown that the standard finite-element codes cannot yet handle these problems (Païdoussis, 2004; p. 1371). More investigation on this issue is necessary.

Some linear studies on problems similar to the problem of a slender flexible cylinder subjected to axial flow were discussed in the Introduction (Chapter 1), including the problem of a cylinder in confined flow, clustered cylinders, and towed and very long cylinders in axial flow. Basically, the nonlinear model of this thesis can be extended to study these cases from a nonlinear point of view. The model of this thesis can also be modified to consider cases of compressible subsonic and supersonic flow.

From a computational point of view there is some work to be done in the future. The first thing to be considered is to optimize the FDM program to increase the speed of convergence, e.g. by using variable time steps, or by using parallel programming methods. This program can also be modified to calculate the Jacobian numerically, so that one should not have to provide the program with an analytical form of the Jacobian. The centre manifold reduction method can also be applied to study the dynamic instability (Hopf bifurcation) of the cylinder analytically. Also, it is worth discretizing the equations of motion by using other methods of discretization, e.g. the one used for the linear model by Hannoyer (1972), in order to investigate the possibility of having faster convergence as compared with the Galerkin technique.

The experiments conducted in this thesis work were on a vertical clamped-clamped cylinder. Other series of experiments can be conducted on the cylinders with the other boundary conditions discussed theoretically in Chapter 4 and Chapter 5 of this thesis, i.e. simply supported, clamped-hinged and hinged-clamped. In all these cases as well as the case of clamped-clamped cylinder studied already in this thesis experimentally, the experiments can be conducted over a wider range of nondimensional flow velocities to make it possible to see the post-flutter behaviour of the system as predicted by theory, i.e. period-2, quasiperiodic and chaotic oscillations. This is possible by using more flexible and longer cylinders or by increasing the maximum attainable flow velocity in the water tunnel.

References

Ashly, H. and Haviland, G. 1950. Bending vibration of a pipe line containing flowing fluid. *Journal of Applied Mechanics* **17**, 229-232.

Augu, N., 1999. Nonlinear dynamics of a cylinder subjected to an axial external flow. Rapport de DEA. Départment de Mécanique, Ecole Centrale de Nantes and Department of Mechanical Engineering, McGill University.

Bajaj, A.K. and Sethna, P.R. 1984. Flow-induced vibations to three-dimensional oscillatory motions in continuous tubes. *SIAM Journal of Applied Mathematics* **44**, 270-286.

Bajaj, A.K. and Sethna, P.R. 1991. Effect of symmetry-breaking perturbations on flow-induced oscillations in tubes. *Journal of Fluids and Structures* **5**, 651-679.

Benjamin, T.B., 1961a. Dynamics of aystem of articulated pipes conveying fluid. I. Theory. *Proceedings of the Royal Society (London)* A **261**, 457-486.

Benjamin, T.B., 1961b. Dynamics of system of articulated pipes conveying fluid. II Experiment. *Proceedings of the Royal Society (London)* A **261**, 487-499.

Bhattacharyya, S.K., Vendhan, C.P. and Sudarsan, K., 2000. The finite element method for hydroelastic instability of underwater towed cylindrical structures. *Journal of Sound and Vibration* **237**, 119-143.

Blevins, R.D., 1994. *Flow-induced vibrations*, 2nd edition. Malabar, Florida: Krieger.

Botez, R.M. and Païdoussis, M.P., 1996. Dynamics of an articulated cylinder in annular flow via non-linear and partially linearized versions of an analytical model. *Journal of Sound and Vibration* **192**, 645-668.

Bourrières, F.-J., 1939. Sur un phénomène d'oscillation auto-entretenue en mécanique des fluides réels. Publications Scientifiques et Techniques du Ministère de l'Air, No. 147.

Burgreen, D., Byrnes, J.J. and Benforado, D.M., 1958. Vibration of rods induced by water in parallel flow. *Transactions ASME* **80**, 991-1003.

Carr, J. 1981. *Applications of Centre Manifold Theory.* New York: Springer-Verlag.

Chen, S.S., 1971. Dynamic stability of a tube conveying fluid. *ASCE Journal of the Engineering Mechanics* Division **97**, 1469-1485.

Chen, S.S., 1975. Vibration of nuclear fuel bundles. *Nuclear Engineering and Design* **35**, 399-422.

Copeland, G.S. & Moon, F.C., 1992. Chaotic flow-induced vibration of a flexible tube with end mass, *Journal of Fluids and Structures* **6**, 705-718; also in *American Society of Mechanical Engineers* AMD-Vol.152, pp. 63-77.

Dalton, C., 1980. Inertia coefficients for riser configurations. *ASME Journal of Energy Resources Technology* **102**, 197-202.

de Langre, E., Païdoussis, M.P., Doaré, O., Modarres-Sadeghi, Y., 2006. Flutter of long flexible cylinders in axial flow. Submitted to *Journal of Fluid Mechanics*.

Dodds, H.L. Jr., and Runyan, H.L., 1965. Effect of high velocity fluid flow on the bending vibrations and static divergence of a simply supported pipe. NASA Technical Note, D-2870.

Doedel, E.J. and Kernéves, J.P. 1986. AUTO: software for continuation and bifurcation problems in ordinary differential equations. Applied Mathematics Report, California Institute of Technology, Pasadena, California, U.S.A. (procurable from doedel@cs.concordia.ca)

Done, G.T.S, and Simpson, A., 1977. Dynamic stability of certain conservative and non-conservative systems. *I.Mech.E. Journal of Mechanical Engineering Science* **19**, 251-263.

Dowling, A.P., 1988a. The dynamics of the towed flexible cylinders. Part 1: Neutrally buoyant elements, *Journal of Fluid Mechanics* **187**, 507-532.

Dowling, A.P., 1988b. The dynamics of the towed flexible cylinders. Part 2: Negatively buoyant elements, *Journal of Fluid Mechanics* **187**, 533-571.

Feodos'ev, V.P., 1951. Vibrations and stability of a pipe when liquid flow through it. *Inzhenernyi Sbornik* **10**, 169-170.

Gregory, R.W. and Païdoussis, M.P., 1966a. Unstable oscillation of tubular cantilevers conveying fluid. I. Theory. *Proceedings of the Royal Society (London)* A **293**, 512-527.

Gregory, R.W. and Païdoussis, M.P., 1966b. Unstable oscillation of tubular cantilevers conveying fluid. II. Experiment. *Proceedings of the Royal Society (London)* A **293**, 528-542.

Grigoryev, U.V., Guskov, A.M. and Svetlisky, V.A., 1979. Rod stability in axial flow of viscous fluid. *Prikladnaia Mekhanika* **15**, 67-73 (in Russian).

Guckenheimer, J. and Holmes, P. 1983 *Nonlinear Oscillations, Dynamical Systems and Bifurcations of Vector Fields.* New York: Springer-Verlag.

Hamy, N., 1971. *The Trebron Sea Chain System.* Trebron Holdings Ltd., Montreal, Québec, Canada.

Hannoyer, M.J., 1972. A solution to linear differential equations in the field of dynamics of continuous systems. Mechanical Engineering Research Laboratories Report, MERL 72-5, McGill University, Montreal, Canada.

Hannoyer, M.J. and Païdoussis, M.P., 1979a. Dynamics of slender tapered beams with internal or external axial flow. Part 1: Theory, *Journal of Applied Mechanics* 46, 45-51.

Hannoyer, M.J. and Païdoussis, M.P., 1979b. Dynamics of slender tapered beams with internal or external axial flow. Part 2: Experiments, *Journal of Applied Mechanics* 46, 45-51.

Hawthorne, W. R., 1961. The early development of the Dracone flexible barge. *Proceedings of the Institution of Mechanical Engineers* **175**, 52-83.

Hill J. L., Swanson, C. P., 1970. Effects of lumped masses on the stability of fluid conveying tubes. *Journal of Applied Mechanics* **37**, 494-497.

Hobson, D.E., 1982. Fluid-elastic instabilities cause by flow in an annulus, *Proceedings of 3rd International Conference on Vibration in Nuclear Plant*, Keswick, pp. 440-463. London: BNES.

Holmes, P.J., 1978. Pipes supported at both ends cannot flutter. *Journal of Applied Mechanics* **45**, 619-622.

Housner, G.W., 1952. Bending vibrations of a pipe line containing flowing fluid. *Journal of Applied Mechanics* **19**, 205-208.

Jendrzejczyk, K. and Chen, S.S., 1985. Experiments of tubes conveying fluid. *Thin-Walled Structures* **3**, 109-134.

Latorre, R. and Zachariadis, P., 1983. Feasibility and economics of fluid cargo transport by submerged flexible barges towed by a tugboat. *Proceedings International*

Symposium on Ship Hydrodynamics and Energy Saving, El Pardo, Spain, pp. X3-1-X3-25. Madrid: Canal de Experiencias.

Lighthill, M. J., 1960. Note on the swimming of slender fish. *Journal of Fluid Mechanics* **9**, 305-317.

Lin, L. and Raptis, A.C., 1986. Acoustic resonances in cylinder bundles oscillating in a compressible fluid. *ASME Journal of Pressure Vessel Technology* **108**, 197-201.

Lopes, J. L., Païdoussis, M.P., Semler, C., 1999. Nonlinear dynamics of a cylinder in steady axial flow. Mechanical Engineering Research Laboratories, Report MERL-99-1, department of Mechanical Engineering, McGill University, Montreal, Québec, Canada.

Lopes, J. L., Païdoussis, M.P., Semler, C., 2002. Linear and nonlinear dynamics of cantilevered cylinders in axial flow. Part 2: The equation of motion. *Journal of Fluids and Structures* **16**, 715-737.

Lundgren, T.S., Sethna, P.R. and Bajaj, A.K., 1979. Stability boundaries for flow induced motions of tubes with an inclined terminal nozzle. *Journal of Sound and Vibration* **64**, 553-571.

Mateescu, D. and Païdoussis, M.P., 1985. The unsteady potential flow in an axially variable annulus and its effects on the dynamics of the oscillating rigid centre-body. *ASME Journal of Fluids Engineering* **107**, 421-427.

Mateescu, D. and Païdoussis, M.P., 1987. Unsteady viscous effects on the annular-flow-induced instabilities of a rigid cylindrical body in a narrow duct. *Journal of Fluids and Structures* **1**, 197-215.

Mateescu, D., Païdoussis, M.P. and Bélanger, F., 1988. Unsteady pressure measurements on an oscillating cylinder in narrow annular flow. *Journal of Fluids and Structures* **2**, 615-628.

Mateescu, D., Païdoussis, M.P. and Bélanger, F., 1994a. Unsteady annular viscous flows between oscillating cylinders. Part I. Computational solutions based on a time-integration method. *Journal of Fluids and Structures* **8**, 489-507.

Mateescu, D., Païdoussis, M.P. and Bélanger, F., 1994b. Unsteady annular viscous flows between oscillating cylinders. Part II. A Hybrid time-integration solution based on azimuthal Fourier expansions for configurations with annular backsteps. *Journal of Fluids and Structures* **8**, 489-507.

Modarres-Sadeghi, Y. 2006. Stability of an Inextensible or extensible cantilever beam subjected to axial flow or a tip-concentrated force. MERL Report. McGill University (under preparation).

Modarres-Sadeghi, Y., M., Païdoussis, M. P., Semler, C and Picot, P. 2003. Nonlinear dynamics of slender cylinders supported at both ends and subjected to axial flow. *Proceedings IUTAM Symposium on Integrated Modeling of fully Coupled Fluid-Structure Interactions* (eds H. Benaroya and T. Wei), Rutgers University, USA.

Modarres-Sadeghi, Y., M.P. Païdoussis, Camargo, A., 2006. The behaviour of fluid-conveying pipes, supported at both ends, by the complete extensible nonlinear equations of motion. *Proceedings of PVP2006-ICPVT11: Pressure Vessels and Piping Division Conference.* Vancouver, British Columbia, Canada.

Modarres-Sadeghi, Y., Semler, C., Wadham-Gagnon, M., Païdoussis, M. P., 2006. Dynamics of cantilevered pipes conveying fluid. Part 3: three dimensional dynamics in the presence of an end-mass. *Journal of Fluids and Structures*, under review.

Mote, Jr, C.D., 1968. Dynamic stability of an axially moving band. *Journal of the Franklin Institute* **285**, 329-346.

Nath Y., and Sandpeet K., 1994. The stability of the Houbolt time marching scheme in nonlinear systems. *Journal of Sound and Vibration* 175, 565-569.

Nikolić, M. and Rajković, M. 2006. Bifurcations in nonlinear models of fluid-conveying pipes supported at both ends. *Journal of Fluids and Structures* 22, 173-195.

Niordson, F.I. 1953. Vibrations of a cylindrical tube containing flowing fluid. *Kungliga Tekniska Hogskolans Handlingar* (Stockholm) No. 73. Also *Acta Polytechnica*, Mechanical Engineering Series, Vol. 3, No. 2, 1954, The Royal Swedish Academy of Engineering Sciences.

Ortloff, C.R. and Ives, J. 1969. On the dynamic motion of a thin flexible cylinder in a viscous stream. *Journal of Fluid Mechanics* **38**, 713-720.

Païdoussis, M.P., 1963. Oscillations of liquid-filled flexible tubes. Ph.D. Thesis, University of Cambridge.

Païdoussis, M.P., 1965. The amplitude of fluid-induced vibration of cylinders in axial flow. Atomic Energy of Canada Report AECL-2225, Chalk River, Onratio, Canada.

Païdoussis, M.P., 1966a. Vibration of cylinders with supported ends, induced by axial flow. *Proceedings Institution of Mechanical Engineers* **180**, 268-278.

Païdoussis, M.P., 1966b. Dynamics of flexible slender cylinders in axial flow. Part 1: Theory. *Journal of Fluid Mechanics* **26**, 717-736.

Païdoussis, M.P., 1966c. Dynamics of flexible slender cylinders in axial flow. Part 2: Experiments. *Journal of Fluid Mechanics* **26**, 737-751.

Païdoussis, M.P., 1968. Stability of towed, totally submerged flexible cylinders. *Journal of Fluid Mechanics* **34**, 273-297.

Païdoussis, M.P., 1970a. Dynamics of submerged towed cylinders. *Eighth Symposium on Naval Hydrodynamics: Hydrodynamics in the Ocean Environment.* United States ONR, ARC-179, pp. 981-1016.

Païdoussis, M.P., 1970b. Dynamics of tubular cantilevers conveying fluid. *Journal of Mechanical Engineering Science* **12**, 85-103.

Païdoussis, M.P., 1973. Dynamics of cylindrical structures subjected to axial flow. *Journal of Sound and Vibration* **29**, 365-385.

Païdoussis, M.P., 1976. Dynamics of fuel strings in axial flow. *Annals of Nuclear Energy* **3**, 19-30.

Païdoussis, M.P., 1979. The dynamics of clusters of flexible cylinders in axial flow: theory and experiments. *Journal of Sound and Vibration* **65**, 391-417.

Païdoussis, M.P., 1980. Flow-induced vibrations in nuclear reactors and heat exchangers: Practical experiences and state of the knowledge. In *Practical Experiences with Flow-Induced Vibrations* (eds E. Naudascher and D. Rockwell), pp. 1-81. Berlin: Springer-Verlag.

Païdoussis, M.P., 1986. Stability of a chain of cylinders traveling underwater. *Proceedings 5th International OMAE Symposium*, Vol. 1, pp. 483-490. New York: ASME.

Païdoussis, M.P., 1991. Pipes conveying fluid: a model dynamical problem. In *Proceedings of CANCAM'91 (Canadian Congress of Applied Mechanics)*, Winnipeg, Manitoba, Canada, pp. 1-33.

Païdoussis, M.P., 1993. Calvin Rice Lecture: Some curiosity-driven research in fluid-structure interactions and its current applications. *ASME Journal of Pressure Vessel Technology* **115**, 2-14.

Païdoussis, M.P., 1998. *Fluid-Structure Interactions: Slender Structures and Axial Flow, Vol. 1*. Academic Press, London.

Païdoussis, M.P., 2004. *Fluid-Structure Interactions: Slender Structures and Axial Flow, Vol. 2*. Elsevier Academic Press, London.

Païdoussis, M.P., 2005. Some unresolved issues in fluid-structure interactions. *Journal of Fluids and Structures* 20, 871-890.

Païdoussis, M.P. and Besançon, P., 1981. Dynamics of arrays of cylinders with internal and external axial flow. *Journal of Sound and Vibration* **76**, 361-380.

Païdoussis, M.P. and Botez, R.M., 1993. Chaotic dynamics of articulated cylinders in confined axial flow. *Journal of Fluids and Structures* **7**, 719-750.

Païdoussis, M.P. and Botez, R.M., 1995. Three routes to chaos for a three-degree-of-freedom articulated cylinder system subjected to annular flow and impacting on the outer pipe. *Nonlinear Dynamics* **7**, 429-450.

Païdoussis, M.P. and Issid, N.T., 1974. Dynamic instability of pipes conveying fluid. *Journal of Sound and Vibration* 33, 267-294.

Païdoussis, M.P. and Ostroja-Strazewski, M., 1981. Dynamics of a flexible cylinder in subsonic axial flow. *AIAA Journal* **19**, 1467-1475.

Païdoussis, M.P. and Semler C., 1993a. Nonlinear and chaotic oscillations of a constrained cantilevered pipe conveying fluid: a full nonlinear analysis. *Nonlinear Dynamics* **4**, 655-670.

Païdoussis, M.P. and Semler C., 1993b. Nonlinear dynamics of a fluid-conveying cantilevered pipe with an intermediate support. *Journal of Fluids and Structures* **7**, 269-298.

Païdoussis, M.P. and Semler C., 1998. Nonlinear dynamics of a fluid-conveying cantilevered pipe with a small mass attached at the free end. *International Journal of Non-Linear Mechanics* **33**, 15-32.

Païdoussis, M.P. and Suss, S., 1977. Stability of a cluster of flexible cylinders in bounded flow. *Journal of Applied Mechanics* **44**, 401-408. Discussion 1978, **45**, 455 and 703.

Païdoussis, M.P. and Yu, B.K., 1976. Elastohydrodynamic and stability of towed slender bodies of revolution. *AIAA Journal of Hydronautics* **10**, 127-134.

Païdoussis, M.P., Chaubernard, J.-P., Genadry, M.R. and El Barbir, K.N., 1983b. Dynamics of a cluster of flexibly interconnected cylinders. Part1. In axial flow. *Journal of Applied mechanics* **50**, 429-435.

Païdoussis, M.P., Curling, L.R. and Gagnon, J.O., 1982. Experiments on fluidelastic instability of cylinder clusters in axial flow. *ASME Journal of Fluids Engineering* **104**, 342-347.

Païdoussis, M.P., El Barbir, K.N., Genadry, M.R. and Chaubernard, J.-P., 1983a. Dynamics of a cluster of flexibly interconnected cylinders. Part1. In vacuum. *Journal of Applied Mechanics* **50**, 421-428.

Païdoussis, M.P., Grinevich E., Adamovic, D., Semler, C., 2002. Linear and nonlinear dynamics of cantilevered cylinders in axial flow. Part 1: Physical Dynamics. *Journal of Fluids and Structures* **16**, 691-713.

Païdoussis, M.P., Mateescu, D. and Sim, W.-G., 1990. Dynamics and stability of a flexible cylinder in a narrow coaxial cylindrical duct subjected to annular flow. *Journal of Applied Mechanics* **57**, 232-240.

Païdoussis, M.P., Semler, C. and Wadham-Gagnon, M., 2006. Dynamics of cantilevered pipes conveying fluid. Part 2: dynamics of the system with intermediate spring support. *Journal of Fluids and Structures*, under review.

Pao, H.P., 1970. Dynamical stability of a towed thin flexible cylinder. *AIAA Journal of Hydronautics* **4**, 144-150.

Park, K.C., 1975. An improved stiffly stable method for direct integration of nonlinear structural dynamic equations. *Journal of Applied Mechanics* **42**, 464-470.

Pavlica, R.T. and Marshall, R.C., 1966. An experimental study of fuel assembly vibrations induced by coolant flow. *Nuclear Engineering and Design* **4**, 54-60.

Pramila, A., 1987. Natural frequencies of a submerged axially moving band. *Journal of Sound and Vibration* **113**, 198-203.

Prokhorovich, V.A., Prokhorovich, P.A. and Smirnov, L.V., 1982. Dynamic stability of a flexible rod in a longitudinal incompressible fluid flow. *Prikladnaya Mekhanika* **18**, 108-112 (translated from Russian).

Quinn, E.P., 1962. Vibration of fuel rods in parallel flow. U.S. Atomic Energy Commission Report GEAP-4059.

Quinn, E.P., 1965. Vibration of SEFOR fuel rods in parallel flow. U.S. Atomic Energy Commission Report GEAP-4966.

Roström, K.G., 1964. Seven-rod fuel element – Vibration test. Ab. Atomenergi (Stockholm), Arbetsrapport RRL-726.

Roström. K.G., and Andersson, N., 1964a. Boiler element for Marviken. Vibration tests with one rod. Ab. Atomenergi (Stockholm), Arbetsrapport RRL-724.

Roström. K.G., and Andersson, N., 1964b. Superheater element for Marviken. Vibration tests with one rod. Ab. Atomenergi (Stockholm), Arbetsrapport RRL-725.

Rousselet, J. and Herrmann, G., 1977. Flutter of articulated pipes at finite amplitude. *Journal of Applied Mechanics* **44**, 154-158.

Rousselet, J. and Herrmann, G., 1981. Dynamic behaviour of continuous cantilevered pipes conveying fluid near critical flow velocities. *Journal of Applied Mechanics* **48**, 943-947.

Semler, C. and Païdoussis, M.P., 1995. Intermittency route to chaos of a cantilevered pipe conveying fluid fitted with a buoyant end-mass. *Journal of Applied Mechanics* **62**, 903-908.

Semler, C., Gentleman, W. C., Païdoussis, M.P., 1996. Numerical solutions of second-order implicit ordinary differential equations. *Journal of Sound and Vibration* **195**, 553-574

Semler, C., Li, G.X. and Païdoussis, M.P., 1994. The non-linear equations of motion of pipes conveying fluid. *Journal of Sound and Vibration* **169**, 577-599.

Semler, C., Lopes, J.-L, Augu, N., Païdoussis, M.P., 2002. Linear and nonlinear dynamics of cantilevered cylinders in axial flow. Part 3: Nonlinear dynamics. *Journal of Fluids and Structures* **16**, 739-759.

Shields, C.M., 1960. N.S. Savannah fuel design and developemenet program – fuel rod vibration. United States Atomic Energy Commission Report GEAP-3583.

SOGREAH 1962. Study of vibrations and load losses in tubular clusters, Société Grenobloise d'Etudes et Applications Hydrauliques, Special Report No. 3, EURAEC-288.

Steindl, A. and Troger, H. 1996, Heteroclinic cycles in three-dimensional post-bifurcation motion of *O*(2)-symmetrical fluid conveying tubes. *Applied Mathematics and Computation* **78**, 269-277.

Stoker, J.J., 1968. *Nonlinear Elasticity.* Gordon and Breach, New York.

Sudarsan, K., Bhattacharyya, S.K. and Vendhan, C.P., 1997. An experimental study of hydrostatic instability of flexible towed underwater cylindrical structures. *Proceedings 16th OMAE Conference*, Yokohama, Japan, Vol. A, pp. 73-80. New York: ASME.

Sugiyama, Y., Kawagoe, H., Kishi, T., Nishiyama, S., 1988. Studies on the stability of pipes conveying fluid (the combined effect of a spring support and a lumped mass). *JSME International Journal*, Series 1, **31**, 20-26.

Taylor, G. I., 1952. Analysis of the swimming of long and narrow animals. *Proceedings of the Royal Society (London)* A**214**, 158-183.

Theodoracatos, V.E. and Calkins, D.E. 1986. An experimental study of elastohydrodynamics of towed flexible cylinders aided by video image processing. *Ocean Engineering* **2**, 587-619.

Thurman, A.L. and Mote, C.D. Jr., 1969. Nonlinear oscillation of a cylinder containing flowing fluid. *ASME Journal of Engineering for Industry* 91, 1147-1155.

Tillerson J.R., and Stricklin J.A., 1970. Numerical methods of integration applied in the nonlinear dynamic analysis of shells of revolution. *Report NASA-CR*-097528. Washington, D.C.: National Aeronautics and Space Administration.

Triantafyllou, G. S., Chryssostomidis, C., 1984. Analytic determination of the buckling speed of towed slender cylindrical beams. *ASME Journal of Energy Resources Technology* **106**, 246-249.

Triantafyllou, G. S., Chryssostomidis, C., 1985. Stability of a string in axial flow. *ASME Journal of Energy Resources Technology* **107**, 421-425.

Triantafyllou, G. S., Chryssostomidis, C., 1989. The dynamics of towed arrays. *ASME Journal of Offshore Mechanics and Arctic Engineering* **111**, 208-213.

Vendhan, C.P., Bhattacharyya, S.K. and Sudarsan, K., 1997. Stability characteristics of slender flexible cylinders in axial flow by the finite element method. *Journal of Sound and Vibration* **208**, 587-601.

Wadham-Gagnon, M., Païdoussis, M. P., Semler, C., 2006. Dynamics of cantilevered pipes conveying fluid, part 1: nonlinear equations of three-dimensional motion. *Journal of Fluids and Structures*, under review.

Wu, R.W.H. and Witmer E.A., 1973. Nonlinear transient responses of structures by the spatial finite element method. *American Institute of Aeronautics and Astronautics Journal* 11, 1110-1117.

A. The coefficients of the tensor-form equations

In this appendix, the coefficients of the tensor-form of the equations of motion (2-68) and (2-69), are presented, as follows:

$$M_{ij}^{u} = (1-\beta)\int_0^1 \psi_i \psi_j d\xi, \qquad C_{ij}^{\ u} = 2\varsigma\lambda_i^u\sqrt{\Pi_0}\,^{*},$$

$$K_{ij}^{\ u} = -\Pi_0\int_0^1 \psi_i\psi_j'' d\xi + \left[\frac{1}{2}\mathcal{U}^2\varepsilon c_t(1+h)+\gamma\right]\int_0^1 \psi_i\psi_j' d\xi,$$

$$\begin{aligned}A_{ijk}^{\ 1} = &-\left(\frac{1}{2}\gamma+\frac{1}{2}\mathcal{U}^2\varepsilon\left(c_n+\frac{1}{2}(h-1)c_t\right)\right)\int_0^1 \psi_i\phi_j'\phi_k' d\xi \\ &+\Bigg(\gamma\left(1-\frac{1}{2}\delta\right)-\mathcal{U}^2\chi+(1-2\nu)\overline{\Pi}\delta \\ &\quad+\overline{\Gamma}\delta+\frac{1}{2}\mathcal{U}^2 c_b(1-\delta)+\frac{1}{2}\mathcal{U}^2\varepsilon c_t(1+h)\left(1-\frac{1}{2}\delta\right)-\Pi_0\Bigg)\int_0^1 \psi_i\phi_j'\phi_k'' d\xi. \\ &-\left(\gamma+\frac{1}{2}\mathcal{U}^2\varepsilon c_t(1+h)\right)\int_0^1 \xi\psi_i\phi_j'\phi_k'' d\xi-\int_0^1 \psi_i\phi_j''\phi_k''' d\xi-\int_0^1 \psi_i\phi_j'\phi_k^{(4)}\ d\xi,\end{aligned}$$

$$A_{ijk}^{\ 2} = \frac{1}{2}\mathcal{U}\sqrt{\beta}\ \varepsilon(c_t-c_n)\int_0^1 \psi_i\phi_j'\phi_k d\xi - 2\chi\mathcal{U}\sqrt{\beta}\int_0^1 \psi_i\phi_j'\phi_k' d\xi,$$

$$A_{ijk}^{\ 3} = \frac{1}{4}\beta\varepsilon\ c_t\int_0^1 \psi_i\phi_j\phi_k d\xi, \qquad A_{ijk}^{\ 4} = -\chi\beta\int_0^1 \psi_i\phi_j'\phi_k d\xi,$$

$$B_{ijkl}^{\ 1} = -\frac{1}{2}\mathcal{U}^2\varepsilon\ c_d\int_0^1 \psi_i\phi_j'\phi_k'\left|\phi_l'\right| d\xi, \qquad B_{ijkl}^{\ 2} = -\frac{1}{2}\mathcal{U}\sqrt{\beta}\varepsilon\ c_d\int_0^1 \psi_i\phi_j'\phi_k\left|\phi_l'\right| d\xi,$$

$$B_{ijkl}^{\ 3} = -\frac{1}{2}\mathcal{U}\sqrt{\beta}\varepsilon\ \mathrm{c_d}\int_0^1 \psi_i\phi_j'\phi_k'\left|\phi_l\right| d\xi, \qquad B_{ijkl}^{\ 4} = -\frac{1}{2}\beta\varepsilon\ c_d\int_0^1 \psi_i\phi_j'\phi_k\left|\phi_l\right| d\xi,$$

---

* Here, λ_i^u is the ith dimensionless eigenvalue of a bar in axial vibration and ς is the damping ratio.

$$M_{ij}^{\ v}=\left(1+\left(\chi-1\right)\beta\right)\int_0^1\phi_i\phi_j d\xi,$$

$$C_{ij}^{\ v}=\frac{1}{2}\mathcal{U}\varepsilon\ c_n\sqrt{\beta}\int_0^1\phi_i\phi_j d\xi+2\chi\mathcal{U}\sqrt{\beta}\int_0^1\phi_i\phi_j' d\xi+2\varsigma\left(\lambda_i^v\right)^{2\,\dagger},$$

$$\begin{aligned}K_{ij}^{\ v}=&\left(\gamma+\frac{1}{2}\mathcal{U}^2\varepsilon\left(c_n+h\ c_t\right)\right)\int_0^1\phi_i\phi_j' d\xi\\&-\left(\gamma\left(1-\frac{1}{2}\delta\right)-\mathcal{U}^2\chi+\left(1-2\nu\right)\overline{\Pi}\delta+\overline{\Gamma}\delta\right.\\&\qquad\left.+\frac{1}{2}\mathcal{U}^2c_b\left(1-\delta\right)+\frac{1}{2}\mathcal{U}^2\varepsilon c_t\left(1+h\right)\left(1-\frac{1}{2}\delta\right)\right)\int_0^1\phi_i\phi_j'' d\xi\\&+\left(\gamma+\frac{1}{2}\mathcal{U}^2\varepsilon c_t\left(1+h\right)\right)\int_0^1\xi\phi_i\phi_j'' d\xi+\int_0^1\phi_i\phi_j^{(4)}\ d\xi,\end{aligned}$$

$$\begin{aligned}D_{ijk}^{\ 1}=&\left(\gamma+\frac{1}{2}\mathcal{U}^2\varepsilon c_t\left(1+h\right)\right)\int_0^1\phi_i\psi_j\phi_k'' d\xi\\&+\left(\gamma\left(1-\frac{1}{2}\delta\right)-2\ \mathcal{U}^2\chi+\left(1-2\nu\right)\overline{\Pi}\delta+\overline{\Gamma}\delta\right.\\&\qquad\left.+\frac{1}{2}\mathcal{U}^2c_b\left(1-\delta\right)+\frac{1}{2}\mathcal{U}^2\varepsilon c_t\left(1+h\right)\left(1-\frac{1}{2}\delta\right)-\Pi_0\right)\int_0^1\phi_i\psi_j''\phi_k' d\xi\\&-\left(\gamma+\frac{1}{2}\mathcal{U}^2\varepsilon\ c_t\left(1+h\right)\right)\int_0^1\xi\phi_i\psi_j''\phi_k' d\xi-\frac{1}{2}\mathcal{U}^2\varepsilon\ \left(c_n-c_t\right)\int_0^1\phi_i\psi_j'\phi_k' d\xi\\&+\left(\gamma\left(1-\frac{1}{2}\delta\right)-4\mathcal{U}^2\chi+\left(1-2\nu\right)\overline{\Pi}\delta+\overline{\Gamma}\delta\right.\\&\qquad\left.+\frac{1}{2}\mathcal{U}^2c_b\left(1-\delta\right)+\frac{1}{2}\mathcal{U}^2\varepsilon c_t\left(1+h\right)\left(1-\frac{1}{2}\delta\right)-\Pi_0\right)\int_0^1\phi_i\psi_j'\phi_k'' d\xi\\&-\left[\gamma+\frac{1}{2}\mathcal{U}^2\varepsilon c_t\left(1+h\right)\right]\int_0^1\xi\phi_i\psi_j'\phi_k'' d\xi-\left[\gamma+\frac{1}{2}\mathcal{U}^2\varepsilon c_t\left(1+h\right)\right]\left(1-\delta\right)\int_0^1\phi_i\psi_j\left(1\right)\phi_k'' d\xi\\&-4\int_0^1\phi_i\psi_j''\phi_k''' d\xi-3\int_0^1\phi_i\psi_j'''\phi_k'' d\xi-2\int_0^1\phi_i\psi_j'\phi_k^{(4)} d\xi-\int_0^1\phi_i\psi_j^{(4)}\phi_k' d\xi,\end{aligned}$$

$$D_{ijk}^{\ 2}=-\chi\mathcal{U}\sqrt{\beta}\left(3\int_0^1\phi_i\psi_j'\phi_k' d\xi+2\int_0^1\phi_i\psi_j\phi_k'' d\xi\right),$$

$$D_{ijk}^{\ 3}=\frac{1}{2}\mathcal{U}\sqrt{\beta}\varepsilon c_n\int_0^1\phi_i\psi_j'\phi_k d\xi-4\chi\mathcal{U}\sqrt{\beta}\int_0^1\phi_i\psi_j'\phi_k' d\xi,$$

---

† λ_i^v is the *i*th dimensionless eigenvalue of a beam in transverse vibration.

$$D_{ijk}{}^{4}=\frac{1}{2}\beta\varepsilon c_n\int_0^1\phi_i\psi_j\phi_k d\xi-2\chi\beta\int_0^1\phi_i\psi_j\phi_k' d\xi, \qquad D_{ijk}{}^{5}=-\chi\beta\int_0^1\phi_i\psi_j\phi_k' d\xi,$$

$$E_{ijk}{}^{1}=\frac{1}{2}\mathcal{U}^2\varepsilon c_d\int_0^1\phi_i\phi_j'\left|\phi_k'\right|d\xi, \qquad E_{ijk}{}^{2}=\frac{1}{2}\mathcal{U}\sqrt{\beta}\varepsilon\ c_d\int_0^1\phi_i\phi_j\left|\phi_k'\right|d\xi,$$

$$E_{ijk}{}^{3}=\frac{1}{2}\mathcal{U}\sqrt{\beta}\varepsilon\ c_d\int_0^1\phi_i\phi_j'\left|\phi_k\right|d\xi, \qquad E_{ijk}{}^{4}=\frac{1}{2}\beta\varepsilon\ c_d\int_0^1\phi_i\phi_j\left|\phi_k\right|d\xi,$$

$$\begin{aligned}F_{ijkl}{}^{1}=&-\frac{1}{2}\left(\gamma+\mathcal{U}^2\varepsilon\left(c_n+\frac{1}{2}c_t\left(h-1\right)\right)\right)\int_0^1\phi_i\phi_j'\phi_k'\phi_l'\ \ d\xi\\ &+\left(\frac{3}{2}\gamma\left(1-\frac{1}{2}\delta\right)-\frac{5}{2}\mathcal{U}^2\chi+\frac{3}{2}(1-2\nu)\bar{\Pi}\delta+\frac{3}{2}\bar{\Gamma}\delta\right.\\ &\quad\left.+\frac{3}{4}\mathcal{U}^2c_b\left(1-\delta\right)+\frac{3}{4}\mathcal{U}^2\varepsilon c_t\left(1+h\right)\left(1-\frac{1}{2}\delta\right)-\frac{3}{2}\Pi_0\right)\int_0^1\phi_i\phi_j'\phi_k'\phi_l''\ \ d\xi\\ &-\left(\frac{3}{2}\gamma+\frac{3}{4}\mathcal{U}^2\varepsilon c_t\left(1+h\right)\right)\int_0^1\xi\phi_i\phi_j'\phi_k'\phi_l''\ \ d\xi-2\int_0^1\phi_i\phi_j'\phi_k'\phi_l^{(4)}d\xi-8\int_0^1\phi_i\phi_j'\phi_k''\phi_l'''\ \ d\xi\\ &-2\int_0^1\phi_i\phi_j''\phi_k''\phi_l''\ \ d\xi,\end{aligned}$$

$$F_{ijkl}{}^{2}=\frac{1}{2}\mathcal{U}\varepsilon\beta\left(c_t-c_n\right)\int_0^1\phi_i\phi_j'\phi_k'\phi_l\ \ d\xi-\chi\mathcal{U}\sqrt{\beta}\left(\frac{7}{2}\int_0^1\phi_i\phi_j'\phi_k'\phi_l'\ \ d\xi+\frac{3}{2}\int_0^1\phi_i\phi_j'\phi_k''\phi_l\ \ d\xi\right),$$

$$F_{ijkl}{}^{3}=\frac{1}{4}\beta\varepsilon\left(c_t-c_n\right)\int_0^1\phi_i\phi_j'\phi_k\phi_l\ \ d\xi-\frac{3}{2}\chi\beta\int_0^1\phi_i\phi_j'\phi_k\phi_l'\ \ d\xi,$$

$$F_{ijkl}{}^{4}=-\frac{1}{4}\frac{\beta^{3/2}\varepsilon c_n}{\mathcal{U}}\int_0^1\phi_i\phi_j\phi_k\phi_l\ \ d\xi, \qquad F_{ijkl}{}^{5}=-\chi\beta\int_0^1\phi_i\phi_j'\phi_k'\phi_l\ \ d\xi.$$

B. An Inextensible or Extensible Cantilever Cylinder Subjected to either an Axial Flow or a Tip-Concentrated Force

In this appendix, the dynamical behaviour of a cantilevered cylinder subjected to axial flow, with an inextensible or extensible centreline is studied very briefly, using the inextensible model of Lopes et al. (2002) and the extensible model of this thesis (presented in Chapter 2). This study is then extended to the case where instead of being subjected to axial flow, the cylinder is subjected to a tip-concentrated force. Three possible arrangements for the forces are considered: (i) a fixed-direction force, (ii) a follower force, and (iii) a subtangential follower force. In all cases, the results are shown in the form of bifurcation diagrams. A more detailed discussion on different problems presented in this appendix can be found in a report (Modarres-Sadeghi, 2006).

B.1. Cantilever cylinder subjected to axial flow

In this section, the nonlinear behaviour of a cantilever cylinder subjected to axial flow is studied. Figure B-1 shows such a cylinder, which is terminated by a short, ogival end. This system has already been studied in a three-part paper by Païdoussis et al. (2002), Lopes et al. (2002) and Semler et al. (2002) with the assumption of an inextensible centreline for the cylinder, leading to one partial differential equation as the governing equation of motion. As discussed in Chapter 1, their results show that the cylinder loses stability by a pitchfork bifurcation and the system buckles in its first mode, followed by a buckling in the second mode; at higher flow the system undergoes a Hopf bifurcation after re-gaining its equilibrium position, as shown in the bifurcation diagram of this case in Figure B-2(a).

Using the nonlinear model of this thesis, a cantilever cylinder can be analysed assuming its centreline to be extensible. Nonlinear equations of motion as presented in Chapter 2 (Equations (2-61) and (2-62)) are used as the governing equations, while the boundary conditions at the tip due to the tapering end are

$$-EAu' - (pA)_L + \tfrac{1}{2}\rho D U^2 C_T \left(\overline{s}_e + s_e h\right) + (m - \rho A) s_e g = 0, \tag{B-1}$$

$$\begin{gathered}-EIv'''' + (m - \rho A) g s_e v' + f \chi \rho \left(\ddot{v} + U\dot{v}'\right) A s_e - f \chi \rho U \left(\dot{v} + Uv'\right) A \\ + \tfrac{1}{2}\rho D \overline{s}_e U^2 C_N \left(\dot{v} + Uv'\right) + \tfrac{1}{2}\rho D U^2 C_T s_e h v' + m s_e \ddot{v} = 0,\end{gathered} \tag{B-2}$$

where $s_e = \dfrac{1}{A}\int_{L-l}^{L} A(s)\, ds$, $\overline{s}_e = \dfrac{1}{D}\int_{L-l}^{L} D(s)\, ds$; $f \to 1$ is taken for a well-streamlined end, and $f \to 0$ for a blunt end. The other parameters are the same as those used in the dimensional equations of motion (Equations (2-61) and (2-62)).

The dimensionless nonlinear equations of motion can be written in the form of

$$F_u\left(\zeta(\xi,\tau), \eta(\xi,\tau), \mathcal{U}\right) = 0, \tag{B-3}$$

$$F_v\left(\zeta(\xi,\tau), \eta(\xi,\tau), \mathcal{U}\right) = 0, \tag{B-4}$$

and the boundary conditions in the form of

$$\zeta(0,\tau) = -\zeta'(1,\tau) + B_u\left(\zeta(\xi,\tau), \mathcal{U}\right) = 0, \tag{B-5}$$

$$\eta(0,\tau) = \eta'(0,\tau) = \eta''(1,\tau) = -\eta'''(1,\tau) + B_v\left(\eta(\xi,\tau), \mathcal{U}\right) = 0, \tag{B-6}$$

where, $B_u\left(\zeta(\xi,\tau), \mathcal{U}\right)$ and $B_v\left(\eta(\xi,\tau), \mathcal{U}\right)$ represent complementary terms in the boundary conditions due to the tapering end. An alternative way of formulating the problem is [see Lopes et al. (2002)]:

$$F_u\left(\zeta(\xi,\tau), \eta(\xi,\tau), \mathcal{U}\right) + \delta(\xi - 1) B_2\left(\zeta(\xi,\tau), \mathcal{U}\right) = 0, \tag{B-7}$$

$$F_v\left(\zeta(\xi,\tau), \eta(\xi,\tau), \mathcal{U}\right) + \delta(\xi - 1) B_v\left(\eta(\xi,\tau), \mathcal{U}\right) = 0, \tag{B-8}$$

where, $\delta(\xi - 1)$ is the Dirac delta function.

The eigenfunctions of a cantilever cylinder for the transverse deformation and those of a fixed-free bar for the axial deformation are used to discretize the partial differential equations. The bifurcation diagram of Figure B-2(b) shows that the system is stable up to $\mathcal{U} = 2.1$, at which a pitchfork bifurcation occurs and the original stable equilibrium position of the cylinder becomes unstable. Although the inextensible model predicts a supercritical pitchfork bifurcation, here, two nonzero unstable branches emanate from the pitchfork bifurcation point, and both go backward. This is a sign of a subcritical pitchfork bifurcation, in which case, one would expect these two unstable branches to reach a limit point at some flow velocity $\mathcal{U} < 2.1$ and then become stable, giving rise to the possibility of a sudden jump in the amplitude of the cylinder from zero to a relatively large value, in a range of flow velocity around $\mathcal{U} = 2.1$. This is not obtained in the numerical results. In fact, for this case, although the solution in the vicinity of the critical point behaves like a subcritical pitchfork bifurcation, the fold and the stable non-trivial solution thereafter cannot be seen. This can be justified as follows: in the present problem the third-order model is valid in the vicinity of the pitchfork bifurcation, where the amplitude of displacement is not large, showing the existence of a subcritical pitchfork bifurcation, but to obtain the nonzero stable solution, one needs a fifth-order model. A similar problem has been discussed in Païdoussis (1998, p. 54), where Equation (2.165) is cubic in the stiffness terms ($O(\epsilon^3)$); so an unstable nonzero solution is obtained in Figure 2.12. Once a fifth-order component is added as in (2.166), both an unstable and a stable solution are obtained as we see in Figure 2.13. The dynamical behaviour related to the second pitchfork bifurcation in Figure B-2(b) (at $\mathcal{U} = 5.6$) suggests an unstable supercritical behaviour. However, in view of the foregoing comments on the necessity of a higher-order mode to follow the dynamics beyond the first bifurcation and at least up to the Hopf bifurcation (* in the figure), the interpretation of the dynamics remains uncertain. In order to investigate if this behaviour is particular to the present problem or not, the simpler problem of a beam (column) under a tip-concentrated force is studied.

B.2. A cantilever beam subjected to tip-concentrated force

The problem of buckling of a beam (column) subjected to a tip-concentrated force is studied in this section. The load can be (i) of fixed direction (Euler's problem); (ii) tangential to the deflection curve (Beck's problem); or (iii) lying slightly ahead or behind the tangent to the elastic line in the process of deformation (Figure B-3). The main interest here is the behaviour of the beam after the point of first instability using a nonlinear model. The first critical points, especially for the case of Euler's and Beck's problems, are very well documented and can be found in the text books (e.g. Ziegler, 1952): $\overline{P} = PL^2/EI$ =2.48 is the critical value for the onset of buckling in Euler's problem and $\overline{P} = 20.05$ is the critical value for the onset of flutter in Beck's problem with no structural damping. The effect of damping on the onset of instability in the latter case has had the most interest for the researchers.

The nonlinear equations of motion for an inextensible or extensible column under various tip-concentrated force are given in Table B-1. Figure B-4 Shows the bifurcation diagrams of an inextensible and extensible column under a fixed-direction force (Euler problem). According to the inextensible theory, the column buckles at $\overline{P} = 2.48$ and the amplitude of buckling increases with force, thereafter. The extensible theory, however, shows a behaviour similar to the one discussed in Section B.1 for the corresponding extensible model: two unstable backward branches are observed with no fold and no stable solution thereafter. If the force acting on the tip is always tangential to the deflection curve (a follower force), the cylinder loses stability by a Hamiltonian Hopf bifurcation at $\overline{P} = 17.03$ and undergoes periodic oscillations thereafter (Figure B-5). It is the type of damping assumed for the results shown in this figure that has produced a critical value for the bifurcation point less than $\overline{P} = 20.05$. Destabilization by damping should not be surprising, as the system is nonconservative. In this case, both inextensible and extensible models give the same results.

A system under subtangential follower force can undergo either a pitchfork or a Hopf bifurcation, depending on the angle that the force makes with the deflection curve. This angle is measured by the parameter γ. It can be shown that for γ <0.5 the system undergoes a pitchfork bifurcation, while for γ >0.5 a Hopf bifurcation destabilizes the system. The case of $\gamma = 0$ and $\gamma = 1$ correspond to Euler's and Beck's problem, respectively. Figure B-6 shows the bifurcation diagrams of this system for three different values of γ. The first bifurcation diagram (Figure B-6(a)), which is for $\gamma = 0$, corresponds to the one shown in Figure B-4(a) for the Euler's problem. The second bifurcation diagram (Figure B-6(b)) is for $\gamma = 0.3$ where the cylinder loses stability by a pitchfork bifurcation and q_1 increases with force for $\overline{P} < 12$. For $\overline{P} > 12$, the value of the first generalized coordinate of the system in the transverse direction (q_1) decreases while q_2 increases (not shown), indicating a change in the buckling mode from the first to the second mode. If $\gamma = 0.7$, the cylinder loses stability by a Hopf bifurcation and undergoes periodic motions thereafter, showing a behaviour very similar to that shown in Figure B-5 for Beck's problem.

The unstable backward branches were observed in Euler's problem for an extensible column as well as the problem of an extensible cantilever cylinder in axial flow. The main reason for which the subsequent stable nonzero solution was not found in both cases is that the model used here is correct only to third-order magnitude, while one needs a model which takes into account terms of higher order of magnitude (fifth order) to find a stable nonzero static solution.

Problem	Equation of motion	BC
Inextensible Euler	$m\ddot{v}+c\dot{v}+EI\left(v^{(4)}+4v'v''v'''+v''^2+v^{(4)}v'^2\right)+P\left(v''+v'^2v''\right)=0$	$EIv'_L=Pv'_L$, $v''_L=0.$
Extensible Euler	$m\ddot{u}+c\dot{u}-EA\left(u''+v'v''\right)-EI\left(v''v'''+v'v^{(4)}\right)-Pv'v''=0,$ $m\ddot{v}+c\dot{v}-EA\left(v'u''+v''u'+\frac{3}{2}v'^2v''\right)+P\left(v''-v'u''-v''u'-\frac{3}{2}v'^2v''\right)$ $+EI\left(v^{(4)}-8v'v''v'''-v'u''-2v'^2v^{(4)}-2v''^3-2u'v^{(4)}-4u''v''-3u'''v''\right)=0,$	$u'_L=0,$ $EIv'_L=Pv'_L$, $v''_L=0.$
Inextensible Beck	$m\ddot{v}+c\dot{v}+EI\left(v^{(4)}+4v'v''v'''+v''^2+v^{(4)}v'^2\right)+P\left(v''+v'^2v''\right)=0$	$v'_L=0,$ $v''_L=0.$
Extensible Beck	$m\ddot{u}+c\dot{u}-EA\left(u''+v'v''\right)-EI\left(v''v'''+v'v^{(4)}\right)-Pv'v''=0,$ $m\ddot{v}+c\dot{v}-EA\left(v'u''+v''u'+\frac{3}{2}v'^2v''\right)+P\left(v''-v'u''-v''u'-\frac{3}{2}v'^2v''\right)$ $+EI\left(v^{(4)}-8v'v''v'''-v'u''-2v'^2v^{(4)}-2v''^3-2u'v^{(4)}-4u''v''-3u'''v''\right)=0.$	$u'_L=0,$ $v'_L=0,$ $v''_L=0.$
Inextensible subtangential	$m\ddot{v}+c\dot{v}+EI\left(v^{(4)}+4v'v''v'''+v^{(4)}v'^2+v''^3\right)+Pv''$ $-\frac{1}{2}P\gamma^2v''{v'_L}^2+P\gamma v'v''v'_L=0$	$-EIv'''=P\left(-1+\gamma\right)v'_L$ $-\frac{1}{2}P\gamma {v'_L}^2$ $+P\left[\frac{1}{2}\gamma^2-\frac{1}{6}\gamma\left(1+\gamma^2\right)\right]{v'_L}^3,$ $v''_L=0.$

Table B-1 Nonlinear equations of motion for the problems discussed in Section B.2, together with the corresponding boundary conditions at the tip

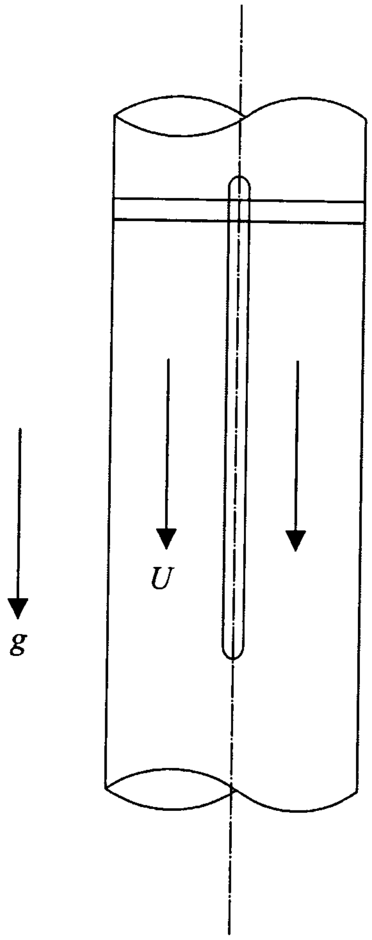

Figure B-1 A cantilever cylinder with a tapering end subjected to axial flow.

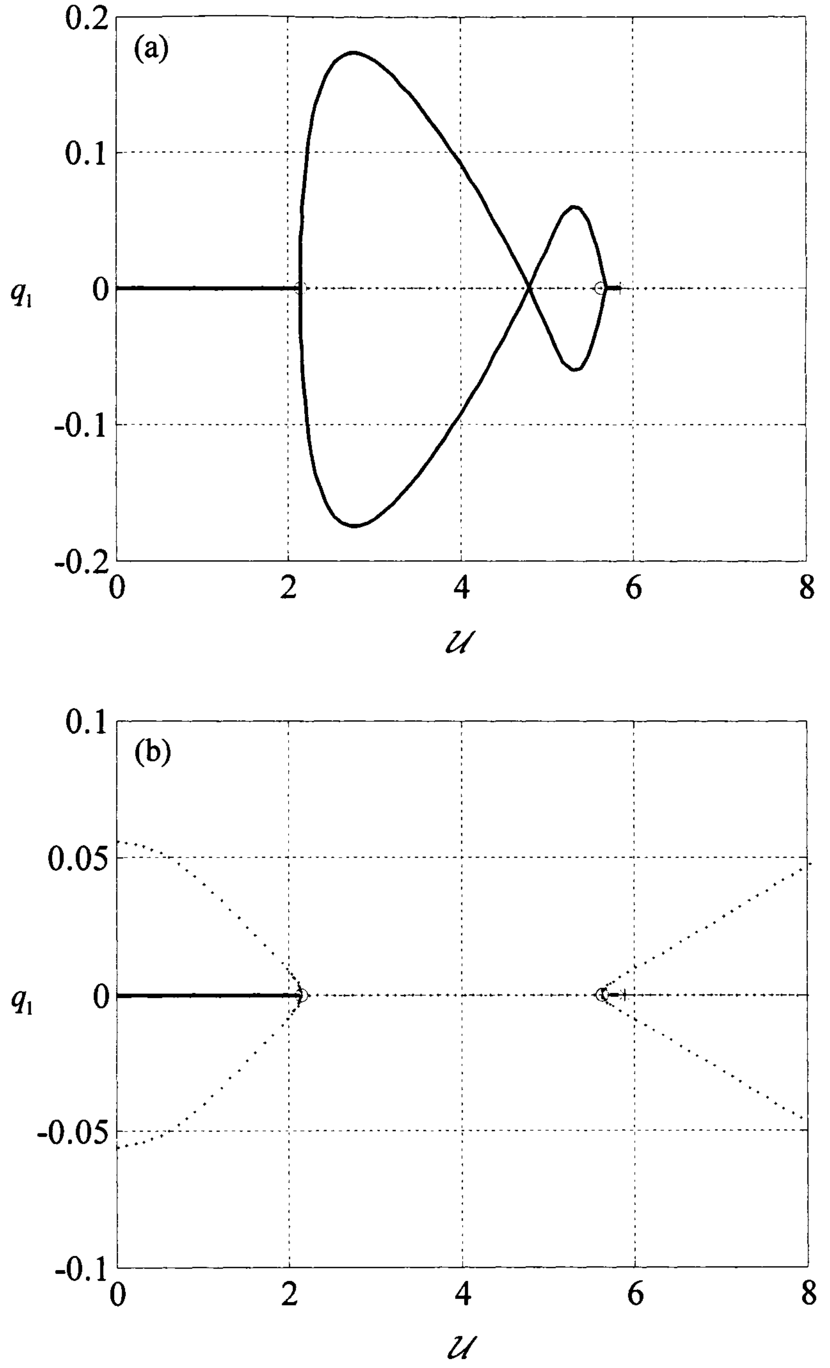

Figure B-2 A typical bifurcation diagram for a cantilever cylinder subjected to axial flow: (a) inextensible model, (b) extensible model.

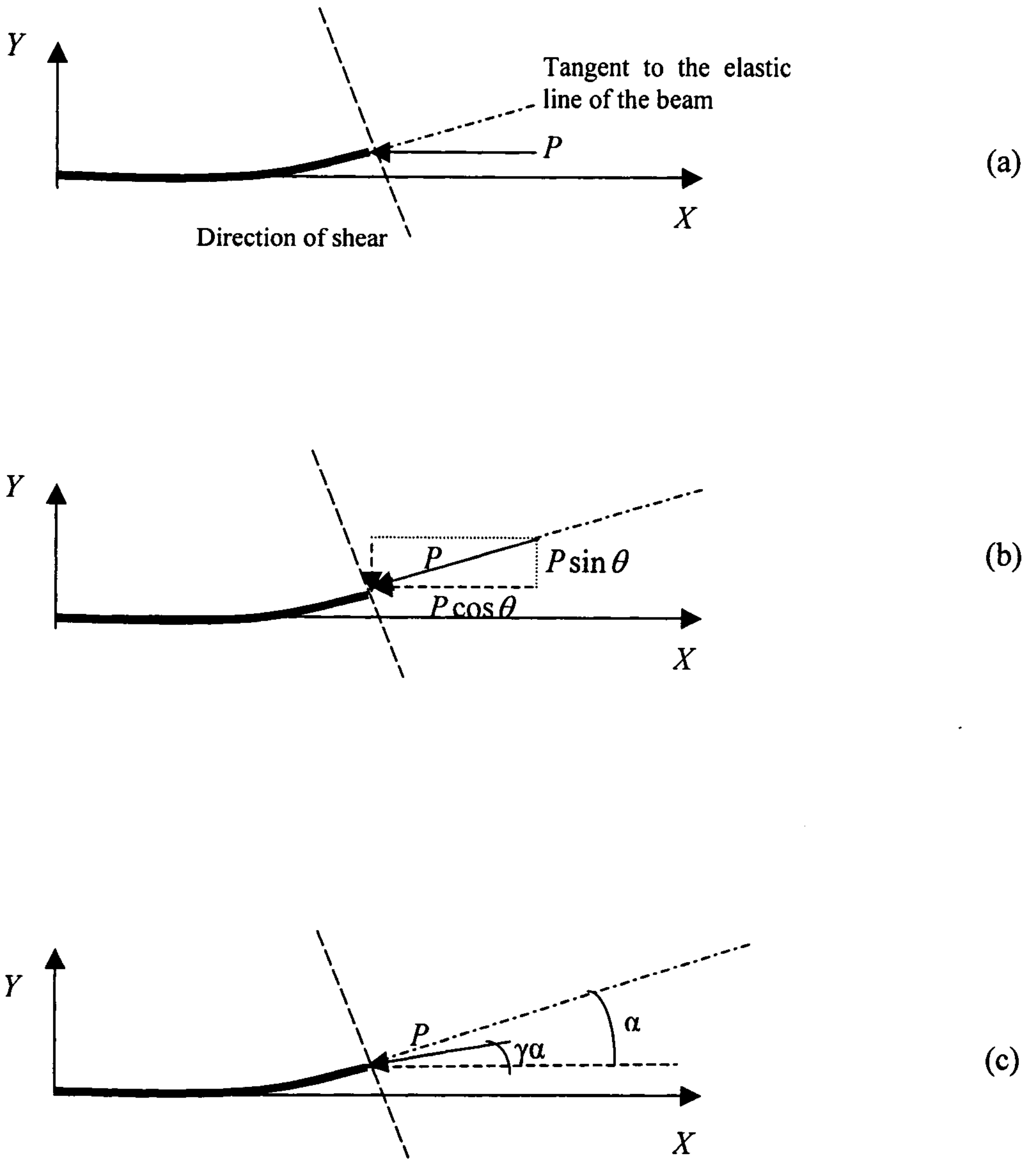

Figure B-3 A cantilever beam (column) subjected to a tip-concentrated force: (a) a fixed-direction force (Euler's problem); (b) a follower force (Beck's problem); and (c) a subtangential follower force.

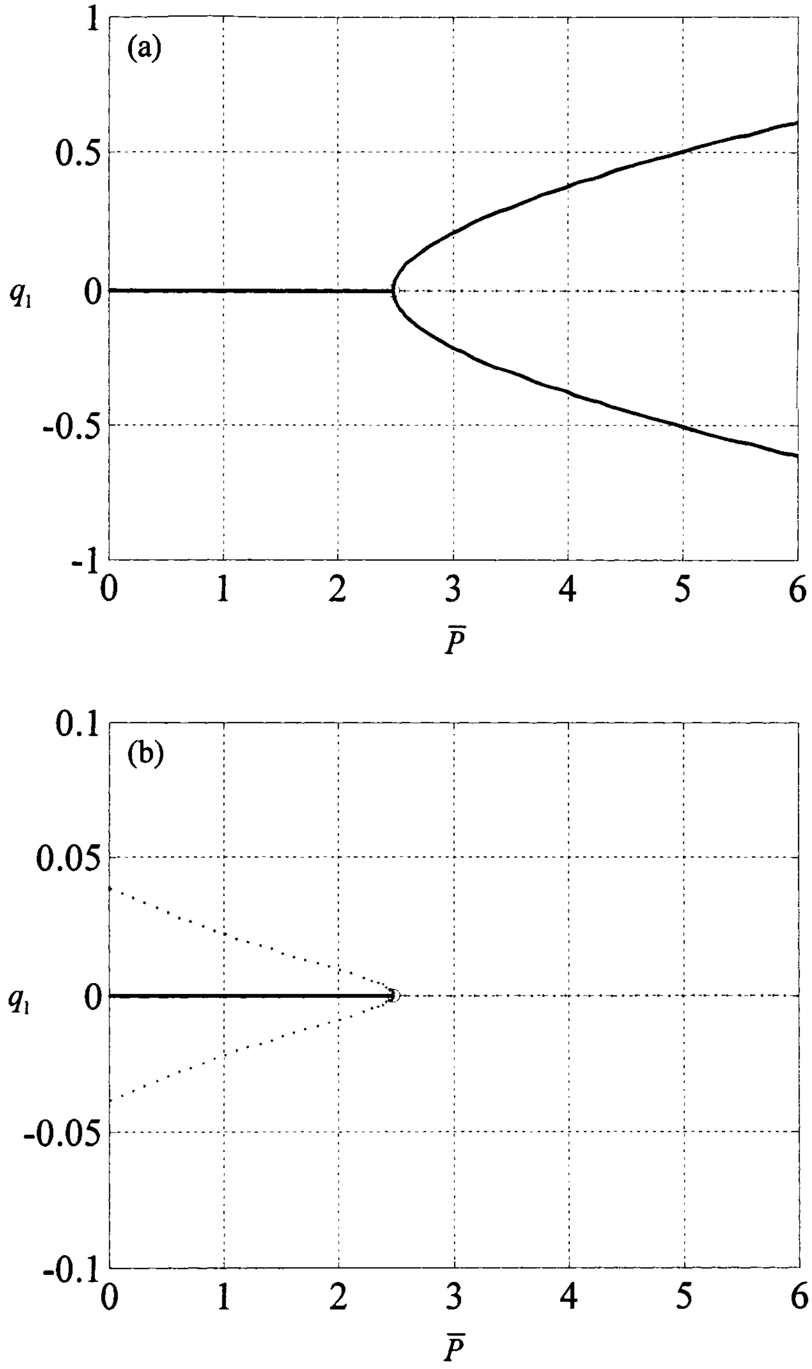

Figure B-4 Typical bifurcation diagram for a cylinder subjected to a fixed-direction tip-concentrated force (system of Figure B-3(a)): (a) inextensible model, (b) extensible model.

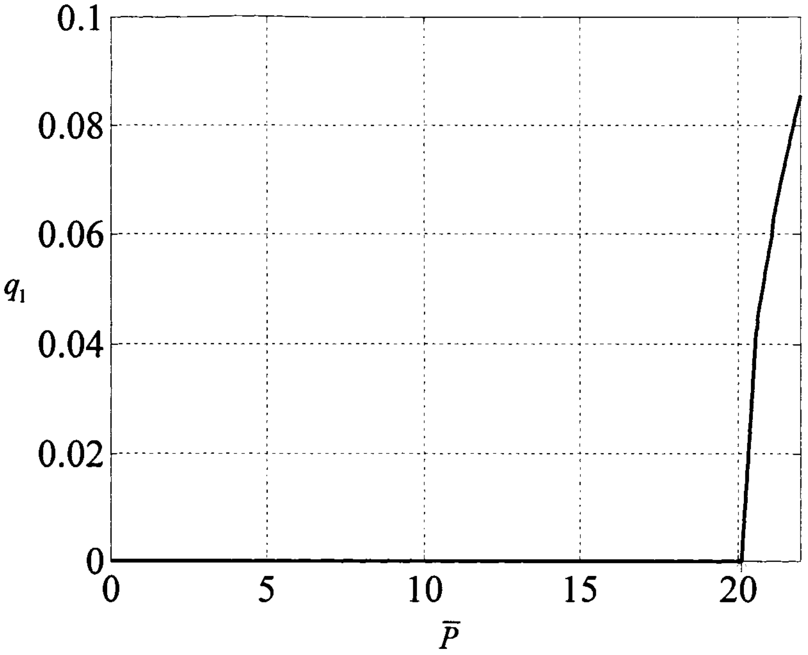

Figure B-5 Typical bifurcation diagram for an inextensible or extensible cylinder subjected to a tip-concentrated follower force (system of Figure B-3(b)).

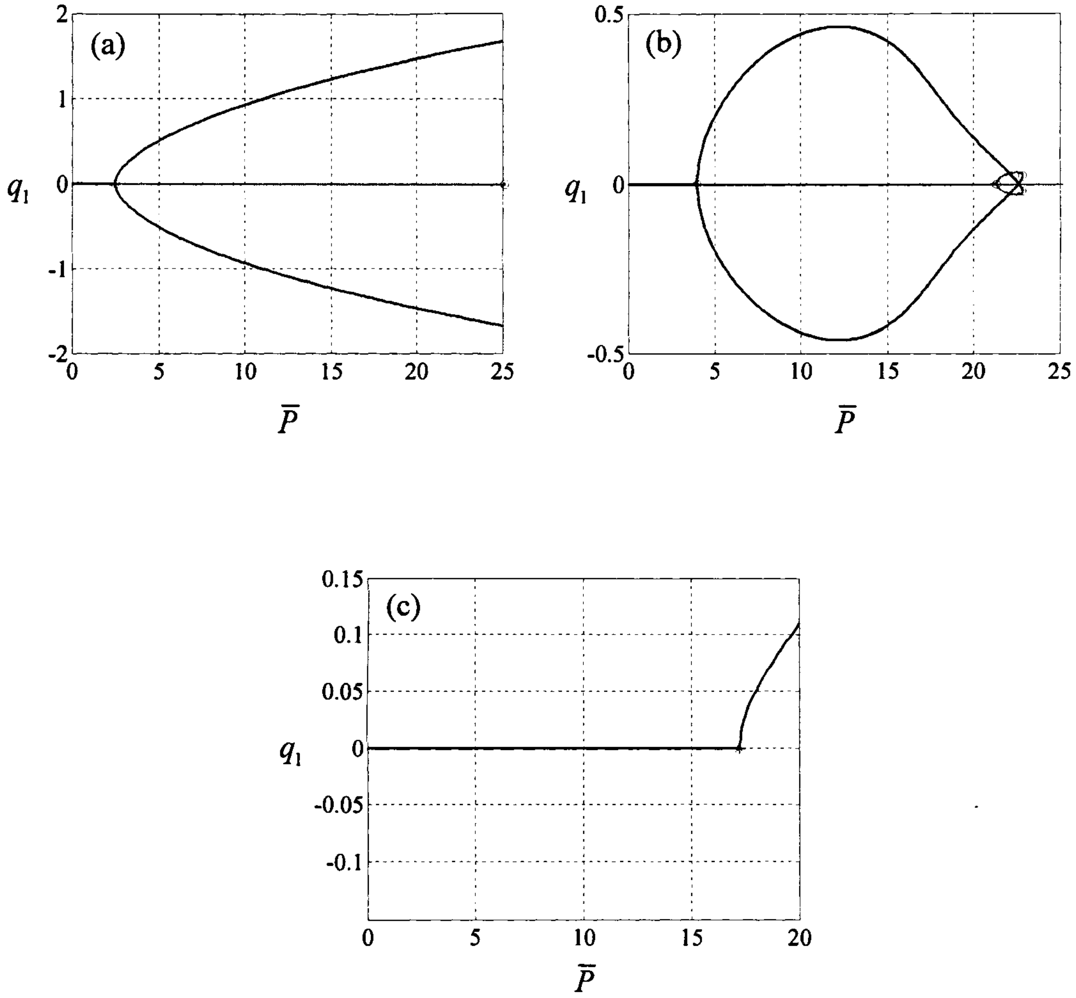

Figure B-6 Typical bifurcation diagram for an inextensible cylinder subjected to a tip-concentrated subtangential follower force (system of Figure B-3(c)) with (a) γ =0, (b) γ =0.3, (c) γ =0.7.

C. Experiments to Measure the Flexural Rigidity and the Damping Factor of the Cylinder

In this appendix, the experiments conducted on a silicone rubber cylinder to measure the flexural rigidity and the modal damping coefficients are discussed. These values have been used in the calculations of Section 6.5 to compare the theoretical results with the results of the third series of experiments.

C.1. Measurement of the flexural rigidity

In order to determine the flexural rigidity of the cylinder, following the method discussed in Païdoussis (1998, Appendix D), the cylinder was hung vertically, cantilevered, and was excited in its first mode. This was done by simply holding the cantilevered cylinder in approximately its first mode configuration and then releasing it. The amplitude of the resulting oscillatory motion was measured by using a non-contacting motion follower device (Figure C-1(a)). The damped frequency of oscillation was then calculated by constructing the PSD plot of this motion (Figure C-1(b)). For the small-diameter cylinder used in the experiments (Table 6-5), it was found that $f_1 = 1.14\ \mathrm{Hz}$. Then, following equation (D.2) in Païdoussis (1998),

$$\frac{\gamma}{\left[\mathrm{Re}(\omega_1)\right]^2} = \frac{g}{\left[\mathrm{Re}(\Omega_1)\right]^2 L} = \frac{9.81}{7.1626^2 \times 0.435} = 0.4396,$$

where $\Omega_1 = 2\pi f_1$ is the dimensional first-mode radian damped frequency, which has been measured in the experiment. Having found the numerical value for $\gamma / \left[\mathrm{Re}(\omega_1)\right]^2$ and using Figure D.4 in Païdoussis (1998), the corresponding gravity parameter can be found: $\gamma \simeq 18$. Then using the nondimensional relation for the gravity parameter ($\gamma = mgL^3/EI$), one can find the flexural rigidity: $EI = 0.0065\ \mathrm{N.m^2}$, and therefore Young's modulus can also be found: $E = EI/I = 2.57 \times 10^6$ Pa.

C.2. Measurement of the modal damping coefficient

To measure the modal damping coefficient, the experiments were conducted on the same cylinder but clamped at both ends, because this was the boundary condition used in the experiments. Again, the cylinder was excited in its first mode and the amplitude of the resulting oscillation was measured. A high-pass filter[1] with cut-off frequency of $f_p = 2$ Hz was used to remove the components of the higher modes. Figure C-2(a,b) shows the filtered vibration signal and its corresponding PSD plot. After construction of a "log-amplitude versus time" plot (Figure C-2(c)) one should divide the slope (slope = 0.4) of the resulting graph by the frequency of oscillation ($f = 5.5$ Hz) to find the logarithmic decrement: $\delta_1 = 0.074$, which is equal to the first-mode modal damping coefficient.

In the same manner and by exciting the cylinder in its second mode by a mechanical exciter and using a band-pass filter with $f_{p1} = 6$ Hz and $f_{p2} = 16$ Hz, it was found that the second-mode modal damping coefficient is $\delta_2 = 1.5/13 = 0.111$ (see Figure C-3). Similarly the third and the fourth mode coefficients were measured as $\delta_3 = 0.172$ and $\delta_4 = 0.208$. It was then assumed that the higher mode coefficients were linearly increasing, i.e., δ_5=0.2570 and δ_6=0.3033, etc.

---

[1] A Chebyshev Type 1 infinite impulse response filter was used.

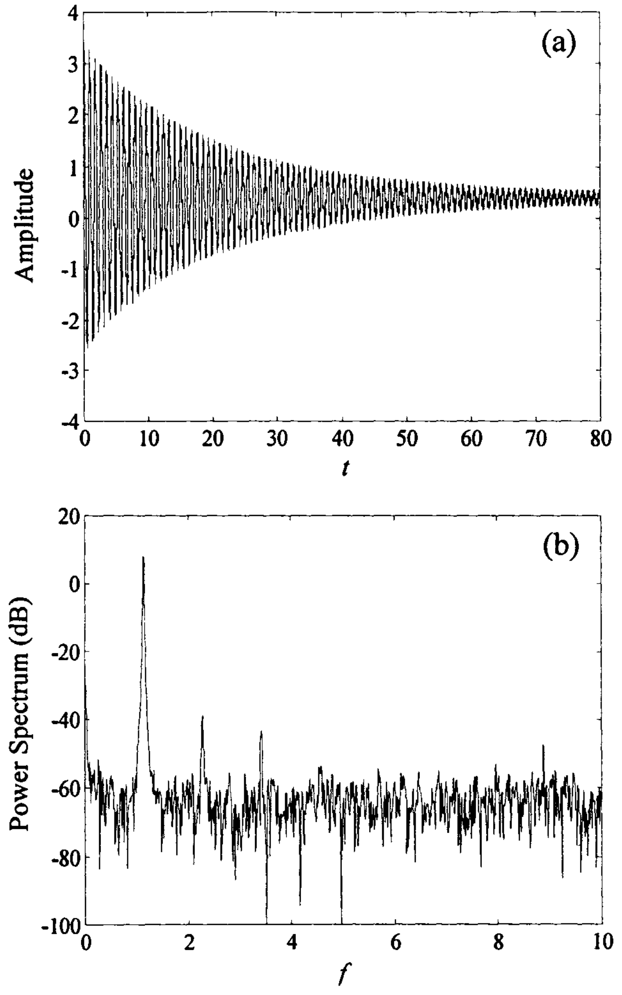

Figure C-1 (a) Time history and (b) PSD plot for the first-mode oscillations of the cantilevered cylinder.

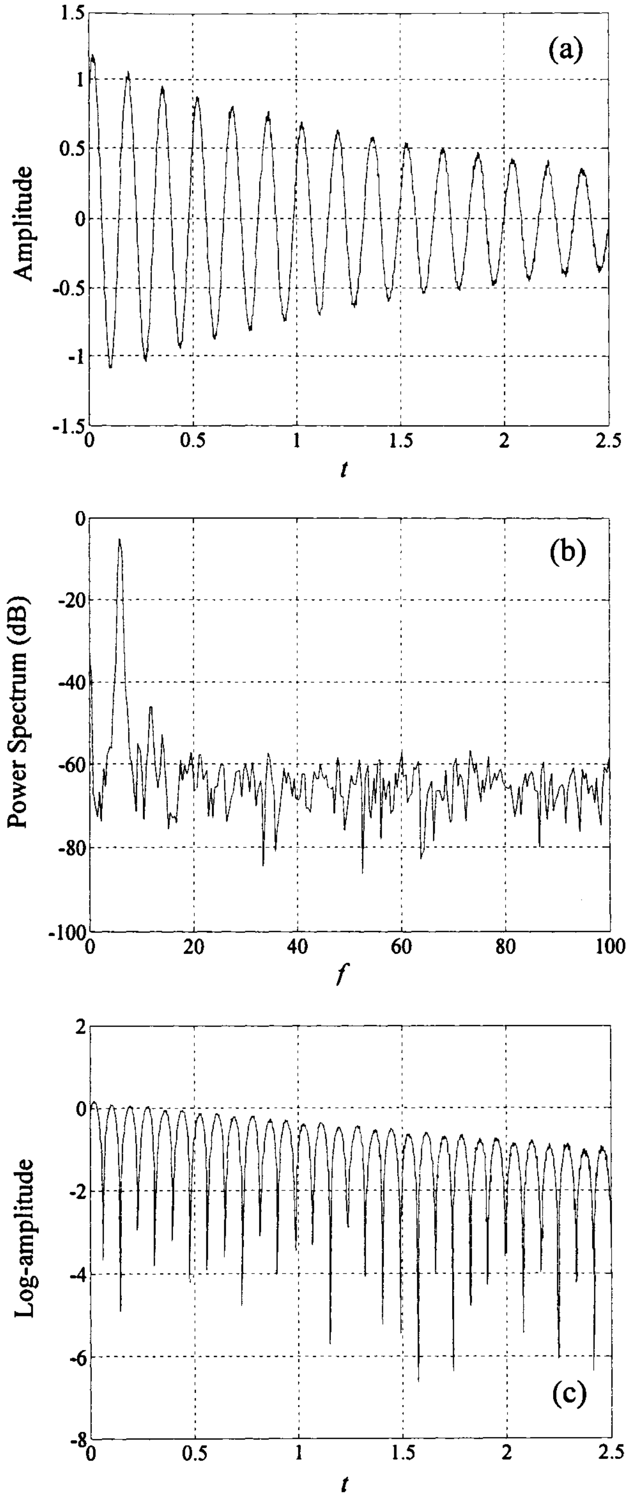

Figure C-2 (a) Time history, (b) PSD plot and (c) the log-amplitude versus time plot of the first-mode oscillation of the clamped-clamped cylinder.

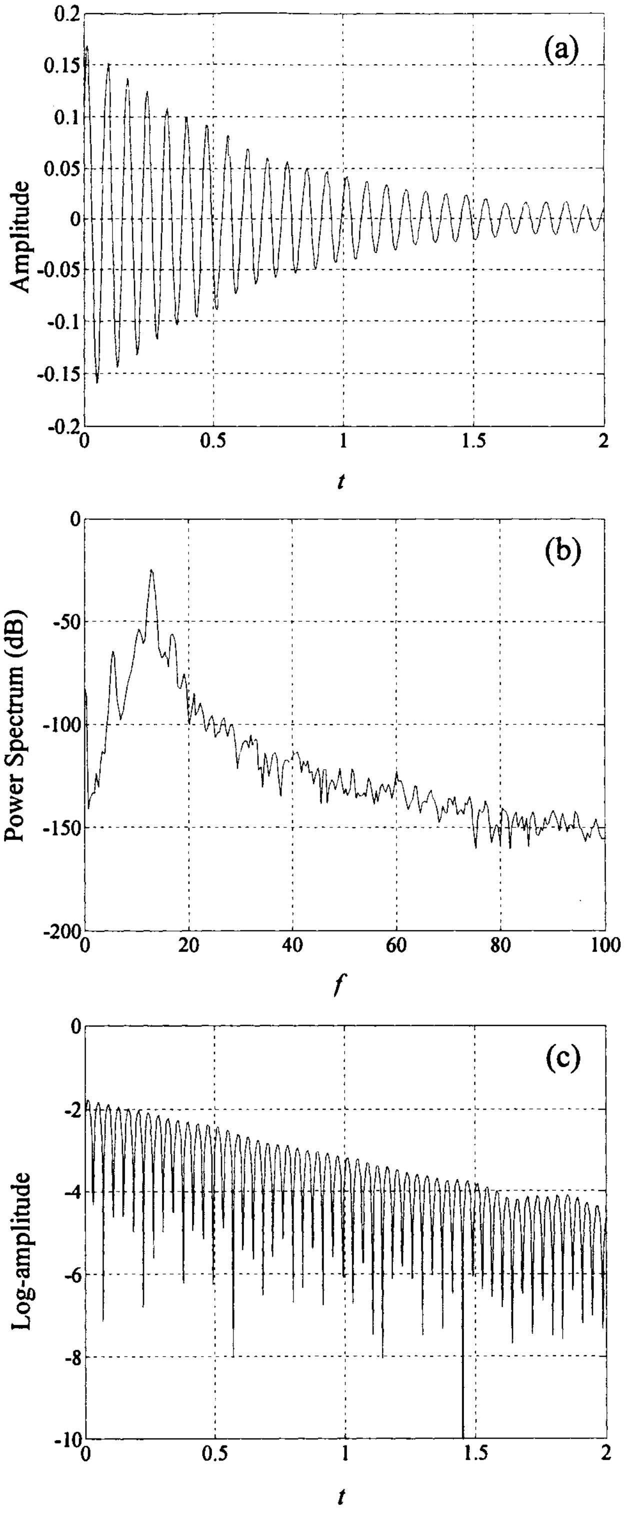

Figure C-3 (a) Time history, (b) PSD plot and (c) the log-amplitude versus time plot of the second-mode oscillation of the clamped-clamped cylinder.